Pristine iota-Carrageenan and Chemically Functionalized Guar gum Polysaccharides for Metal-ion Complexation and CuS-based Nanocomposite Preparation

Le, Trung Anh

[Link to publication](#)

Trung-Anh Le

Pristine iota-Carrageenan and Chemically Functionalized Guar gum Polysaccharides for Metal-ion Complexation and CuS-based Nanocomposite Preparation

Åbo Akademi
University

Trung-Anh Le
Born 1991

Previous studies
  B.Sc. (Hons) in Chemistry, University of Science - VNUHCM, Vietnam 2013
  M.Sc. in Chemistry, Technion - Israel Institute of Technology, Israel 2017

Pristine iota-Carrageenan and Chemically Functionalized Guar gum Polysaccharides for Metal-ion Complexation and CuS-based Nanocomposite Preparation

Trung-Anh Le

Table of contents

Abstract

Natural polysaccharides are ubiquitous in nature and have been widely used in human history as food, materials, fuels, and medicine. To cope with climate crisis and develop a more sustainable economy, promoting the use of natural polysaccharides and other products from oxygenic photosynthesis is of great interest.

In this work, anionic iota-carrageenan (CG) polysaccharide was employed to prepare an iota-carrageenan/CuS covellite (CG/CuS) nanocomposite using a gel/liquid interface precipitation process similarly to chemobrionics. This approach showed how pristine natural polysaccharides such as CG could be effortlessly utilized to develop high-end products for humidity and temperature sensing.

Despite great potential of pristine natural polysaccharides in fabricating novel materials, chemical modifications of natural polysaccharides still play a crucial role in altering and enriching physical, chemical and biological properties, as well as applications of natural polysaccharides. Due to fascinating physicochemical properties, biodegradability, biocompatibility, natural abundancy and low cost, non-ionic guar gum (GG) polysaccharide was chosen as a model material to study how chemical modifications can substantially change properties of GG and extend its applications.

An extensive analysis on reported chemical modification approaches of GG was conducted to examine recent advances in this field, as well as structure-property relationships and applications of GG-based materials. Among the four commonly used chemical reactions on GG, namely, nucleophilic reactions, graft polymerization, partial oxidation and cross-linking, nucleophilic reactions were adopted in this study due to the simplicity, accessibility and diversity of chemical reaction conditions and reagents. Different nucleophilic reactions were successfully carried out in

aqueous medium at room temperature without using toxic organic solvents, allowing the introduction of different organic functional groups and moieties such as amine, thiol, xanthate, benzoic acid, catechol and tosylate to GG. The chemical modification of GG by xanthate and benzoic acid groups was chosen for further study due to their great potential applications.

Being a soft base according to the hard and soft acid and base (HSAB) theory, xanthate functional groups on guar gum-xanthate (GG-X) allowed GG-X to coordinate more strongly to a wide range of soft metal ions, which have great potential in heavy metal removal, wastewater treatment, cross-linked hydrogel preparation, etc. In addition, GG-X offered dual functionalities as a surfactant and an organic matrix in the formation of GG-X/CuS nanocomposite colloidal dispersions, which showed printability and electrical responsiveness in humidity sensing.

Benzoic acid moieties contain aromatic benzene rings and carboxylic acid groups, which offer interesting intermolecular interactions, coordination chemistry and swelling properties at mildly acidic environments to GG. Guar gum-benzoic acid (GG-BA) was found biocompatible to living cells (mouse embryonic fibroblasts and human mammary epithelial cells). Therefore, GG-BA could be explored further as coacervates and cross-linked hydrogels for biomedical applications, e.g. wound dressing, bioadhesives and drug delivery.

Svensk sammanfattning

Naturliga polysackarider är allmänt förekommande i naturen och har använts i stor utsträckning i människohistoria som mat, material, bränsle och medicin. För att klara av klimatkrisen och utveckla en mer hållbar ekonomi är det av stort intresse att främja användningen av naturliga polysackarider och andra produkter från syreproducerande fotosyntes.

I detta arbete användes anjonisk jota-karragenan (CG) polysackarid för att framställa en jota-karragenan/CuS covellit (CG/CuS) nanokomposit med användning av en gel/vätskegränssnittsutfällningsprocess som liknar kemobrionik. Detta tillvägagångssätt visade hur orörda naturliga polysackarider utan ansträngning kunde användas för att utveckla avancerade produkter för fukt- och temperaturavkänning.

Trots den stora potentialen hos orörda naturliga polysackarider vid tillverkning av nya material, spelar kemiska modifieringar av naturliga polysackarider fortfarande en avgörande roll för att förändra och berika fysiska, kemiska och biologiska egenskaper samt tillämpningar av naturliga polysackarider. På grund av fascinerande fysikalisk-kemiska egenskaper, biologisk nedbrytbarhet, biokompatibilitet, naturlig överflöd och låg kostnad, valdes nonjonisk guargummi (GG) polysackarid som modellmaterial för att studera hur kemiska modifieringar kan väsentligt förändra egenskaperna hos GG och utöka dess tillämpningar.

En omfattande analys av rapporterade metoder för kemisk modifiering av GG genomfördes för att undersöka de senaste framstegen inom detta område, såväl som struktur-egenskapsförhållanden och potentiella tillämpningar av GG-baserade material. Bland de fyra vanligaste kemiska reaktionerna på GG, nämligen nukleofila reaktioner, ymppolymerisation, partiell oxidation och tvärbindning, antogs nukleofila reaktioner i denna studie på grund av enkelheten, tillgängligheten och mångfalden av kemiska reaktionsförhållanden och reagens. Olika nukleofila reaktioner genomfördes framgångsrikt i vattenhaltigt medium vid

rumstemperatur utan att använda giftiga organiska lösningsmedel, vilket möjliggjorde införandet av olika organiska funktionella grupper och delar såsom amin, tiol, xantat, bensoesyra, katekol och tosylat till GG. Den kemiska modifieringen av GG av xantat- och bensoesyragrupper valdes för vidare studier på grund av deras stora potentiella tillämpningar.

Som en mjuk bas från teorin om hård och mjuk syra och bas (HSAB) tillät xantatgrupper på guargummi-xantat (GG-X) GG-X att koordinera starkare till ett brett spektrum av mjuka metalljoner, som har stor potential vid borttagning av tungmetaller, avloppsvattenbehandling, tvärbunden hydrogelberedning etc. Dessutom erbjöd GG-X dubbla funktioner som ett ytaktivt ämne och en organisk matris vid bildning av GG-X/CuS nanokomposit kolloidal dispersion, som visade tryckbarhet och elektrisk känslighet vid fuktavkänning.

Bensoesyradelar innehåller aromatiska bensenringar och karboxylsyragrupper, vilket erbjuder intressanta intermolekylära interaktioner, koordinationskemi och svällningsegenskaper i milt sura miljöer till GG. Guargummi-bensoesyra (GG-BA) visade sig vara biokompatibel med levande celler (embryonala musfibroblaster och humana bröstepitelceller). Därför skulle GG-BA kunna utforskas vidare som koacervat och tvärbundna hydrogeler för biomedicinska tillämpningar, t.ex. sårförband, bioadhesiver och läkemedelstillförsel.

List of Publications

Main publications

Paper I **CuS-carrageenan composite grown from the gel/liquid interface**
Morad Zouheir, **Trung-Anh Le**, Janno Torop, Kostiantyn Nikiforow, Muhammad Khatib, Orr Zohar, Hossam Haick, and Tan-Phat Huynh*
ChemSystemsChem 3, no. 4 (2021): e2000063

Paper II **Current advances in the Chemical functionalization and Potential applications of Guar gum and its derivatives**
Trung-Anh Le*, and Tan-Phat Huynh*
European Journal of Organic Chemistry (2023): 111852

Paper III **Synthesis, characterization, and humidity-responsiveness of guar gum xanthate and its nanocomposite with copper sulfide covellite**
Trung-Anh Le, Morad Zouheir, Kostiantyn Nikiforow, Muhammad Khatib, Orr Zohar, Hossam Haick, and Tan-Phat Huynh*
International Journal of Biological Macromolecules 206 (2022): 105-114

Paper IV   **Synthesis, characterization and biocompatibility of guar gum-benzoic acid**

Trung-Anh Le, Yong Guo, Jun-Nian Zhou, Jiaqi Yan, Hongbo Zhang, and Tan-Phat Huynh*

Authorship contribution

Paper I   **The author** contributed to the conceptualization of the study and was responsible for the methodology, investigation and writing (review and editing) of XRD, FTIR and TGA studies. **Morad Zouheir** was responsible for the conceptualization of the study, its methodology, visualization, investigation and writing (original draft, review and editing). **Janno Torop** contributed to the methodology, investigation, and writing (review and editing) of chemobrionics. **Kostiantyn Nikiforow** was responsible for the methodology, investigation and writing (review and editing) of XPS studies. **Muhammad Khatib, Orr Zohar and Prof. Hossam Haick** contributed to the methodology, investigation and writing (review and editing) of humidity sensing studies. **Prof. Tan-Phat Huynh** supervised the work, was responsible for the methodology, investigation and writing (review and editing). All authors reviewed and approved the final manuscript.

Paper II   **The author** was responsible for the conceptualization of the study, its methodology, investigation, analysis, visualization and writing (original draft, review and editing). **Prof. Tan-Phat Huynh** supervised the work, was responsible for the methodology, investigation and writing (review and editing). All authors reviewed and approved the final manuscript.

Paper III   **The author** was responsible for the conceptualization of the study, its methodology, investigation, visualization and writing (original draft, review and editing). **Morad Zouheir** was responsible for methodology, investigation and writing (review and editing) of GG-X/CuS nanocomposite synthesis, humidity sensing studies. **Kostiantyn Nikiforow** contributed to the

methodology, investigation and writing (review and editing) of XPS studies. **Muhammad Khatib, Orr Zohar and Prof. Hossam Haick** were responsible for methodology, investigation and writing (review and editing) of humidity sensing studies. **Prof. Tan-Phat Huynh** supervised the work, was responsible for methodology, investigation and writing (review and editing) of cyclic voltammetry and humidity sensing studies. All authors reviewed and approved the final manuscript.

Paper IV   **The author** was responsible for the conceptualization of the study, its methodology, investigation, visualization and writing (original draft, review and editing). **Jiaqi Yan** was responsible for methodology, investigation and writing (review and editing) of TEM studies. **Yong Guo, Prof. Jun-Nian Zhou and Prof. Hongbo Zhang** were responsible for methodology, investigation and writing (review and editing) of cell biocompatibility studies. **Prof. Tan-Phat Huynh** supervised the work, was responsible for methodology, investigation and writing (review and editing) of computational studies. All authors reviewed and approved the final manuscript.

Supporting publications

Paper SI   Synthetic Chemistry for Molecular Imprinting

Tan-Phat Huynh*, and **Trung-Anh Le**

Molecularly Imprinted Polymers for Analytical Chemistry Applications. Vol. 28. Royal Society of Chemistry. 2018. 28-64

1   Introduction

Throughout the human history, natural polysaccharides and other products of oxygenic photosynthesis have been utilized intensively by humans as food, fuels, materials, medication, etc. [1,2]. In the recent years, as climate, food and energy crises have become pressing issues globally, long-term holistic strategies, practical solutions and immediate actions are of paramount interest [3–10]. Nature has found out sustainable oxygenic photosynthetic pathways for solar energy utilization, carbon fixation and metabolism, which result in the formation of diverse polysaccharide-based products [11–15]. Promoting the use of natural polysaccharides as food, medicine, fuels and materials, therefore, can offer sustainable long-term solutions to address these crises [16–21].

To enrich physicochemical and biological properties of polysaccharide-based materials and extend their applicability, various chemical modification approaches of pristine polysaccharides and/or incorporation of polysaccharide matrices with different organic and inorganic materials have been considered, resulting in the development of numerous advanced materials [22–26]. While the incorporation of organic and inorganic materials into pristine polysaccharide matrices can offer simple yet efficient ways to synergize beneficial properties of different components [27], chemical modifications of polysaccharides typically provide more radical alterations in properties of polysaccharide-based materials, allowing fundamental changes in the behavior of the materials [28,29].

2 Objectives of the work

The overall objective of this work was to demonstrate not only the great potential of pristine natural polysaccharides in developing new materials, but also how chemical functionalization can play a crucial role in altering and enriching physical and chemical properties of natural polysaccharides, hence, extending their potential applications.

Natural polysaccharides such as anionic iota-carrageenan were employed directly to formulate inorganic/organic nanocomposites with potential applications in humidity and temperature sensing (Paper I).

Various chemical modification approaches of non-ionic guar gum were examined to find out green and sustainable synthetic pathways using commercially available and affordable chemicals (Paper II).

Among different organic functional groups and moieties, which were successfully chemically introduced to guar gum, xanthate and benzoic acid groups were further examined. Different characterization techniques and application demonstrations were carried out to highlight impacts of xanthate and benzoic acid groups on physical and chemical properties of guar gum (Paper III, IV).

3   Background and literature review

3.1   Carrageenan (CG)

Carrageenan (CG) is a family of natural linear anionic sulfated galactans obtained from different edible red marine algae. Typical repeating units of CG consist of sulfated β-D-galactose (Gal) and 3,6-anhydro-α-D-galactose (3,6-AHG) linked together via α-1,3 and β-1,4-glycosidic bonds. Depending on the solubility in potassium chloride aqueous solutions as well as the number and position of organosulfate moieties, CG can be classified into different types, namely alpha- (α-), beta- (β-), gamma- (γ-), delta- (δ-), epsilon- (ε-), theta- (θ), iota- (ι), kappa- (κ-), lamda- (λ-), mu- (μ-) and nu-CG (ν-CG) [30].

Among these types of CG, commercially available κ-, ι-, and λ-CG with one, two and three organosulfate groups per repeating unit, respectively, are of great interest due to their fascinating antioxidant, antimicrobial, antiviral, anticancer, anticoagulant and immunomodulatory properties [31–35]. Moreover, these CGs can also be easily incorporated with other nanomaterials to develop nanocomposites with novel properties [36,37]. In aqueous solutions, gelation of κ-CG normally yields firm, brittle gels and ι-CG gives soft, elastic gels due to the formation of helical conformations, while dissolution of λ-CG only results in viscous solutions [38–40].
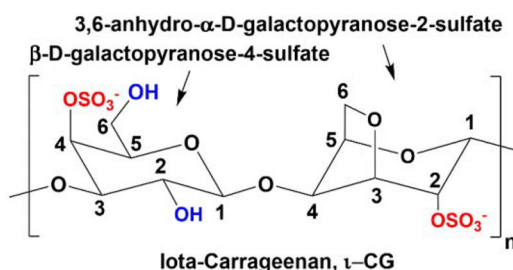
Fig. 1. Chemical structure of ι-CG.

In this work, ι-CG (or simply CG) was chosen to form nanocomposites with copper sulfide covellite (CuS) due to its capacity of forming soft and

elastic gels in water. ι-CG contains repeating units of β-D-galactopyranose-4-sulfate linked to 3,6-anhydro-α-D-galactopyranose-2-sulfate via β-1,4-glycosidic linkages (Fig. 1) [41,42]. Due to the presence of organosulfate groups, ι-CG is an anionic polysaccharide and can easily form coordinate covalent bonds with metal ions.

3.2   Guar gum (GG)

3.2.1 Introduction

Guar gum (GG) is found naturally in seeds of cluster bean *(Cyamopsis tetragonolobus)*. Endosperm of guar seed consists mainly of non-ionic galactomannan polysaccharide (around 80%) and other minor components such as water, ash, protein, and fat [43]. Recently, GG has gained more attention in different research fields due to its biocompatibility, biodegradability, natural abundancy, low cost, etc. [44–51]. In energy research, for instance, GG has been explored as a green binder in Li-ion batteries [52–54], a biodegradable electrolyte in zinc-ion batteries [55,56], perovskite-based zinc-air batteries [57], and dye-sensitized solar cells [58]. Moreover, GG can also enhance the production of biogas and activity of photocatalysts [59–63]. In agriculture and construction, GG has been employed as a stabilizer for soil treatment [64–66], concrete additives and corrosion inhibitors in metal protection [67–69]. Additionally, various GG-based biomaterials such as bio-ink in 3D printing and biofilms for food packaging have been fabricated [70–75]. In biomedical research, GG is an interesting biomaterial for wound dressing, healing and drug delivery [76–79]. Despite various fascinating properties and reported applications of natural GG, limitations in uncontrollable swelling, susceptibility to bacterial contamination and rapid biodegradation of pristine GG still exist, and therefore, further research on chemical modification and functionalization of GG is of great interest [45].

3.2.2 Chemical structure and properties of GG

Natural galactomannan polysaccharide of GG contains β-D-mannose (Man) backbones and α-D-galactose (Gal) branches with an average Man:Gal ratio varying from 1.8:1 to 2:1 and a significantly high molecular weight up to millions of Dalton [80]. Typical repeating units of GG are composed of two β-D-mannopyranose linked together by β-1,4-glycosidic bonds to form galactomannan main chains, and one α-D-galactopyranose side chain bonded to the main chain via α-1,6-glycosidic bonds (Fig. 2). In addition, each GG repeating unit has three anhydroglucose units (AGUs) on an average, with nine hydroxyl (-OH) functional groups in total. The chemical formula of these AGUs can be approximated as $C_6H_{10}O_5$ or $C_6H_7O_2(OH)_3$ to highlight the presence of the three average -OH groups in each AGU. Even though GG is the least hygroscopic polysaccharide among different types of gums, hydrophilic GG has high solubility even in cold water due to its unique structure and numerous remaining -OH groups [81–83]. Additionally, the -OH groups also behave as reactive sites for possible chemical modification and derivatization of pristine GG [84–86]. In terms of nucleophilicity, less bulky primary -OH groups are more nucleophilic than secondary -OH groups [87]. Since there are three average -OH groups in each AGU of GG, the degree of derivatization or substitution (DS) of AGU might be up to three.
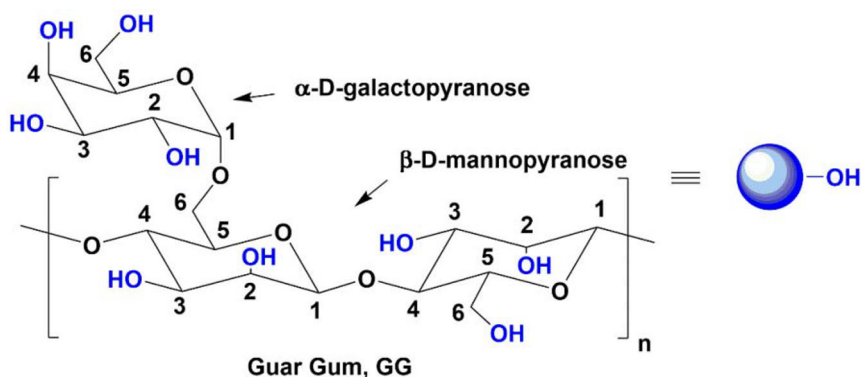
Fig. 2. Chemical structure of GG.

3.2.3 Current progress in the chemical functionalization of GG and its derivatives [88]

In the recent years, various chemical modification methods have been performed on GG to introduce new functional groups and biologically reactive moieties. Herein, the latest chemical functionalization approaches of GG and its derivatives are reviewed briefly. Even though physical blending offers great simplicity to the modification of materials including GG [89–92], this approach is not covered here because direct chemical modifications of GG are not normally carried out.
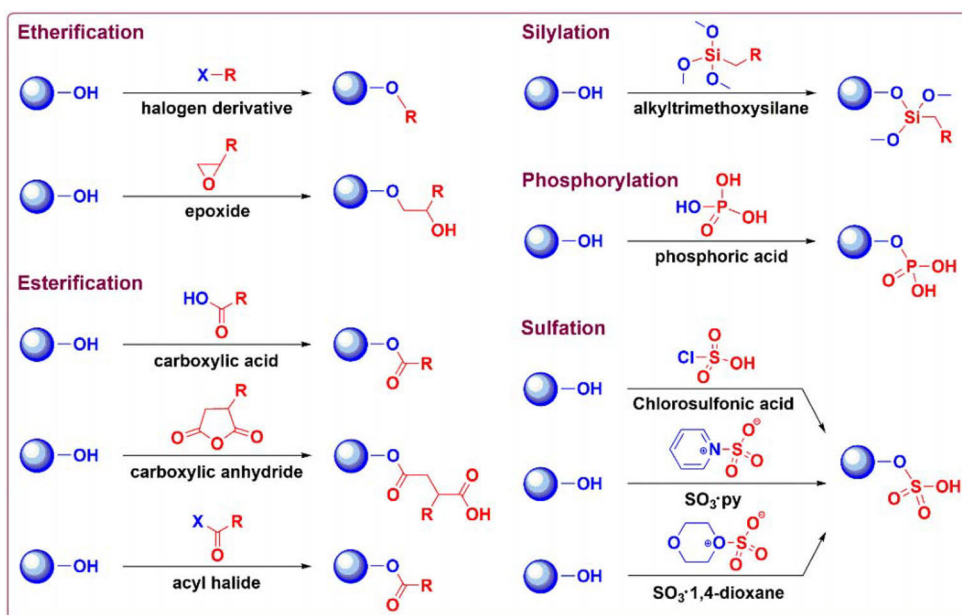
Fig. 3. Possible etherfication, esterification, silylation, phosphorylation and sulfation approaches of GG. Reproduced with permission from Paper II. Copyright 2023, Elsevier.

Among different chemical reactions, etherification allows one of the simplest synthetic pathways to modify -OH groups in GG (Fig. 3). Typical etherification of GG is performed under inert atmosphere (e.g. Ar, N_2) via two major stages, namely, activation of -OH groups in alkaline solutions and nucleophilic substitution reaction with electrophilic etherifying reagents.

Various alkyl halides have been employed as alkylating agents such as 3-(hexadecyloxy)-1-chloropropan-2-ol for hydroxypropylation [93–95], methyl iodide for methylation [96–98], monochloroacetic acid or sodium chloroacetate for carboxymethylation [84,99–103], and N-(3-chloro-2-hydroxypropyl)-trimethyl ammonium chloride for quaternization (cationization) of GG [104–106]. In addition, different epoxides such as 2,3-epoxypropyltrimethylammonium chloride [107,108], glycidyl methacrylate [109], propylene oxide [110], etc. can also be used for etherification of GG.

Esterification of -OH groups in GG is also a commonly used functionalization approach (Fig. 3). Esterification of GG by different carboxylic acids, carboxylic acid anhydrides and acyl halides is typically carried out in aprotic solvents such as acetone, acetonitrile, dichloromethane, and dimethylsulfoxide with an assistance of basic catalysts such as 4-dimethylaminopyridine, trimethylamine, etc. [111–118].

Moreover, due to the high affinity of Si towards O and the particularly high stability of Si-O bonds, silylation (silanization) of -OH groups offers effective chemical modification pathways to introduce new functionalities to different materials [119–125]. For instance, (3-aminopropyl)trimethoxysilane and (3-aminopropyl)triethoxysilane have been used to silylate -OH groups of GG and introduce amino ($-NH_2$) groups at the same time to develop catalytic centers on GG [126,127].

In addition, phosphorylation is ubiquitous in nature and has been employed to enrich chemical properties and potential applications of materials, including polysaccharides [128–132]. Recently, phosphorylation of GG has been performed to cross-link GG and soya lecithin to develop a novel photocatalytic system with zero-valent iron [133], or to introduce phosphonic acid moieties to GG for removal of uranyl (UO_2^{2+}) ions in wastewater [134].

Sulfation of polysaccharides is also of great interest due to its ability to modify physicochemical properties of the materials [28,29]. Different sulfating agents, such as chlorosulfonic acid-pyridine, chlorosulfonic acid-1,4-

dioxane, sulfur trioxide-pyridine and sulfamic acid-1,4-dioxane with urea-based activators, have been reported for sulfation of GG to examine its anticoagulant and antithrombotic properties, as well as synthetic possibilities (Fig. 3) [135–137].
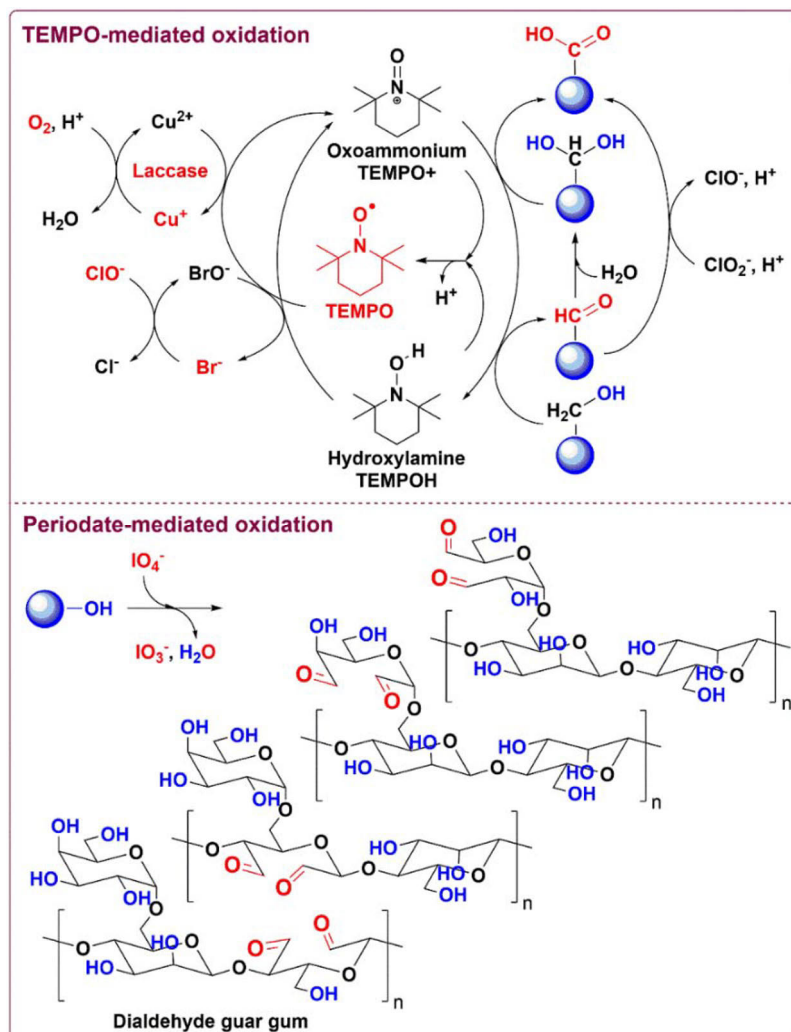
Fig. 4. TEMPO-mediated (O_2-Laccase-TEMPO and NaOCl-NaBr-TEMPO systems) and periodate-mediated oxidation of GG. Reproduced with permission from Paper II. Copyright 2023, Elsevier.

Recently, partial oxidation of -OH groups on polysaccharides has become increasingly popular since it can convert nucleophilic hydroxyl

groups to electrophilic aldehyde and/or carboxylic acid moieties, resulting in other possible chemical reactions such as nucleophilic addition, condensation, cross-linking, etc. [138,139]. Regioselective oxidation of primary C_6-OH groups on GG might be done using 2,2,6,6-tetramethylpiperidine-1-oxyl radical (TEMPO)-mediated oxidation pathway [140,141]. Typically, hypochlorite ions are used as oxidizing agents in the presence of bromide and TEMPO catalysts (NaOCl-NaBr-TEMPO system) [142–145]. Additionally, O_2 oxidant can also be used with laccase enzymes and TEMPO mediator (O_2-Laccase-TEMPO system) for the same purpose (Fig. 4) [146–149]. In addition, oxidative cleavage of vicinal 1,2-diols on GG by periodate (periodate-mediated oxidation) could be readily performed on C_2-OH and C_3-OH of mannose backbone, and C_2-OH, C_3-OH and C_4-OH of galactose side groups to produce different dialdehyde GG products [150–157]. Further oxidation of aldehyde groups in dialdehyde GG products to carboxylic acids by chlorite ions is also possible (Fig. 4) [158].

In recent years, graft polymerization such as step-growth, ring-opening and free-radical graft polymerization of GG has drawn much attention due to the availability of diverse monomers for these graft reactions (Fig. 5). For instance, GG-based polyurethanes have been fabricated as stabilizers, emulsifiers, thickeners or binding agents via step-growth polymerization of -OH groups on GG and isocyanate (-NCO) functional groups from isophorone diisocyanate (IPDI) [159,160]. Moreover, ring-opening polymerization of ε-caprolactone (ε-CL) and GG in the presence of tetra(phenylethynyl)tin catalyst has also been studied [161,162].

Free-radical graft polymerization (FRGP) is so far one of the most common approaches to graft polysaccharides [163,164]. Typically, the initiation step of FRGP begins by using free-radical initiators. Then, vinyl-containing monomers are added to the reaction mixture together with multifunctional cross-linkers for the propagation step of FRGP [165]. During the initiation step, free-radical initiators such as ceric(IV) ammonium nitrate,

ammonium persulfate, potassium persulfate and sodium persulfate can be activated by physical processes (e.g. heating, microwave irradiation, etc.) or chemical reactions with reducing agents such as bisulfite (HSO_3^-), metabisulfite ($S_2O_5^{2-}$), N,N,N',N'-tetramethylethylenediamine and ascorbic acid to form free-radicals for the propagation step [166–173]. A wide range of vinyl-monomers have been employed in the FRGP of GG such as acrylamide (AAm) [174], 2-acrylamidoglycolic acid (AGA) [175–177], 2-acrylamido-2-methyl-1-propane sulfonic acid (AMPS) [178,179], acrylic acid (AA) [180–183], acrylonitrile (AN) [184], ethyl acrylate (EA) [185], 2-hydroxyl ethyl methacrylate (HEMA) [186] and N-isopropylacrylamide (NIPAAm) [187,188], with cross-linkers such as [N,N'-methylenebisacrylamide (MBAAm) and tetra(ethyleneglycol)diacrylate (TEGDA)] [189–192].
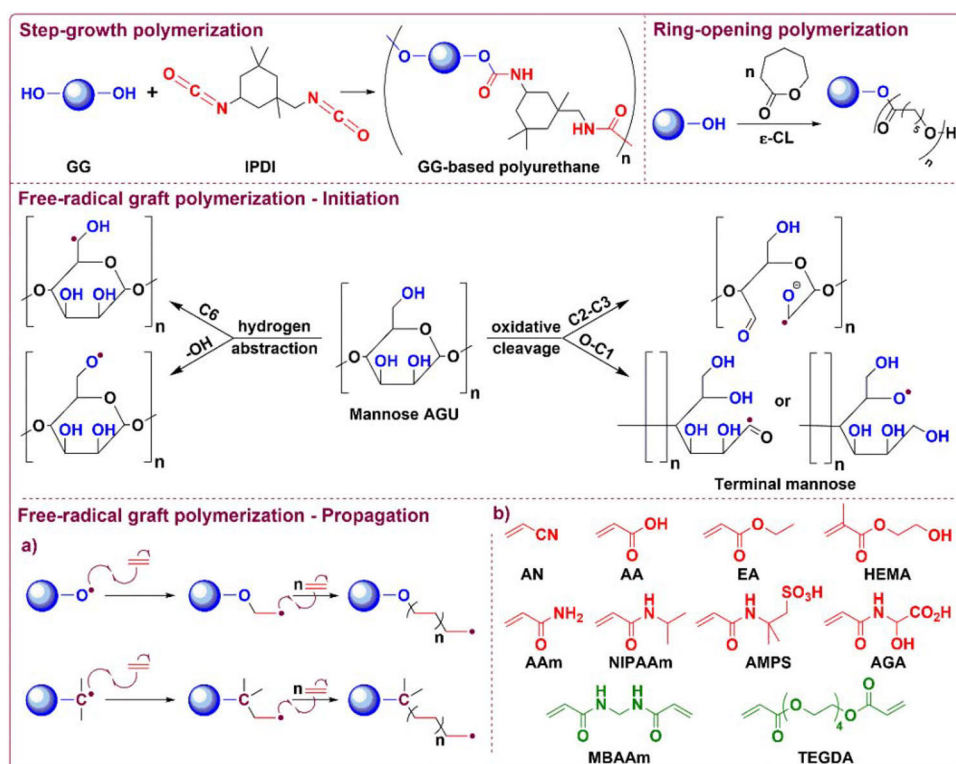
Fig. 5. Reported step-growth, ring-opening and free-radical graft polymerization of GG with vinyl-monomers (red) and cross-linkers (green). Reproduced with permission from Paper II. Copyright 2023, Elsevier.

Moreover, different cross-linking pathways have been examined to develop complex structures of GG-based materials (Fig. 6). Borax (anhydrous sodium tetraborate, sodium tetraborate pentahydrate or sodium tetraborate decahydrate), boric acid and sodium borohydride can be used as precursors to form borate ester linkers for GG [193–205]. Ether, ester, amide, hemiacetal, acetal and imine are also common carbon-based cross-linking functional groups for GG [70,95,114,117,134,149,150,153–155,206–209]. In addition, silicate esters, phosphate esters and zirconium alkoxide linkages can be effectively used for the cross-linking of GG [102,110,187,210–213].
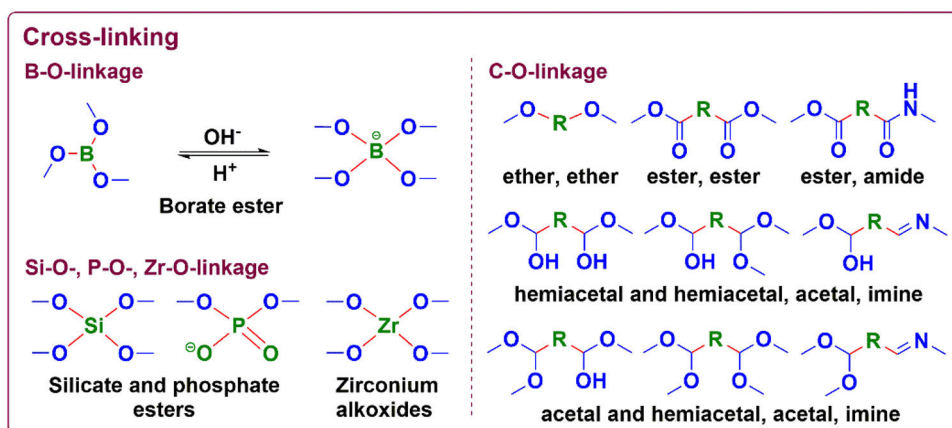
Fig. 6. Recently reported chemical linkages for cross-linking of GG. Reproduced with permission from Paper II. Copyright 2023, Elsevier.

3.3 Copper sulfide covellite (CuS)

Binary copper sulfide compounds have been well-known in various research fields, such as surface plasmon resonance, photocatalysis, chemical and biological sensing, molecular imaging, tumor therapy, cancer theranostics, etc. due to their special thermochemical, electrochemical, p-type semiconducting, low-cost, low-toxic and biocompatible properties [214–220]. Depending on the oxidation state of Cu, its stoichiometry and atomic arrangement, copper sulfide can exist in stoichiometric [e.g. chalcocite (Cu_2S), covellite (CuS)] and non-stoichiometric phases [e.g. yarrowite ($Cu_{1.12}S$),

spionkopite ($Cu_{1.39}S$), geerite ($Cu_{1.6}S$), anilite ($Cu_{1.75}S$), digenite ($Cu_{1.8}S$), roxbyite ($Cu_{1.81}S$) and djurleite ($Cu_{1.94\text{ - }1.97}S$)] [221]. These phases can be experimentally distinguished by powder X-ray diffractometry (XRD) (Fig. 7) and their relationships can also be described by a phase diagram [222,223].
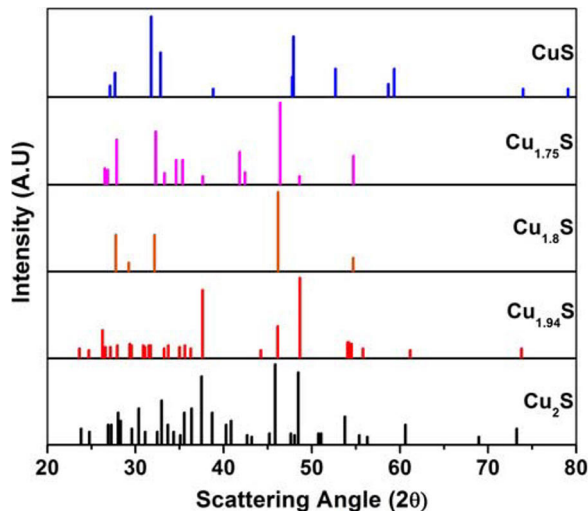
Fig. 7. X-ray diffraction patterns of the different copper sulfide phases. The data are obtained from the International Centre for Diffraction Data (ICDD) (Reproduced with permission from [223]. Copyright 2019, Wiley.)

Among the reported copper sulfide phases, covellite (CuS) stands out due to its stability, simple synthetic routes, metallic-like and superconducting properties [225–227]. Under ambient conditions, CuS adopts a hexagonal crystal structure with $P6_3/mmc$ space group, while phase transition of CuS to an orthorhombic structure (Cmcm space group) at around 55 K has been reported [228]. The hexagonal unit cell of CuS (or Cu_3S_3) consists of layers of tetrahedral CuS_4, trigonal planar CuS_3 and linked together via S-S disulfide bonds (Fig. 8). Three S ions in the unit cell of CuS could be described by two oxidation states, namely, S^{2-} [S(1)] and S_2^{2-} [S(2)]. Meanwhile, the presence of one Cu^{2+} and two Cu^+ ions in tetrahedral [Cu(2)] or trigonal planar [Cu(1)] sites have also been suggested to give a proposed $(Cu^{4/3+})_3(S_2^{2-})(S^{2-})$ ionic model. The exact oxidation states and position of these ions in the CuS hexagonal unit cell, however, are still under discussion [224,229–231].
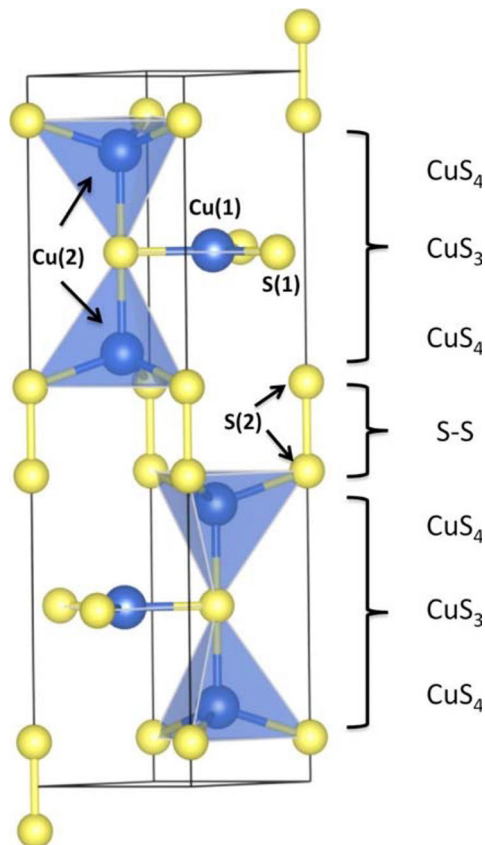
Fig. 8. Hexagonal unit cell of CuS covellite. Reproduced with permission from [224]. Copyright 2014, ACS Publications.

Several synthetic approaches of CuS nanocomposites have been reported such as aqueous precipitation by different precursors and surfactants, solvothermal processes, hot injection, thermolysis, chemical vapor deposition, etc. to yield various morphologies of CuS, namely, nanotube, nanorod, nanowire, nanoflake, nanosheet, nanodisk, nanocube, hollow nanosphere, nanocage, and nanoflower [232,233]. Meanwhile, different CuS-based nanoheterostructures, which consist of more than one component fused into one nanoparticle or more than one distinct phase in individual nanoparticles, have been explored via cation exchange methods [234]. Moreover, various nanocomposites of CuS, inorganic and/or organic materials have also been prepared and studied [235–238].

3.4 Chemobrionics and surfactant-assisted precipitation in the fabrication of polysaccharide-based nanocomposites

In recent decades, fabrication methods of nanomaterials via top-down and bottom-up approaches have been of great interest [239,240]. The top-down synthetic approach involves breaking processes of bulk materials to nano-scaled products via physicochemical methods such as etching, laser ablation, lithography, mechanical milling, sputtering, etc. Meanwhile, the bottom-up approach is based on chemical reactions of ions, atoms and molecules to form nanostructures. Due to simplicity, wet-chemical methods such as precipitation, co-precipitation, solvothermal and sol-gel methods are routinely used in chemical laboratories [241]. To demonstrate how polysaccharides can be valuable materials in the bottom-up synthesis of nanomaterials, chemobrionics and surfactant-assisted precipitation of CuS covellite by iota-carrageenan and guar gum-xanthate, respectively, were chosen.

Chemobrionics has been well-known for centuries as chemical gardens, the chemical formation of hollow tubular structures under non-equilibrium conditions due to the presence of a semipermeable precipitation membrane, steep concentration gradients, osmotic and buoyancy forces [242]. In nature, chemobrionics can be found as hollow tubes of ice (brinicles) in sea ice and hydrothermal vents in deep sea [243–246]. In chemical laboratories, chemobrionics can be carried out via various methods such as seed growth, injection growth, membrane growth, bubble guidance, varying gravity, etc. [242]. In addition, interfaces between semipermeable hydrogel membranes and aqueous solutions are also fascinating candidates in chemobrionics (Scheme 1) [247–249]. Typically, a homogeneous aqueous solution of ions with lower osmotic pressure is placed on top of a counterion-containing hydrogel network with higher osmotic pressure. As a semipermeable membrane forms at the interface of the hydrogel and aqueous

solution, water diffusion and osmotic force allow the swelling of hydrogel and development of a concentration gradient in the hydrogel network. While the osmotic pressure increases in the hydrogel network, the hydrogel membrane ruptures and releases a flow of counterion-containing fluid upwards into the aqueous solution of ions, resulting in precipitation of these ions and their counterions into hollow tubular structures. Then, continuous formation and rupture processes of the semipermeable membrane at the tube tip allows the elongation of the tube based on osmotic and buoyant forces, and further precipitation of ions and counterions. When the tubes reach to a certain length, structural collapse of the tubes might occur due to gravity, ending the growing process.
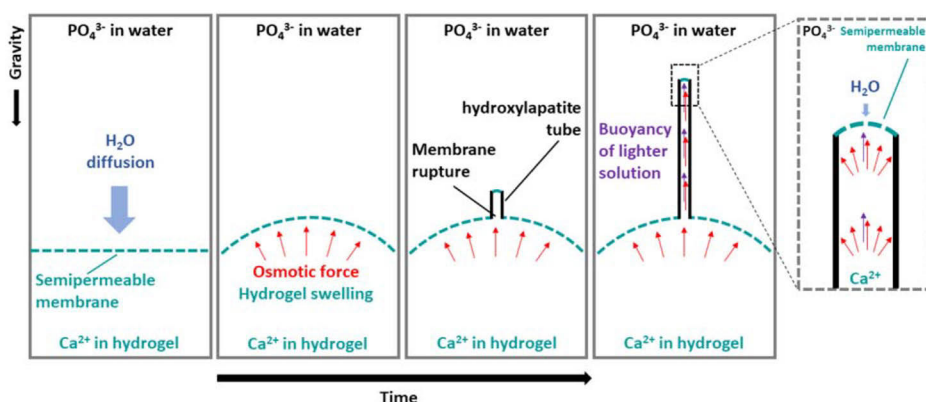
Scheme 1. Chemobrionics of hydroxylapatite $Ca_{10}(PO_4)_6(OH)_2$ from an interface between a Ca^{2+}-containing semipermeable hydrogel membrane and a PO_4^{3-} aqueous solution [247].

To have a better control in wet-chemical synthesis of nanomaterials, various surfactants have been utilized as capping, dispersing, oxidation etching, structure-directing and weak reducing agents [250]. Surfactants are amphiphilic organic molecules with hydrophilic and hydrophobic groups that can interact with both polar and nonpolar phases [251]. In wet-chemical synthesis of nanomaterials, electron lone pairs from hydrophilic groups of surfactants can form coordinate covalent bonds with vacant orbitals on the

surface of nanomaterials, hence, alternating the structure, morphology, physical and chemical properties of the nanomaterials (Fig. 9) [252–255].
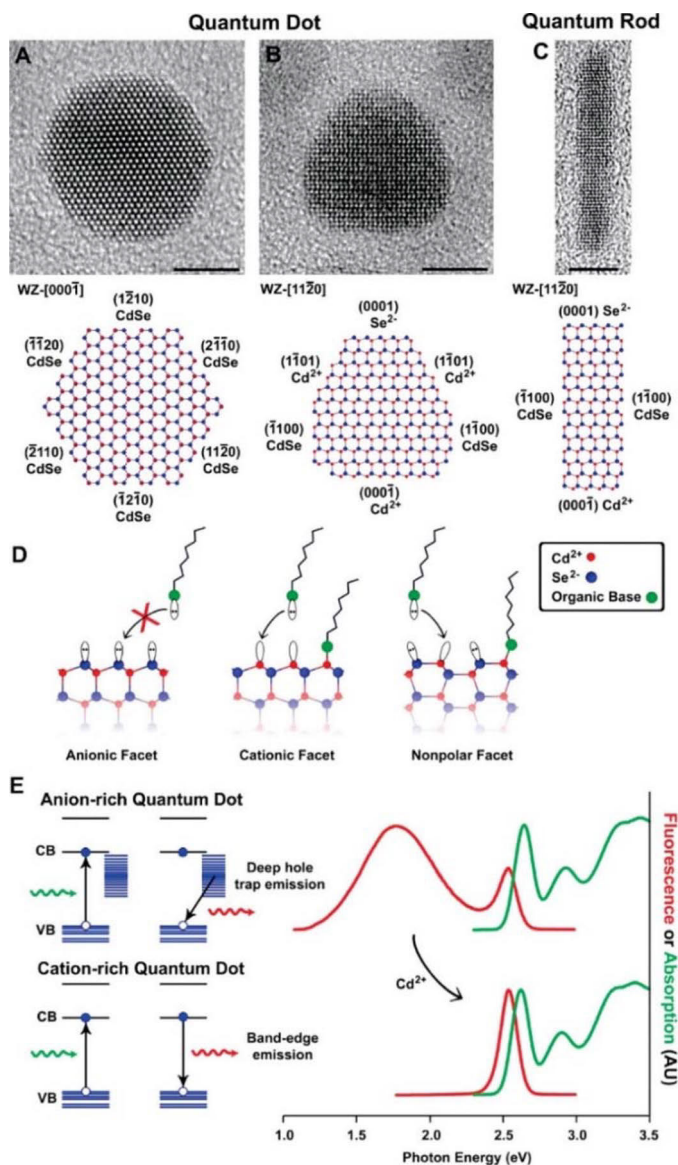
Fig. 9. Surface properties of CdSe nanocrystals. Transmission electron microscope (TEM) images of quasi-spherical quantum dots (A, B), a quantum rod (C) with scale bars of 5 nm, and their atomic models identified by Wurtzite (WZ) Miller indices. Terminal dangling orbitals of cationic Cd^{2+}, anionic Se^{2-} and nonpolar CdSe crystal facets (D). Effects of surface hole traps on the fluorescence of 2.1 nm nanocrystals (E). Reproduced with permission from [253]. Copyright 2010, ACS Publications.

4 Materials and methods

4.1 Chemicals

4.1.1 Polysaccharides

ι-Carrageenan was purchased from CP Kelco for chemobrionics of CuS. Guar gum was purchased from Sigma Aldrich for synthesis of GG-X, GG-X/CuS nanocomposite and GG-BA.

4.1.2 Reagents

4-(Bromomethyl)benzoic acid (BBA) 97% was used to prepare GG-BA. Carbon disulfide (CS_2) 99% was used for the synthesis of GG-X. Sodium hydroxide (NaOH) 97% and hydrochloric acid (HCl) 37% were used to activate GG and neutralize GG products, respectively. All the reagents were purchased from Sigma Aldrich.

4.1.3 Salts

$Cu(NO_3)_2 \cdot 3H_2O$ 99.9% and Na_2S were used to prepare CuS. $AlCl_3$ 99%, $CdCl_2$ 99.99%, $CoCl_2 \cdot 6H_2O$ 98%, $CuCl_2$ 97%, $FeCl_2 \cdot 4H_2O$ 99%, $FeCl_3 \cdot 6H_2O$ 99%, $Ni(NO_3)_2 \cdot 6H_2O$ 98.5%, $PbCl_2$ 98%, $PtCl_2$ 98%, $SnCl_2$ 98% and $ZnCl_2$ 98% were used as metal cation precursors for the demonstration of GG-X metal ion complexation. Potassium ethyl xanthogenate $C_2H_5OCS_2K$ (Et-X) 96% was used as a reference for the quantification of xanthate groups on GG-X using UV-Vis spectrophotometry. Na_2CO_3 99% and $NaHCO_3$ 99.5% were used to prepare a carbonate-bicarbonate buffer solution at pH 10. All the salts were purchased from Sigma-Aldrich and they were used as received without further purification.

4.1.4 Solvents

Acetone 99.9%, hexanol 99.5% and toluene 99.8% were used as volatile organic compounds to test the sensing capacity of GG-X/CuS nanocomposite.

Ethanol (EtOH) 99.8% and methanol (MeOH) 99.8% were used during the synthesis of GG-BA and GG-X. All the solvents were purchased from Sigma-Aldrich and they were used as received without further purification.

4.1.5 NMR solvents

Deuterated dimethylsulfoxide (DMSO-d6) 99.96% was purchased from Sigma-Aldrich and used directly in NMR studies.

4.2 Methods of synthesis

4.2.1 ι-Carrageenan/copper sulfide covellite (CG/CuS) nanocomposite

3.00 g of CG was dissolved in 100.0 mL distilled water at 50 °C to obtain a homogenous 3 wt% CG stock solution. Meanwhile, 0.242 g (1.00 mmol) of $Cu(NO_3)_2 \cdot 3H_2O$ was dissolved by 1.00 mL water in a vial to yield a Cu^{2+} 1.00 M precursor solution. Then, 10.0 mL of 3 wt% CG solution was added to the Cu^{2+} vial, which was heated to 90 °C under vigorous stirring to yield a homogenous viscous solution of Cu^{2+} (around 0.1 M) and CG (around 3 wt%). As this viscous solution cooled down to room temperature, a firm gel of CG and Cu^{2+} (CG/Cu^{2+} gel phase) was formed. At the same time, aqueous solutions of Na_2S 0.1 M (liquid phases) were prepared and HCl was used to adjust the pH of these liquid phases to get HS^- solutions at pH 7, 10 and 13. To prepare CG/CuS nanocomposites via chemobrionics, 10.0 mL of each previously prepared HS^- solution at pH 7, 10 and 13 was introduced on top of CG/Cu^{2+} gel phase in the prepared vials, resulting in three types of samples CG/CuS pH 7, CG/CuS pH 10 and CG/CuS pH 13 (Scheme 2). The formation and growth of black CG/CuS nanocomposites became noticeable after 20 min. After 48 h of reaction, the remaining liquid was carefully removed from the reaction vials, while the obtained black CG/CuS nanocomposites were washed by a mixture of 80:20% v/v EtOH:H_2O once by absolute EtOH and then transferred to petri dishes for drying under vacuum.

Additionally, a CuS sample was prepared by mixing 0.1M Cu(NO$_3$)$_2$·3H$_2$O and 0.1M Na$_2$S under the same reaction condition without CG for comparison purpose.
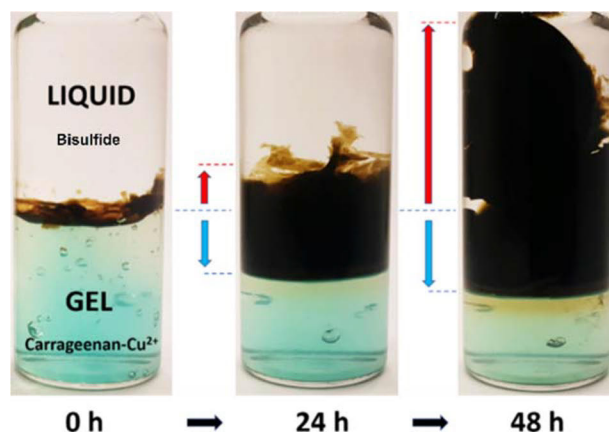
Scheme 2. Upward and downward growth (red and blue arrows, respectively) of CG/CuS nanocomposite from the interface of CG/Cu^{2+} hydrogel and hydrosulfide solution in 48 h. Reproduced with permission from Paper I. Copyright 2021, Wiley.

4.2.2 Guar gum xanthate (GG-X) and guar gum xanthate/copper sulfide covellite (GG-X/CuS) nanocomposite

12.22 g NaOH (296.3 mmol) was dissolved in 200.0 mL distilled N$_2$-purged water, followed by a gradual addition of 2.00 g GG (12.35 mmol AGU) under vigorous stirring in 30 min. Then, 4.455 mL CS$_2$ (73.7 mmol) was introduced to the GG solution for xanthation reaction, which took place in 2.5 h at room temperature. Eventually, the reaction was quenched, and the GG-X product was precipitated by MeOH antisolvent. Excess MeOH was then used to wash the GG-X product from inorganic xanthate byproducts. Then, the final GG-X product was dried in vacuum to give a reaction yield of 87.2%.

600.0 mg of pure GG-X (0.452 mmol X) powder was dissolved in 32.0 mL distilled water to obtain a homogenous yellow aqueous solution. Meanwhile, 608.0 mg of CuCl$_2$ (4.386 mmol) was dissolved in 8.0 mL distilled water to prepare a Cu^{2+} solution. Then, the two solutions were mixed together

to obtain a viscous mixture of GG-X and Cu^{2+} (GG-X/Cu^{2+}) under vigorous stirring. To this GG-X/Cu^{2+} mixture, 61.5 mL of aqueous Na_2S 0.1 M (6.15 mmol) solution was introduced dropwise during 15 min under vigorous stirring to yield copper sulphide dispersed in GG-X (GG-X/CuS). The obtained solution was sonicated for 15 min and concentrated by a hotplate at 85 °C in 2 h to get 48.0 mL of a homogeneous solution. Finally, the product solution was purified by solvent precipitation using EtOH antisolvent and redissolved in water (Scheme 3).
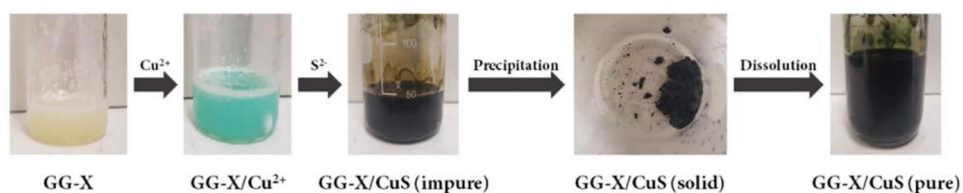
Scheme 3. Synthesis of the GG-X/CuS nanocomposite.

In addition, several other samples were prepared in similar synthetic conditions for comparison. An inorganic xanthate (Inorg-X) control solution for UV–Vis spectrophotometry was synthesized by adding 30.0 μL CS_2 to 2.0 mL of NaOH 1 M in 2.5 h under N_2 atmosphere. The CuS (HS^-) reference sample was prepared by adding Cu^{2+} to an alkaline solution of HS^- at pH 10.5, while the CuS (OH^-) reference sample was obtained by adding HS^- to a Cu^{2+} solution at pH 10.5 to mimic the preparation of GG-X/CuS in the absence of GG-X. The GG/CuS reference sample was also synthesized using 600 mg of GG instead of GG-X at the same pH of 10.5.

To demonstrate the metal complexation capacity of GG-X, metal ion solutions with the same molar concentrations of 37.68 mM (Al^{3+}, Cr^{3+}, Fe^{3+}) and 56.52 mM (Cd^{2+}, Co^{2+}, Cu^{2+}, Fe^{2+}, Ni^{2+}, Sn^{2+}, Pb^{2+}, Pt^{2+}, Zn^{2+}) were prepared in acidified water. Meanwhile, 15.0 mg GG-X was dissolved completely in 1 mL neutral water in different vials. Then, 100 μL of each metal ion solution was transferred to the GG-X vials to allow metal complexation reactions. The pH of the final gel-like products was recorded in the range of 9.5–10.5.

4.2.3 Guar gum benzoic acid (GG-BA)

5.73 g of NaOH (138.94 mmol) was dissolved in 500 mL N_2-purged water, followed by an addition of 5.00 g of GG (30.875 mmol AGU) under vigorous stirring in 30 min at room temperature. Then, 6.845 g of BBA (30.875 mmol) was added to the GG solution and the mixture was kept under stirring overnight at room temperature. To quench the reaction, HCl (37%) was added until the pH of the solution dropped to 1. Excess EtOH was used to precipitate and purify the GG-BA. The final product was vacuum-dried to yield 7.62 g of GG-BA (83.1% reaction yield).

4.3 Characterization methods

4.3.1 Proton nuclear magnetic resonance (^{1}H NMR) spectroscopy [256,257]

NMR spectroscopy studies the interaction between electromagnetic radiation of radio frequency waves and nuclear spins under an external magnetic field ($\overrightarrow{B_0}$). Spinning protons possess angular momentum $\vec{L}$ and charge, resulting in intrinsic magnetic moments $\vec{\mu}$ (Eqn. 1). When protons are placed in an external static magnetic field $\overrightarrow{B_0}$, magnetic moments of protons $\vec{\mu}$ couple with $\overrightarrow{B_0}$ to yield new magnetic energy states (Eqn. 2). Since protons have a nuclear spin quantum number I of 1/2, they can adopt 2I + 1 = 2 spin states, namely, +1/2 (α, spin up, parallel to $\overrightarrow{B_0}$) and -1/2 (β, spin down, antiparallel to $\overrightarrow{B_0}$), with their corresponding energy levels $E_{+1/2}$ and $E_{-1/2}$, respectively (Zeeman effect, Eqn. 3). By supplying electromagnetic radiation with energy equal to the energy difference ΔE between $E_{+1/2}$ and $E_{-1/2}$, magnetic transitions between the two spin states of protons can be carried out (Eqn. 4, 5, Fig. 10).
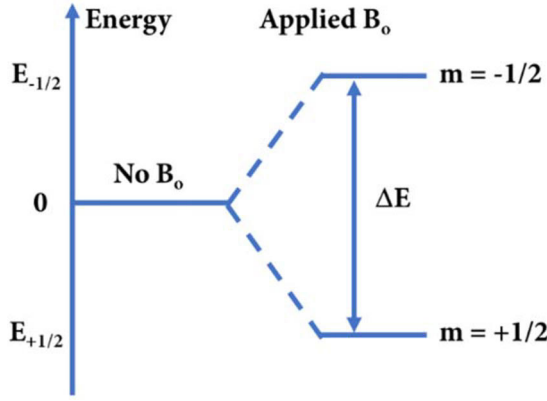
Fig. 10. Magnetic energy levels of protons with spin quantum number of 1/2 without and with an external static magnetic field.

$$\vec{\mu} = \gamma \, \vec{L} \tag{1}$$

$\vec{\mu}$ nuclear magnetic moment

γ magnetogyric or gyromagnetic ratio

$\vec{L}$ nuclear angular momentum

$$E = -\mu \, B_0 = -\frac{\gamma \, m \, h}{2\pi} \, B_0 \tag{2}$$

E   magnetic energy

B_o magnetic flux density

m   magnetic quantum states

h   Planck constant

$$E_{\pm 1/2} = \mp \frac{\gamma h}{4\pi} \, B_0 \tag{3}$$

$$E_{photon} = h\nu = \Delta E = E_{-1/2} - E_{+\frac{1}{2}} = \frac{\gamma h}{2\pi} \, B_0 \tag{4}$$

$$\nu = \frac{\gamma}{2\pi} \, B_0 \tag{5}$$

ν Larmor precession frequency

Recently, pulsed Fourier transform (FT) NMR has dominated modern NMR studies comparing to continuous wave (CW) NMR. In typical pulsed FT-NMR experiments, pulses of electromagnetic radiofrequency (rf) impose torques on proton spins, hence, switching proton spin states from +1/2 to -1/2. The applied rf pulses can be controlled so that the macroscopic magnetic

moment $\vec{M}$ (vector sum of individual magnetic moments, $\vec{M} = \sum \vec{\mu_i}$) might be transverse or antiparallel to $\vec{B_0}$ (90º and 180º pulses). Then, relaxation of nuclear spins via spin-lattice and spin-spin interaction begins to return the nuclear spins to their lowest energy states. Decreases in the intensity of $\vec{M}$ over time are recorded as free induction decay (FID) files and processed by Fourier transformation technique to yield typical NMR spectra, which show signal intensity versus frequency (chemical shift) of different proton environments.

Depending on surrounding electrons and nuclei, protons of interest might experience different chemical environments, yielding different proton signals at different chemical shifts (δ) in NMR spectra. For instance, surrounding electrons possess their own intrinsic magnetic fields $\sigma\vec{B_0}$, which can interfere with the interaction between $\vec{B_0}$ and protons (shielding effect), resulting in different local applied magnetic fields $\vec{B}_{local}$ (Eqn. 6). As the local electron density around protons increases, protons become more shielded and shielding constant σ increases, leading to a decrease in δ and upfield or high-field signal shifts (Eqn. 7 and 8). The chemical shift is highly sensitive to electronegativity and induced magnetic field (magnetic anisotropy from π electrons) of neighbouring nuclei, as well as solvent media. In addition, neighbouring NMR-active nuclei can also give more information (e.g. multiplet structures) on the protons of interest via spin-spin interaction (coupling).

$$B_{local} = B_0 - \sigma B_0 = (1 - \sigma)\, B_0 \tag{6}$$

B_{local} local magnetic flux density that determines the magnetic resonance behaviour of protons

σ NMR shielding constant

$$v = \frac{\gamma}{2\pi}\, B_{local} = \frac{\gamma\,(1-\sigma)}{2\pi}\, B_0 \tag{7}$$

$$\delta = \frac{v - v_{ref}}{v_{ref}} \cdot 10^6 = \frac{\sigma_{ref} - \sigma}{1 - \sigma_{ref}} \cdot 10^6 \approx (\sigma_{ref} - \sigma) \cdot 10^6 \tag{8}$$

δ NMR chemical shift

^{1}H-NMR spectra of the samples in this work were measured with a Bruker AVANCE-III NMR-system 400 MHz (Bruker Inc., Billerica, MA, USA) at 298.15 K.

4.3.2 Powder X-ray diffractometry (XRD) [258]

Upon exposure to electromagnetic X-ray waves, atoms in solid lattices can scatter these X-ray waves, followed by their constructive or destructive interference to result in X-ray diffraction phenomena. Conditions for constructive interference of scattered X-rays (X-ray diffraction) can be described by the Bragg's law (Eqn. 9, Fig. 11). Due to specific arrangements of atoms and ions in crystalline materials, each crystalline phase structure has characteristic interplanar d-spacing, resulting in unique patterns of diffraction signals at different scattering angles. From these diffraction patterns, phase structures of crystalline materials can be identified. In addition, crystallite size in solid crystalline compounds can be approximated using the Scherrer equation (Eqn. 10).
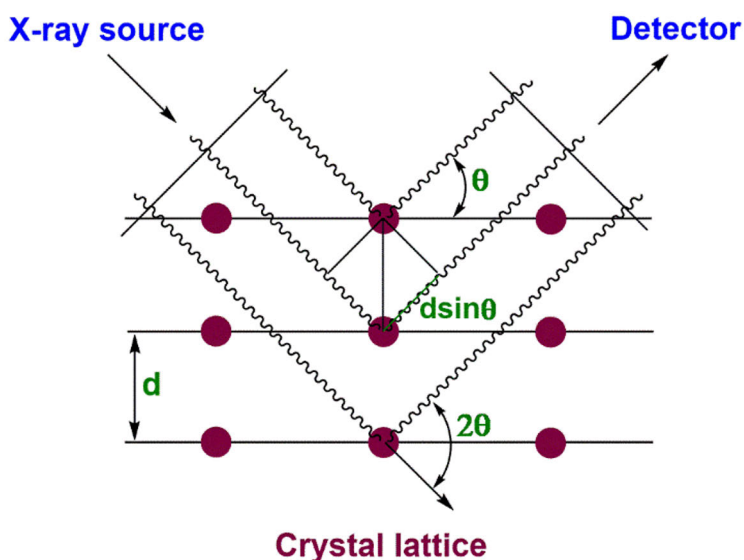
Fig. 11. Diffraction of X-rays by a crystal lattice.

$$n \, \lambda = 2 \, d \, sin\theta \tag{9}$$

<div style="padding-left:2em">

n diffraction order (integer)

λ incident X-ray wavelength

d crystal interplanar spacing

θ incidence angle

</div>

$$D = \frac{K \, \lambda}{FWHM \, cos \, (\theta)} \tag{10}$$

<div style="padding-left:2em">

D crystallite size

K Scherrer constant (= 0.9)

FWHM full width at half maximum

θ Bragg angle (e.g. half of the 2θ position of the (110) diffraction peak in CuS samples)

</div>

In this work, a Bruker D8 Discover diffractometer (Bruker Inc., Billerica, MA, USA) was used to measure XRD spectra of samples. An X-ray K780 (Cu Kα anode, λ = 1.5418 Å) generator was employed at 40 kV voltage and 40 mA current. The diffraction angle was measured within the range from 10° to 80° with a resolution of 0.04° at room temperature.

4.3.3 Scanning electron microscopy - energy dispersive X-ray spectroscopy (SEM-EDS) and transmission electron microscopy (TEM) [259]

Due to the resolution limitation of optical microscopy based on visible light, which is approximately half of the visible light wavelength (around 200 nm), wave-like behaviour of high-energy electrons can be exploited instead to study material morphology on nanoscale. When incident primary electron beam interacts with the sample surface, different types of events may occur, such as transmission, elastic or inelastic back- and forward-scattering, as well as excitation of electrons, which results in the formation of characteristic X-rays, secondary electrons and Auger electrons (Fig. 12). In SEM, secondary electrons from the sample are normally detected to construct SEM images. Additionally, characteristic X-rays can be utilized for elemental analysis and

mapping in SEM-EDS. Meanwhile, TEM images are created based on transmitted electrons.
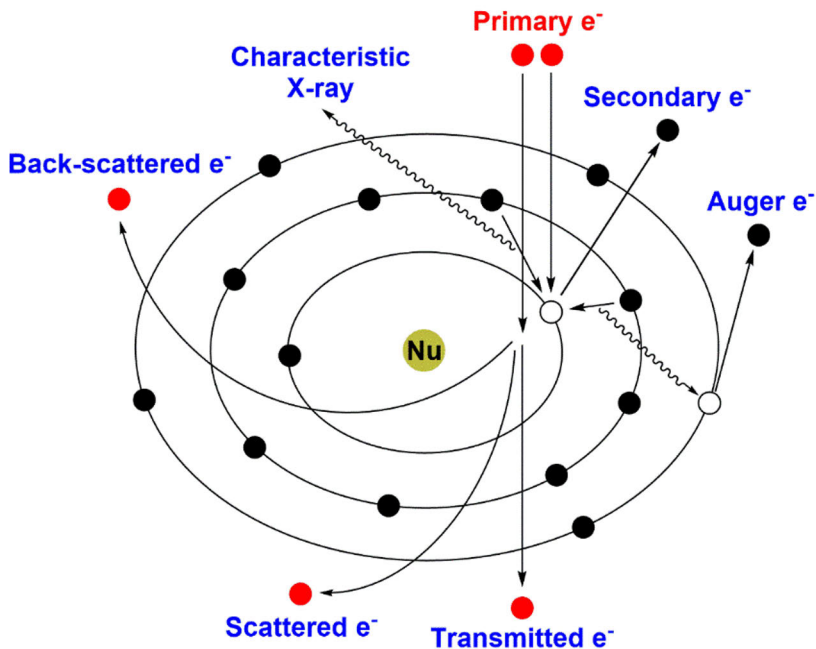
Fig. 12. Schematic illustration of possible events between an incident primary electron beam and electrons in atomic shells of a sample.

In this study, material morphology was studied by using a LEO Gemini 1530 scanning electron microscope (Leo Electron Microscopy Inc., Thornwood, NY, USA), while elemental mapping was carried out using energy dispersive X-ray spectroscopy (Thermo Scientific ultradry silicon drift detector) on the same SEM device. Samples were coated with a conductive carbon adhesive tape and the obtained SEM images were examined using Image J software. Particle size distribution curves were plotted based on 50 particles of GG, 150 particles of GG-BA and 200 particles of CuS in GG-X/CuS.

A JEM-1400 plus transmission electron microscope equipped with an OSIS Quemesa 11 Mpix bottom mounted digital camera (Jeol Ltd., Akishima, Tokyo, Japan) was used for TEM experiments. The samples were dispersed on

standard copper TEM grids and resultant TEM images were examined using Image J software.

4.3.4 Ultraviolet-visible (UV-Vis) absorption spectroscopy [260]

UV-Vis absorption spectroscopy studies interactions between ultraviolet-visible radiation and valence electrons of a sample. In molecules, UV-Vis radiation can cause electronic transitions between molecular orbitals, alternating molecular electronic states. Once molecules are in electronic excited sates, different relaxation pathways of excited electrons can take place, e.g. non-radiative vibrational relaxation, internal conversion, intersystem crossing or radiative fluorescence and phosphorescence (Fig. 13). In addition, Beer Lambert's law can be used to quantify the concentration of sample solutions from their absorption spectra (Eqn. 11).
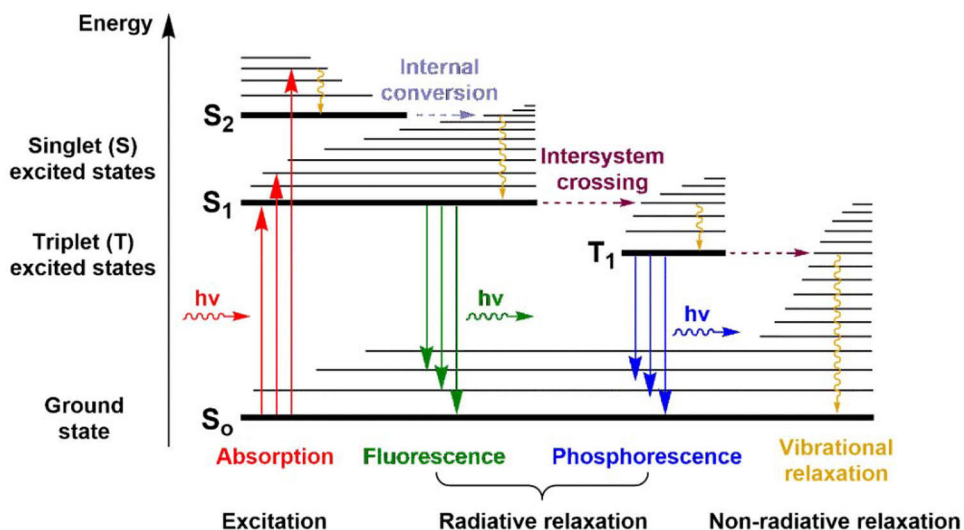
Fig. 13. A Jablonski diagram of molecular electronic states, non-radiative and radiative electronic transitions.

$$A = log \left(\frac{I_0}{I}\right) = log \left(\frac{1}{T}\right) = 2 - log \ (\%T) = \varepsilon \, c \, l \qquad (11)$$

A   absorbance

I_0 incident intensity

I   transmitted intensity

T   transmittance

% T percent transmittance

ε molar absorption (extinction) coefficient

c   concentration

l   sample path length

   The UV–Vis spectra of all studied samples were measured with a Shimadzu UV-2501PC spectrophotometer (Shimadzu Inc., Kyoto, Japan) in the wavelength range from 190 to 900 nm (near IR) with a resolution of 0.5 nm, in quartz cells (1×1 cm^2) at room temperature.

4.3.5 Attenuated total reflectance - Fourier-transform infrared (ATR-FTIR) spectroscopy [260]

Infrared absorption spectroscopy examines vibrations of chemical bonds when they absorb infrared electromagnetic radiation, hence, allowing a quick and effective approach to identify and confirm various chemical bonds. In classical mechanics, vibration of chemical bonds between atoms can be modelled as springs connecting different masses with different stretching and bending vibrational modes (Fig. 14). Different chemical bonds and their varying vibrational modes have unique resonance wavenumbers (i.e. reciprocal wavelengths), which are utilized for the identification of chemical bonds. In quantum mechanics, molecular symmetry and point group theory can also be used to describe the nuclear position and motion in molecular vibrations.

   Attenuated total reflectance allows a convenient route to measure FTIR spectra of solid and liquid samples. Its principle is based on total internal reflection at an interface of two media when incident infrared radiation travels from a medium of higher refractive index n_1 (e.g. diamond) to another with lower refractive index n_2. From Snell's law, the critical angle required for total internal reflection is calculated as θ_c and to observe this phenomenon, the incidence angle θ_1 must be greater than θ_c (Eqn. 12, 13). During the total

internal reflection at the interface between two media, a small portion of the incident IR waves (evanescent waves) penetrates the interface into the sample medium of lower refractive index and gets absorbed by chemical bonds in the sample before reflection occurs (Fig. 15). Depending on the nature of chemical bonds in the measured sample, certain wavenumbers are absorbed, resulting in attenuation of the incident IR waves. Then, the obtained ATR-FTIR spectra are processed to give similar spectra as traditional FTIR measurements using KCl pellets.
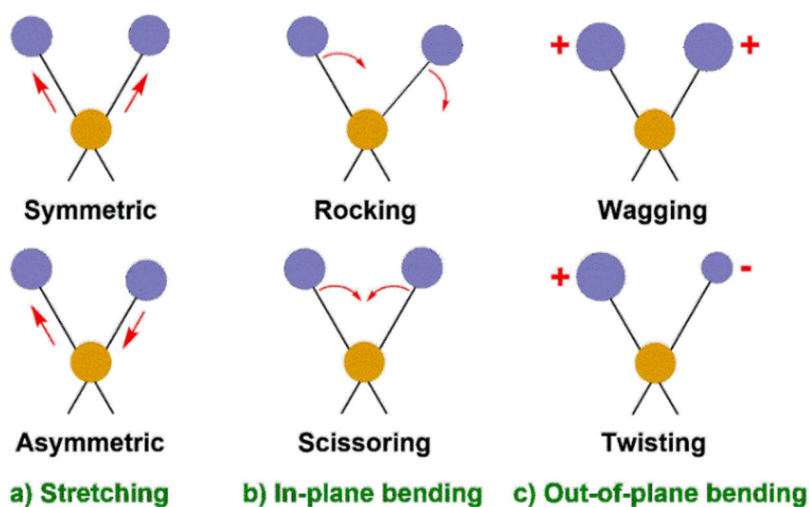
Fig.14. Several types of molecular vibrations (+ and – signs indicate motion of atoms toward and away from the reader, respectively).
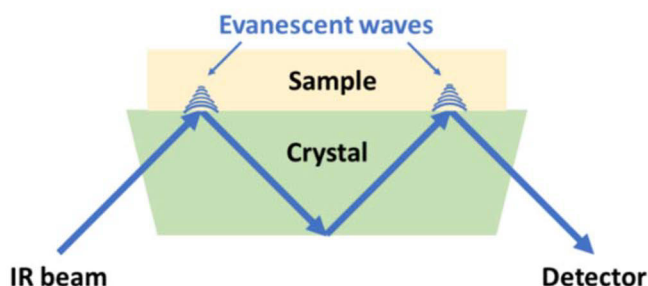
Fig. 15. Demonstration of evanescent waves in an ATR-FTIR apparatus with a sample placed on an internal reflection crystal of high refractive index.

$$n_1 sin\theta_1 = n_1 sin\theta_2 \qquad\qquad\qquad (12)$$

$\quad$ n_1, n_2 $\quad$ refractive indices

$\quad$ θ_1, θ_2 $\quad$ incidence and refraction angles

$$sin\theta_c = \frac{n_2}{n_1} \qquad\qquad\qquad (13)$$

$\quad$ θ_c $\quad$ critical angle

IR spectra in this work were recorded between 400 and 4000 cm^{-1} with a resolution of 4.0 cm^{-1} by using a Nicolet™ iS50 ATR-FTIR spectrometer (Thermo Scientific Inc., Waltham, MA, USA).

4.3.6 Thermogravimetric analysis (TGA) [261]

Thermal analysis can be employed to examine thermal behaviour of studied materials. As the temperature increases at a constant rate in a specific atmosphere, changes in weight of an analyte due to physical and chemical processes (e.g. water desorption, glass transition, melting, vaporization, sublimation, polymorph conversion, combustion, decomposition, degradation, etc.) are recorded and processed as TGA curves. Moreover, to detect weight changes of an analyte more easily, the first derivative of a TGA curve with respect to temperature can be taken, resulting in differential thermogravimetric (DTG) curves.

In this study, TGA measurements were performed with a Netzsch STA 449 F1 Jupiter thermogravimetric analyzer (Netzsch Instruments Inc., Featherstone, Wolverhampton, UK) under N_2 inert atmosphere. The studied temperature ranged between 30 and 600 °C using a heating rate of 10 °C min^{-1}. Dry samples were kept in vacuum before measurement. Then, 2–10 mg of the sample was placed into an aluminium pan. Finally, the obtained TGA and DTG curves were analyzed with a Netzsch TGA software.

5 Results and discussion

5.1 ι-Carrageenan/CuS covellite (CG/CuS) nanocomposite [262]

5.1.1 Synthesis

Chemobrionics was employed to explore a novel and unique bottom-up synthetic approach for CG/CuS nanocomposite (Fig. 17). 3 wt% of CG and 0.1 M of Cu^{2+} and HS^- solutions have been found as the optimal condition for CG/CuS growth. While varying pH of CG/Cu^{2+} hydrogel showed negligible effects to the nanocomposite, the pH of the HS^- solution phase had a significant impact on the nanocomposite growth and therefore was examined further at pH 7, 10 and 13.
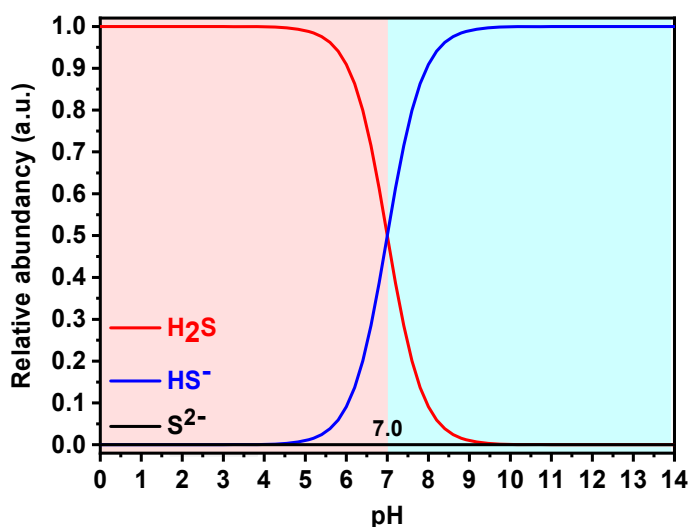
Fig. 16. Relative abundancy of H_2S and HS^- species in water at different pH.

In water, hydrosulfuric acid (H_2S) is a weak diprotic acid with pK_{a1} of around 7.0 and estimated pK_{a2} of 19 ± 2. Due to very high pK_{a2}, H_2S behaves more similar to monoprotic acids and can be deprotonated into hydrogensulfide or bisulfide (HS^-) (Eqn. 14), while sulfide (S^{2-}) is rarely

obtained even at very high pH (Fig. 16). The formation of CuS, therefore, can be described as in Eqn. 15 and 16, with their corresponding solubility product constant in acid (K_{spa}) and solubility product constant (K_{sp}) at 25 °C [263]. K_{sp} indicates that the formation of CuS in alkaline solution is thermodynamically much more favoured than in neutral and mildly acidic solutions.

$$H_2S_{(aq)} \rightleftharpoons H^+_{(aq)} + HS^-_{(aq)} \tag{14}$$

$$Cu^{2+}_{(aq)} + H_2S_{(aq)} \rightleftharpoons CuS_{(s)} + 2H^+_{(aq)} \quad K_{spa} = 6 \cdot 10^{-16} \tag{15}$$

$$Cu^{2+}_{(aq)} + HS^-_{(aq)} + OH^-_{(aq)} \rightleftharpoons CuS_{(s)} + H_2O_{(l)} \quad K_{sp} = 6 \cdot 10^{-37} \tag{16}$$
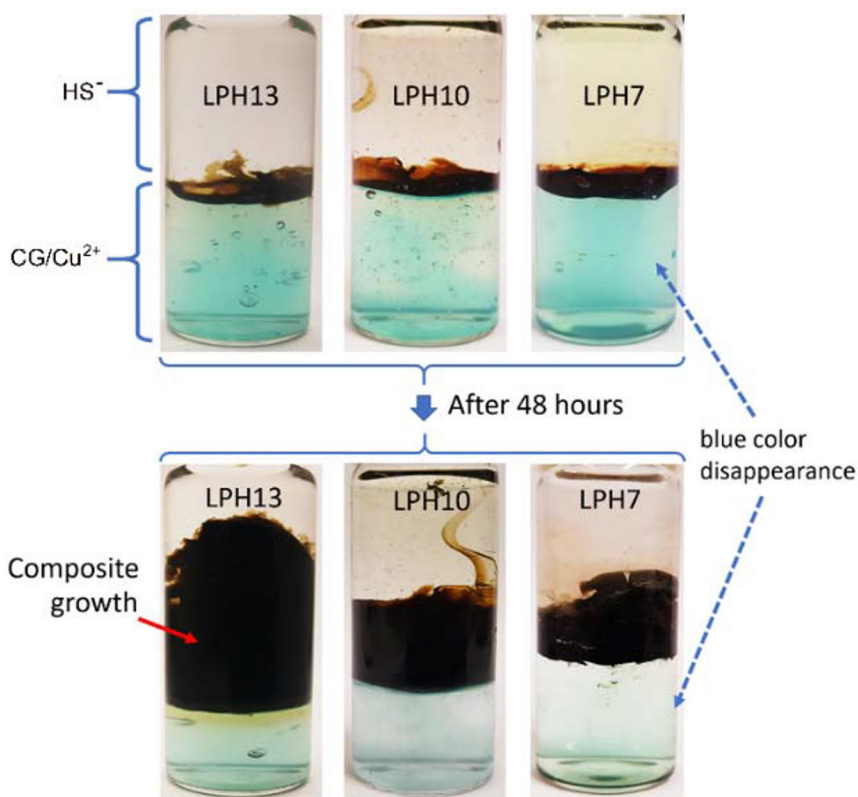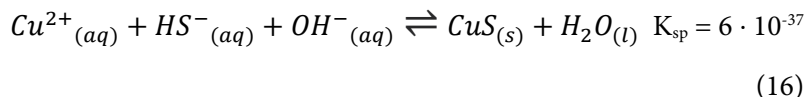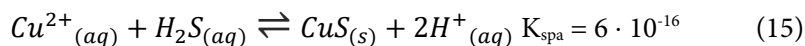
Fig. 17. Growth of CG/CuS nanocomposite under different pH of HS⁻ solutions. Reproduced with permission from Paper I. Copyright 2021, Wiley.

At pH 7, H₂S and HS⁻ were found simultaneously in the solution with a molar ratio of around 1:1, allowing the formation of CuS via both Eqn. 15 and

16. At pH 10 and 13, HS$^-$ dominated the solution phase and the precipitation of CuS occurred mainly by Eqn. 16. Since the formation of CuS by HS$^-$ in the alkaline solution was thermodynamically more favoured than that by H$_2$S, more CuS product was observed in the reaction systems at pH 10 and 13 than at pH 7 (Fig. 17). Moreover, increasing the concentration of OH$^-$ from pH 10 to 13 also enhanced the reaction kinetics, and shifted the reaction equilibrium to gain more CuS product.

It should be noted that even though the growth of CG/CuS nanocomposite occurred readily under the optimal synthetic condition, tubular morphology of CuS was not observed, which could be explained due to the strong complexation between the CG gel matrix and Cu^{2+} diminishing the formation of jets from the CG/Cu^{2+} interface [249].

5.1.2 Characterization

5.1.2.1 FTIR

While the FTIR spectrum of CuS was omitted for clarity since no significant absorption bands were observed, the FTIR spectrum of CG in Fig. 18 has the typical absorption bands of CG. In the diagnostic region (> 1500 cm^{-1}), CG had a broad O-H stretching vibration band at 3425 cm^{-1}, C-H stretching bands at 2968 cm^{-1} and 2903 cm^{-1} and a water deformation band at 1630 cm^{-1}. In the fingerprint region (< 1500 cm^{-1}), an ester sulfate O=S=O symmetric stretching signal at 1218 cm^{-1}, a C-O stretching band at 1025 cm^{-1} and a C-O-C stretching band of 3,6-anhydro-D-galactose at 926 cm^{-1} were detected [264–266]. Moreover, these vibration signals of CG were also found in the FTIR spectra of CG/CuS samples, hence, confirming the presence of CG in these composites.
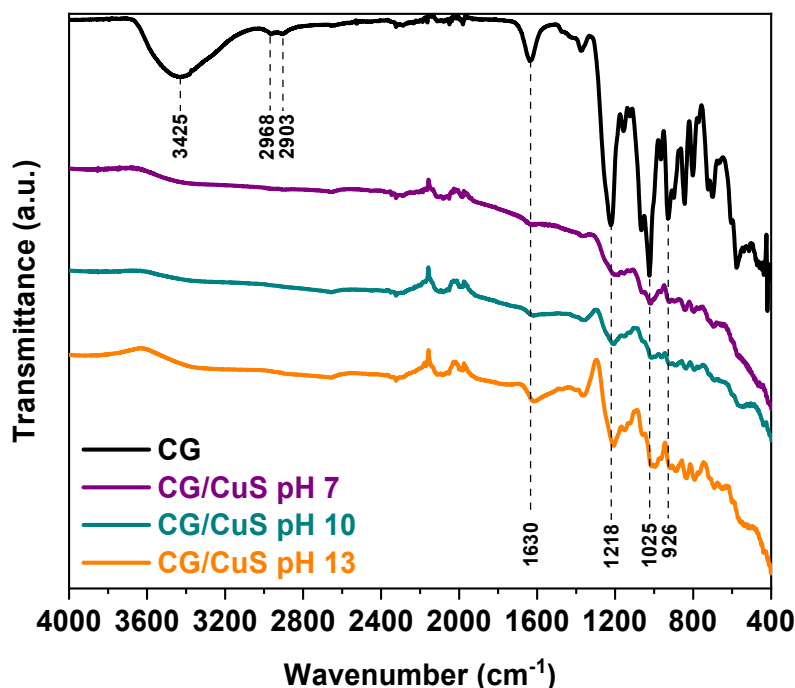
Fig. 18. FTIR spectra of CG (black) and CG/CuS at pH 7, 10 and 13 in purple, dark cyan, and orange, respectively. Reproduced with permission from Paper I. Copyright 2021, Wiley.

5.1.2.2 XRD

The X-ray diffractogram of CG showed a broad diffused peak around $2\theta = 22°$, indicating an amorphous phase structure (Fig. 19) [267,268]. Meanwhile, the X-ray diffractograms of CuS control sample in the absence of CG, and CG/CuS samples prepared at pH 7, 10 and 13 possessed characteristic peaks of CuS covellite when compared to the CuS covellite reference (JCPDS file no. 79-2321) [269,270]. Broad peaks at around 22° in the XRD spectra of CG/CuS samples were attributed to the presence of CG in the CG/CuS composites. In addition, the average crystallite size of CuS in CG/CuS decreased from 13.5 nm to 12.4 nm and 10.1 nm as pH increased from 7 to 10 and 13, respectively. This could be explained such that as the pH increases, higher concentration of OH⁻ increases the nucleation rate of CuS, resulting in the formation of more CuS nuclei and smaller crystallite size [271].
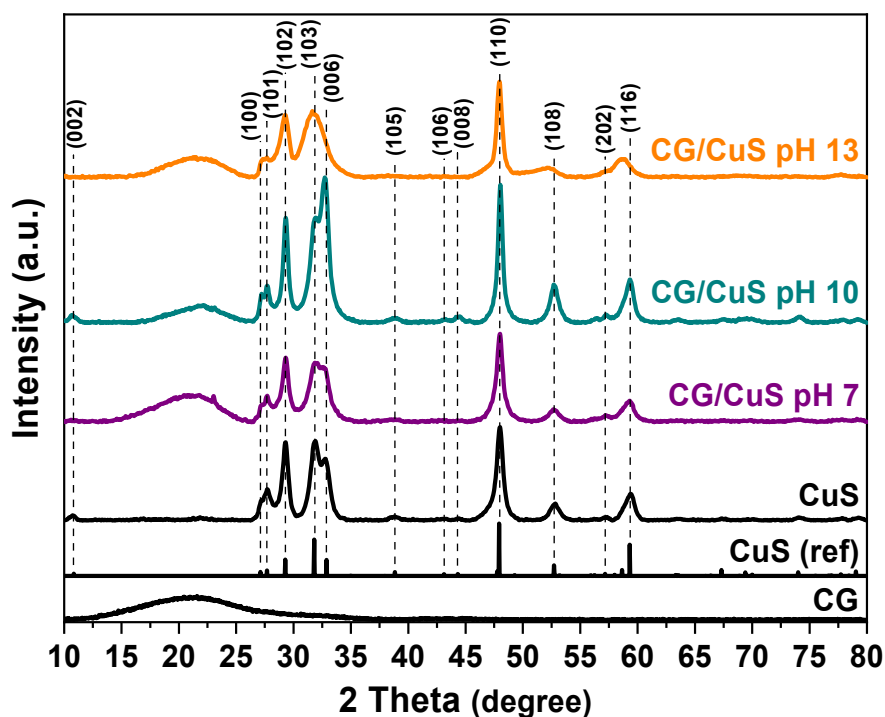
Fig. 19. XRD spectra of CG, CuS reference, controlled CuS, CG/CuS at pH 7, 10 and 13. Reproduced with permission from Paper I. Copyright 2021, Wiley.

5.1.2.3 SEM

SEM micrographs of the CG/CuS samples (Fig. 20 C, E, G) indicated an incorporation of CuS nanoparticles (particle size less than 40 nm) and CG particles (particle size of several microns) into the composite structures. Interestingly, a separation of CuS nanoparticles and CG particles into small domains in the composites after chemobrionics was observed. After purification, while the morphology of CuS remained approximately the same as in the CuS control sample (Fig. 20 A), changes in morphology of CG (Fig. 20 B) were noticed (Fig. 20 D, F, H). The CG particles in CG/CuS samples at three pH values appeared with smaller sizes after purification. In addition, irregularly shaped CG particles in CG/CuS samples at pH 7 had leaf-like morphology after the purification. Meanwhile, CG particles in CG/CuS samples at pH 10 and 13 still possessed irregular shapes.
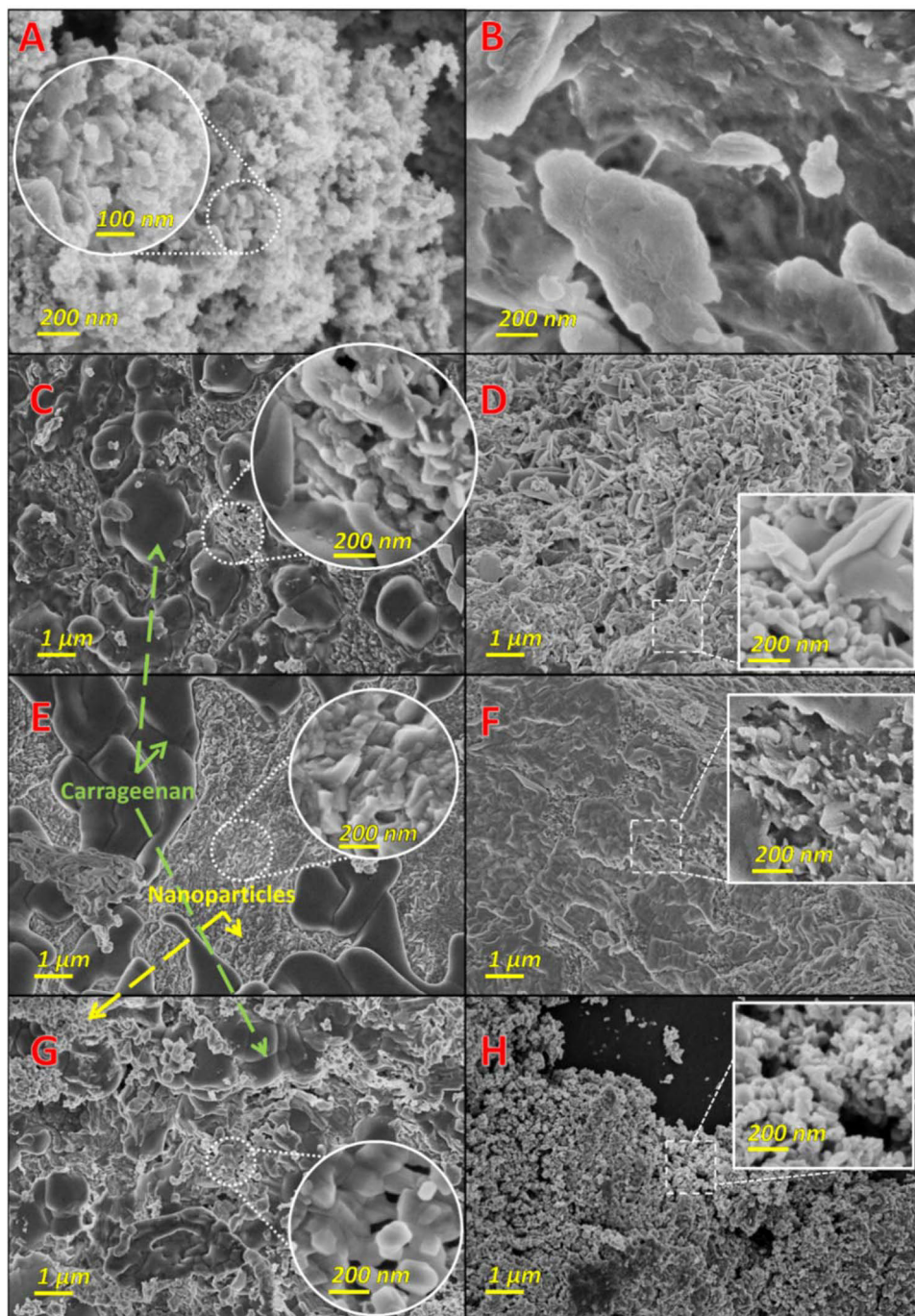
Fig. 20. SEM micrographs of CuS control sample (A), CG (B), CG/CuS at pH 7, 10, 13 before (C, E, G, respectively) and after purification (D, F, H, respectively). Reproduced with permission from Paper I. Copyright 2021, Wiley.

5.1.2.4 TGA-DTG
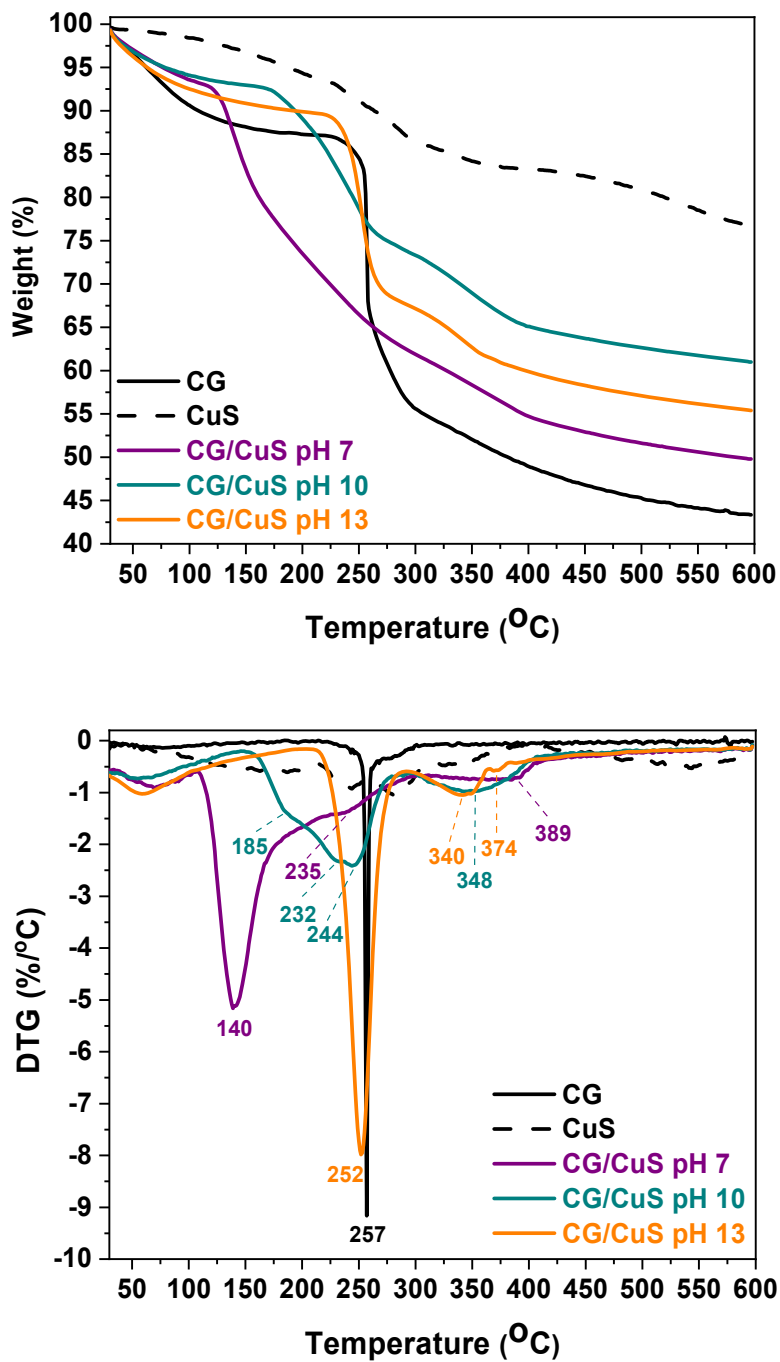
Fig. 21. TGA (top) and DTG (bottom) thermograms of CG, CuS, CG/CuS at pH 7, 10 and 13. Reproduced with permission from Paper I. Copyright 2021, Wiley.

Thermogravimetric analysis in N_2 atmosphere showed water removal from the tested samples at temperatures below 180 °C (Fig. 21). In the studied temperature range, CG had a sharp weight decrease of 32.3% at 257 °C, which was attributed to the dissociation of sulfur dioxide from CG [264,267,272]. Meanwhile, a gradual weight loss due to transformation of CuS into Cu_xS (1 < x ≤ 2) and vaporization of released S within the temperature range of 200-600 °C has been detected [273,274]. The thermogram of CG/CuS pH 7 indicated three major degradation events of the sample at 140, 235 and 389 °C, with weight losses of 20.2, 10.9 and 9.5%, respectively. For CG/CuS pH 10, degradation events at around 185, 232 and 244 °C overlapped with one another to give a total weight loss of 18.9%, while another degradation at 348 °C was also observed with a weight decrease of 9.8%. Moreover, the thermogram of CG/CuS pH 13 showed a distinct weight loss of 22.1% at 252 °C, and two continuous degradation events at 340 and 374 °C with a total weight loss of 8.4%. Based on the total weight loss, CG/CuS pH 7 seemed to be the least thermally stable sample, while CG/CuS pH 10 was more thermally stable than CG/CuS pH 13.

5.1.3 Potential applications

CG/CuS composites have shown great potential for humidity and temperature sensing [Paper I, Fig. 7]. The varying resistance of the CG/CuS-based sensor upon water exposure can be attributed to variations in electrical permittivity of the composite and/or the swelling of hydrophilic CG polysaccharide in the composite, leading to an increase in distance and hopping conductivity between CuS nanoparticles [275,276]. Additionally, the CG/CuS-based sensor also showed a promising linear and reversible response towards the temperature range between 30 and 80 °C, under ambient condition.

5.2 Guar gum-xanthate (GG-X) and guar gum-xanthate/CuS covellite (GG-X/CuS) nanocomposite [277]

5.2.1 Synthesis
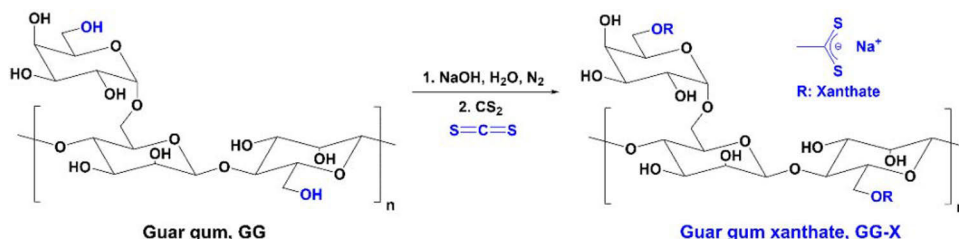
Scheme 4. Xanthation of GG. Reproduced with permission from Paper III. Copyright 2022, Elsevier.

Xanthation of GG polysaccharide was carried out by a reaction between hydroxyl groups of GG and CS_2 in an alkaline aqueous solution with a reaction yield of around 87% (Scheme 4, Eqn. 17). During the reaction, N_2 purging was required to avoid further oxidation of xanthate groups. In aqueous media, besides the main xanthation reaction, other side reactions might also take place simultaneously to yield inorganic by-products under complex equilibria (e.g. Eqn. 18) [278]. Nevertheless, these by-products were easily removed from the GG-X product by MeOH.

$$GG - OH_{(aq)} + OH^-_{(aq)} + CS_{2(aq)} \rightarrow GG - OCS_2^-_{(aq)} + H_2O_{(l)}$$

(17)

$$2CS_{2(aq)} + 5OH^-_{(aq)} \rightarrow CO_3^{2-}_{(aq)} + CS_3^{2-}_{(aq)} + HS^-_{(aq)} + 2H_2O_{(l)}$$

(18)
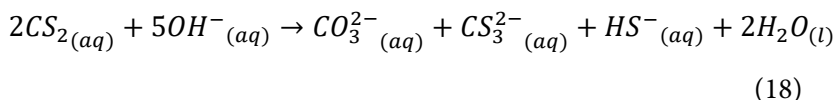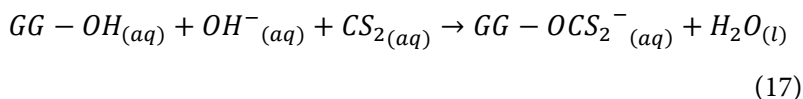
Surfactant-assisted precipitation of CuS in the presence of GG-X was then examined to show a potential application of GG-X polysaccharide both as a surfactant and as a matrix for the precipitation and dispersion of CuS into a GG-X/CuS nanocomposite. To study beneficial effects of GG-X on the

preparation of CuS in GG-X/CuS nanocomposites, control samples such as CuS (HS⁻), CuS (OH⁻) and GG/CuS were prepared.

5.2.2 Characterization

5.2.2.1 UV-Vis
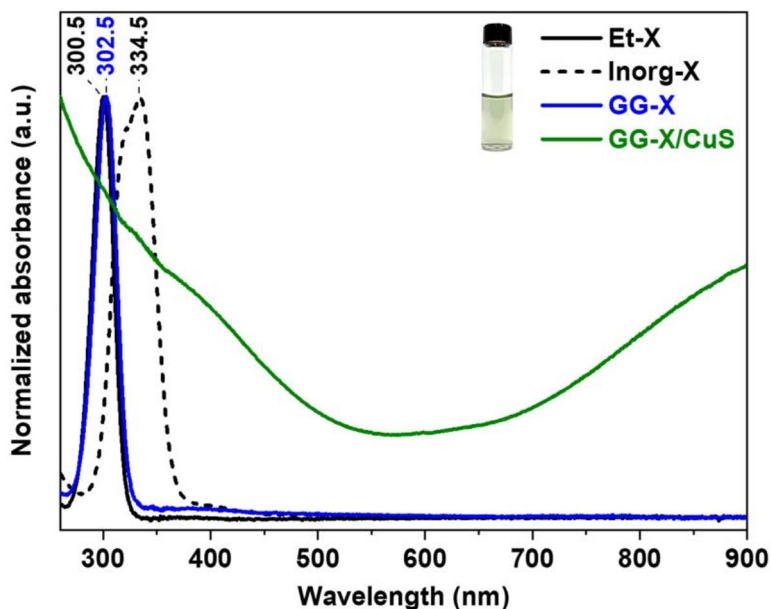
Fig. 22. UV-Vis absorption spectra of Et-X reference, Inorg-X control sample, GG-X and GG-X/CuS (black, dashed black, blue and green, respectively) in an aqueous carbonate-bicarbonate buffer solution at pH 10.5. Reproduced with permission from Paper III. Copyright 2022, Elsevier.

The UV–Vis absorption spectra showed an absorption band of the pure GG-X product in water at 302.5 nm, which was similar to the absorption band of the Et-X reference at 300.5 nm, while no inorganic by-product was observed around 334.5 nm (Fig. 22). Moreover, the degree of substitution (DS) and grafting density (GD) of xanthate on GG was approximated as 0.132 and 4.4%, respectively, resulting in the chemical formula of $C_6H_{9.868}O_5(CS_2Na)_{0.132}$ for each GG-X anhydroglucose unit. Due to the presence of the GG-X capping agent, insoluble CuS nanoparticles could be dispersed in water into a green

transparent homogeneous colloidal dispersion. The UV-Vis absorption spectrum of this aqueous dispersion, therefore, was easily measured from UV to near IR radiation range [236,279]. While absorption of CuS in the UV-Vis range can be attributed to electronic transitions within the optical band gap of this semiconductor [280], absorption in near IR wavelengths is due to localized surface plasmon resonance (LSPR) of free carriers (i.e. excited electrons in the conduction band and holes in the valance band) in the CuS semiconductor [281,282].

5.2.2.2 FTIR

The FTIR spectrum of the GG reference showed O–H stretching and C–H stretching vibration bands from -OH and CH_2 groups around 3325 and 2904 cm^{-1}, respectively, as well as GG ring stretching at 1640 cm^{-1} in the diagnostic region (Fig. 23). Additionally, absorption peaks of GG due to C-OH, CH_2OH stretching and CH_2 twisting vibrations were observed at 1143, 1064 and 1014 cm^{-1}, respectively in the fingerprint region. In addition, a characteristic peak of galactose and mannose at 874 cm^{-1} was detected [283–285]. Meanwhile, the presence of xanthate groups in GG-X was verified by new absorption bands at 1149 and 1057 cm^{-1} due to S-C-S stretching and C=S stretching vibrations [286,287]. Moreover, the FTIR spectrum of GG-X/CuS showed similarities with that of GG-X (e.g. C=S stretching vibration at 1057 cm^{-1}), hence, confirming the presence of GG-X in GG-X/CuS.
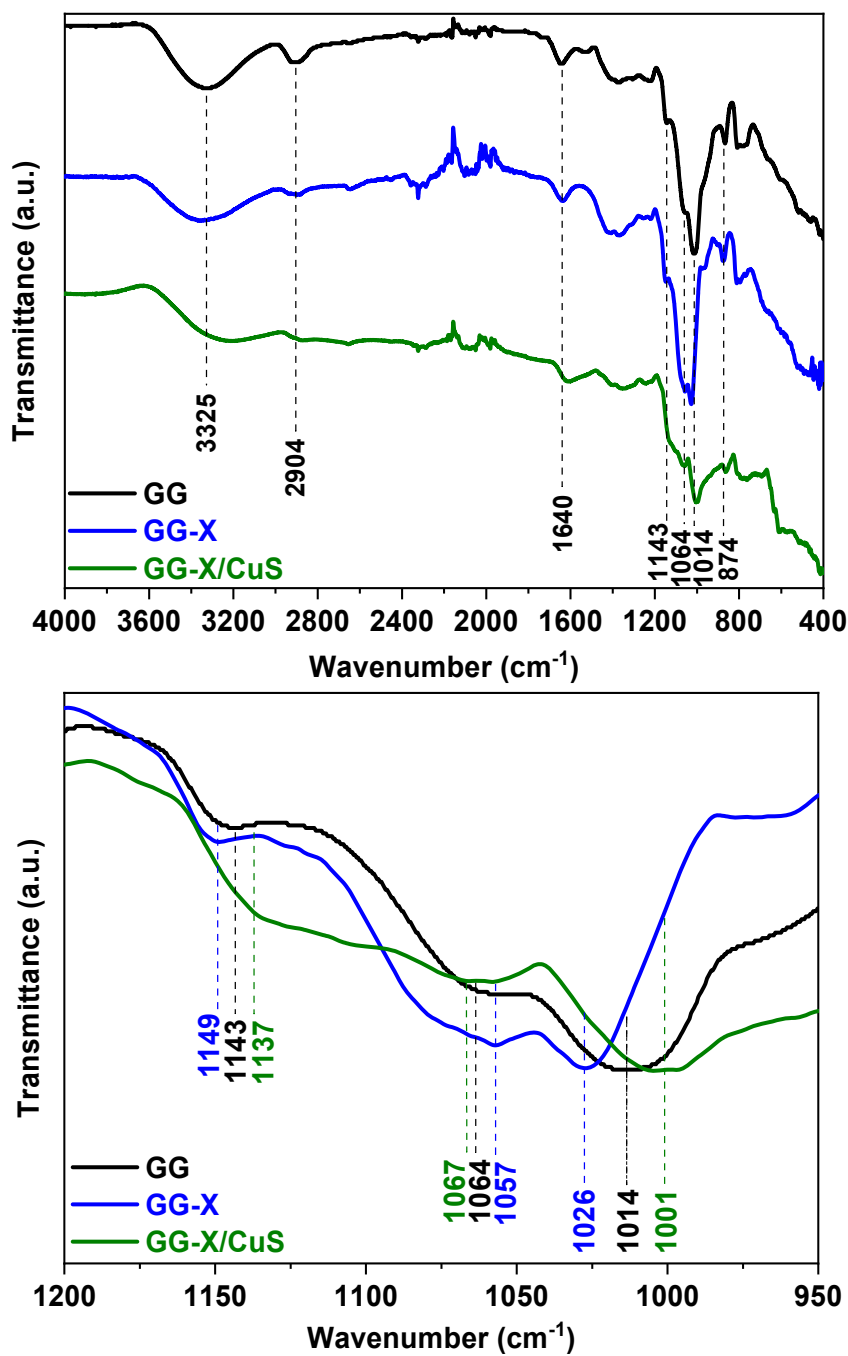
Fig. 23. FTIR spectra of GG, GG-X, GG/CuS. Reproduced with permission from Paper III. Copyright 2022, Elsevier.

5.2.2.3 XRD
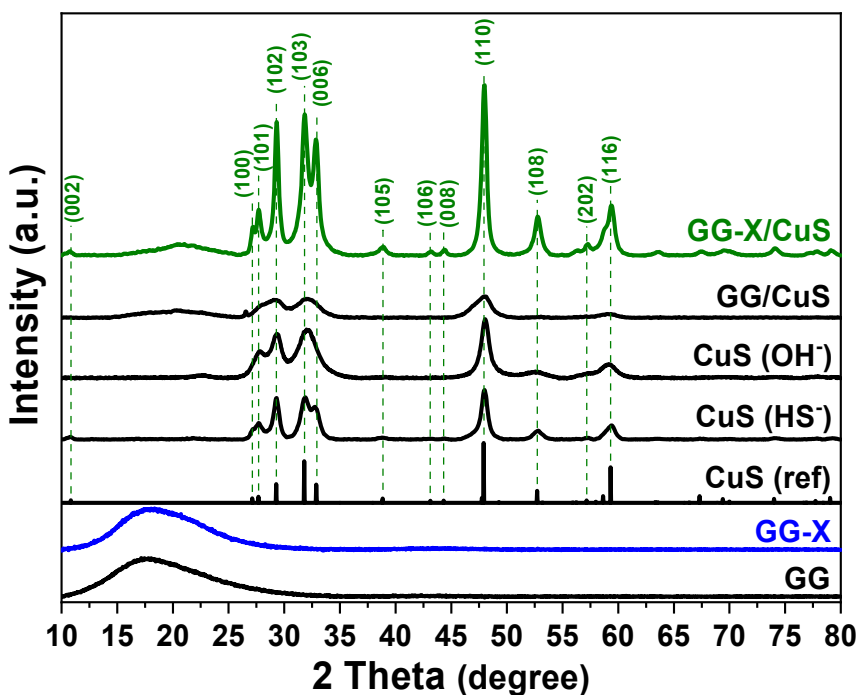
Fig. 24. XRD spectra of CG, CuS reference, controlled CuS, CG/CuS at pH 7, 10 and 13. Reproduced with permission from Paper III. Copyright 2022, Elsevier.

The X-ray diffractograms of both GG and GG-X had broad peaks at around 2θ = 18°, indicating their amorphous phase structure (Fig. 24). Meanwhile, the CuS covellite phase structure in CuS (HS$^-$), CuS (OH$^-$), GG/CuS and GG-X/CuS was confirmed when compared to the CuS covellite reference. In addition, small broad signals at 2θ of around 20.5° could be attributed to the presence of amorphous GG and GG-X in GG/CuS and GG-X/CuS, respectively.

During the pH-dependent precipitation of CuS, GG-X can offer not only a GG polysaccharide matrix with remaining hydroxyl functional groups and xanthate capping functional groups, but also an intrinsic pH environment of around 10. It was, therefore, important to examine whether beneficial effects of GG-X on the synthesis of CuS result from the alkaline pH environment, the presence of GG matrix and/or xanthate groups (Table 1). Among the four

tested samples, CuS (OH$^-$) and GG/CuS had broad XRD peaks and smaller crystallite sizes (9.1 and 5.1 nm, respectively) when compared to 11.7 nm of the CuS (HS$^-$) control sample, and therefore, excluding beneficial effects of the alkaline environment and the presence of GG polysaccharide matrix in forming crystalline CuS covellite. Meanwhile, CuS in GG-X/CuS possessed the most distinctly sharp XRD peaks and the largest crystallite size (15.6 nm), which emphasized the advantage of employing GG-X in enhancing the crystallite size of CuS, hence, potentially relating to its electrical conductivity [288].

Table 1: Synthetic conditions of CuS covellite particles and their crystallite size in CuS (HS$^-$), CuS (OH$^-$), GG/CuS and GG-X/CuS samples. (+) means yes, (-) means no.

Sample	CuS (HS$^-$)	CuS (OH$^-$)	GG/CuS	GG-X/CuS
Addition order	(i) HS$^-$ + OH$^-$ (ii) Cu^{2+}	(i) OH$^-$ (ii) Cu^{2+} (iii) HS$^-$	(i) GG + OH$^-$ (ii) Cu^{2+} (iii) HS$^-$	(i) GG-X (ii) Cu^{2+} (iii) HS$^-$
Alkaline pH 10.5	+	+	+	+
GG matrix	-	-	+	+
Xanthate groups	-	-	-	+
Crystallite size of CuS, nm	11.7	9.1	5.1	15.6

5.2.2.4 SEM-EDS

SEM analysis indicated irregular morphology of GG in GG, GG-X and GG-X/CuS samples (Fig. 25 a, b and g, respectively) with particle size in the range of 30-90 μm, as well as some degree of GG particle aggregation in GG-X and GG-X/CuS. Elemental mapping by EDS was carried out to confirm the presence of C (red), O (lime), S (blue) and Cu (cyan) elements in GG-X and GG-X/CuS. C and O atoms could be easily detected in both samples in Fig. 25 d and j. Meanwhile, S atoms in GG-X and GG-X/CuS, as well as Cu atoms from CuS of

GG-X/CuS were observed in Fig. 25 f, l and h, respectively. More interestingly, individual CuS nanoparticles (average length of 230 ± 31 nm) were found distributed uniformly throughout the GG-X polysaccharide matrix (Fig. 26), compared to separated domains of CuS nanoparticles that were found in CG/CuS (Section 5.1.2.3).
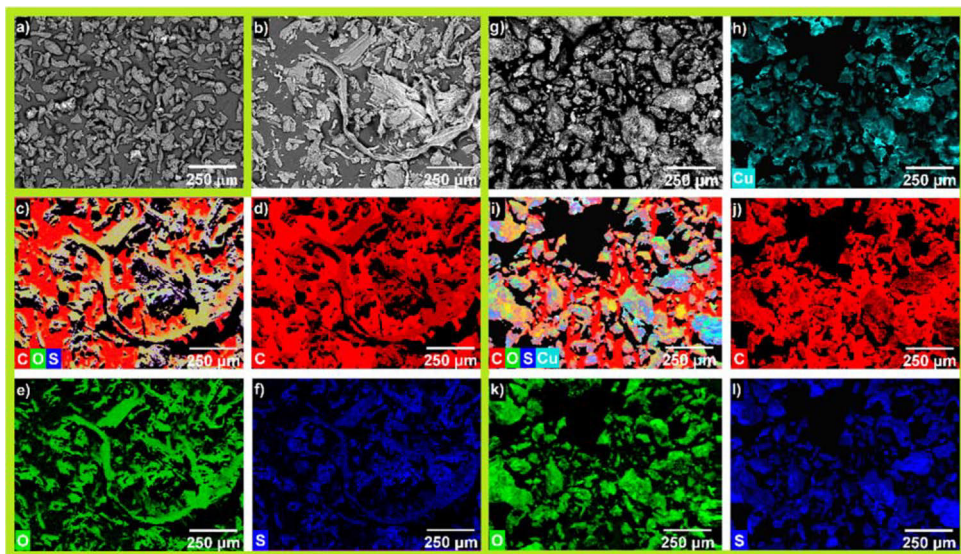
Fig. 25. SEM micrographs of GG (a), GG-X (b) and GG-X/CuS (g) as well as the EDS elemental mapping of GG-X (c-f) and GG-X/CuS (h-l). Carbon, oxygen, sulfur and copper are shown in red, lime, blue and cyan, respectively. Reproduced with permission from Paper III. Copyright 2022, Elsevier.
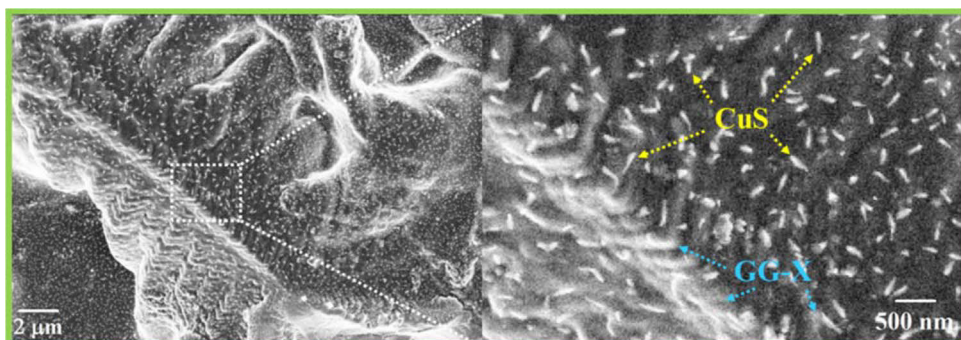
Fig. 26. SEM micrographs of GG-X/CuS. Reproduced with permission from Paper III SI. Copyright 2022, Elsevier.

5.2.2.5 TGA-DTG
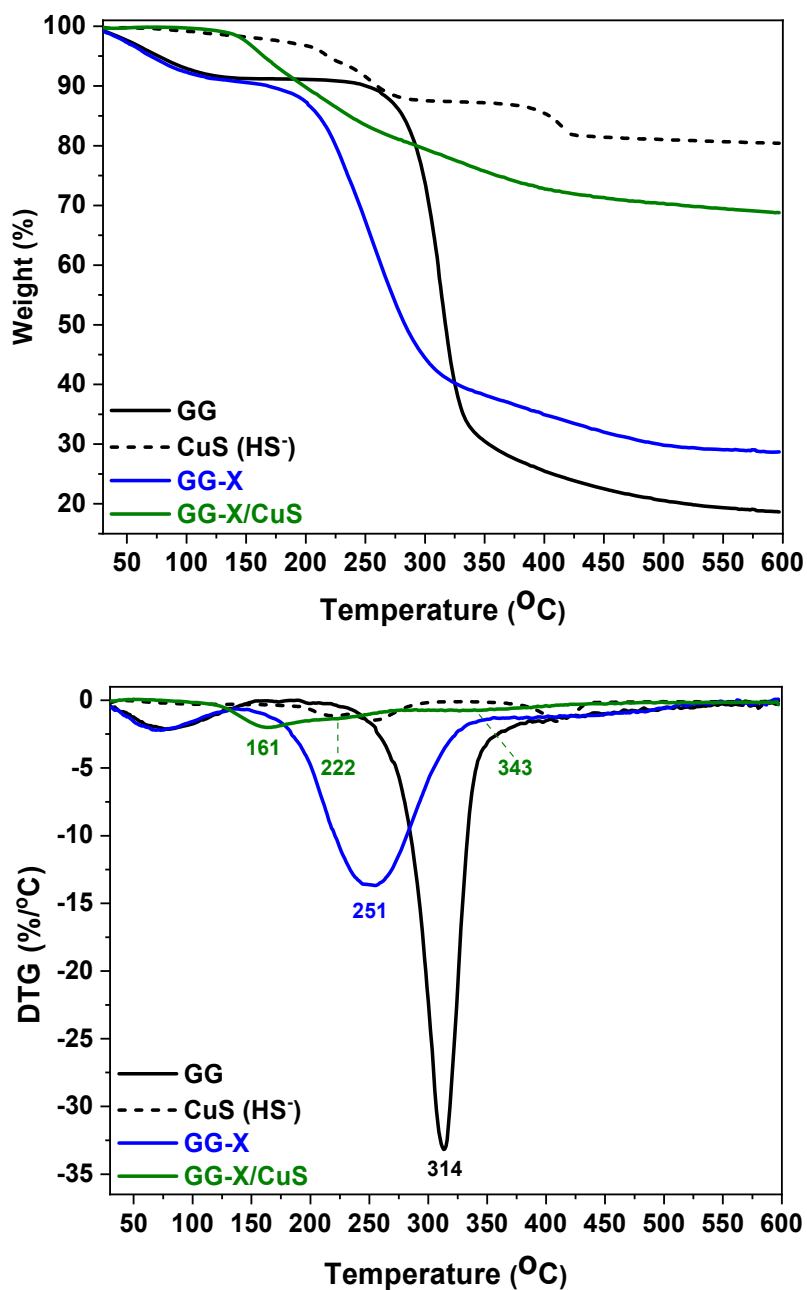
Fig. 27. TGA (top) and DTG (bottom) thermograms of GG, CuS (HS⁻), GG-X and GG-X/CuS. Reproduced with permission from Paper III. Copyright 2022, Elsevier.

Under N_2 atmosphere, the thermograms of GG reference showed two major weight losses at around 78 °C and 314 °C due to water desorption and thermal degradation of galactomannan chains, respectively (Fig. 27) [284]. Meanwhile, the thermograms of GG-X also exhibited two similar thermal events around 72 °C because of water desorption and 251 °C due to the degradation of xanthate groups and galactomannan chains [289]. Within the studied temperature range, a gradual weight loss of CuS was also observed due to moisture removal, CuS degradation to Cu_xS ($1 < x \leq 2$) and vaporization of released S (similarly to Section. 5.1.2.4). In addition, GG-X/CuS possessed three major thermal events, namely, water desorption at around 161 °C, removal of lattice water, decomposition of xanthate groups, galactomannan backbone and/or CuS into Cu_xS ($1 < x \leq 2$) at around 222 and 343 °C.

5.2.3 Potential applications

Metal ion complexation plays a crucial role in numerous fields [290–294]. From the hard and soft acid and base (HSAB) theory, metal ions can be classified as hard (Al^{3+}, Cr^{3+}, Fe^{3+}), borderline (Co^{2+}, Cu^{2+}, Fe^{2+}, Ni^{2+}, Pb^{2+}, Sn^{2+}, Zn^{2+}), and soft (Cd^{2+}, Pt^{2+}) acids [295]. Since pristine GG contains hydroxyl functional groups, which can be classified as hard bases, metal ion complexation by GG is typically limited to hard (Al^{3+}) and borderline (Pb^{2+}) acids, rather than soft acids (Cd^{2+}) (Fig. 28). The introduction of S-containing xanthate groups to GG, however, reversed the coordinating capacity of GG. Fig. 29 shows that GG-X with soft-base xanthate groups could easily form complexation to a wide range of soft and borderline acids, rather than the hard acids. This indicates great potential of GG-X in metal ion complexation for the synthesis of cross-linked hydrogels and removal of heavy metal ions in wastewater treatment (Scheme 5).
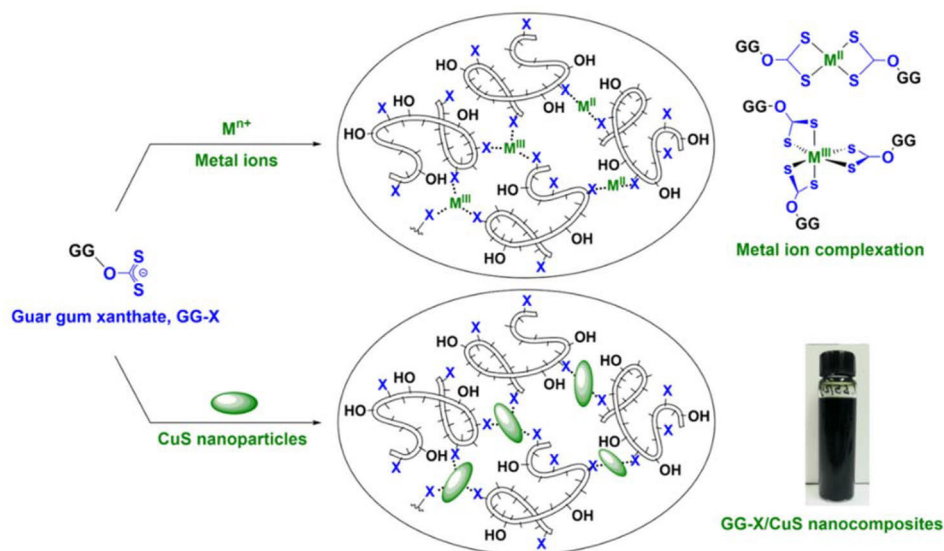
Scheme 5. Potential applications of GG-X in metal ion complexation and CuS-based nanocomposite formation. Reproduced with permission from Paper III. Copyright 2022, Elsevier.
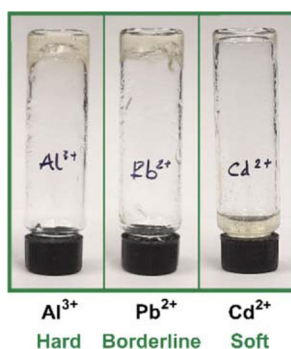
Fig. 28. Metal-ion complexation of pristine GG with Al^{3+}, Pb^{2+} and Cd^{2+} under pH 10. Reproduced with permission from Paper III SI. Copyright 2022, Elsevier.
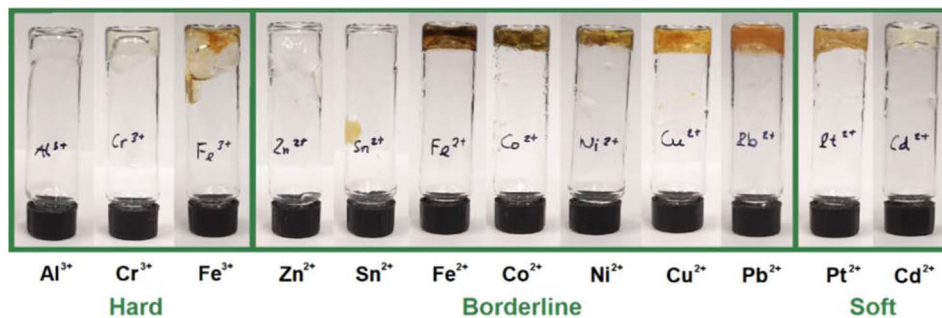
Fig. 29. Metal-ion complexation of GG-X with hard, borderline and soft acids under pH 10. Reproduced with permission from Paper III. Copyright 2022, Elsevier.

Moreover, GG-X has been found as a valuable surfactant and polysaccharide matrix to prepare organic/inorganic composites (Scheme 5). The GG-X/CuS composite showed potential in humidity sensing with a greater range of resistance variation, and hence, greater sensitivity compared to the GG/CuS control sample. Within the tested relative humidity between 80 and 10%, a linear normalized resistance decrease has been determined with some degree of hysteresis. The resistance variation of GG-X/CuS upon water exposure shared similar mechanisms with those of CG/CuS [Paper III, Fig. 5 b, c].

5.3 Guar gum-benzoic acid (GG-BA) [296]

5.3.1 Synthesis
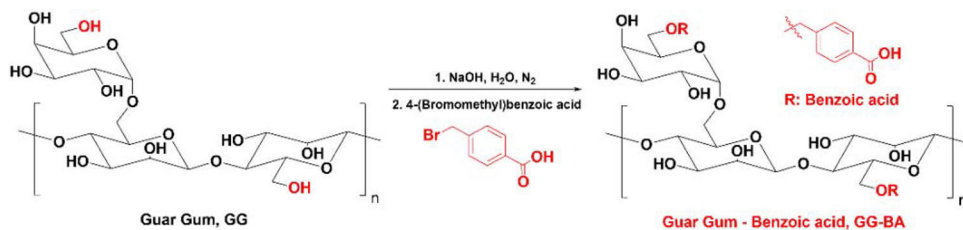
Scheme 6. Synthesis of GG-BA. Reproduced with permission from Paper IV. Copyright 2022, Elsevier.

Benzoic acid moieties were successfully introduced to GG via a nucleophilic substitution reaction between 4-(bromomethyl)benzoic acid (BBA) and GG in a N_2-purged alkaline aqueous solution at room temperature with a reaction yield of 83% (Scheme 6).

5.3.2 Characterization

5.3.2.1 ^{1}H-NMR

While hydrophilic pristine GG had poor solubility in DMSO solvent, GG-BA was found more hydrophobic due to the presence of benzoic acid (BA) groups, hence, ^{1}H NMR spectrum of GG-BA in polar aprotic DMSO-d_6 was easily obtained as shown in Fig. 30. The ^{1}H NMR spectrum of GG-BA showed proton signals with chemical shift between 3.4 and 5.0 ppm. These signals were attributed to aliphatic protons (CH, CH$_2$) from the galactomannan chains and protons from remaining hydroxyl groups of GG. Besides, ortho and meta proton signals from BA groups of GG-BA were detected in the typical aromatic chemical shift range between 7.3 to 8.0 ppm with good agreement to ^{1}H NMR spectrum of the BBA reference [Paper IV, Fig. S1]. In addition, a small proton signal of –CO$_2$H from BA in GG-BA was also observed at a chemical shift of around 12.8 ppm. Meanwhile, the degree of substitution of GG-BA was calculated from the intensity of the aliphatic and aromatic proton signals as

0.1639, suggesting a grafting density of 5.5% and a chemical formula of $C_6H_{9.8361}O_5(C_8H_7O_2)_{0.1639}$ for AGU of GG-BA.
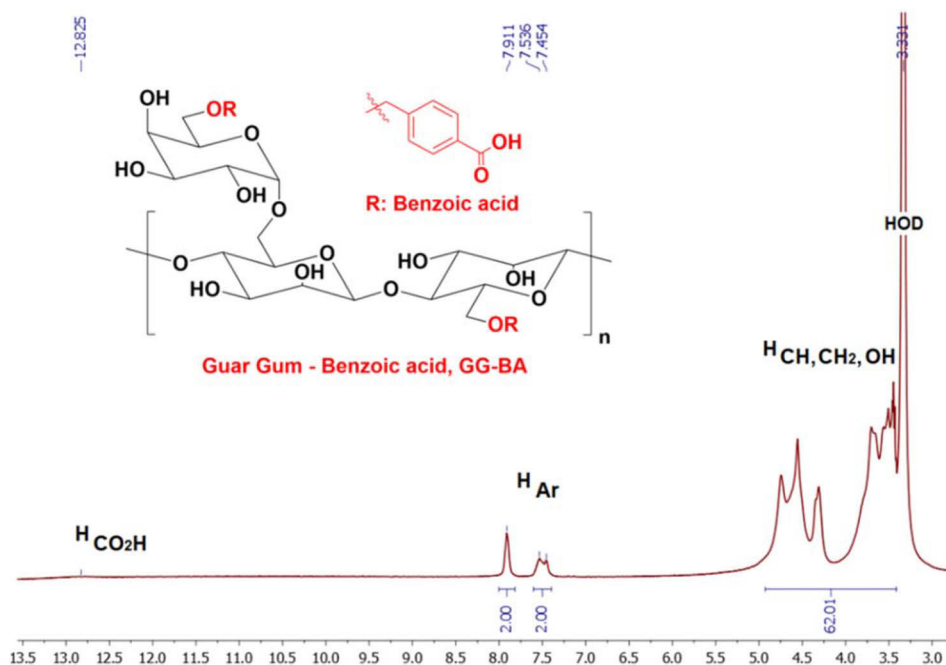
Fig. 30. ^{1}H NMR spectrum of GG-BA in DMSO-d_6 at 25 °C. Reproduced with permission from Paper IV. Copyright 2022, Elsevier.

5.3.2.2 UV-Vis

The UV–Vis spectra showed that the absorption spectrum of GG extended from 700 nm to 190 nm with two distinct maxima around 341.0 and 262.0 nm. Meanwhile, the BBA reference did not absorb visible light and possessed a major absorption maximum at 246.5 nm, as well as a small absorption band around 290.0 nm (Fig. 31). Due to different molar absorption coefficients of the galactomannan backbone and the BA moieties in GG-BA, and a similar absorption spectrum of GG-BA to that of BBA with no absorption band in the visible radiation range, the absorption spectrum of GG-BA might result mainly from the presence of BA groups. Comparing to the BBA reference, GG-BA had a blue-shifted absorption maximum at 236.5 nm and a small absorption band

around 280 nm, which might be attributed to the blue-shifted absorption of BA and/or the absorption of galactomannan backbone from GG.
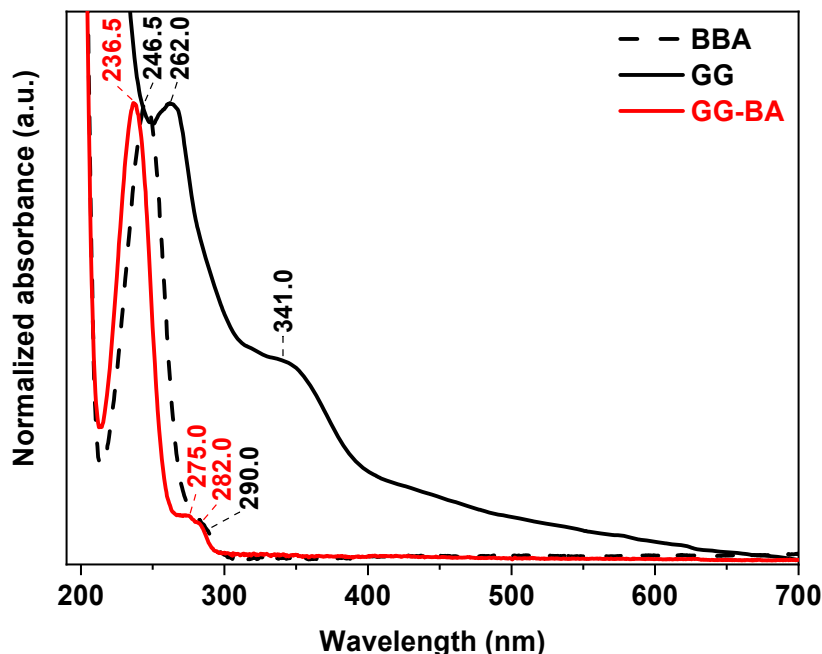
Fig. 31. UV-Vis absorption spectra of BBA, GG reference and GG-BA (dashed black, black and red, respectively) in aqueous solutions at pH 1.01. Reproduced with permission from Paper IV. Copyright 2022, Elsevier.

5.3.2.3 FTIR

Typical vibration peaks of the GG reference were observed at 3330, 2920, 1645, 1143, 1065, 1012 and 867 cm^{-1} from O–H stretching, C–H stretching, ring stretching, C-OH stretching, CH$_2$OH stretching, CH$_2$ twisting vibrations and characteristic galactomannan chains, respectively (Fig. 32), which were similar to those described in Section 5.2.2.2. Comparing to GG, the FTIR spectrum of GG-BA showed new signals at 1694 cm^{-1} and 1255 cm^{-1}, which were attributed to C=O and C-O stretching vibrations from carboxylic acid groups of BA in GG-BA.
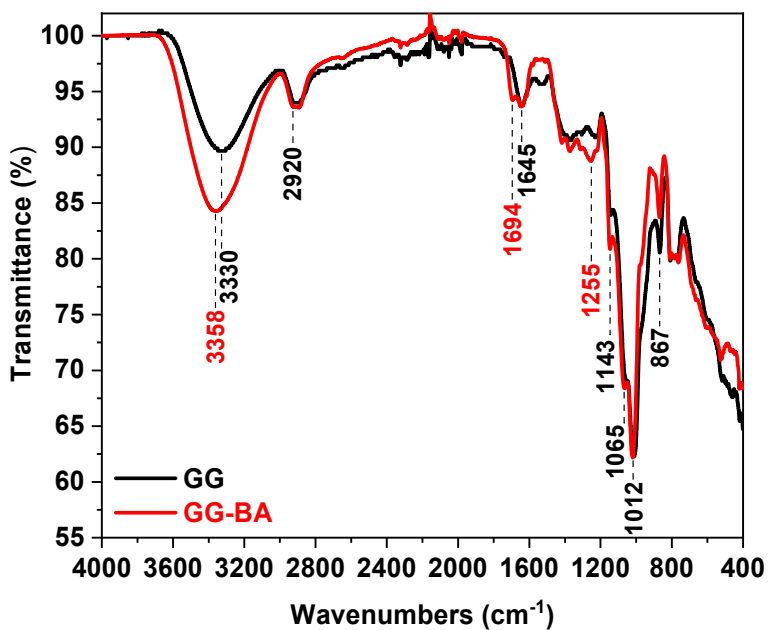
Fig. 32. FTIR spectra of BBA, GG reference and GG-BA. Reproduced with permission from Paper IV. Copyright 2022, Elsevier.

5.3.2.4 XRD
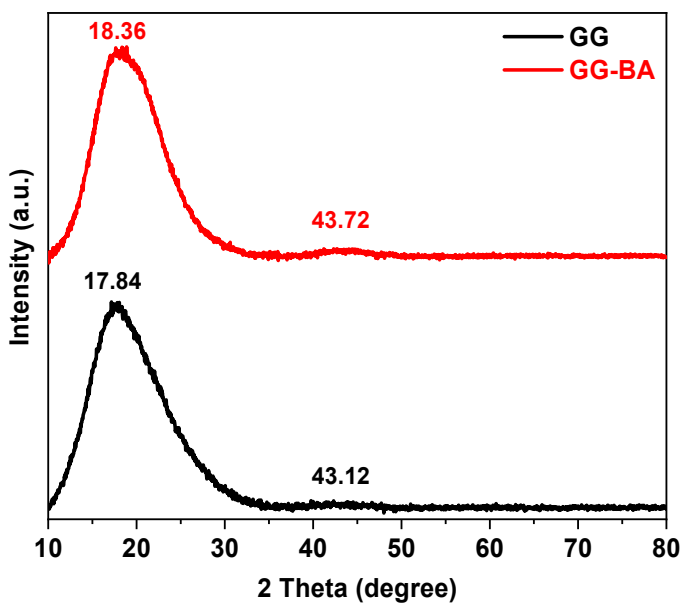
Fig. 33. XRD spectra of the GG reference and GG-BA. Reproduced with permission from Paper IV. Copyright 2022, Elsevier.

The X-ray diffractograms of GG and GG-BA (Fig. 33) had broad diffused peaks around similar 2θ values of 17.84, 18.36, 43.12 and 43.72°, suggesting an amorphous phase structure of both GG and GG-BA.

5.3.2.5 SEM and TEM

SEM analysis showed irregular shapes of both GG and GG-BA particles with particle size of 637 ± 16 and 196 ± 17 nm, respectively (Fig. 34 a, b). Meanwhile, TEM micrographs showed a more spherical morphology of GG and GG-BA with smaller particle size of around 400-600 and 100-200 nm for GG and GG-BA, respectively (Fig. 34 c, d). Both SEM and TEM analyses indicated a significant particle size decrease by nearly three-fold of GG-BA compared to GG, which might be due to dissolution and precipitation processes during the chemical functionalization of GG into GG-BA.
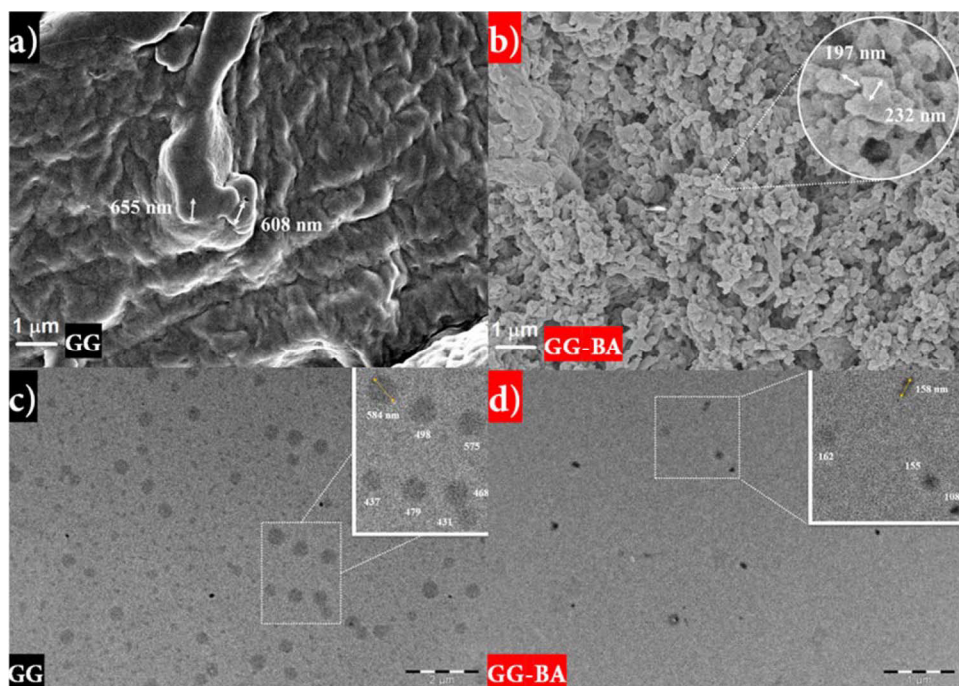
Fig. 34. SEM (a, b) and TEM (c, d) micrographs of GG (a, c) and GG-BA (b, d). Reproduced with permission from Paper IV. Copyright 2022, Elsevier.

5.3.2.6 TGA-DTG
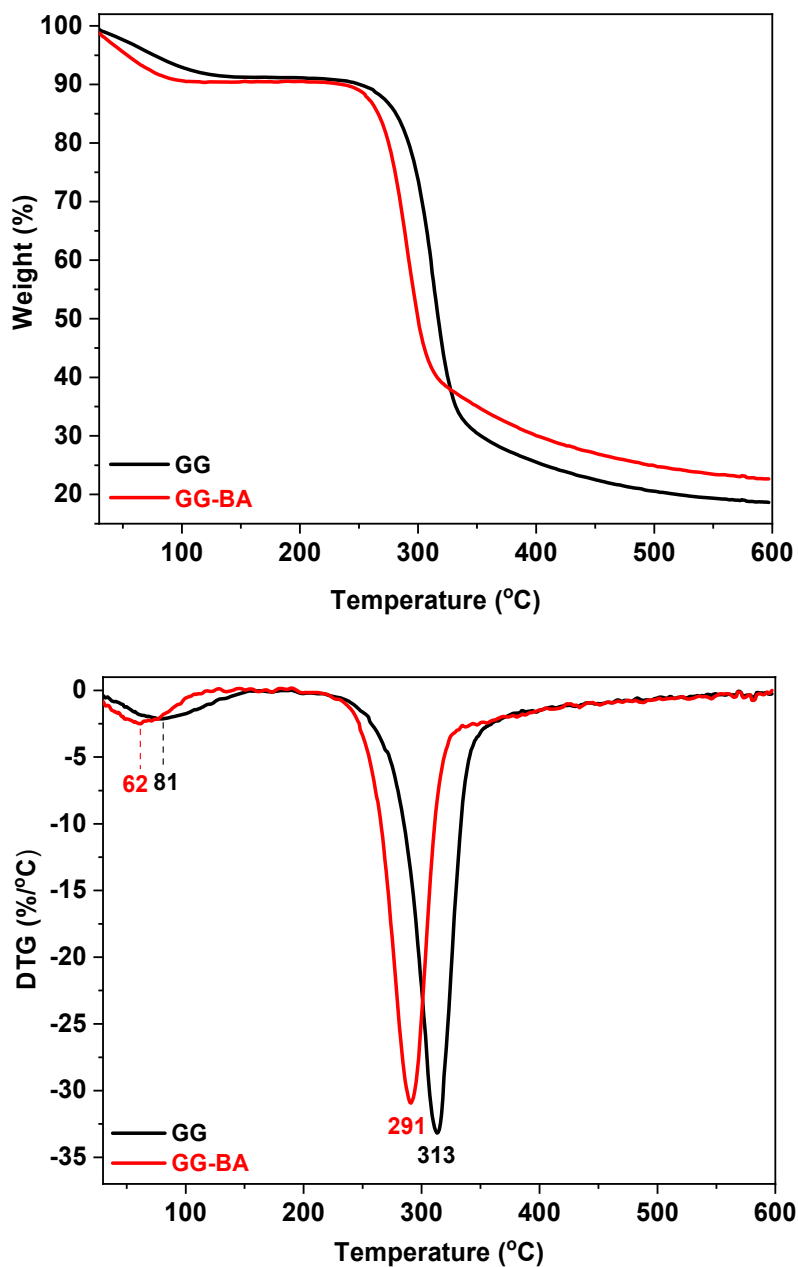
Fig. 35. TGA (top) and DTG (bottom) thermograms of GG and GG-BA.
Reproduced with permission from Paper IV. Copyright 2022, Elsevier.

Under N_2 atmosphere, the TGA and DTG thermograms of GG and GG-BA showed two major thermal degradation events (Fig. 35). Moisture removal of GG and GG-BA was detected around 81 and 62 °C, respectively, with similar weight losses of around 8%. The lower temperature for water desorption of GG-BA compared to that of GG was attributed to the increase in hydrophobicity of GG-BA due to the presence of benzene rings in the BA moieties. Moreover, the DTG curves indicated that GG-BA thermally degraded at a lower temperature than GG (at around 291 and 313 °C, respectively). Nevertheless, a smaller weight loss of 57.9% was noted in GG-BA compared to that of 66.1% in GG from the TGA thermograms. This could be attributed to a smaller grain size, hence, a larger surface area of GG-BA particles, allowing a more efficient heat transfer process, and therefore, lowering the degradation temperature range.

5.3.3 Potential applications

GG-BA was found biocompatible to mesenchymal and epithelial cells, which are the two main types of connective cells mainly consisting of tissues and organs [Paper IV, Fig. 6]. GG-BA, therefore, has great potential to be developed into biomaterials. Due to the presence of carboxylic acid functional groups in the benzoic acid moieties of GG-BA, deprotonation of GG-BA can be readily carried out at neutral to mildly alkaline pH to obtain anionic GG-BA, which could be exploited in complex coacervation and drug delivery systems similarly to previously reported carboxylic acid-containing GG derivatives (Scheme 7) [297,298]. In addition, coordination chemistry between benzoic acid moieties in GG-BA and various metal cations could also be explored to yield novel structures and materials (Scheme 8) [299–301].
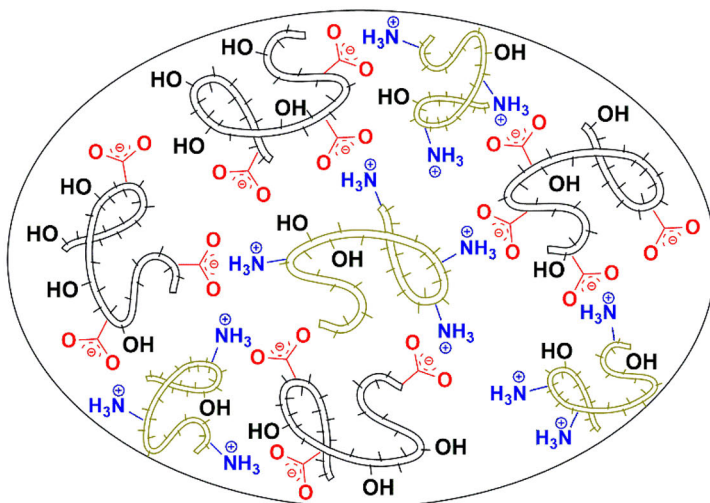
Scheme 7. Possible complex coacervation of anionic GG-BA and a cationic polysaccharide.
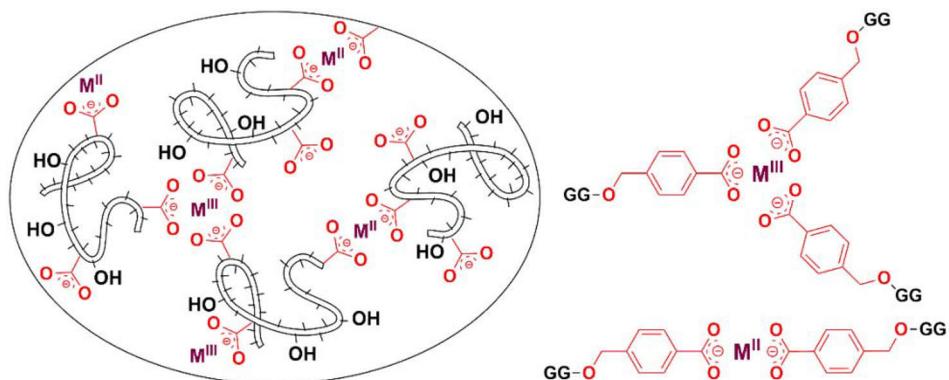
Scheme 8. Possible coordination chemistry of GG-BA and metal cations to form cross-linked hydrogels.

6 Conclusions and outlook

In this thesis, natural biodegradable polysaccharides have been shown to be excellent building blocks to fabricate novel materials. Natural polysaccharides can be used directly in their native forms or chemically functionalized to significantly alter their chemical properties.

Pristine anionic CG was firstly chosen to fabricate a CG/CuS nanocomposite via a novel precipitation process at a gel/liquid interface that mimicked natural chemobrionics. This synthetic approach offered a simple yet efficient way to prepare inorganic/organic nanocomposites, which could be used in humidity and temperature sensing (Paper I).

Then, to demonstrate how chemical functionalization can significantly alter properties of natural polysaccharides and extend their applicability, non-ionic GG was chosen as a model polysaccharide. An extensive review on different chemical modification approaches of GG was conducted to analyze recent advances in this field. Various chemical reagents and reaction pathways such as nucleophilic reactions, graft polymerization, partial oxidation and cross-linking for the functionalization of GG and its derivatives were examined. In addition, structure-property relationships and potential applications of GG-based materials were also discussed (Paper II).

Subsequently, nucleophilic substitution reactions were chosen and optimized to chemically modify GG in aqueous medium at room temperature without using toxic organic solvents. By employing these synthetic conditions, a number of organic functional groups and moieties such as amine, thiol, xanthate, benzoic acid, catechol and tosylate have been successfully conjugated to GG. In the scope of this study, chemical modification of GG with xanthate and benzoic acid groups was chosen to discuss further.

Xanthate functional groups were successfully introduced to GG, yielding GG-X. The presence of xanthate in GG-X could substantially alter the coordination chemistry of native GG towards various metal ions, which

showed great potentials in heavy metal removal, wastewater treatment, cross-linked hydrogel preparation, etc. Moreover, GG-X was used as a surfactant to support the synthesis of CuS covellite nanoparticles and simultaneously as an organic matrix to form a GG-X/CuS nanocomposite. The homogeneous colloidal dispersion of GG-X/CuS in water was stable for months and showed electrical responsiveness to humidity changes as well as printability. This material could therefore be developed further into humidity sensors and potentially printable electrically conductive inks (Paper III).

Benzoic acid was another fascinating organic moiety to be chemically linked to GG, resulting in GG-BA. Benzoic acid moieties contain aromatic benzene rings and carboxylic acid groups, which could offer interesting intermolecular interactions and coordination chemistry to GG polysaccharide. GG-BA showed good biocompatibility to living cells (mouse embryonic fibroblasts and human mammary epithelial cells) and was an excellent starting material to fabricate biomaterials such as coacervates and hydrogels for drug delivery, wound dressing and bioadhesives (Paper IV). Further development of GG-BA into cross-linked hydrogels and coacervates for biological applications is being carried out.

Natural polysaccharides such as CG and GG are ubiquitous in nature and have been widely used in human history. Even though various pristine natural polysaccharides can be employed directly, further chemical modifications of natural polysaccharides, however, can substantially enrich and alter properties of these materials, hence, extending their applicability in many fields such as medicine, biomaterials and biofuels. Modifying properties of natural polysaccharides and formulating complex materials using polysaccharides and other organic and inorganic materials by chemical approaches can offer green and sustainable solutions to deal with climate change, food and energy crises. Therefore, these materials are of paramount interest for future research.

7   Acknowledgement

This research work was done under the supervision of Assoc. Prof. Tan-Phat Huynh and Prof. Jouko Peltonen in the Faculty of Science and Engineering, Åbo Akademi University. I wish to express my deepest gratitude to my supervisors for their continuous guidance, support, and inspiration.

Generous financial support from the Doctoral network in Materials research (DNMR) fellowship, Åbo Akademi University, and a research grant from the Magnus Ehrnrooth foundation and the Finnish Society of Sciences and Letters are gratefully acknowledged.

Throughout this journey, many fruitful collaborations have been made between researchers from different countries namely, China, France, Israel, Morocco, and Poland. Thank you for your invaluable perspectives and contributions to this work.

To my lab members at Fyke and especially Kena, thank you so much for your advice, assistance, all the memories and joys that we shared together.

To my beloved family, your infinite love and encouragement have made this work come true.

8 Bibliography

[1]   Vitousek PM, Ehrlich PR, Ehrlich AH, Matson PA. Human Appropriation of
       the Products of Photosynthesis. Bioscience 1986;36:368–73.
       https://doi.org/10.2307/1310258.

[2]   Rojstaczer S, Sterling SM, Moore NJ. Human Appropriation of Photosynthesis
       Products. Science (1979) 2001;294:2549–52.
       https://doi.org/10.1126/science.1064375.

[3]   Roubík H, Lošťák M, Ketuama CT, Procházka P, Soukupová J, Hakl J, et al.
       Current coronavirus crisis and past pandemics - What can happen in post-
       COVID-19 agriculture? Sustain Prod Consum 2022;30:752–60.
       https://doi.org/10.1016/j.spc.2022.01.007.

[4]   Creutzig F. Fuel crisis: slash demand in three sectors to protect economies
       and climate. Nature 2022;606:460–2. https://doi.org/10.1038/d41586-022-
       01616-z.

[5]   Le T, Huynh T. The Combination of Hydrogen and Methanol Production
       through Artificial Photosynthesis—Are We Ready Yet? ChemSusChem
       2018;11:2654–72. https://doi.org/10.1002/cssc.201800731.

[6]   Rogelj J, Geden O, Cowie A, Reisinger A. Net-zero emissions targets are
       vague: three ways to fix. Nature 2021;591:365–8.
       https://doi.org/10.1038/d41586-021-00662-3.

[7]   Jeffry L, Ong MY, Nomanbhay S, Mofijur M, Mubashir M, Show PL.
       Greenhouse gases utilization: A review. Fuel 2021;301:121017.
       https://doi.org/10.1016/j.fuel.2021.121017.

[8]   Goswami RK, Mehariya S, Obulisamy PK, Verma P. Advanced microalgae-
       based renewable biohydrogen production systems: A review. Bioresour
       Technol 2021;320:124301.
       https://doi.org/10.1016/j.biortech.2020.124301.

[9]   Hesham AE-L, Kaur T, Devi R, Kour D, Prasad S, Yadav N, et al. Current
       Trends in Microbial Biotechnology for Agricultural Sustainability:

Conclusion and Future Challenges, 2021, p. 555–72.
https://doi.org/10.1007/978-981-15-6949-4_22.

[10]   Horton P, Long SP, Smith P, Banwart SA, Beerling DJ. Technologies to deliver
         food and climate security through agriculture. Nat Plants 2021;7:250–5.
         https://doi.org/10.1038/s41477-021-00877-2.

[11]   Nelson N, Ben-Shem A. The complex architecture of oxygenic
         photosynthesis. Nat Rev Mol Cell Biol 2004;5:971–82.
         https://doi.org/10.1038/nrm1525.

[12]   Janssen PJD, Lambreva MD, Plumeré N, Bartolucci C, Antonacci A,
         Buonasera K, et al. Photosynthesis at the forefront of a sustainable life. Front
         Chem 2014;2. https://doi.org/10.3389/fchem.2014.00036.

[13]   Biel K, Fomina I. Benson-Bassham-Calvin cycle contribution to the organic
         life on our planet. Photosynthetica 2015;53:161–7.
         https://doi.org/10.1007/s11099-015-0112-7.

[14]   Junge W. Oxygenic photosynthesis: history, status and perspective. Q Rev
         Biophys 2019;52:e1. https://doi.org/10.1017/S0033583518000112.

[15]   Sánchez-Baracaldo P, Cardona T. On the origin of oxygenic photosynthesis
         and Cyanobacteria. New Phytologist 2020;225:1440–6.
         https://doi.org/10.1111/nph.16249.

[16]   Lovegrove A, Edwards CH, De Noni I, Patel H, El SN, Grassby T, et al. Role of
         polysaccharides in food, digestion, and health. Crit Rev Food Sci Nutr
         2017;57:237–53. https://doi.org/10.1080/10408398.2014.939263.

[17]   Dave PN, Gor A. Natural Polysaccharide-Based Hydrogels and Nanomaterials.
         Handbook of Nanomaterials for Industrial Applications, Elsevier; 2018, p.
         36–66. https://doi.org/10.1016/B978-0-12-813351-4.00003-1.

[18]   Gopinath V, Saravanan S, Al-Maleki AR, Ramesh M, Vadivelu J. A review of
         natural polysaccharides for drug delivery applications: Special focus on
         cellulose, starch and glycogen. Biomedicine & Pharmacotherapy
         2018;107:96–108. https://doi.org/10.1016/j.biopha.2018.07.136.

[19] Silva ACQ, Silvestre AJD, Vilela C, Freire CSR. Natural Polymers-Based Materials: A Contribution to a Greener Future. Molecules 2021;27:94. https://doi.org/10.3390/molecules27010094.

[20] Pattnaik F, Tripathi S, Patra BR, Nanda S, Kumar V, Dalai AK, et al. Catalytic conversion of lignocellulosic polysaccharides to commodity biochemicals: a review. Environ Chem Lett 2021;19:4119–36. https://doi.org/10.1007/s10311-021-01284-x.

[21] Baranwal J, Barse B, Fais A, Delogu GL, Kumar A. Biopolymer: A Sustainable Material for Food and Medical Applications. Polymers (Basel) 2022;14:983. https://doi.org/10.3390/polym14050983.

[22] Šimkovic I. Unexplored possibilities of all-polysaccharide composites. Carbohydr Polym 2013;95:697–715. https://doi.org/10.1016/j.carbpol.2013.03.040.

[23] Abdul Khalil HPS, Chong EWN, Owolabi FAT, Asniza M, Tye YY, Rizal S, et al. Enhancement of basic properties of polysaccharide-based composites with organic and inorganic fillers: A review. J Appl Polym Sci 2019;136:47251. https://doi.org/10.1002/app.47251.

[24] Nadar SS, Vaidya L, Maurya S, Rathod VK. Polysaccharide based metal organic frameworks (polysaccharide–MOF): A review. Coord Chem Rev 2019;396:1–21. https://doi.org/10.1016/j.ccr.2019.05.011.

[25] Torres FG, De-la-Torre GE. Polysaccharide-based triboelectric nanogenerators: A review. Carbohydr Polym 2021;251:117055. https://doi.org/10.1016/j.carbpol.2020.117055.

[26] Priya S, Batra U, R.N. S, Sharma S, Chaurasiya A, Singhvi G. Polysaccharide-based nanofibers for pharmaceutical and biomedical applications: A review. Int J Biol Macromol 2022;218:209–24. https://doi.org/10.1016/j.ijbiomac.2022.07.118.

[27] Zheng Y, Monty J, Linhardt RJ. Polysaccharide-based nanocomposites and their applications. Carbohydr Res 2015;405:23–32. https://doi.org/10.1016/j.carres.2014.07.016.

[28]   Xu Y, Wu Y, Sun P, Zhang F, Linhardt RJ, Zhang A. Chemically modified polysaccharides: Synthesis, characterization, structure activity relationships of action. Int J Biol Macromol 2019;132:970–7. https://doi.org/10.1016/j.ijbiomac.2019.03.213.

[29]   Xie L, Shen M, Hong Y, Ye H, Huang L, Xie J. Chemical modifications of polysaccharides and their anti-tumor activities. Carbohydr Polym 2020;229:115436. https://doi.org/10.1016/j.carbpol.2019.115436.

[30]   Necas J, Bartosikova L. Carrageenan: a review. Vet Med (Praha) 2013;58:187–205. https://doi.org/10.17221/6758-VETMED.

[31]   Campo VL, Kawano DF, Silva DB da, Carvalho I. Carrageenans: Biological properties, chemical modifications and structural analysis – A review. Carbohydr Polym 2009;77:167–80. https://doi.org/10.1016/j.carbpol.2009.01.020.

[32]   Yegappan R, Selvaprithiviraj V, Amirthalingam S, Jayakumar R. Carrageenan based hydrogels for drug delivery, tissue engineering and wound healing. Carbohydr Polym 2018;198:385–400. https://doi.org/10.1016/j.carbpol.2018.06.086.

[33]   Sedayu BB, Cran MJ, Bigger SW. A Review of Property Enhancement Techniques for Carrageenan-based Films and Coatings. Carbohydr Polym 2019;216:287–302. https://doi.org/10.1016/j.carbpol.2019.04.021.

[34]   Pacheco-Quito E-M, Ruiz-Caro R, Veiga M-D. Carrageenan: Drug Delivery Systems and Other Biomedical Applications. Mar Drugs 2020;18:583. https://doi.org/10.3390/md18110583.

[35]   Jiang J-L, Zhang W-Z, Ni W-X, Shao J-W. Insight on structure-property relationships of carrageenan from marine red algal: A review. Carbohydr Polym 2021;257:117642. https://doi.org/10.1016/j.carbpol.2021.117642.

[36]   Aga MB, Dar AH, Nayik GA, Panesar PS, Allai F, Khan SA, et al. Recent insights into carrageenan-based bio-nanocomposite polymers in food applications: A review. Int J Biol Macromol 2021;192:197–209. https://doi.org/10.1016/j.ijbiomac.2021.09.212.

[37] Sharma G, Khosla A, Kumar A, Kaushal N, Sharma S, Naushad M, et al. A comprehensive review on the removal of noxious pollutants using carrageenan based advanced adsorbents. Chemosphere 2022;289:133100. https://doi.org/10.1016/j.chemosphere.2021.133100.

[38] Rochas C, Rinaudo M. Mechanism of gel formation in ?-carrageenan. Biopolymers 1984;23:735–45. https://doi.org/10.1002/bip.360230412.

[39] Imeson AP. Carrageenan and furcellaran. Handbook of Hydrocolloids, Elsevier; 2009, p. 164–85. https://doi.org/10.1533/9781845695873.164.

[40] Li L, Ni R, Shao Y, Mao S. Carrageenan and its applications in drug delivery. Carbohydr Polym 2014;103:1–11. https://doi.org/10.1016/j.carbpol.2013.12.008.

[41] VIANA A, NOSEDA M, DUARTE M, CEREZO A. Alkali modification of carrageenans. Part V. The iota?nu hybrid carrageenan from and its cyclization to iota-carrageenan. Carbohydr Polym 2004;58:455–60. https://doi.org/10.1016/j.carbpol.2004.08.006.

[42] Genicot-Joncour S, Poinas A, Richard O, Potin P, Rudolph B, Kloareg B, et al. The Cyclization of the 3,6-Anhydro-Galactose Ring of ι-Carrageenan Is Catalyzed by Two d-Galactose-2,6-Sulfurylases in the Red Alga *Chondrus crispus*. Plant Physiol 2009;151:1609–16. https://doi.org/10.1104/pp.109.144329.

[43] Chudzikowski RJ. Guar gum and its applications. Journal of the Society of Cosmetics Chemists 1971;22:43–60.

[44] Huang Q, Liu S, Wang G, Wu B, Zhang Y. Coalbed methane reservoir stimulation using guar-based fracturing fluid: A review. J Nat Gas Sci Eng 2019;66:107–25. https://doi.org/10.1016/j.jngse.2019.03.027.

[45] George A, Shah PA, Shrivastav PS. Guar gum: Versatile natural polymer for drug delivery applications. Eur Polym J 2019;112:722–35. https://doi.org/10.1016/j.eurpolymj.2018.10.042.

[46]   Jana S, Maiti S, Jana S, Sen KK, Nayak AK. Guar gum in drug delivery
         applications. Natural Polysaccharides in Drug Delivery and Biomedical
         Applications, Elsevier; 2019, p. 187–201. https://doi.org/10.1016/B978-0-
         12-817055-7.00007-8.

[47]   Nayak AK, Hasnain MS, Pal K, Banerjee I, Pal D. Gum-based hydrogels in drug
         delivery. Biopolymer-Based Formulations, Elsevier; 2020, p. 605–45.
         https://doi.org/10.1016/B978-0-12-816897-4.00025-4.

[48]   Verma D, Sharma SK. Recent advances in guar gum based drug delivery
         systems and their administrative routes. Int J Biol Macromol 2021;181:653–
         71. https://doi.org/10.1016/j.ijbiomac.2021.03.087.

[49]   Saya L, Malik V, Singh A, Singh S, Gambhir G, Singh WR, et al. Guar gum based
         nanocomposites: Role in water purification through efficient removal of dyes
         and metal ions. Carbohydr Polym 2021;261:117851.
         https://doi.org/10.1016/j.carbpol.2021.117851.

[50]   Abdel-raouf ME-S, Sayed A, Mostafa M. Application of Guar Gum and Its
         Derivatives in Agriculture, 2022, p. 1–17. https://doi.org/10.1007/978-3-
         030-76523-1_5-1.

[51]   Dehghani Soltani M, Meftahizadeh H, Barani M, Rahdar A, Hosseinikhah SM,
         Hatami M, et al. Guar (Cyamopsis tetragonoloba L.) plant gum: From
         biological applications to advanced nanomedicine. Int J Biol Macromol
         2021;193:1972–85. https://doi.org/10.1016/j.ijbiomac.2021.11.028.

[52]   Huang L-H, Li C-C. Effects of interactions between binders and different-
         sized silicons on dispersion homogeneity of anodes and electrochemistry of
         lithium-silicon batteries. J Power Sources 2019;409:38–47.
         https://doi.org/10.1016/j.jpowsour.2018.10.087.

[53]   Yin Z-W, Zhang T, Zhang S-J, Deng Y-P, Peng X-X, Wang J-Q, et al.
         Understanding the role of water-soluble guar gum binder in reducing
         capacity fading and voltage decay of Li-rich cathode for Li-ion batteries.
         Electrochim Acta 2020;351:136401.
         https://doi.org/10.1016/j.electacta.2020.136401.

[54] Kaur S, Santra S. Application of Guar Gum and its Derivatives as Green Binder/Separator for Advanced Lithium-Ion Batteries. ChemistryOpen 2022;11. https://doi.org/10.1002/open.202100209.

[55] Huang Y, Zhang J, Liu J, Li Z, Jin S, Li Z, et al. Flexible and stable quasi-solid-state zinc ion battery with conductive guar gum electrolyte. Mater Today Energy 2019;14:100349. https://doi.org/10.1016/j.mtener.2019.100349.

[56] Xu R, Zhou J, Gong H, Qiao L, Li Y, Li D, et al. Environment-friendly degradable zinc-ion battery based on guar gum-cellulose aerogel electrolyte. Biomater Sci 2022;10:1476–85. https://doi.org/10.1039/D1BM01747K.

[57] Bhardwaj U, Sharma A, Mathur A, Halder A, Kushwaha HS. Novel guar-gum electrolyte to aggrandize the performance of LaMnO $_3$ perovskite-based zinc-air batteries. Electrochemical Science Advances 2022;2. https://doi.org/10.1002/elsa.202100056.

[58] Gunasekaran A, Sorrentino A, Asiri AM, Anandan S. Guar gum-based polymer gel electrolyte for dye-sensitized solar cell applications. Solar Energy 2020;208:160–5. https://doi.org/10.1016/j.solener.2020.07.084.

[59] Guo H, Shi S, Li G, Ji C, Fu C, Shen Y, et al. Biodegradation of guar gum and its enhancing effect on biogas production from coal. Fuel 2022;311:122606. https://doi.org/10.1016/j.fuel.2021.122606.

[60] Rezk MY, Zeitoun M, El-Shazly AN, Omar MM, Allam NK. Robust photoactive nanoadsorbents with antibacterial activity for the removal of dyes. J Hazard Mater 2019;378:120679. https://doi.org/10.1016/j.jhazmat.2019.05.072.

[61] Balachandramohan J, Sivasankar T, Sivakumar M. Facile sonochemical synthesis of Ag2O-guar gum nanocomposite as a visible light photocatalyst for the organic transformation reactions. J Hazard Mater 2020;385:121621. https://doi.org/10.1016/j.jhazmat.2019.121621.

[62] Balachandramohan J, Singh R, Sivasankar T, Manickam S. Sonochemical synthesis of highly efficient Ag3PO4-Guar gum nanocomposite with photo-oxidation property under visible light irradiation. Chemical Engineering and

Processing - Process Intensification 2021;168:108549. https://doi.org/10.1016/j.cep.2021.108549.

[63]   Kumar A, Kumari S, Parmanand, Sharma SK. Constructing the nanomixture of guar gum and Fe3O4 for photocatalytic degradation of dyes and heavy metal. Journal of Materials Science: Materials in Electronics 2022;33:2643–53. https://doi.org/10.1007/s10854-021-07472-3.

[64]   Sujatha ER, Saisree S. Geotechnical behaviour of guar gum-treated soil. Soils and Foundations 2019;59:2155–66. https://doi.org/10.1016/j.sandf.2019.11.012.

[65]   Anandha Kumar S, Sujatha ER, Pugazhendi A, Jamal MT. Guar gum-stabilized soil: a clean, sustainable and economic alternative liner material for landfills. Clean Technol Environ Policy 2021. https://doi.org/10.1007/s10098-021-02032-z.

[66]   Vydehi KV, Moghal AAB. Compressibility Characteristics of Guar Gum-Treated Expansive Soil, 2022, p. 339–45. https://doi.org/10.1007/978-981-16-1831-4_31.

[67]   Radvand T, Toufigh V. Properties of concrete containing Guar gum. European Journal of Environmental and Civil Engineering 2022;26:2736–52. https://doi.org/10.1080/19648189.2020.1767217.

[68]   Palumbo G, Berent K, Proniewicz E, Banaś J. Guar Gum as an Eco-Friendly Corrosion Inhibitor for Pure Aluminium in 1-M HCl Solution. Materials 2019;12:2620. https://doi.org/10.3390/ma12162620.

[69]   Shamsheera KO, Prasad AR, Jaseela PK, Joseph A. Effect of surfactant addition to Guar Gum and protection of mild steel in hydrochloric acid at high temperatures: Experimental and theoretical studies. J Mol Liq 2021;331:115807. https://doi.org/10.1016/j.molliq.2021.115807.

[70]   Indurkar A, Bangde P, Gore M, Reddy P, Jain R, Dandekar P. Optimization of guar gum-gelatin bioink for 3D printing of mammalian cells. Bioprinting 2020;20:e00101. https://doi.org/10.1016/j.bprint.2020.e00101.

[71]   Liu F, Chang W, Chen M, Xu F, Ma J, Zhong F. Film-forming properties of guar gum, tara gum and locust bean gum. Food Hydrocoll 2020;98:105007. https://doi.org/10.1016/j.foodhyd.2019.03.028.

[72]   Kirtil E, Aydogdu A, Svitova T, Radke CJ. Assessment of the performance of several novel approaches to improve physical properties of guar gum based biopolymer films. Food Packag Shelf Life 2021;29:100687. https://doi.org/10.1016/j.fpsl.2021.100687.

[73]   Gasti T, Hiremani VD, Kesti SS, Vanjeri VN, Goudar N, Masti SP, et al. Physicochemical and Antibacterial Evaluation of Poly (Vinyl Alcohol)/Guar Gum/Silver Nanocomposite Films for Food Packaging Applications. J Polym Environ 2021;29:3347–63. https://doi.org/10.1007/s10924-021-02123-4.

[74]   Rahman S, Chowdhury D. Guar gum-sodium alginate nanocomposite film as a smart fluorescence-based humidity sensor: A smart packaging material. Int J Biol Macromol 2022;216:571–82. https://doi.org/10.1016/j.ijbiomac.2022.07.008.

[75]   Deshmukh RK, Akhila K, Ramakanth D, Gaikwad KK. Guar gum/carboxymethyl cellulose based antioxidant film incorporated with halloysite nanotubes and litchi shell waste extract for active packaging. Int J Biol Macromol 2022;201:1–13. https://doi.org/10.1016/j.ijbiomac.2021.12.198.

[76]   Martín-Illana A, Cazorla-Luna R, Notario-Pérez F, Bedoya LM, Ruiz-Caro R, Veiga MD. Freeze-dried bioadhesive vaginal bigels for controlled release of Tenofovir. European Journal of Pharmaceutical Sciences 2019;127:38–51. https://doi.org/10.1016/j.ejps.2018.10.013.

[77]   Das S, Bera D, Pal K, Mondal D, Karmakar P, Das S, et al. Guar gum micro-vehicle mediated delivery strategy and synergistic activity of thymoquinone and piperine: An in vitro study on bacterial and hepatocellular carcinoma cells. J Drug Deliv Sci Technol 2020;60:101994. https://doi.org/10.1016/j.jddst.2020.101994.

[78] Jhundoo HD, Siefen T, Liang A, Schmidt C, Lokhnauth J, Moulari B, et al. Anti-inflammatory effects of acacia and guar gum in 5-amino salicylic acid formulations in experimental colitis. Int J Pharm X 2021;3:100080. https://doi.org/10.1016/j.ijpx.2021.100080.

[79] Caldera-Villalobos M, Cabrera-Munguía DA, Becerra-Rodríguez JJ, Claudio-Rizo JA. Tailoring biocompatibility of composite scaffolds of collagen/guar gum with metal–organic frameworks. RSC Adv 2022;12:3672–86. https://doi.org/10.1039/D1RA08824F.

[80] Bourbon AI, Pinheiro AC, Ribeiro C, Miranda C, Maia JM, Teixeira JA, et al. Characterization of galactomannans extracted from seeds of Gleditsia triacanthos and Sophora japonica through shear and extensional rheology: Comparison with guar gum and locust bean gum. Food Hydrocoll 2010;24:184–92. https://doi.org/10.1016/j.foodhyd.2009.09.004.

[81] Prabaharan M. Prospective of guar gum and its derivatives as controlled drug delivery systems. Int J Biol Macromol 2011;49:117–24. https://doi.org/10.1016/j.ijbiomac.2011.04.022.

[82] Torres MD, Moreira R, Chenlo F, Vázquez MJ. Water adsorption isotherms of carboxymethyl cellulose, guar, locust bean, tragacanth and xanthan gums. Carbohydr Polym 2012;89:592–8. https://doi.org/10.1016/j.carbpol.2012.03.055.

[83] Thombare N, Jha U, Mishra S, Siddiqui MZ. Guar gum as a promising starting material for diverse applications: A review. Int J Biol Macromol 2016;88:361–72. https://doi.org/10.1016/j.ijbiomac.2016.04.001.

[84] Dodi G, Hritcu D, Popa MI. Carboxymethylation of guar gum: synthesis and characterization. Cellulose Chemistry and Technology 2011;45:171–6.

[85] Chandrika KP, Singh A, Rathore A, Kumar A. Novel cross linked guar gum-g-poly(acrylate) porous superabsorbent hydrogels: Characterization and swelling behaviour in different environments. Carbohydr Polym 2016;149:175–85. https://doi.org/10.1016/j.carbpol.2016.04.077.

[86]   Thombare N, Jha U, Mishra S, Siddiqui MZ. Borax cross-linked guar gum hydrogels as potential adsorbents for water purification. Carbohydr Polym 2017;168:274–81. https://doi.org/10.1016/j.carbpol.2017.03.086.

[87]   Thombare N, Mishra S, Siddiqui MZ, Jha U, Singh D, Mahajan GR. Design and development of guar gum based novel, superabsorbent and moisture retaining hydrogels for agricultural applications. Carbohydr Polym 2018;185:169–78. https://doi.org/10.1016/j.carbpol.2018.01.018.

[88]   Le T-A, Huynh T-P. Current advances in the chemical functionalization and potential applications of guar gum and its derivatives. Eur Polym J 2023;184:111852. https://doi.org/10.1016/j.eurpolymj.2023.111852.

[89]   Ghauri ZH, Islam A, Qadir MA, Gull N, Haider B, Khan RU, et al. Development and evaluation of pH-sensitive biodegradable ternary blended hydrogel films (chitosan/guar gum/PVP) for drug delivery application. Sci Rep 2021;11:21255. https://doi.org/10.1038/s41598-021-00452-x.

[90]   Wang J, Huang Y, Liu B, Li Z, Zhang J, Yang G, et al. Flexible and anti-freezing zinc-ion batteries using a guar-gum/sodium-alginate/ethylene-glycol hydrogel electrolyte. Energy Storage Mater 2021;41:599–605. https://doi.org/10.1016/j.ensm.2021.06.034.

[91]   Mofradi M, Karimi H, Dashtian K, Ghaedi M. Processing Guar Gum into polyester fabric based promising mixed matrix membrane for water treatment. Carbohydr Polym 2021;254:116806. https://doi.org/10.1016/j.carbpol.2020.116806.

[92]   Bhat VG, Narasagoudr SS, Masti SP, Chougale RB, Vantamuri AB, Kasai D. Development and evaluation of Moringa extract incorporated Chitosan/Guar gum/Poly (vinyl alcohol) active films for food packaging applications. Int J Biol Macromol 2022;200:50–60. https://doi.org/10.1016/j.ijbiomac.2021.12.116.

[93]   Ray L, Karthik R, Srivastava V, Singh SP, Pant AB, Goyal N, et al. Efficient antileishmanial activity of amphotericin B and piperine entrapped in enteric

coated guar gum nanoparticles. Drug Deliv Transl Res 2021;11:118–30. https://doi.org/10.1007/s13346-020-00712-9.

[94]   Tyagi R, Sharma P, Nautiyal R, Lakhera AK, Kumar V. Synthesis of quaternised guar gum using Taguchi L(16) orthogonal array. Carbohydr Polym 2020;237:116136. https://doi.org/10.1016/j.carbpol.2020.116136.

[95]   Yu X, Cheng C, Peng X, Zhang K, Yu X. A self-healing and injectable oxidized quaternized guar gum/carboxymethyl chitosan hydrogel with efficient hemostatic and antibacterial properties for wound dressing. Colloids Surf B Biointerfaces 2022;209:112207. https://doi.org/10.1016/j.colsurfb.2021.112207.

[96]   Risica D, Dentini M, Crescenzi V. Guar gum methyl ethers. Part I. Synthesis and macromolecular characterization. Polymer (Guildf) 2005;46:12247–55. https://doi.org/10.1016/j.polymer.2005.10.083.

[97]   Tripathi J, Ambolikar R, Gupta S, Jain D, Bahadur J, Variyar PS. Methylation of guar gum for improving mechanical and barrier properties of biodegradable packaging films. Sci Rep 2019;9:14505. https://doi.org/10.1038/s41598-019-50991-7.

[98]   Tripathi J, Ambolikar R, Gupta S, Variyar PS. Preparation and characterization of methylated guar gum based nano-composite films. Food Hydrocoll 2022;124:107312. https://doi.org/10.1016/j.foodhyd.2021.107312.

[99]   Pal S. Carboxymethyl guar: Its synthesis and macromolecular characterization. J Appl Polym Sci 2009;111:2630–6. https://doi.org/10.1002/app.29338.

[100]   Gong H, Liu M, Chen J, Han F, Gao C, Zhang B. Synthesis and characterization of carboxymethyl guar gum and rheological properties of its solutions. Carbohydr Polym 2012;88:1015–22. https://doi.org/10.1016/j.carbpol.2012.01.057.

[101]   Kundu S, Das A, Basu A, Ghosh D, Datta P, Mukherjee A. Carboxymethyl guar gum synthesis in homogeneous phase and macroporous 3D scaffolds design

for tissue engineering. Carbohydr Polym 2018;191:71–8.
https://doi.org/10.1016/j.carbpol.2018.03.007.

[102] Dalei G, Das S, Das SP. Non-thermal plasma assisted surface nano-textured carboxymethyl guar gum/chitosan hydrogels for biomedical applications. RSC Adv 2019;9:1705–16. https://doi.org/10.1039/C8RA09161G.

[103] Hasan AMA, Keshawy M, Abdel-Raouf ME-S. Atomic force microscopy investigation of smart superabsorbent hydrogels based on carboxymethyl guar gum: Surface topography and swelling properties. Mater Chem Phys 2022;278:125521. https://doi.org/10.1016/j.matchemphys.2021.125521.

[104] Pal S, Mal D, Singh RP. Synthesis and characterization of cationic guar gum: A high performance flocculating agent. J Appl Polym Sci 2007;105:3240–5. https://doi.org/10.1002/app.26440.

[105] Huang Y, Yu H, Xiao C. pH-sensitive cationic guar gum/poly (acrylic acid) polyelectrolyte hydrogels: Swelling and in vitro drug release. Carbohydr Polym 2007;69:774–83. https://doi.org/10.1016/j.carbpol.2007.02.016.

[106] Banerjee C, Ghosh S, Sen G, Mishra S, Shukla P, Bandopadhyay R. Study of algal biomass harvesting using cationic guar gum from the natural plant source as flocculant. Carbohydr Polym 2013;92:675–81. https://doi.org/10.1016/j.carbpol.2012.09.022.

[107] Wan X, Guo C, Feng J, Yu T, Chai X-S, Chen G, et al. Determination of the Degree of Substitution of Cationic Guar Gum by Headspace-Based Gas Chromatography during Its Synthesis. J Agric Food Chem 2017;65:7012–6. https://doi.org/10.1021/acs.jafc.7b03144.

[108] Nakamura A, Ozaki M, Murakami K. Elucidation of the aggregation mechanism of bentonite with cationic guar gum as flocculant and application to filtration. Colloids Surf A Physicochem Eng Asp 2020;596:124660. https://doi.org/10.1016/j.colsurfa.2020.124660.

[109] Reis AC, dos Santos L V., Santos KR, Lima-Tenório MK, Paludo KS, Maurício MR, et al. Chemically crosslinked guar gum hydrogels: An investigation on

the water transport and its relationship with hydrocortisone release. Int J Pharm 2022;617:121626. https://doi.org/10.1016/j.ijpharm.2022.121626.

[110] Gao J, Grady BP. Hydroxypropylation of Guar Splits: Kinetics and Rheology. Ind Eng Chem Res 2019;58:11673–9. https://doi.org/10.1021/acs.iecr.9b01674.

[111] S. R, M. P. Multi-functional FITC-silica@gold nanoparticles conjugated with guar gum succinate, folic acid and doxorubicin for CT/fluorescence dual imaging and combined chemo/PTT of cancer. Colloids Surf B Biointerfaces 2020;186:110701. https://doi.org/10.1016/j.colsurfb.2019.110701.

[112] Soni N, Shah NN, Singhal RS. Dodecenyl succinylated guar gum hydrolysate as a wall material for microencapsulation: Synthesis, characterization and evaluation. J Food Eng 2019;242:133–40. https://doi.org/10.1016/j.jfoodeng.2018.08.030.

[113] Zhang Z, Mao J, Yang B, Yang X, Zhang W, Zhang C, et al. Experimental evaluation of a novel modification of anionic guar gum with maleic anhydride for fracturing fluid. Rheol Acta 2019;58:173–81. https://doi.org/10.1007/s00397-019-01131-5.

[114] Yuan X, Amarnath Praphakar R, Munusamy MA, Alarfaj AA, Suresh Kumar S, Rajan M. Mucoadhesive guargum hydrogel inter-connected chitosan-g-polycaprolactone micelles for rifampicin delivery. Carbohydr Polym 2019;206:1–10. https://doi.org/10.1016/j.carbpol.2018.10.098.

[115] Zhang M, He J, Deng M, Gong P, Zhang X, Fan M, et al. Rheological behaviours of guar gum derivatives with hydrophobic unsaturated long-chains. RSC Adv 2020;10:32050–7. https://doi.org/10.1039/D0RA04322B.

[116] Das A, Kundu S, Ghosh SK, Basu A, Gupta M, Mukherjee A. Guar gum cinnamate ouzo nanoparticles for bacterial contact killing in water environment. Carbohydr Res 2020;491:107983. https://doi.org/10.1016/j.carres.2020.107983.

[117] Das A, Das A, Basu A, Datta P, Gupta M, Mukherjee A. Newer guar gum ester/chicken feather keratin interact films for tissue engineering. Int J Biol

Macromol 2021;180:339–54.
https://doi.org/10.1016/j.ijbiomac.2021.03.034.

[118] Bhattacharyya R, Chowdhury P. Hydrogels of Acryloyl guar gum-g-(acrylic acid-co-3sulfopropylacrylate) for high-performance adsorption and release of gentamicin sulphate. Journal of Polymer Research 2021;28:286. https://doi.org/10.1007/s10965-021-02633-8.

[119] Richter SC, Oestreich M. Emerging Strategies for C–H Silylation. Trends Chem 2020;2:13–27. https://doi.org/10.1016/j.trechm.2019.07.003.

[120] Tyagi A, Yadav N, Khan J, Singh S, Kumar Hazra C. Transition-Metal-Free C–H Silylation: An Emerging Strategy. Asian J Org Chem 2021;10:334–54. https://doi.org/10.1002/ajoc.202000584.

[121] Ashraf MA, Liu Z, Li C, Zhang D. Recent advances in catalytic silylation of hydroxyl-bearing compounds: A green technique for protection of alcohols using Si–O bond formations. Appl Organomet Chem 2021;35. https://doi.org/10.1002/aoc.6131.

[122] Ghosh S, Lai D, Hajra A. Visible-light-induced silylation: an update. Org Biomol Chem 2021;19:2399–415. https://doi.org/10.1039/D1OB00082A.

[123] Yan F, Jiang Y, Sun X, Bai Z, Zhang Y, Zhou X. Surface modification and chemical functionalization of carbon dots: a review. Microchimica Acta 2018;185:424. https://doi.org/10.1007/s00604-018-2953-9.

[124] Bee S-L, Abdullah MAA, Bee S-T, Sin LT, Rahmat AR. Polymer nanocomposites based on silylated-montmorillonite: A review. Prog Polym Sci 2018;85:57–82. https://doi.org/10.1016/j.progpolymsci.2018.07.003.

[125] Kuciński K, Stachowiak-Długyńska H, Hreczycho G. Catalytic silylation of O–nucleophiles via Si–H or Si–C bond cleavage: A route to silyl ethers, silanols and siloxanes. Coord Chem Rev 2022;459:214456. https://doi.org/10.1016/j.ccr.2022.214456.

[126] Baran T, Yılmaz Baran N, Menteş A. Highly active and recyclable heterogeneous palladium catalyst derived from guar gum for fabrication of

biaryl compounds. Int J Biol Macromol 2019;132:1147–54.
https://doi.org/10.1016/j.ijbiomac.2019.04.042.

[127]   Krishna, Kumari S, Yadav D, Sharma SK. Cu (II) Schiff base complex grafted
        guar gum: Catalyst for benzophenone derivatives synthesis. Appl Catal A Gen
        2020;601:117529. https://doi.org/10.1016/j.apcata.2020.117529.

[128]   Kamerlin SCL, Sharma PK, Prasad RB, Warshel A. Why nature really chose
        phosphate. Q Rev Biophys 2013;46:1–132.
        https://doi.org/10.1017/S0033583512000157.

[129]   Li C-P, Enomoto H, Hayashi Y, Zhao H, Aoki T. Recent advances in
        phosphorylation of food proteins: A review. LWT - Food Science and
        Technology 2010;43:1295–300. https://doi.org/10.1016/j.lwt.2010.03.016.

[130]   Sbei N, Martins GM, Shirinfar B, Ahmed N. Electrochemical Phosphorylation
        of Organic Molecules. The Chemical Record 2020;20:1530–52.
        https://doi.org/10.1002/tcr.202000096.

[131]   Knouse KW, Flood DT, Vantourout JC, Schmidt MA, Mcdonald IM, Eastgate
        MD, et al. Nature Chose Phosphates and Chemists Should Too: How
        Emerging P(V) Methods Can Augment Existing Strategies. ACS Cent Sci
        2021;7:1473–85. https://doi.org/10.1021/acscentsci.1c00487.

[132]   Xia S, Zhai Y, Wang X, Fan Q, Dong X, Chen M, et al. Phosphorylation of
        polysaccharides: A review on the synthesis and bioactivities. Int J Biol
        Macromol 2021;184:946–54.
        https://doi.org/10.1016/j.ijbiomac.2021.06.149.

[133]   Sharma G, Kumar A, Sharma S, Al-Muhtaseb AH, Naushad Mu, Ghfar AA, et al.
        Fabrication and characterization of novel Fe0@Guar gum-crosslinked-soya
        lecithin nanocomposite hydrogel for photocatalytic degradation of methyl
        violet dye. Sep Purif Technol 2019;211:895–908.
        https://doi.org/10.1016/j.seppur.2018.10.028.

[134]   Hamza MF, Fouda A, Elwakeel KZ, Wei Y, Guibal E, Hamad NA.
        Phosphorylation of Guar Gum/Magnetite/Chitosan Nanocomposites for

Uranium (VI) Sorption and Antibacterial Applications. Molecules 2021;26:1920. https://doi.org/10.3390/molecules26071920.

[135] de Oliveira Barddal HP, Faria FAM, Nogueira AV, Iacomini M, Cipriani TR. Anticoagulant and antithrombotic effects of chemically sulfated guar gum. Int J Biol Macromol 2020;145:604–10. https://doi.org/10.1016/j.ijbiomac.2019.12.210.

[136] Kazachenko AS, Akman F, Sagaama A, Issaoui N, Malyar YN, Vasilieva NYu, et al. Theoretical and experimental study of guar gum sulfation. J Mol Model 2021;27:5. https://doi.org/10.1007/s00894-020-04645-5.

[137] Kazachenko AS, Malyar YN, Vasilyeva NYu, Borovkova VS, Issaoui N. Optimization of guar gum galactomannan sulfation process with sulfamic acid. Biomass Convers Biorefin 2021. https://doi.org/10.1007/s13399-021-01895-y.

[138] Cumpstey I. Chemical Modification of Polysaccharides. ISRN Org Chem 2013;2013:1–27. https://doi.org/10.1155/2013/417672.

[139] Coseri S, Biliuta G, Simionescu BC, Stana-Kleinschek K, Ribitsch V, Harabagiu V. Oxidized cellulose—Survey of the most recent achievements. Carbohydr Polym 2013;93:207–15. https://doi.org/10.1016/j.carbpol.2012.03.086.

[140] Pierre G, Punta C, Delattre C, Melone L, Dubessay P, Fiorati A, et al. TEMPO-mediated oxidation of polysaccharides: An ongoing story. Carbohydr Polym 2017;165:71–85. https://doi.org/10.1016/j.carbpol.2017.02.028.

[141] Isogai A. TEMPO-catalyzed oxidation of polysaccharides. Polym J 2022;54:387–402. https://doi.org/10.1038/s41428-021-00580-1.

[142] Ding B, Ye Y qing, Cheng J, Wang K, Luo J, Jiang B. TEMPO-mediated selective oxidation of substituted polysaccharides—an efficient approach for the determination of the degree of substitution at C-6. Carbohydr Res 2008;343:3112–6. https://doi.org/10.1016/j.carres.2008.09.005.

[143] Sakakibara CN, Sierakowski MR, Lucyszyn N, de Freitas RA. TEMPO-mediated oxidation on galactomannan: Gal/Man ratio and chain flexibility

dependence. Carbohydr Polym 2016;153:371–8.
https://doi.org/10.1016/j.carbpol.2016.07.114.

[144] Petkowicz CLO, Reicher F, Mazeau K. Conformational analysis of galactomannans: from oligomeric segments to polymeric chains. Carbohydr Polym 1998;37:25–39. https://doi.org/10.1016/S0144-8617(98)00051-4.

[145] de Seixas-Junior CH, de Carvalho MM, Jacumazo J, Piazza RD, Parchen GP, de Freitas RA. Interaction of guar gum galactomannans with the anionic surfactant sodium lauryl ether sulphate. Int J Biol Macromol 2020;165:713–21. https://doi.org/10.1016/j.ijbiomac.2020.09.216.

[146] Lavazza M, Formantici C, Langella V, Monti D, Pfeiffer U, Galante YM. Oxidation of galactomannan by laccase plus TEMPO yields an elastic gel. J Biotechnol 2011;156:108–16. https://doi.org/10.1016/j.jbiotec.2011.08.029.

[147] Witayakran S, Ragauskas AJ. Synthetic Applications of Laccase in Green Chemistry. Adv Synth Catal 2009;351:1187–209. https://doi.org/10.1002/adsc.200800775.

[148] Tromp SA, Matijošytė I, Sheldon RA, Arends IWCE, Mul G, Kreutzer MT, et al. Mechanism of Laccase-TEMPO-Catalyzed Oxidation of Benzyl Alcohol. ChemCatChem 2010;2:827–33. https://doi.org/10.1002/cctc.201000068.

[149] Ponzini E, Natalello A, Usai F, Bechmann M, Peri F, Müller N, et al. Structural characterization of aerogels derived from enzymatically oxidized galactomannans of fenugreek, sesbania and guar gums. Carbohydr Polym 2019;207:510–20. https://doi.org/10.1016/j.carbpol.2018.11.100.

[150] Dai L, Cheng T, Wang Y, Wang B, Duan C, Ke H, et al. A self-assembling guar gum hydrogel for efficient oil/water separation in harsh environments. Sep Purif Technol 2019;225:129–35. https://doi.org/10.1016/j.seppur.2019.05.070.

[151] Duan M, Ma J, Fang S. Synthesis of hydrazine-grafted guar gum material for the highly effective removal of organic dyes. Carbohydr Polym 2019;211:308–14. https://doi.org/10.1016/j.carbpol.2019.01.112.

[152] Ma J, Fang S, Shi P, Duan M. Hydrazine-Functionalized guar-gum material capable of capturing heavy metal ions. Carbohydr Polym 2019;223:115137. https://doi.org/10.1016/j.carbpol.2019.115137.

[153] Duan C, Liu C, Meng X, Gao K, Lu W, Zhang Y, et al. Facile synthesis of Ag NPs@ MIL-100(Fe)/ guar gum hybrid hydrogel as a versatile photocatalyst for wastewater remediation: Photocatalytic degradation, water/oil separation and bacterial inactivation. Carbohydr Polym 2020;230:115642. https://doi.org/10.1016/j.carbpol.2019.115642.

[154] Yavari Maroufi L, Ghorbani M, Tabibiazar M. A Gelatin-Based Film Reinforced by Covalent Interaction with Oxidized Guar Gum Containing Green Tea Extract as an Active Food Packaging System. Food Bioproc Tech 2020;13:1633–44. https://doi.org/10.1007/s11947-020-02509-7.

[155] Maroufi LY, Tabibiazar M, Ghorbani M, Jahanban-Esfahlan A. Fabrication and characterization of novel antibacterial chitosan/dialdehyde guar gum hydrogels containing pomegranate peel extract for active food packaging application. Int J Biol Macromol 2021;187:179–88. https://doi.org/10.1016/j.ijbiomac.2021.07.126.

[156] Pandit AH, Nisar S, Imtiyaz K, Nadeem M, Mazumdar N, Rizvi MMA, et al. Injectable, Self-Healing, and Biocompatible N , O -Carboxymethyl Chitosan/Multialdehyde Guar Gum Hydrogels for Sustained Anticancer Drug Delivery. Biomacromolecules 2021;22:3731–45. https://doi.org/10.1021/acs.biomac.1c00537.

[157] Wen Y, Xie Z, Xue S, Li W, Ye H, Shi W, et al. Functionalized polymethyl methacrylate-modified dialdehyde guar gum containing hydrazide groups for effective removal and enrichment of dyes, ion, and oil/water separation. J Hazard Mater 2022;426:127799. https://doi.org/10.1016/j.jhazmat.2021.127799.

[158] Ganie SA, Naik RA, Ali A, Mir TA, Mazumdar N. Preparation, characterization, release and antianemic studies of guar gum functionalized Iron complexes. Int J Biol Macromol 2021;183:1495–504. https://doi.org/10.1016/j.ijbiomac.2021.05.125.

[159]   Anjum A, Zuber M, Zia KM, Anjum MN, Aftab W. Preparation and characterization of guar gum based polyurethanes. Int J Biol Macromol 2021;183:2174–83. https://doi.org/10.1016/j.ijbiomac.2021.06.025.

[160]   Ma J, Zhou J, Liu G, Luo Z, Yan K, Yao H, et al. Synthesis and Properties of Waterborne Polyurethane Modified with Guar Gum Polysaccharide. ChemistrySelect 2020;5:2348–53. https://doi.org/10.1002/slct.201904054.

[161]   El Assimi T, Roko Blažic, El Kadib A, Raihane M, Beniazza R, Luinstra GA, et al. Synthesis of poly(ε-caprolactone)-grafted guar gum by surface-initiated ring-opening polymerization. Carbohydr Polym 2019;220:95–102. https://doi.org/10.1016/j.carbpol.2019.05.049.

[162]   El Assimi T, Chaib M, Raihane M, El Meziane A, Khouloud M, Benhida R, et al. Poly(ε-caprolactone)-g-Guar Gum and Poly(ε-caprolactone)-g-Halloysite Nanotubes as Coatings for Slow-Release DAP Fertilizer. J Polym Environ 2020;28:2078–90. https://doi.org/10.1007/s10924-020-01750-7.

[163]   Kumar R, Sharma RKr, Singh AP. Grafted cellulose: a bio-based polymer for durable applications. Polymer Bulletin 2018;75:2213–42. https://doi.org/10.1007/s00289-017-2136-6.

[164]   Kumar D, Gihar S, Shrivash MK, Kumar P, Kundu PP. A review on the synthesis of graft copolymers of chitosan and their potential applications. Int J Biol Macromol 2020;163:2097–112. https://doi.org/10.1016/j.ijbiomac.2020.09.060.

[165]   Huynh T-P, Le T-A. CHAPTER 2. Synthetic Chemistry for Molecular Imprinting, 2018, p. 28–64. https://doi.org/10.1039/9781788010474-00028.

[166]   Lee J, von Gunten U, Kim J-H. Persulfate-Based Advanced Oxidation: Critical Assessment of Opportunities and Roadblocks. Environ Sci Technol 2020;54:3064–81. https://doi.org/10.1021/acs.est.9b07082.

[167]   Wacławek S, Lutze H V., Grübel K, Padil VVT, Černík M, Dionysiou DionysiosD. Chemistry of persulfates in water and wastewater treatment: A

review. Chemical Engineering Journal 2017;330:44–62. https://doi.org/10.1016/j.cej.2017.07.132.

[168] Sarac AS. Redox polymerization. Prog Polym Sci 1999;24:1149–204. https://doi.org/10.1016/S0079-6700(99)00026-X.

[169] Feng XD, Guo XQ, Qiu KY. Studies on the initiation mechanism of persulfate/aliphatic secondary amine system in vinyl polymerization. Polymer Bulletin 1987;18. https://doi.org/10.1007/BF00255817.

[170] Feng X-D. The role of amine in vinyl radical polymerization. Makromolekulare Chemie Macromolecular Symposia 1992;63:1–18. https://doi.org/10.1002/masy.19920630105.

[171] Nikolic V, Velickovic S, Popovic A. Amine activators influence on grafting reaction between methacrylic acid and starch. Carbohydr Polym 2012;88:1407–13. https://doi.org/10.1016/j.carbpol.2012.02.027.

[172] Bajpai UDN, Mishra V, Rai S. Grafting of poly(acrylonitrile) onto guar gum using potassium persulfate/ascorbic acid redox initiating system. J Appl Polym Sci 1993;47:717–22. https://doi.org/10.1002/app.1993.070470415.

[173] Hou X, Zhan G, Huang X, Wang N, Ai Z, Zhang L. Persulfate activation induced by ascorbic acid for efficient organic pollutants oxidation. Chemical Engineering Journal 2020;382:122355. https://doi.org/10.1016/j.cej.2019.122355.

[174] Mahto A, Mishra S. The removal of textile industrial Dye-RB-19 using Guar gum-based adsorbent with thermodynamic and kinetic evaluation parameters. Polymer Bulletin 2022;79:3353–78. https://doi.org/10.1007/s00289-021-03663-4.

[175] Palem RR, Madhusudana Rao K, Kang TJ. Self-healable and dual-functional guar gum-grafted-polyacrylamidoglycolic acid-based hydrogels with nano-silver for wound dressings. Carbohydr Polym 2019;223:115074. https://doi.org/10.1016/j.carbpol.2019.115074.

[176] Palem RR, Shimoga G, Kang TJ, Lee S-H. Fabrication of multifunctional Guar gum-silver nanocomposite hydrogels for biomedical and environmental applications. Int J Biol Macromol 2020;159:474–86. https://doi.org/10.1016/j.ijbiomac.2020.05.041.

[177] Palem RR, Shimoga G, Rao KSVK, Lee S-H, Kang TJ. Guar gum graft polymer-based silver nanocomposite hydrogels: synthesis, characterization and its biomedical applications. Journal of Polymer Research 2020;27:68. https://doi.org/10.1007/s10965-020-2026-8.

[178] Elsaeed ShimaaM, Zaki EG, Omar WAE, Ashraf Soliman A, Attia AM. Guar Gum-Based Hydrogels as Potent Green Polymers for Enhanced Oil Recovery in High-Salinity Reservoirs. ACS Omega 2021;6:23421–31. https://doi.org/10.1021/acsomega.1c03352.

[179] Singh A, Liu M, Ituen E, Lin Y. Anti-Corrosive Properties of an Effective Guar Gum Grafted 2-Acrylamido-2-Methylpropanesulfonic Acid (GG-AMPS) Coating on Copper in a 3.5% NaCl Solution. Coatings 2020;10:241. https://doi.org/10.3390/coatings10030241.

[180] Sharma S, Afgan S, Deepak, Kumar A, Kumar R. l-Alanine induced thermally stable self-healing guar gum hydrogel as potential drug vehicle for sustained release of hydrophilic drug. Materials Science and Engineering: C 2019;99:1384–91. https://doi.org/10.1016/j.msec.2019.02.074.

[181] HaqAsif A, Karnakar RR, Sreeharsha N, Gite V V., Borane N, Al-Dhubiab BE, et al. pH and Salt Responsive Hydrogel based on Guar Gum as a Renewable Material for Delivery of Curcumin: A Natural Anti-Cancer Drug. J Polym Environ 2021;29:1978–89. https://doi.org/10.1007/s10924-020-01934-1.

[182] Gihar S, Kumar D, Kumar P. Facile synthesis of novel pH-sensitive grafted guar gum for effective removal of mercury (II) ions from aqueous solution. Carbohydrate Polymer Technologies and Applications 2021;2:100110. https://doi.org/10.1016/j.carpta.2021.100110.

[183] Karnakar RR, Gite V V. Eco-friendly slow release of ZnSO4 as a micronutrient from poly (acrylic acid: acrylamide) and guar gum based crosslinked

biodegradable hydrogels. Polymer-Plastics Technology and Materials 2022;61:691–708.

[184] Pal RR, Kumar D, Raj V, Rajpal V, Maurya P, Singh S, et al. Synthesis of pH-sensitive crosslinked guar gum-g-poly(acrylic acid-co-acrylonitrile) for the delivery of thymoquinone against inflammation. Int J Biol Macromol 2021;182:1218–28. https://doi.org/10.1016/j.ijbiomac.2021.05.072.

[185] Singh A, Ansari KR, Quraishi MA, Kaya S, Erkan S. Chemically modified guar gum and ethyl acrylate composite as a new corrosion inhibitor for reduction in hydrogen evolution and tubular steel corrosion protection in acidic environment. Int J Hydrogen Energy 2021;46:9452–65. https://doi.org/10.1016/j.ijhydene.2020.12.103.

[186] Mahto A, Mishra S. Design, development and validation of guar gum based pH sensitive drug delivery carrier via graft copolymerization reaction using microwave irradiations. Int J Biol Macromol 2019;138:278–91. https://doi.org/10.1016/j.ijbiomac.2019.07.063.

[187] Das S, Subuddhi U. Guar gum–poly(N-isopropylacrylamide) smart hydrogels for sustained delivery of 5-fluorouracil. Polymer Bulletin 2019;76:2945–63. https://doi.org/10.1007/s00289-018-2526-4.

[188] Mitra M, Mahapatra M, Dutta A, Deb M, Dutta S, Chattopadhyay PK, et al. Fluorescent Guar Gum- g -Terpolymer via In Situ Acrylamido-Acid Fluorophore-Monomer in Cell Imaging, Pb(II) Sensor, and Security Ink. ACS Appl Bio Mater 2020;3:1995–2006. https://doi.org/10.1021/acsabm.9b01146.

[189] Dinari M, Shirani MA, Maleki MH, Tabatabaeian R. Green cross-linked bionanocomposite of magnetic layered double hydroxide/guar gum polymer as an efficient adsorbent of Cr(VI) from aqueous solution. Carbohydr Polym 2020;236:116070. https://doi.org/10.1016/j.carbpol.2020.116070.

[190] Samanta HS, Ray SK. Synthesis of interpenetrating network (IPN) hydrogels based on acrylic acid (AAc) and guar gum and its application as drug

delivery for pyridoxine hydrochloride (vitamin B6). Journal of Polymer Research 2021;28:479. https://doi.org/10.1007/s10965-021-02848-9.

[191] Singh J, Dhaliwal AS. Effective Removal of Methylene Blue Dye Using Silver Nanoparticles Containing Grafted Polymer of Guar Gum/Acrylic Acid as Novel Adsorbent. J Polym Environ 2021;29:71–88. https://doi.org/10.1007/s10924-020-01859-9.

[192] Sand A, Vyas A. Superabsorbent polymer based on guar gum-graft-acrylamide: synthesis and characterization. Journal of Polymer Research 2020;27:43. https://doi.org/10.1007/s10965-019-1951-x.

[193] Marco-Dufort B, Tibbitt MW. Design of moldable hydrogels for biomedical applications using dynamic covalent boronic esters. Mater Today Chem 2019;12:16–33. https://doi.org/10.1016/j.mtchem.2018.12.001.

[194] da Silva JAL. Borate esters of polyols: Occurrence, applications and implications. Inorganica Chim Acta 2021;520:120307. https://doi.org/10.1016/j.ica.2021.120307.

[195] Maseda M, Miyazaki Y, Takamuku T. Thermodynamics for complex formation of boric acid and borate with hydroxy acids and diols. J Mol Liq 2021;341:117343. https://doi.org/10.1016/j.molliq.2021.117343.

[196] Dai L, Nadeau B, An X, Cheng D, Long Z, Ni Y. Silver nanoparticles-containing dual-function hydrogels based on a guar gum-sodium borohydride system. Sci Rep 2016;6:36497. https://doi.org/10.1038/srep36497.

[197] Wei H, Gao H, Wang X. Development of novel guar gum hydrogel based media for abrasive flow machining: Shear-thickening behavior and finishing performance. Int J Mech Sci 2019;157–158:758–72. https://doi.org/10.1016/j.ijmecsci.2019.05.022.

[198] Cheng Y, Pang K, Xu X, Yuan P, Zhang Z, Wu X, et al. Borate crosslinking synthesis of structure tailored carbon-based bifunctional electrocatalysts directly from guar gum hydrogels for efficient overall water splitting. Carbon N Y 2020;157:153–63. https://doi.org/10.1016/j.carbon.2019.10.024.

[199] Liu J, Wang S, Wang C, Zhao F, Lei S, Yi H, et al. Influence of nanomaterial morphology of guar-gum fracturing fluid, physical and mechanical properties. Carbohydr Polym 2020;234:115915. https://doi.org/10.1016/j.carbpol.2020.115915.

[200] Pugliese R, Gelain F. Characterization of elastic, thermo-responsive, self-healable supramolecular hydrogel made of self-assembly peptides and guar gum. Mater Des 2020;186:108370. https://doi.org/10.1016/j.matdes.2019.108370.

[201] Cao D, Lv Y, Zhou Q, Chen Y, Qian X. Guar gum/gellan gum interpenetrating-network self-healing hydrogels for human motion detection. Eur Polym J 2021;151:110371. https://doi.org/10.1016/j.eurpolymj.2021.110371.

[202] Dassanayake RS, Rajakaruna E, Abidi N. Borax-Cross-Linked Guar Gum-Manganese Dioxide Composites for Oxidative Decolorization of Methylene Blue. J Nanomater 2019;2019:1–11. https://doi.org/10.1155/2019/7232715.

[203] Wang B, Dai L, Yang G, Bendrich G, Ni Y, Fang G. A highly efficient thermo responsive palladium nanoparticles incorporated guar gum hydrogel for effective catalytic reactions. Carbohydr Polym 2019;226:115289. https://doi.org/10.1016/j.carbpol.2019.115289.

[204] Talodthaisong C, Boonta W, Thammawithan S, Patramanon R, Kamonsutthipaijit N, Hutchison JA, et al. Composite guar gum-silver nanoparticle hydrogels as self-healing, injectable, and antibacterial biomaterials. Mater Today Commun 2020;24:100992. https://doi.org/10.1016/j.mtcomm.2020.100992.

[205] Deka R, Sarma S, Patar P, Gogoi P, Sarmah JK. Highly stable silver nanoparticles containing guar gum modified dual network hydrogel for catalytic and biomedical applications. Carbohydr Polym 2020;248:116786. https://doi.org/10.1016/j.carbpol.2020.116786.

[206] Orsu P, Matta S. Fabrication and characterization of carboxymethyl guar gum nanocomposite for application of wound healing. Int J Biol Macromol 2020;164:2267–76. https://doi.org/10.1016/j.ijbiomac.2020.07.322.

[207] Bag J, Mukherjee S, Ghosh SK, Das A, Mukherjee A, Sahoo JK, et al. Fe3O4 coated guargum nanoparticles as non-genotoxic materials for biological application. Int J Biol Macromol 2020;165:333–45. https://doi.org/10.1016/j.ijbiomac.2020.09.144.

[208] Rao Z, Liu S, Wu R, Wang G, Sun Z, Bai L, et al. Fabrication of dual network self-healing alginate/guar gum hydrogels based on polydopamine-type microcapsules from mesoporous silica nanoparticles. Int J Biol Macromol 2019;129:916–26. https://doi.org/10.1016/j.ijbiomac.2019.02.089.

[209] Gupta VK, Agarwal S, Ahmad R, Mirza A, Mittal J. Sequestration of toxic congo red dye from aqueous solution using ecofriendly guar gum/ activated carbon nanocomposite. Int J Biol Macromol 2020;158:1310–8. https://doi.org/10.1016/j.ijbiomac.2020.05.025.

[210] Butt A, Jabeen S, Nisar N, Islam A, Gull N, Iqbal SS, et al. Controlled release of cephradine by biopolymers based target specific crosslinked hydrogels. Int J Biol Macromol 2019;121:104–12. https://doi.org/10.1016/j.ijbiomac.2018.10.018.

[211] Khan MUA, Raza MA, Razak SIA, Abdul Kadir MR, Haider A, Shah SA, et al. Novel functional antimicrobial and biocompatible arabinoxylan/guar gum hydrogel for skin wound dressing applications. J Tissue Eng Regen Med 2020;14:1488–501. https://doi.org/10.1002/term.3115.

[212] Khan MUA, Iqbal I, Ansari MNM, Razak SIA, Raza MA, Sajjad A, et al. Development of Antibacterial, Degradable and pH-Responsive Chitosan/Guar Gum/Polyvinyl Alcohol Blended Hydrogels for Wound Dressing. Molecules 2021;26:5937. https://doi.org/10.3390/molecules26195937.

[213] Aydogdu A, Radke CJ, Bezci S, Kirtil E. Characterization of curcumin incorporated guar gum/orange oil antimicrobial emulsion films. Int J Biol

Macromol 2020;148:110–20.
https://doi.org/10.1016/j.ijbiomac.2019.12.255.

[214] Goel S, Chen F, Cai W. Synthesis and Biomedical Applications of Copper
Sulfide Nanoparticles: From Sensors to Theranostics. Small 2014;10:631–45.
https://doi.org/10.1002/smll.201301174.

[215] Liu Y, Liu M, Swihart MT. Plasmonic Copper Sulfide-Based Materials: A Brief
Introduction to Their Synthesis, Doping, Alloying, and Applications. The
Journal of Physical Chemistry C 2017;121:13435–47.
https://doi.org/10.1021/acs.jpcc.7b00894.

[216] Isac L, Cazan C, Enesca A, Andronic L. Copper Sulfide Based Heterojunctions
as Photocatalysts for Dyes Photodegradation. Front Chem 2019;7.
https://doi.org/10.3389/fchem.2019.00694.

[217] Liu Y, Ji M, Wang P. Recent Advances in Small Copper Sulfide Nanoparticles
for Molecular Imaging and Tumor Therapy. Mol Pharm 2019;16:3322–32.
https://doi.org/10.1021/acs.molpharmaceut.9b00273.

[218] Poudel K, Gautam M, Jin SG, Choi H-G, Yong CS, Kim JO. Copper sulfide: An
emerging adaptable nanoplatform in cancer theranostics. Int J Pharm
2019;562:135–50. https://doi.org/10.1016/j.ijpharm.2019.03.043.

[219] Huynh T-P. Chemical and biological sensing with nanocomposites prepared
from nanostructured copper sulfides. Nano Futures 2020;4:032001.
https://doi.org/10.1088/2399-1984/ab9a28.

[220] Ain N ul, Abdul Nasir J, Khan Z, Butler IS, Rehman Z. Copper sulfide
nanostructures: synthesis and biological applications. RSC Adv
2022;12:7550–67. https://doi.org/10.1039/D1RA08414C.

[221] Majumdar D. Recent progress in copper sulfide based nanomaterials for high
energy supercapacitor applications. Journal of Electroanalytical Chemistry
2021;880:114825. https://doi.org/10.1016/j.jelechem.2020.114825.

[222]   Chakrabarti DJ, Laughlin DE. The Cu-S (Copper-Sulfur) system. Bulletin of
         Alloy Phase Diagrams 1983;4:254–71.
         https://doi.org/10.1007/BF02868665.

[223]   Mulla R, Rabinal MHK. Copper Sulfides: Earth-Abundant and Low-Cost
         Thermoelectric Materials. Energy Technology 2019;7:1800850.
         https://doi.org/10.1002/ente.201800850.

[224]   Morales-García A, Soares AL, Dos Santos EC, de Abreu HA, Duarte HA. First-
         Principles Calculations and Electron Density Topological Analysis of
         Covellite (CuS). J Phys Chem A 2014;118:5823–31.
         https://doi.org/10.1021/jp4114706.

[225]   Di Benedetto F, Borgheresi M, Caneschi A, Chastanet G, Cipriani C, Gatteschi
         D, et al. First evidence of natural superconductivity: covellite. European
         Journal of Mineralogy 2006;18:283–7. https://doi.org/10.1127/0935-
         1221/2006/0018-0283.

[226]   Saunders AE, Ghezelbash A, Smilgies D-M, Sigman , Michael B., Korgel BA.
         Columnar Self-Assembly of Colloidal Nanodisks. Nano Lett 2006;6:2959–63.
         https://doi.org/10.1021/nl062419e.

[227]   Coughlan C, Ibáñez M, Dobrozhan O, Singh A, Cabot A, Ryan KM. Compound
         Copper Chalcogenide Nanocrystals. Chem Rev 2017;117:5865–6109.
         https://doi.org/10.1021/acs.chemrev.6b00376.

[228]   Fjellvåg H, Grønvold F, Stølen S, Andresen AF, Müller-Käfer R, Simon A. Low-
         temperature structural distortion in CuS. Zeitschrift Für Kristallographie
         1988;184:111–21. https://doi.org/10.1524/zkri.1988.184.1-2.111.

[229]   Mazin II. Structural and electronic properties of the two-dimensional
         superconductor CuS with $1\frac{1}{3}$ -valent copper. Phys Rev B
         2012;85:115133. https://doi.org/10.1103/PhysRevB.85.115133.

[230]   Conejeros S, Moreira I de PR, Alemany P, Canadell E. Nature of Holes,
         Oxidation States, and Hypervalency in Covellite (CuS). Inorg Chem
         2014;53:12402–6. https://doi.org/10.1021/ic502436a.

[231]   Arora S, Kabra K, Joshi KB, Sharma BK, Sharma G. Structural, elastic, thermodynamic and electronic properties of covellite, CuS. Physica B Condens Matter 2020;582:311142. https://doi.org/10.1016/j.physb.2018.11.007.

[232]   Shamraiz U, Hussain RA, Badshah A. Fabrication and applications of copper sulfide (CuS) nanostructures. J Solid State Chem 2016;238:25–40. https://doi.org/10.1016/j.jssc.2016.02.046.

[233]   Nikam AN, Pandey A, Fernandes G, Kulkarni S, Mutalik SP, Padya BS, et al. Copper sulphide based heterogeneous nanoplatforms for multimodal therapy and imaging of cancer: Recent advances and toxicological perspectives. Coord Chem Rev 2020;419:213356. https://doi.org/10.1016/j.ccr.2020.213356.

[234]   Liu M, Liu Y, Gu B, Wei X, Xu G, Wang X, et al. Recent advances in copper sulphide-based nanoheterostructures. Chem Soc Rev 2019;48:4950–65. https://doi.org/10.1039/C8CS00832A.

[235]   Ba Y, Zhou S, Jiao S, Pan W. Fabrication of polyaniline/copper sulfide/poly(ethylene terephthalate) thread electrode for flexible fiber-shaped supercapacitors. J Appl Polym Sci 2018;135:46769. https://doi.org/10.1002/app.46769.

[236]   Peng J, Zheng B, Jia S, Gao J, Tang D. *In situ* thermal fabrication of copper sulfide–polymer hybrid nanostructures for tunable plasmon resonance. Nanoscale Adv 2020;2:2303–8. https://doi.org/10.1039/C9NA00668K.

[237]   Samdhyan K, Chand P, Anand H, Saini S. Development of carbon-based copper sulfide nanocomposites for high energy supercapacitor applications: A comprehensive review. J Energy Storage 2022;46:103886. https://doi.org/10.1016/j.est.2021.103886.

[238]   Xie Y, Gan C, Li Z, Liu W, Yang D, Qiu X. Fabrication of a Lignin-Copper Sulfide-Incorporated PVA Hydrogel with Near-Infrared-Activated Photothermal/Photodynamic/Peroxidase-like Performance for Combating

Bacteria and Biofilms. ACS Biomater Sci Eng 2022;8:560–9.
https://doi.org/10.1021/acsbiomaterials.1c01406.

[239] Khanna P, Kaur A, Goyal D. Algae-based metallic nanoparticles: Synthesis,
characterization and applications. J Microbiol Methods 2019;163:105656.
https://doi.org/10.1016/j.mimet.2019.105656.

[240] Baig N, Kammakakam I, Falath W. Nanomaterials: a review of synthesis
methods, properties, recent progress, and challenges. Mater Adv
2021;2:1821–71. https://doi.org/10.1039/D0MA00807A.

[241] Abid N, Khan AM, Shujait S, Chaudhary K, Ikram M, Imran M, et al. Synthesis
of nanomaterials using various top-down and bottom-up approaches,
influencing factors, advantages, and disadvantages: A review. Adv Colloid
Interface Sci 2022;300:102597. https://doi.org/10.1016/j.cis.2021.102597.

[242] Barge LM, Cardoso SSS, Cartwright JHE, Cooper GJT, Cronin L, De Wit A, et al.
From Chemical Gardens to Chemobrionics. Chem Rev 2015;115:8652–703.
https://doi.org/10.1021/acs.chemrev.5b00014.

[243] Cartwright JHE, Escribano B, González DL, Sainz-Díaz CI, Tuval I. Brinicles as
a Case of Inverse Chemical Gardens. Langmuir 2013;29:7655–60.
https://doi.org/10.1021/la4009703.

[244] Corliss JB, Dymond J, Gordon LI, Edmond JM, von Herzen RP, Ballard RD, et
al. Submarine Thermal Springs on the Galápagos Rift. Science (1979)
1979;203:1073–83. https://doi.org/10.1126/science.203.4385.1073.

[245] Russell MJ. The Alkaline Solution to the Emergence of Life: Energy, Entropy
and Early Evolution. Acta Biotheor 2007;55:133–79.
https://doi.org/10.1007/s10441-007-9018-5.

[246] Mielke RE, Russell MJ, Wilson PR, McGlynn SE, Coleman M, Kidd R, et al.
Design, Fabrication, and Test of a Hydrothermal Reactor for Origin-of-Life
Experiments. Astrobiology 2010;10:799–810.
https://doi.org/10.1089/ast.2009.0456.

[247] Fogde A, Qudsia S, Le T, Sandberg T, Huynh T. (Calcium-Phosphate)/Carrageenan Gardens Grown from the Gel/Liquid Interface. ChemSystemsChem 2021;3. https://doi.org/10.1002/syst.202000064.

[248] Hughes EAB, Robinson TE, Moakes RJA, Chipara M, Grover LM. Controlled self-assembly of chemical gardens enables fabrication of heterogeneous chemobrionic materials. Commun Chem 2021;4:145. https://doi.org/10.1038/s42004-021-00579-y.

[249] Steenbjerg Ibsen CJ, Mikladal BF, Bjørnholt Jensen U, Birkedal H. Hierarchical Tubular Structures Grown from the Gel/Liquid Interface. Chemistry - A European Journal 2014;20:16112–20. https://doi.org/10.1002/chem.201402741.

[250] Song T, Gao F, Guo S, Zhang Y, Li S, You H, et al. A review of the role and mechanism of surfactants in the morphology control of metal nanoparticles. Nanoscale 2021;13:3895–910. https://doi.org/10.1039/D0NR07339C.

[251] Shaban SM, Kang J, Kim D-H. Surfactants: Recent advances and their applications. Composites Communications 2020;22:100537. https://doi.org/10.1016/j.coco.2020.100537.

[252] Scher EC, Manna L, Alivisatos AP. Shape control and applications of nanocrystals. Philosophical Transactions of the Royal Society of London Series A: Mathematical, Physical and Engineering Sciences 2003;361:241–57. https://doi.org/10.1098/rsta.2002.1126.

[253] Smith AM, Nie S. Semiconductor Nanocrystals: Structure, Properties, and Band Gap Engineering. Acc Chem Res 2010;43:190–200. https://doi.org/10.1021/ar9001069.

[254] Yang S, Prendergast D, Neaton JB. Tuning Semiconductor Band Edge Energies for Solar Photocatalysis via Surface Ligand Passivation. Nano Lett 2012;12:383–8. https://doi.org/10.1021/nl203669k.

[255] Heinz H, Pramanik C, Heinz O, Ding Y, Mishra RK, Marchon D, et al. Nanoparticle decoration with surfactants: Molecular interactions, assembly,

and applications. Surf Sci Rep 2017;72:1–58.
https://doi.org/10.1016/j.surfrep.2017.02.001.

[256] Günther H. NMR spectroscopy: basic principles, concepts and applications in
        chemistry. 3rd ed. John Wiley & Sons; 2013.

[257] Claridge TD. High-Resolution: NMR Techniques in Organic Chemistry. vol.
        27. 3rd ed. Elsevier; 2016.

[258] Lee M. X-Ray diffraction for materials research: from fundamentals to
        applications. CRC Press; 2017.

[259] Michler GH. Electron Microscopy of Polymers. Springer; 2008.

[260] Skoog S DA, West DM, Holler FJ, Crouch SR. Fundamentals of Analytical
        Chemistry. 10th ed. Cengage; 2022.

[261] Wagner M. Thermal Analysis in Practice: Fundamental Aspects. Carl Hanser
        Verlag GmbH Co KG; 2017.

[262] Zouheir M, Le T, Torop J, Nikiforow K, Khatib M, Zohar O, et al. CuS-
        Carrageenan Composite Grown from the Gel/Liquid Interface.
        ChemSystemsChem 2021;3. https://doi.org/10.1002/syst.202000063.

[263] Myers RJ. The new low value for the second dissociation constant for H2S: Its
        history, its best value, and its impact on the teaching of sulfide equilibria. J
        Chem Educ 1986;63:687. https://doi.org/10.1021/ed063p687.

[264] Jumaah FN, Mobarak NN, Ahmad A, Ghani MA, Rahman MYA. Derivative of
        iota-carrageenan as solid polymer electrolyte. Ionics (Kiel) 2015;21:1311–
        20. https://doi.org/10.1007/s11581-014-1306-x.

[265] Chitra R, Sathya P, Selvasekarapandian S, Monisha S, Moniha V, Meyvel S.
        Synthesis and characterization of iota-carrageenan solid biopolymer
        electrolytes for electrochemical applications. Ionics (Kiel) 2019;25:2147–57.
        https://doi.org/10.1007/s11581-018-2687-z.

[266] Ghani NAA, Othaman R, Ahmad A, Anuar FH, Hassan NH. Impact of
        purification on iota carrageenan as solid polymer electrolyte. Arabian

Journal of Chemistry 2019;12:370–6. https://doi.org/10.1016/j.arabjc.2018.06.008.

[267] Kim SS, Kim HW, Yuk SH, Oh SY, Pak PK, Lee HB. Blood and cell compatibility of gelatin-carrageenan mixtures cross-linked by glutaraldehyde. Biomaterials 1996;17:813–21. https://doi.org/10.1016/0142-9612(96)81419-0.

[268] Moniha V, Alagar M, Selvasekarapandian S, Sundaresan B, Boopathi G. Conductive bio-polymer electrolyte iota-carrageenan with ammonium nitrate for application in electrochemical devices. J Non Cryst Solids 2018;481:424–34. https://doi.org/10.1016/j.jnoncrysol.2017.11.027.

[269] Kumar P, Gusain M, Nagarajan R. Synthesis of Cu$_{1.8}$S and CuS from Copper-Thiourea Containing Precursors; Anionic (Cl$^-$, NO$_3$$^-$, SO$_4$$^{2-}$) Influence on the Product Stoichiometry. Inorg Chem 2011;50:3065–70. https://doi.org/10.1021/ic102593h.

[270] Kalanur SS, Chae SY, Joo OS. Transparent Cu1.8S and CuS thin films on FTO as efficient counter electrode for quantum dot solar cells. Electrochim Acta 2013;103:91–5. https://doi.org/10.1016/j.electacta.2013.04.041.

[271] Pramanik NC, Seok S Il, Ahn BY. Effects of reactant concentration and OH− ions on the formation of nanocrystalline BaTiO3 in solution. Mater Res Bull 2007;42:497–504. https://doi.org/10.1016/j.materresbull.2006.06.022.

[272] Varghese JS, Chellappa N, Fathima NN. Gelatin–carrageenan hydrogels: Role of pore size distribution on drug delivery process. Colloids Surf B Biointerfaces 2014;113:346–51. https://doi.org/10.1016/j.colsurfb.2013.08.049.

[273] Auyoong YL, Yap PL, Huang X, Abd Hamid SB. Optimization of reaction parameters in hydrothermal synthesis: a strategy towards the formation of CuS hexagonal plates. Chem Cent J 2013;7:67. https://doi.org/10.1186/1752-153X-7-67.

[274] Brunetti B, Piacente V, Scardala P. Study on sulfur vaporization from covellite (CuS) and anilite (Cu1.75S). J Alloys Compd 1994;206:113–9. https://doi.org/10.1016/0925-8388(94)90018-3.

[275] Godovski DYu, Sukharev VYa, Volkov AV, Moskvina MA. Absorption induced response of electrophysical characteristics of filled polymer-composite. Journal of Physics and Chemistry of Solids 1993;54:1613–20. https://doi.org/10.1016/0022-3697(93)90357-W.

[276] Adkar D, Hake A, Jadkar S, Adhyapak P, Mulik U, Amalnerkar D. Humidity Sensing Performance of <I>In-Situ</I> Fabricated Cu/Cu<SUB>2</SUB>O/Cu<SUB>2</SUB>S-Polymer Nanocomposite via Polyphenylene Sulphide Cyclisation Route. J Nanosci Nanotechnol 2011;11:6815–22. https://doi.org/10.1166/jnn.2011.4254.

[277] Le T-A, Zouheir M, Nikiforow K, Khatib M, Zohar O, Haick H, et al. Synthesis, characterization, and humidity-responsiveness of guar gum xanthate and its nanocomposite with copper sulfide covellite. Int J Biol Macromol 2022;206:105–14. https://doi.org/10.1016/j.ijbiomac.2022.02.132.

[278] Gondhalekar SC, Pawar PJ, Dhumal SS, Thakre SS. Mechanism of xanthation reaction in viscose process. Cellulose 2019;26:1595–604. https://doi.org/10.1007/s10570-018-2213-5.

[279] Xie Y, Riedinger A, Prato M, Casu A, Genovese A, Guardia P, et al. Copper Sulfide Nanocrystals with Tunable Composition by Reduction of Covellite Nanocrystals with Cu [+] Ions. J Am Chem Soc 2013;135:17630–7. https://doi.org/10.1021/ja409754v.

[280] Reddy TS, Kumar MCS. Temperature-Dependent Properties of Co-evaporated CuS Thin Films. Brazilian Journal of Physics 2021;51:1575–83. https://doi.org/10.1007/s13538-021-00956-x.

[281] Luther JM, Jain PK, Ewers T, Alivisatos AP. Localized surface plasmon resonances arising from free carriers in doped quantum dots. Nat Mater 2011;10:361–6. https://doi.org/10.1038/nmat3004.

[282] Hsu S-W, On K, Tao AR. Localized Surface Plasmon Resonances of Anisotropic Semiconductor Nanocrystals. J Am Chem Soc 2011;133:19072–5. https://doi.org/10.1021/ja2089876.

[283] Movasaghi Z, Rehman S, ur Rehman DrI. Fourier Transform Infrared (FTIR) Spectroscopy of Biological Tissues. Appl Spectrosc Rev 2008;43:134–79. https://doi.org/10.1080/05704920701829043.

[284] Cerqueira MA, Souza BWS, Simões J, Teixeira JA, Domingues MRM, Coimbra MA, et al. Structural and thermal characterization of galactomannans from non-conventional sources. Carbohydr Polym 2011;83:179–85. https://doi.org/10.1016/j.carbpol.2010.07.036.

[285] Mudgil D, Barak S, Khatkar BS. X-ray diffraction, IR spectroscopy and thermal characterization of partially hydrolyzed guar gum. Int J Biol Macromol 2012;50:1035–9. https://doi.org/10.1016/j.ijbiomac.2012.02.031.

[286] Liang S, Guo X, Feng N, Tian Q. Application of orange peel xanthate for the adsorption of Pb2+ from aqueous solutions. J Hazard Mater 2009;170:425–9. https://doi.org/10.1016/j.jhazmat.2009.04.078.

[287] Zhu Y, Hu J, Wang J. Competitive adsorption of Pb(II), Cu(II) and Zn(II) onto xanthate-modified magnetic chitosan. J Hazard Mater 2012;221–222:155–61. https://doi.org/10.1016/j.jhazmat.2012.04.026.

[288] Grijalva H, Inoue M, Boggavarapu S, Calvert P. Amorphous and crystalline copper sulfides, CuS. J Mater Chem 1996;6:1157. https://doi.org/10.1039/jm9960601157.

[289] Dunn JG, Chamberlain AC, Fisher NG, Avraamides J. The influence of activated carbon on the thermal decomposition of sodium ethyl xanthate. Journal of Thermal Analysis 1997;49:1399–408. https://doi.org/10.1007/BF01983698.

[290] Kaur B, Kaur N, Kumar S. Colorimetric metal ion sensors – A comprehensive review of the years 2011–2016. Coord Chem Rev 2018;358:13–69. https://doi.org/10.1016/j.ccr.2017.12.002.

[291] Wu Y, Pang H, Liu Y, Wang X, Yu S, Fu D, et al. Environmental remediation of heavy metal ions by novel-nanomaterials: A review. Environmental Pollution 2019;246:608–20. https://doi.org/10.1016/j.envpol.2018.12.076.

[292] Qasem NAA, Mohammed RH, Lawal DU. Removal of heavy metal ions from wastewater: a comprehensive and critical review. NPJ Clean Water 2021;4:36. https://doi.org/10.1038/s41545-021-00127-0.

[293] Mao S, Gao M. Functional organoclays for removal of heavy metal ions from water: A review. J Mol Liq 2021;334:116143. https://doi.org/10.1016/j.molliq.2021.116143.

[294] Li X, Jiang F, Liu M, Qu Y, Lan Z, Dai X, et al. Synthesis, Characterization, and Bioactivities of Polysaccharide Metal Complexes: A Review. J Agric Food Chem 2022;70:6922–42. https://doi.org/10.1021/acs.jafc.2c01349.

[295] Pearson RG. Hard and soft acids and bases, HSAB, part 1: Fundamental principles. J Chem Educ 1968;45:581. https://doi.org/10.1021/ed045p581.

[296] Le T-A, Guo Y, Zhou J-N, Yan J, Zhang H, Huynh T-P. Synthesis, characterization and biocompatibility of guar gum-benzoic acid. Int J Biol Macromol 2022;194:110–6. https://doi.org/10.1016/j.ijbiomac.2021.11.180.

[297] Timilsena YP, Akanbi TO, Khalid N, Adhikari B, Barrow CJ. Complex coacervation: Principles, mechanisms and applications in microencapsulation. Int J Biol Macromol 2019;121:1276–86. https://doi.org/10.1016/j.ijbiomac.2018.10.144.

[298] Dalei G, Das S. Carboxymethyl guar gum: A review of synthesis, properties and versatile applications. Eur Polym J 2022;176:111433. https://doi.org/10.1016/j.eurpolymj.2022.111433.

[299] Agarwal RA, Gupta NK. CO2 sorption behavior of imidazole, benzimidazole and benzoic acid based coordination polymers. Coord Chem Rev 2017;332:100–21. https://doi.org/10.1016/j.ccr.2016.11.002.

[300]   Yuan S, Liu T-F, Feng D, Tian J, Wang K, Qin J, et al. A single crystalline porphyrinic titanium metal–organic framework. Chem Sci 2015;6:3926–30. https://doi.org/10.1039/C5SC00916B.

[301]   Carter KP, Ridenour JA, Kalaj M, Cahill CL. A Thorium Metal-Organic Framework with Outstanding Thermal and Chemical Stability. Chemistry – A European Journal 2019;25:7114–8. https://doi.org/10.1002/chem.201901610.

Original publications

CuS-carrageenan composite grown from the gel/liquid interface

Morad Zouheir, **Trung-Anh Le**, Janno Torop, Kostiantyn Nikiforow, Muhammad Khatib, Orr Zohar, Hossam Haick, and Tan-Phat Huynh*

ChemSystemsChem

I

CuS-Carrageenan Composite Grown from the Gel/Liquid Interface

Morad Zouheir,[a] Trung-Anh Le,[a] Janno Torop,[b] Kostiantyn Nikiforow,[c] Muhammad Khatib,[d] Orr Zohar,[d] Hossam Haick,[d] and Tan-Phat Huynh*[a]

The aim of this study is to highlight novel CuS-carrageenan nanocomposites grown from the interface between sulfide solutions (liquid phases) and Cu-ι-carrageenan gels. Several parameters including pH, copper and carrageenan concentration of the hydrogel that influence the growth of the nanocomposite have been examined. The most effective parameter is the initial pH of the liquid phase, hence, three growing samples at pH 7, 10 and 13 were selected for further studies and referred as LPH7, LPH10 and LPH13. Three CuS-carrageenan nanocomposites obtained from the three pH conditions were purified and examined in detail using several characterization techniques such as X-ray diffraction (XRD), Fourier transform infrared spectroscopy (FTIR), thermogravimetric analysis (TGA), scanning electron microscopy (SEM) and X-ray photoelectron spectroscopy (XPS). The structure, composition, properties as well as the growth mechanism of the nanocomposite have been studied. Additionally, the electrical conductivity of the nanocomposite was exploited to be used as a sensor of relative humidity and temperature.

1. Introduction

Chemical gardens (or chemobrionics) featuring typical micro- and nano-tubular structures result from self-organizing precipitation processes.[1–5] Besides unique synthetic routes, these processes allow not only the development of new methodologies to understand non-equilibrium chemical systems and the origin of life, but also the exploration of potential methods to drastically enhance future materials design. Traditional chemical gardens are grown from a salt seed placed in a counterion solution. However, some examples of non-traditional gardens have been reported such as the 2D gardens, organic gardens, and garden of cement nanotubes.[6–8] More interesting morphologies as well as physical and chemical properties have been found when chemobrionics evolves a gel/liquid interface.[9–12] The gel (or hydrogel) herein is formulated from water-soluble biopolymers with salts. The process results in precipitation of diverse materials and some have found their applications, for example, in biomedicine.[10,11]

Among biopolymers, carrageenans have been extensively investigated due to their unique properties such as high-water content, softness, flexibility and biocompatibility.[13–15] The presence of many hydroxyl groups and anionic sulfate groups in their structures makes carrageenan a hydrophilic, anionic polyelectrolyte. Carrageenan belongs to a family of linear sulfated polysaccharides, which can be found in red edible seaweeds (such as achondrus, eucheuma, and gigartina).[16,17] Carrageenans are used mainly for thickening, suspending, stabilizing, and gelling, thus appeared in many food and cosmetic products as well as pharmaceutical industries.[18] Carrageenan is categorized into three forms, namely, kappa, iota and lambda depending on the number and position of ester sulfate groups.[19] All carrageenan types are soluble in hot water at temperatures above their gel melting points to yield viscoelastic hydrogels.[20] These hydrogels maintain their shapes when tipped out of containers and yet retain the vapor pressure and ionic conductivity of the liquid from which they are made.[21] κ- and ι-carrageenan form thermo-reversible gels on cooling in the presence of suitable counter-ions through the formation of "double-helix" structure.[22] ι-carrageenan has less specific ionic binding, but increased ionic strength, which allows helices to form junction zones in soft elastic gels with good freeze-thaw stability. Not only are cations such as Na^+, K^+, Mg^{2+}, Ca^{2+} being used as gelling agents of the carrageenan-based hydrogel, but also Cu^{2+}, Fe^{2+}, and Zn^{2+} exhibit similar trends.[21]

In this report, we take a step further, i.e. converting the Cu^{2+}-complexed carrageenan hydrogels into the CuS-carrageenan nanocomposite by utilizing the novel precipitation process at the gel/liquid interface. Cu_xS as nanoscale particles,

[a] M. Zouheir, T.-A. Le, Dr. T.-P. Huynh
Laboratory of Molecular Sciences and Engineering
Åbo Akademi University
20500 Turku (Finland)
E-mail: tan.huynh@abo.fi
[b] Dr. J. Torop
Institute of Technology
University of Tartu
Nooruse 1, 50411, Tartu (Estonia)
[c] Dr. K. Nikiforow
Institute of Physical Chemistry Polish Academy of Sciences
44/52 Kasprzaka, 01-224 Warsaw (Poland)
[d] Dr. M. Khatib, O. Zohar, Prof. H. Haick
The Department of Chemical Engineering
Technion – Israel Institute of Technology
Haifa 3200003 (Israel)

ChemSystemsChem

Articles
doi.org/10.1002/syst.202000063

Chemistry
Europe
European Chemical
Societies Publishing

particularly covellite-phase CuS nanocrystals, exhibit an outstanding structural performance, such as excellent photoelectric properties compared with individual molecules or bulk form. CuS exhibits numerous applications as semiconductors photocatalysts, solar radiation absorbers, catalysts, polymer surface coatings, cathodic materials, nanoscale switches, electroluminescent devices and sensors.[19,23–25] Herein, the grown CuS-carrageenan nanocomposite was successfully applied as the active material for sensing of relative humidity (RH) and temperature.

2. Materials and Methods

2.1. Preparation

In order to prepare the gel phase, 3 g of ι-carrageenan (CP Kelco) was dissolved under stirring into 100 mL of distilled water at 50 °C to obtain 3 $wt\%$ ι-carrageenan solution. Then 0.242 g of $Cu(NO_3)_2 \cdot 3H_2O$ (Sigma) was dissolved into 1 mL of water in several small vials. Those vials were placed in a water bath at 90 °C. Immediately, 10 ml of the prepared 3 $wt\%$ ι-carrageenan solution was added to each vial with fast stirring using spatula to avoid local jellification. When a homogeneous blue solution is obtained in each vial, the solutions were allowed to cool down to form a firm gel (of ~0.1 M Cu-$(NO_3)_2 \cdot 3H_2O$ and 3 $wt\%$ ι-carrageenan). The liquid phases of 0.1 M Na_2S (Sigma) were prepared with three different pH 7, 10 and 13 to study the pH effect on the growth. Diluted HCl solution was used for pH adjustment. To form a gel/liquid interface system, 10 mL of each prepared Na_2S solution was poured into the vials that contain the prepared hydrogel. A composite started to grow and became noticeable after 20 min

(Figure 1). The growth ended after 48 hours and the process is recorded on a time-laps video (Video 1, SI). The remaining liquid was carefully poured out of the vial without losing the grown black structures. Then those structures were dried in the vacuum chamber for 3 days for the purpose of characterization. For further purification of the grown materials, salt elimination was done by washing the composites with a mixture of 80:20 v/v% ethanol: water three times, then with absolute ethanol one time before placing them into the vacuum chamber. The purification of the materials was confirmed by XRD. Depending on the liquid phase pH used in each vial during the growth of the composites, the obtained materials will be referred hereafter as LPH7, LPH10 and LPH13 for pH 7, 10 and 13 respectively before or after purification.

A precipitated CuS using 0.1 M $Cu(NO_3)_2 \cdot 3H_2O$ and 0.1 M Na_2S was prepared, washed and dried to be used as a reference sample. ι-carrageenan was also used as a reference.

2.2. Characterization Instruments

X-ray diffraction (XRD) pattern of the grown Cu_xS-carrageenan composite was characterized with a Bruker AXS D8 Discover instrument by using a scintillator point detector and copper Kα1 radiation ($\lambda = 1.54060$ Å). The measurements were performed using grazing incidence diffraction between 10° and 80°, using a step size of 0.04° and an incidence angle of 0.3°. The HighScore Plus (v.3.0.5) software was used for relative phase abundance estimation by employing Rietveld's refinement. From the corresponding XRD peaks, the mean crystallite size was calculated according to Scherrer equation.[26]

Scanning Electron Microscopy (SEM) images of CuS-carrageenan composites before and after purification, ι-carrageenan

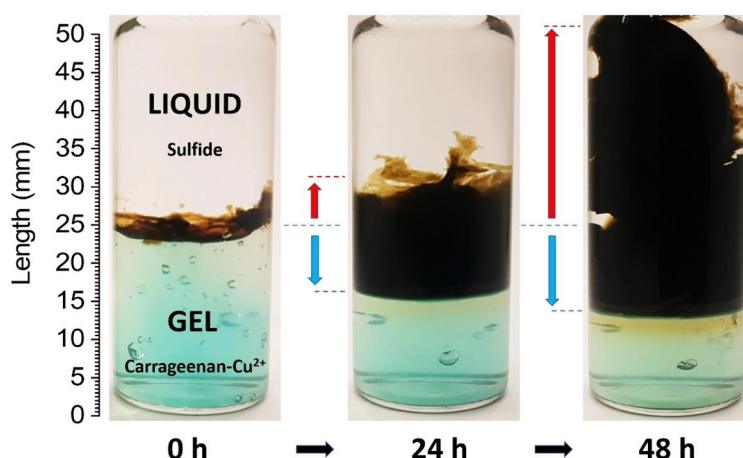**Figure 1.** The CuS-carrageenan composite is grown from the interface of the Cu-ι-carrageenan hydrogel and sulfide solution. The growth was recorded for 48 h. The spatial growth of the composites is directed by red and blue arrows (the red arrows are for upward growth of the composite into the solution and the blue arrows are for downward growth of the composite into the gel). The temporal growth is shown by black arrows.

ChemSystemsChem

Articles
doi.org/10.1002/syst.202000063

Chemistry Europe
European Chemical
Societies Publishing

and the precipitated CuS have been captured using a Zeiss Leo Gemini 1530 instrument equipped with Schottky Field Emitter.

Thermal gravimetric analysis (TGA) was performed under N_2 inert atmosphere from room temperature to 600 °C at a heating rate of 10 °C/min by a Netzch STA 449 F1 Jupiter thermogravimetric analyser. Differential thermogravimetric (DTG) curves were also plotted to detect significant weight changes.

Solid-state Fourier transform infrared spectra of the composites as well as the reference materials were measured with the Attenuated Total Reflectance Fourier transform infrared spectrometer (ATR-FTIR) using the iS50 ATR on a Thermo Scientific Nicolet iS50.

X-ray photoelectron spectroscopic (XPS) measurements were performed using the PHI 5000 VersaProbe (ULVAC-PHI) spectrometer with monochromatic Al K_α radiation (hν = 1486.6 eV) from an X-ray source operating at 100 μm spot size, 25 W and 15 kV. The high-resolution (HR) XPS spectra were collected with the hemispherical analyzer at the pass energy of 23.5 eV and the energy step size of 0.1 eV. The X-ray beam was incident at the sample surface at the angle of 45° with respect to the surface normal, and the analyzer axis was located at 45° with respect to the surface. The CasaXPS software was used to evaluate the XPS data using set of the sensitivity factors supplied by PHI. Deconvolution of all HR XPS spectra were performed using a Shirley background and a Gaussian peak shape with 30% Lorentzian character.

2.3. Humidity and Temperature Sensing

For an application of the grown materials as temperature and relative humidity sensors, 120 mg of each purified dry materials was transferred into small vials. Then, 1 ml of 95 °C distilled water was added with stirring till getting a homogenous black viscous liquid. Meanwhile, thin film platinum integrated electrodes of 5-μm gap (Micrux) were washed with ethanol and dried in oven under 95 °C for 5 min. After using an adhesive tape to control the coating thickness (Figure S1 in the SI), the substrates were plasma-treated for 5 min before film coating. The black viscous liquid was spread on the heated glass surface using a spatula. The film formed on the glass while cooling down, the tape was removed and the coated glass was again placed into the oven at 95 °C for 2 min, Figure S1 in the SI shows the final obtained sensor.

For gas and humidity sensing, the sensors were loaded into a stainless-steel chamber and exposed to cycles of vacuum and N_2 with varying concentration of gases or water while measuring their resistance. A computer-controlled bubbler was filled with the corresponding liquid, and then N_2 was bubbled through. The resulting gas mixture (N_2 and organic compounds/ water) was diluted to obtain the desired concentrations. For temperature measurements, the sensors were loaded into a stainless-steel chamber with controllable temperature. The resistance of the sensors was recorded under varying constant values of temperature, starting from 30 °C to 80 °C and back to 30 °C in steps of 10/−10 °C. The normalized resistance was calculated according to the following equation: $R_{Normalized}$ = (R−

R_0) / R_0, where R_0 is the initial resistance value. Temperature coefficient of resistance (TCR) was calculated from the graph of $R_{normalized}$ versus Temperature, and it is equal to the slope.

3. Results and Discussion

3.1. pH Effect on the Growth

In our system, the high pH of the sulfide solutions ensures that anions are available as sulfides predominantly, which is a very high driving force for crystallization to occur. The larger the difference of pH, the more quickly the composites grow which ends up with higher yield of the final products (Figure 2). Particularly, the obtained composite of LPH13 is much more than those of LPH10 and LPH7 after 48 h in both directions (upward and downward) of the growth. A recorded video (SI) shows in detail the growth process during 48 hours of LPH13 and the mechanism of the growth is proposed as follow. When the liquid and gel are brought into contact, the Cu^{2+} reacted with S^{2-} in the solution. The large difference in pH and ionic speciation leads to a high driving force for crystallization at the interface and a rapid formation of a dense mineralized layer. This new interface now forms a 'barrier' over which large osmotic pressure can build up. However, this drive is not strong enough to break the Cu-complexed carrageenan matrix in order to form jets (e.g. like what reported by Ibsen et al.[9]). As a result, the whole precipitated system is pushed upwards to the liquid (Figure 2).

Other effects (Figure S2-S4, SI) on the growth were studied in order to maximize the growth such as pH of the hydrogel, copper and carrageenan concentration and sulfide concentration. The maximum growth was, however, recorded with LPH13.

3.2. Characterization

3.2.1. X-Ray Diffraction (XRD)

Before interpreting XRD patterns of the grown materials, the XRD patterns of two reference samples, i.e. the precipitated CuS (without carrageenan) and ι-carrageenan, were recorded (Figure 3). The characteristic peaks of the precipitated CuS at 10.8, 27.4, 29.5, 31.8, 32.9, 48.1, 52.8 and 59.2° of 2θ correspond to crystal planes (002), (101), (102), (103), (006), (110), (108) and (116), respectively, and match the hexagonal phase of CuS (covellite) identified with card No.06-0464 or No.65-3561,[27,28] it could be also identified by JCPDS card No. 01–1281.[29,30] The XRD pattern of ι-carrageenan possesses broad diffused peaks, indicating the presence of amorphous structure.[31,32]

In order to investigate the CuS-carrageenan composites, herein LPH13, LPH10, and LPH7, in details, their XRD patterns are divided into two sets: before (Figure 3A) and after purification (Figure 3B). LPH13 sample before purification in Figure 3A shows identical peaks as the precipitated CuS, confirming the presence of the covellite phase along with the broad diffused peak of the amorphous ι-carrageenan. However,

ChemSystemsChem

Articles
doi.org/10.1002/syst.202000063

Chemistry Europe
European Chemical
Societies Publishing
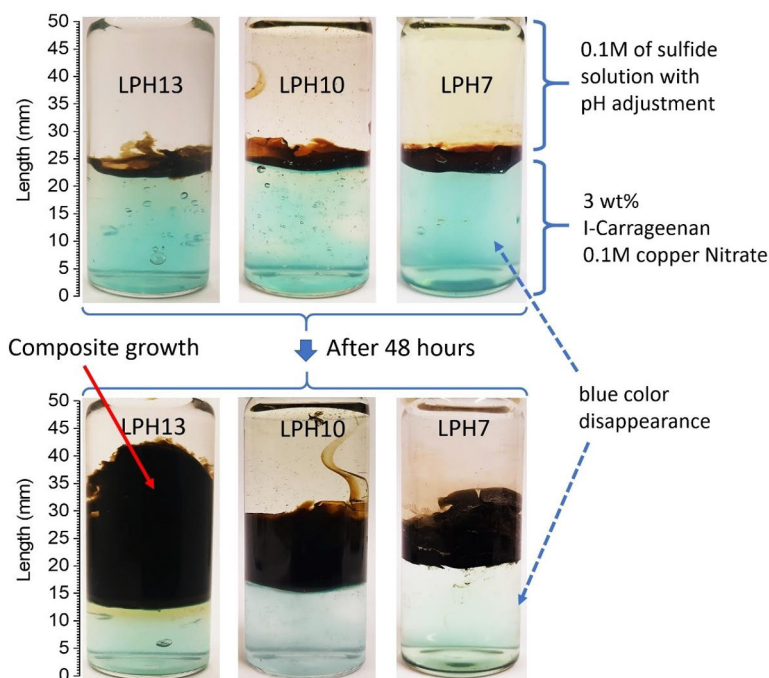
Figure 2. Liquid phase pH effect on the growth of the nanocomposite.
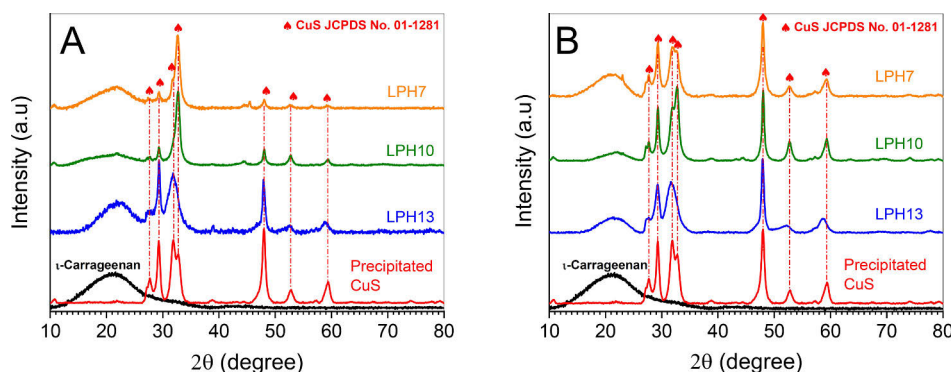
Figure 3. XRD patterns and phase identification for the grown samples (A) before and (B) after purification.

LPH10 and LPH7 without purification display a very sharp peak at 32.7° of 2θ, overlapping the peaks of the CuS phase. This could be explained by the presence of some impurities.[31,33]

Figure 3B shows the XRD patterns of purified CuS-carrageenan composites. Indeed, the crystalline peaks of the impurities were absent from all pattern after purification, leaving the same covellite phase to appear in more intense peaks. The purification also confirms the existence of ι-

carrageenan in its amorphous form at about 22°[34] similarly to the one before purification (Figure 3A). Washing by a mixture of ethanol:water (80:20, v:v) serves efficiently to purify all composites without removing the carrageenan[33] as well as copper sulfide particles. No peak of sodium chloride, sodium nitrate or from any other possible phases has been detected in the composite (Figure 3B). The presence of CuS crystals in the grown composites could be explained by the diffusion of

ChemSystemsChem

Articles
doi.org/10.1002/syst.202000063

Chemistry Europe
European Chemical
Societies Publishing

copper ions from the gel phase towards the liquid phase which contains sulfide ions. The ions assisted the growth of the composite by allowing the carrageenan to drift from the gel phase towards the liquid phase. Due to variation of pH, not only the amount of grown composite changes but also crystalline sizes of CuS variate. Calculations reveal that LPH13 copper sulfide has an average crystallite size of 10.1 nm. The average crystallite size of copper sulfide increases slightly for LPH10 and LPH7 to 12.4 nm and 13.5 nm respectively.

3.2.2. Fourier Transform Infrared Spectroscopy (FTIR)

Although FTIR spectrum of the reference CuS does not have any obvious band (Figure 4), FTIR is a great method to confirm further the existence of the polymer ι-carrageenan in the grown materials (Figure 4). Before purification, the grown material LPH13 exhibit almost all intense vibrational bands at 697, 723, 926, 1025, 1218 and 1630 cm^{-1} which has been observed from the ι-carrageenan. These bands can be assigned to C-4 of galactose (697 cm^{-1}),[35] the C–C stretching band (926 cm^{-1}),[36] the CH$_2$ symmetric stretching (1025 cm^{-1}),[37] ester sulfate vibrational band (1218–1260 cm^{-1}),[38,39] and H–O–H deformation band (1630 cm^{-1})[40] of the ι-carrageenan. Finally, the broad band at 3425 cm^{-1} could be assigned to the stretching of hydroxyl group.[31,33,41] Although the existence of ι-carrageenan in the LPH13 grown composite has been confirmed, the LPH7 and LPH10 before purification do not exhibit any bands neither for the ι-carrageenan. However, the FTIR spectra of the purified LPH7 and LPH10 (Figure 4B) exhibit all the bands attributed to those of ι-carrageenan which confirms that signal-masking impurities were washed successfully from the CuS-carrageenan composite. The bands of the purified LPH13 (Figure 4B) appear to be more intense than before washing. The purification was effectively an important step to produce CuS-carrageenan composite. The FTIR results are in good agreement with those of XRD.

3.2.3. Scanning Electron Microscopy (SEM)

SEM technique was applied to investigate the morphology of the grown composites. Figure 5 are selected SEM micrographs for LPH7, LPH10 and LPH13 before and after purification, as well as for referenced ι-carrageenan and precipitated CuS (Figure 5A and 5B).

The grown materials LPH7, LPH10 and LPH13 before purification (Figure 5C, 5E, and 5G) share alike morphology. ι-carrageenan of the composite is separated into domains which look differently from ι-carrageenan Figure 5B. Before purification, the grown LPH7, LPH10 and LPH13 composites seem to have larger particle size due to the presence of impurities. After purification, as XRD suggests, impurities are removed to expose pure CuS covellite particles. These CuS particles have small particle size of less than 40 nm, according to SEM, which is on a similar scale to the crystallite size of around 10–14 nm determined by XRD. which are probably the CuS covellite according to the XRD results. As XRD reveals that the crystallite size of CuS is very small, the same result is confirmed by SEM images. The particles are also similar to precipitated CuS; however, they appear more homogeneous. The purification process changes the morphology of the carrageenan as well, the carrageenan in washed LPH7 sample forms a leaf shape Figure 5D, while the LPH10 and LPH13 do not exhibit the same morphology (Figure 5F and 5H).

3.2.4. Thermogravimetric Analysis (TGA)

Figure 6 illustrates the TGA and DTG curves of the three grown composites LPH7, LPH10 and LPH13 before and after purification as well as the reference ι-carrageenan and precipitated CuS. Below 180 °C, all the samples exhibit small gradual weight losses due to the removal of moisture. Thermal degradation of the carrageenan reference sample starts at about 257 °C with a noticeable weight loss (sharp decrease) of around 32.34 % (Figure S5A).[32,34,42] Under N$_2$ inert atmosphere thermal decom-
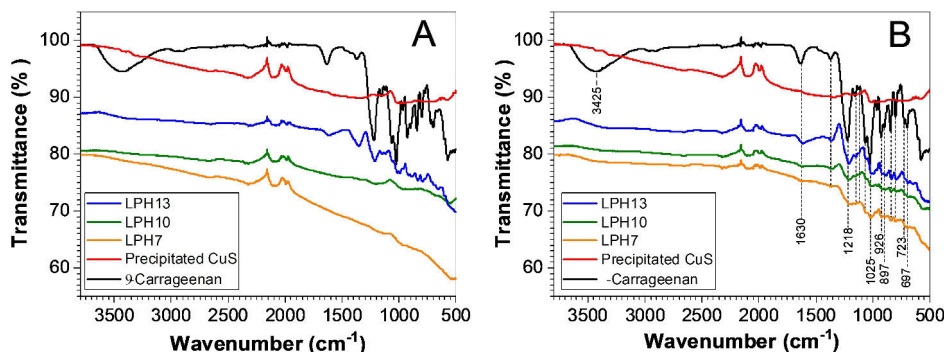
Figure 4. The FTIR-ATR spectra of the three grown composites LPH7, LPH10 and LPH13 (a) before and (b) after purification; ι-carrageenan; and precipitated CuS as reference materials.

ChemSystemsChem

Articles
doi.org/10.1002/syst.202000063

Chemistry
Europe
European Chemical
Societies Publishing
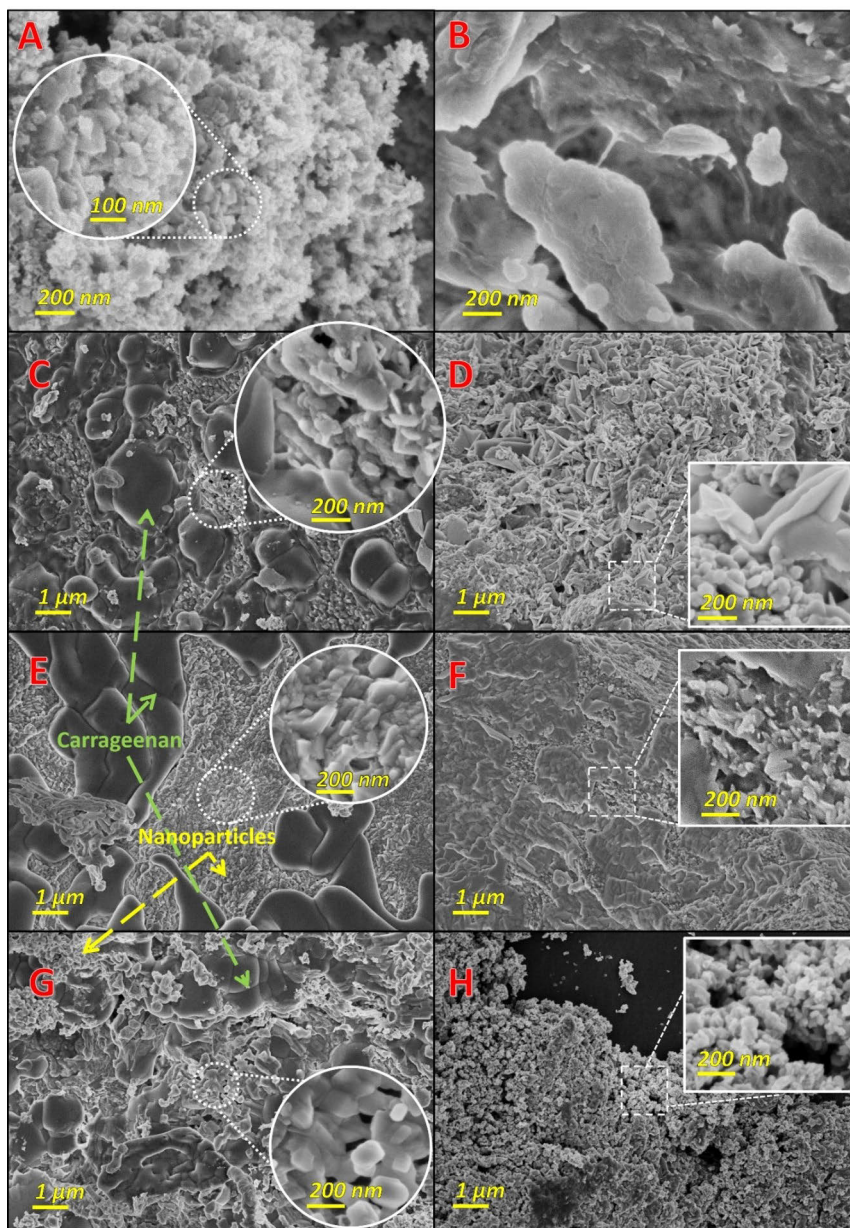
Figure 5. The SEM micrographs of the precipitated CuS (A), ι-carrageenan (B), LPH7 (C), LPH10 (E) LPH13 (G) composites before purification, and LPH7 (D), LPH10 (F), LPH13 (H) after purification. The figure displays the micrographs with two magnification 10k× and 100k×.

position of CuS reference sample occurs in the temperature range of 200–600 °C with a total weight loss of around 16.95 % (Figure S5B) due to the gradual transformation of CuS into Cu_2S.[43,44]

ChemSystemsChem

Articles
doi.org/10.1002/syst.202000063

Chemistry
Europe
European Chemical
Societies Publishing
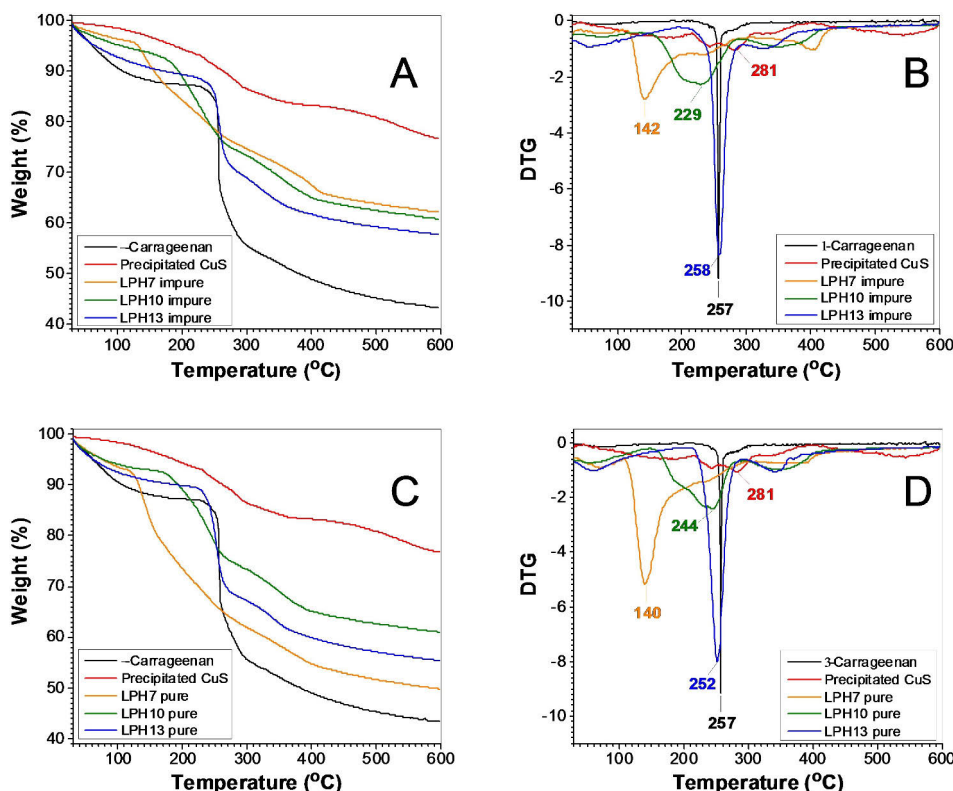
Figure 6. Thermogravimetric (A) and their differential scanning calorimetry (B) analyses of carrageenan, precipitated CuS, LPH7, LPH10 and LPH13 mixtures before purification; (C) and (D) are the mixtures after purification.

Before the purification, among the three composites, LPH13 shows the greatest thermal stability with a total weight loss of 27.21 %, followed by LPH10 (30.43 %) and LPH7 (31.66 %) (Figure 6A and Figure S5D, S5F, and S5H). DTG curves show that the thermal degradation of LPH13, LPH10 and LPH7 begins around 258, 229, 142 °C respectively (Figure 6B and Figure S5C, S5E, and S5G). After purification, LPH10 becomes more thermally stable (total weight loss of 28.76 %) than LPH13 (30.49 %) and LPH7 remains as the least stable sample (40.6 %) (Figure 6C). DTG curves of the purified samples show no significant changes (Figure 6D). The thermal degradation of LPH13, LPH10 and LPH7 occurs around 252, 244, 140 °C respectively.

3.2.5. X-ray Photoelectron Spectroscopy (XPS)

High resolution XPS spectra of carbon, oxygen and sulfur of carrageenan reference sample are presented in Figure S6. Careful deconvolution of C1s spectra suggests 4 chemical states of carbon (Figure S6a). Peak occurring at 248.8 eV, 286.4 eV, and 287.8 eV could be identified as due to C—C/C—H bond, C—O bond,[45,46] and O—C—O bond,[47] respectively, which are in good agreement with a chemical structure of the carrageenan molecule. The last carbon peak located at 289.1 eV caused probably by the presence of carboxyl group, originated from adventitious carbon compounds. Oxygen XPS spectra of the carrageenan sample also is in good agreement with theory. O1s spectra is presented on Figure S6b, 2 chemical states observed. Origin of the O1s peak observed at 531.8 eV is probably S—O bond[48,49] from carrageenan sulphate groups, second O1s peak at 532.9 eV could be assigned to C—O bond.[46] Small peak located at 536.2 eV is probably a Na KLL peak which suggest that sodium is present in carrageenan as a leftover from manufacturing process. Sulfur S2p spectra presented on Figure S6c. Due to spin-orbit coupling the S2p state is present as peak doublet (2p3/2 and 2p1/2) separated by 1.2 eV. The S2p3/2 position (168.7 eV) is attributed to the presence of S(VI) from the carrageenan's sulfate.[50,51]

Carbon (Figure S6a), oxygen (Figure S6b), sulfur (Figure S6c) spectra of the LPH7, LPH10, LPH13 samples show significant resemblance to reference carrageenan spectrum. Deconvolution

ChemSystemsChem

Articles
doi.org/10.1002/syst.202000063

Chemistry
Europe
European Chemical
Societies Publishing

of carbon spectra also produce 4 peaks at the similar positions and therefore could be assigned in the same manner as in carrageenan. Oxygen spectra shows peaks for S—O and C—O bond and as for the sulfur we can see sulfate S2p doublet at 168 eV. The above findings confirm the presence of the carrageenan in the treated samples also. In addition, XPS confirms the presence of copper in the composites by analyzing the Cu 2p spectra (Figure S6d). These spectra show two peaks centered at 952.4 eV (Cu 2p1/2) and 932.5 eV (Cu 2p3/2). Considering general chemical structure of the samples the origin of the Cu 2p 3/2 peak located at around 932.5 eV is a copper (II) sulfide. Even though the presence of Cu(I) oxide which Cu2p3/2 peak is also expected at the same position,[45] it is unlikely since no oxide O1s peak at 529–530 eV is observed.[46] The samples also shows satellite peaks (at ~940 and ~944 eV) of different intensity on the higher binding energy side of Cu 2p1/2 and Cu 2p3/2, which is consistent with the data reported in literature.[52] These peaks indicate existence of phases containing copper in the Cu^{2+} state.[53] Second smaller Cu2p3/2 peak located at higher binding energies (935 eV) and could be associated with a copper bounded with the sulphate groups of carrageenan.[54]

3.3. Humidity- and Temperature-Responsive CuS-Carrageenan Composites

This section highlights the potential application of the CuS-carrageenan nanocomposite for RH and temperature sensing. Figure S1A shows the platinum integrated electrode coated with CuS-carrageenan nanocomposite. The electrical-resistance responses of the nanocomposite is a function of the variation of the RH or the temperature.

Figure 7 displays the sensing performance of LPH13-coated sensor. The test at different level of humidity was recorded using cycles starting from 0 to 80% then from 80% to 5% (Figure 7A). At each cycle, the sensor was humidified then dehumidified. All humidity levels display a rapid absorption of

water molecules compared to its desorption, which is much slower. First, the response to 0, 5 and 10% RH was very similar. Then, the sensor resistance starts to increase drastically from 20% to 80% RH. When decreasing the RH from 80% to 5%, the resistance does not return to the same baseline due to slow kinetics of water desorption. Yet, the sensor is still more or less reversible. Moreover, the optimization of CuS-carrageenan composite impedance during its synthesis, could control the sensor response by adjusting the concentration of copper and sulfide to get a desired resistance as well as better swelling properties.[55] As determined in the characterization section, the LPH13 after purification is composed of CuS (covellite) nano-particles mixed with ι-carrageenan. Hence, the variation of the sensor resistance is attributed to either the change in electrical permittivity of the polymer matrix or the swelling of the hydrophilic carrageenan.[56] The precipitated CuS (covellite) was tested as well. It has a metal like conductivity; however, it does not exhibit any changes of its resistance during the variation of the RH as shown in Figure 7A.

The sensitivity of the sensor towards temperature was recorded in Figure 7B. The sensor was exposed to different constant temperatures starting from 30 to 80 and back to 30 °C. The responses indicate its capacity to detect rapid changes of temperature in the examined range. At this range, the sensor shows a promising linear and reversible response under ambient conditions. The sensitivity to temperature change was evaluated by the temperature coefficient of resistance (TCR) °C^{-1} that was shown to be 2100 ppm °C^{-1} for LPH13. This value is close to values shown with recently developed temperature sensors,[57–59] and to that of bulk Ag and Pt (the widely used material for temperature sensors) that show TCR values of 3800 and 3900 ppm °C^{-1}, respectively.[60]

Responses of LPH13 samples was recorded for acetone, formic acid, hexanol and toluene (Figure S7). In general, the resistance variation toward these substances was arbitrary and needs further future investigations.
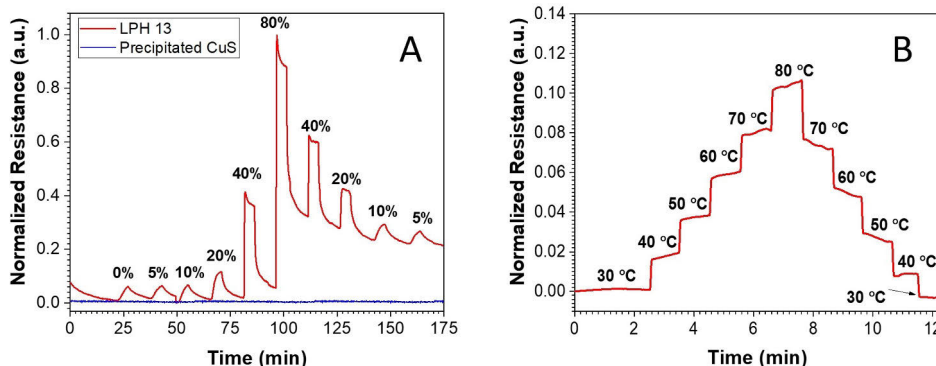

Figure 7. Responses of LPH13 coated sensor to (A) RH and (B) temperature.

ChemSystemsChem

Articles
doi.org/10.1002/syst.202000063

Chemistry Europe
European Chemical
Societies Publishing

4. Conclusion

This paper highlights a novel method to grow the CuS-carrageenan nanocomposite from the interface of a sulfide solution and Cu-ι-carrageenan hydrogel. pH and concentration of sulfide solution effects on the growth and structures of the nanocomposites were examined in detail. We conclude that the nanocomposite is homogeneous and chemically stable especially after purification. Moreover, comparing to carrageenan or CuS solely, the CuS-carrageenan nanocomposite has properties of both the polymer and semiconductor which explains its ease of coating and electrical conductivity in order to be used as the sensing material. Another advantage of this material is the possibility of adjusting its conductivity as well as its swelling properties, by varying the concentrations of copper and sulfide precursors or adjusting the pH of the liquid phase during synthesis. As a result, the nanocomposite is exploited in the form of RH and temperature sensor of which decent responses to both stimuli were reported. Last but not least, the reported method is also applicable for synthesizing FeS- and ZnS-carrageenan nanocomposite (Figure S8 in the SI) which make it intriguing for further investigation of other composite materials.

Conflict of Interest

The authors declare no conflict of interest.

Keywords: carrageenan · chemical gardens · chemobrionics · copper sulfide · nanocomposites

[1] L. M. Barge, *Chem. Rev.* **2015**, *115*, 8652–8703.
[2] Y. Ding, B. Batista, O. Steinbock, J. H. E. Cartwright, S. S. S. Cardoso, *Proc. Natl. Acad. Sci. USA* **2016**, *113*, 9182–9186.
[3] F. Haudin, J. H. E. Cartwright, A. De Wit, *J. Phys. Chem. C* **2015**, *119*, 15067–15076.
[4] G. Pampalakis, *Chem. Eur. J.* **2016**, *22*, 6779–6782.
[5] S. S. S. Cardoso, J. H. E. Cartwright, O. Steinbock, D. A. Stone, N. L. Thomas, *Struct. Chem.* **2017**, *28*, 33–37.
[6] P. Kumar, D. Horváth, Á. Tóth, *Soft Matter* **2020**, *16*, 8325–8329.
[7] E. Bormashenko, Y. Bormashenko, O. Stanevsky, R. Pogreb, *Chem. Phys. Lett.* **2006**, *417*, 341–344.
[8] T. Huynh, *ChemSystemsChem* **2021**, *3*, e2000031.
[9] C. J. S. Ibsen, B. F. Mikladal, U. B. Jensen, H. Birkedal, *Chem. Eur. J.* **2014**, *20*, 16112–16120.
[10] E. A. B. Hughes, R. L. Williams, S. C. Cox, L. M. Grover, *Langmuir* **2017**, *33*, 2059–2067.
[11] E. A. B. Hughes, S. C. Cox, M. E. Cooke, O. G. Davies, R. L. Williams, T. J. Hall, L. M. Grover, *Adv. Healthcare Mater.* **2018**, *7*, 1701166.
[12] A. Fogde, S. Qudsia, T.-A. Le, T. Sandberg, T.-P. Huynh, *ChemSystemsChem*, **2021**, *3*, e200064.

[13] J. R. Padhi, D. Nayak, A. Nanda, P. R. Rauta, S. Ashe, B. Nayak, *Carbohydr. Polym.* **2016**, *153*, 292–301.
[14] A. Fogde, B. Kurtén, T. Sandberg, T. P. Huynh, *J. Chem. Educ.* **2020**, *97*, 3702–3706.
[15] M. Khatib, O. Zohar, H. Haick, *Adv. Mater.* **2021**, 2004190.
[16] M. Muthukrishnan, C. Shanthi, S. Selvasekarapandian, R. Manjuladevi, P. Perumal, P. C. Selvin, *Ionics* **2019**, *25*, 203–214.
[17] D. Yang, S. Gao, H. Yang, *Food Hydrocolloids* **2020**, *99*, 105317.
[18] D. Yang, H. Yang, *LWT-Food Sci. Technol.* **2020**, *126*, 109281.
[19] D. Li, D. Yang, X. Yang, Y. Wang, Z. Guo, Y. Xia, S. Sun, S. Guo, *Angew. Chem. Int. Ed.* **2016**, *55*, 15925–15928; *Angew. Chem.* **2016**, *128*, 16157–16160.
[20] A. G. Viana, M. D. Noseda, M. E. R. Duarte, A. S. Cerezo, *Carbohydr. Polym.* **2004**, *58*, 455–460.
[21] B. T. Nguyen, T. Nicolai, L. Benyahia, C. Chassenieux, *Carbohydr. Polym.* **2014**, *112*, 10–15.
[22] S. J. L. P. Perez, G. C. Claudio, *J. Mol. Graphics Modell.* **2020**, *98*, 107588.
[23] S. K. Mathew, N. P. Rajesh, M. Ichimura, Udayalakshmi, *Mater. Lett.* **2008**, *62*, 591–593.
[24] Y. Li, W. Lu, Q. Huang, C. Li, W. Chen, *Nanomedicine* **2010**, *5*, 1161–1171.
[25] T.-P. Huynh, *Nano Futur.* **2020**, *4*, 032001.
[26] A. Bollero, S. Fernández, K. Zuzek Rozman, Z. Samardzija, M. Grossberg, *Thin Solid Films* **2012**, *520*, 4184–4189.
[27] J. Ludwig, L. An, B. Pattengale, Q. Kong, X. Zhang, P. Xi, J. Huang, *J. Phys. Chem. Lett.* **2015**, *6*, 2671–2675.
[28] S. M. Hosseinpour-Mashkani, M. Salavati-Niasari, F. Mohandes, K. Venkateswara-Rao, *Mater. Sci. Semicond. Process.* **2013**, *16*, 390–402.
[29] Y. Lu, X. Meng, G. Yi, J. Jia, *J. Colloid Interface Sci.* **2011**, *356*, 726–733.
[30] Y. Lu, J. Jia, C. Lu, J. Huang, X. Feng, *Mater. Lett.* **2019**, *243*, 176–179.
[31] V. Moniha, M. Alagar, S. Selvasekarapandian, B. Sundaresan, G. Boopathi, *J. Non-Cryst. Solids* **2018**, *481*, 424–434.
[32] S. S. Kim, H. W. Kim, S. H. Yuk, S. Y. Oh, P. K. Pak, H. B. Lee, *Biomaterials* **1996**, *17*, 813–821.
[33] N. A. A. Ghani, R. Othaman, A. Ahmad, F. H. Anuar, N. H. Hassan, *Arab. J. Chem.* **2019**, *12*, 370–376.
[34] F. N. Jumaah, N. N. Mobarak, A. Ahmad, M. A. Ghani, M. Y. A. Rahman, *Ionics* **2015**, *21*, 1311–1320.
[35] C. Rochas, M. Lahaye, W. Yaphe, *Bot. Mar.* **1986**, *29*, 335–340.
[36] N. Rajeswari, S. Selvasekarapandian, S. Karthikeyan, C. Sanjeeviraja, Y. Iwai, J. Kawamura, *Ionics* **2013**, *19*, 1105–1113.
[37] K. K. Maurya, N. Srivastava, S. A. Hashmi, S. Chandra, *J. Mater. Sci.* **1992**, *27*, 6357–6364.
[38] M. Hema, S. Selvasekarapandian, G. Hirankumar, A. Sakunthala, D. Arunkumar, H. Nithya, *Spectrochim. Acta Part A* **2010**, *75*, 474–478.
[39] L. Pereira, A. M. Amado, A. T. Critchley, F. van de Velde, P. J. A. Ribeiro-Claro, *Food Hydrocolloids* **2009**, *23*, 1903–1909.
[40] S. Karthikeyan, S. Selvasekarapandian, M. Premalatha, S. Monisha, G. Boopathi, G. Aristatil, A. Arun, S. Madeswaran, *Ionics* **2017**, *23*, 2775–2780.
[41] V. Moniha, M. Alagar, S. Selvasekarapandian, B. Sundaresan, R. Hemalatha, G. Boopathi, *J. Solid State Electrochem.* **2018**, *22*, 3209–3223.
[42] J. S. Varghese, N. Chellappa, N. N. Fathima, *Colloids Surf. B* **2014**, *113*, 346–351.
[43] M. Foldvari, *Handbook of Thermo-Gravimetric System of Minerals and Its Use in Geological Practice*, **2011**.
[44] B. Brunetti, V. Piacente, P. Scardala, *J. Alloys Compd.* **1994**, *206*, 113–119.
[45] J. F. Moulder, W. F. Stickle, K. D. Bomben, *Handbook of X-Ray Photoelectron Spectroscopy, Perkin Elmer Corporation, Eden Prairie, MN*, **1992**.
[46] A. P. Terzyk, *Colloids Surf. A* **2001**, *177*, 23–45.
[47] E. G. Beamson, D. Briggs, *47. XPS of Polymers Database*, Ed. by G. Beamson and D. Briggs, original electronic database, ISBN 0-9537848-4-3, surfacespectra.com, **2012**.
[48] M. Wahlqvist, A. Shchukarev, *J. Electron Spectrosc. Relat. Phenom.* **2007**, *156–158*, 310–314.
[49] B. J. Lindberg, K. Hamrin, G. Johansson, U. Gelius, A. Fahlman, C. Nordling, K. Siegbahn, *Phys. Scr.* **1970**, *1*, 286–298.
[50] P. H. L. Lima, S. V. A. Pereira, R. B. Rabello, E. Rodriguez-Castellón, M. M. Beppu, D. Mantovani, R. S. Vieira, *Colloids Surf. B* **2013**, *111*, 719–725.
[51] S. B. R. Berton, G. A. M. de Jesus, R. M. Sabino, J. P. Monteiro, S. A. S. Venter, M. L. Bruschi, K. C. Popat, M. Matsushita, A. F. Martins, E. G. Bonafé, *Carbohydr. Res.* **2020**, *487*, 107883.
[52] C. C. Chusuei, M. A. Brookshier, D. W. Goodman, *Langmuir* **1999**, *15*, 2806–2808.

[53] T. Yano, M. Ebizuka, S. Shibata, M. Yamane, *J. Electron Spectrosc. Relat. Phenom.* **2003**, *131–132*, 133–144.
[54] C. D. Wagner, A. V. Naumkin, A. Kraut-Vass, J. W. Allison, C. J. Powell, J. R. Rumble, *J. NIST Standard Reference Database 20, Ver. 3.4*, **2006**.
[55] K. Okamoto, S. Kawai, *Jpn. J. Appl. Phys.* **1973**, *12*, 1130–1138.
[56] D. Y. Godovski, V. Y. Sukharev, A. V. Volkov, M. A. Moskvina, *J. Phys. Chem. Solids* **1993**, *54*, 1613–1620.
[57] Q. Hua, J. Sun, H. Liu, R. Bao, R. Yu, J. Zhai, C. Pan, Z. L. Wang, *Nat. Commun.* **2018**, *9*, 244.
[58] M. Khatib, O. Zohar, W. Saliba, H. Haick, *Adv. Mater.* **2020**, *32*, 2000246.

[59] T.-P. Huynh, H. Haick, *Adv. Mater.* **2016**, *28*, 138–143.
[60] Z. Cui, F. R. Poblete, Y. Zhu, *ACS Appl. Mater. Interfaces* **2019**, *11*, 17836–17842.

ChemSystemsChem

Supporting Information

CuS-Carrageenan Composite Grown from the Gel/Liquid Interface

Morad Zouheir, Trung-Anh Le, Janno Torop, Kostiantyn Nikiforow, Muhammad Khatib, Orr Zohar, Hossam Haick, and Tan-Phat Huynh*
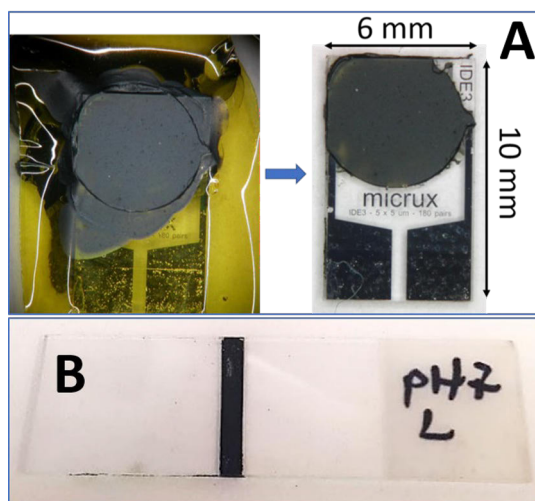
Figure S1. Coating the (A) platinum integrated electrode and (B) microscope glass slide with CuS-carrageenan. The coating area is encircled using a high temperature-resistant tape.
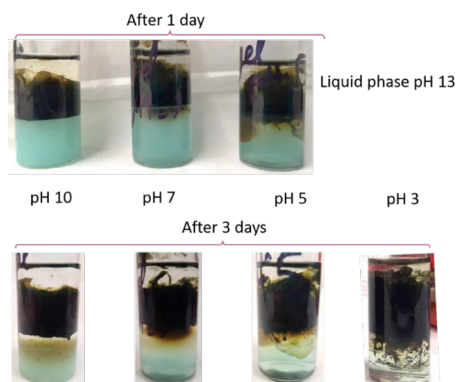
Figure S2. Effect of gel-phase pH on the growth of the nanocomposite.
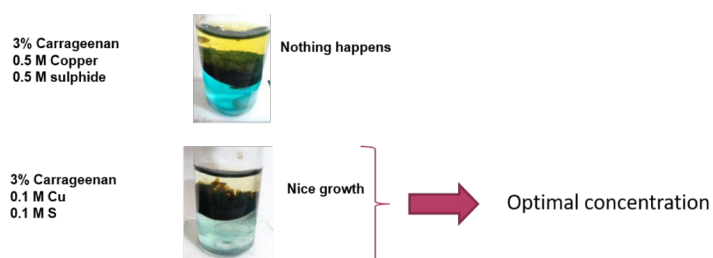
Figure S3. Effect of copper and sulfide concentrations on the growth of the nanocomposite
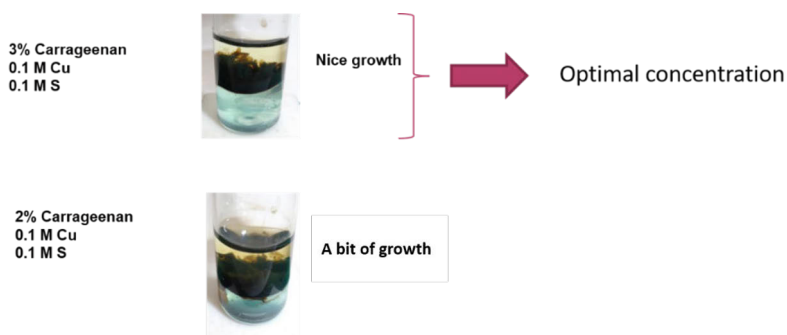
Figure S4. Effect of carrageenan concentration on the growth of the nanocomposite
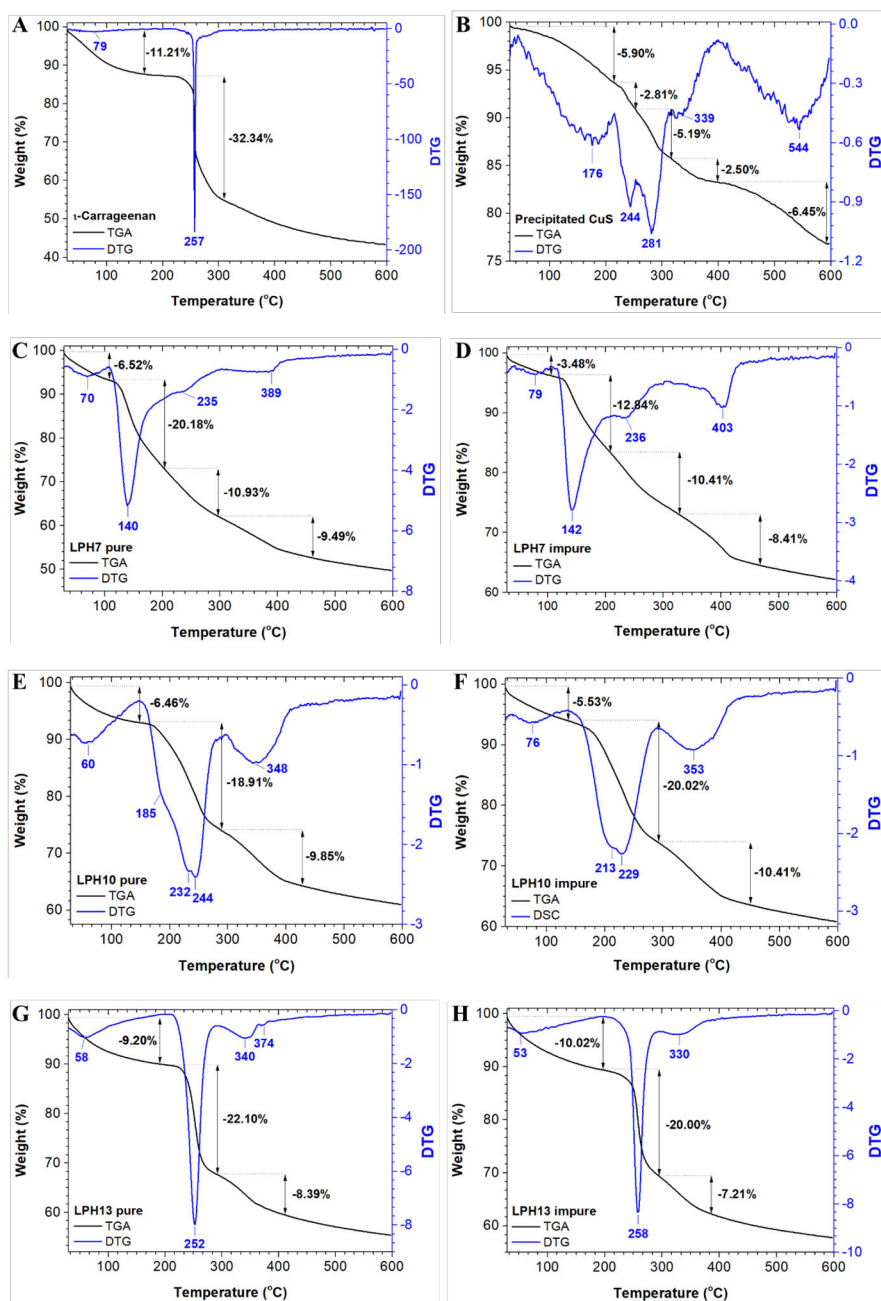
Figure S5. Interpretation of the weight loss of (A) ι-carrageenan, (B) precipitated CuS, (C&D) LPH7, (E&F) LPH10, and (G&H) LPH13 after and before purification
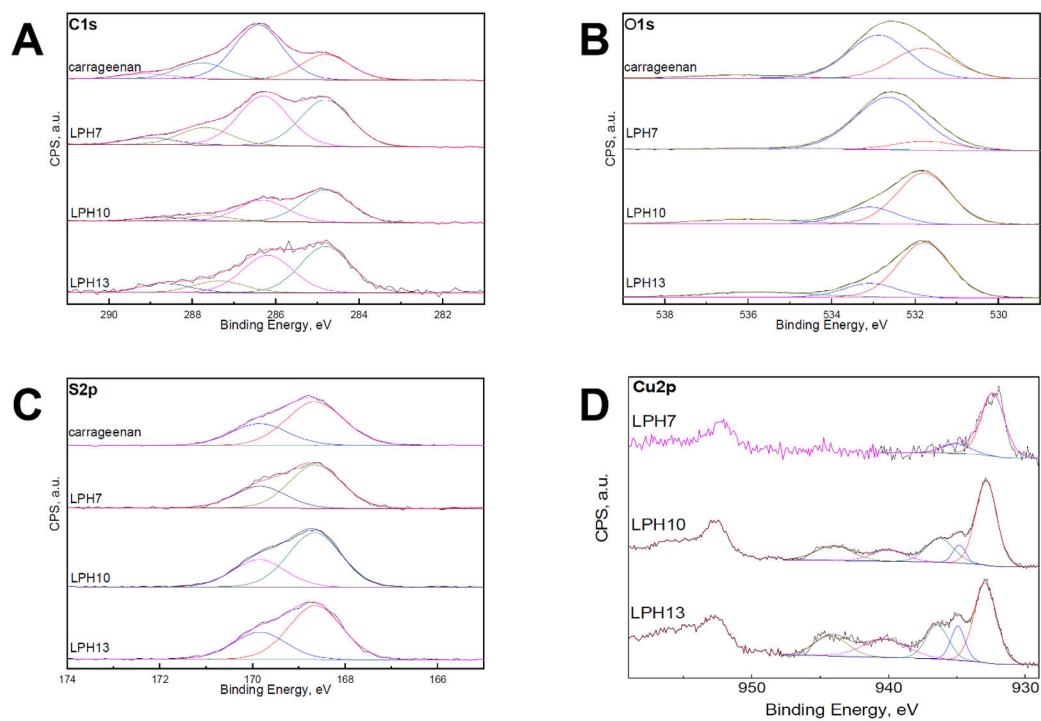
Figure S6. High resolution XPS spectra of the (a) carbon, (b) oxygen, (c) sulfur, and (d) copper for carrageenan reference sample and LPH7, LPH, 10, and LPH13 samples.
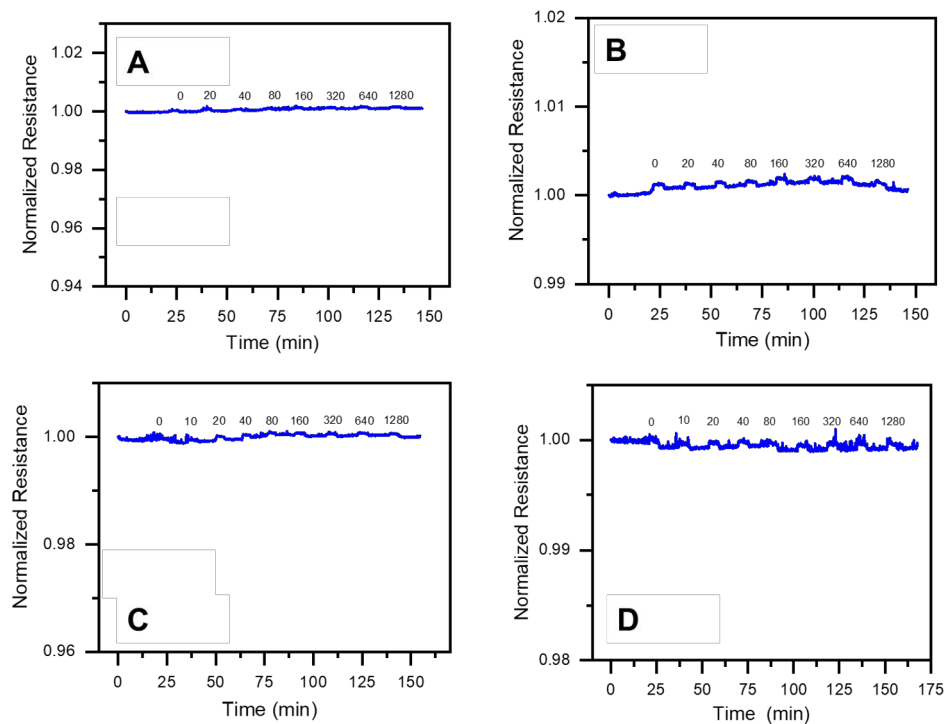
Figure S7. Responses of LPH13 coated sensor to (A) acetone, (B) formic acid, (C) hexanol, and (D) toluene
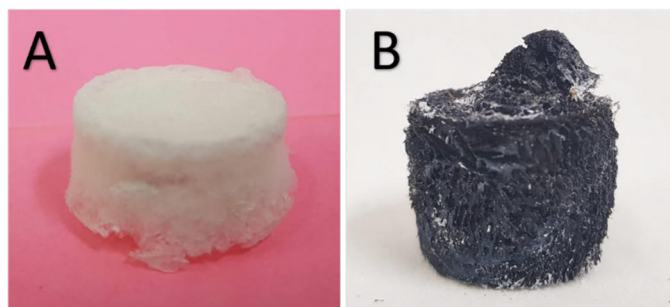
Figure S8. Collected grown (A) ZnS-carrageenan and (B) FeS-carrageenan composites as freeze-dried bulks

Current advances in the Chemical functionalization and Potential applications of Guar gum and its derivatives

Trung-Anh Le*, and Tan-Phat Huynh*

II

Current advances in the chemical functionalization and potential applications of guar gum and its derivatives

Trung-Anh Le *, Tan-Phat Huynh *

Laboratory of Molecular Sciences and Engineering, Åbo Akademi University, Henrikinkatu 2, 20500 Turku, Finland

ARTICLE INFO

ABSTRACT

Guar gum (GG) from seeds of cluster bean *(Cyamopsis tetragonolobus)* contains mainly non-ionic galactomannan polysaccharide. Due to fascinating properties, great natural abundancy, low cost, biocompatibility and biodegradability, natural GG polysaccharide has been studied and employed in various research fields and industries. To explore and extend full potentials of GG, further chemical functionalization of the material is essential. This review highlights recent progress in the chemical modification of GG and its derivatives based on nucleophilic reactions, partial oxidation, graft polymerization and cross-linking with diverse chemical reagents and reaction pathways. Moreover, further insights into structure–property relationships as well as potential applications of the materials are also provided and discussed.

1. Introduction

Recently, dramatic climate changes have reached to the critical point globally and drastic actions are urgently demanded. To overcome these challenges, holistic effort and strategies have been considered such as reducing greenhouse gases [1,2], preventing pollution in different forms [3,4], replacing fossil fuels by renewable fuels [5,6], practicing more sustainable and productive agriculture [7,8], etc. Since natural

photosynthesis can utilize solar energy and reduce carbon dioxide green-house gas in the atmosphere to produce useful polysaccharide products, promoting the use of polysaccharides as materials, food and medicine has been one of the most sustainable approaches to cope with climate changes and to ensure sustainable human activities.

Over the years, great attention has been drawn to novel materials research of guar gum (GG) in various fields (Fig. 1), due to GG's natural abundancy, low cost, biocompatibility, biodegradability, and accessible

---

; GA-cl-GG-IA-keratin, GA-cross-linked GG-IA-keratin; GA, Fe^{3+}-cl-GG/SAL/DA-STMS/GA, GA, Fe^{3+}-cross-linked GG/SAL/DA-STMS/GA; Gal, galactose; GE, grafting efficiency; GelG, gellan gum; GG, guar gum; GG-APSi, GG-(3-aminopropyl)silane; GG-APSi-FFR, GG-APSi-furfural; GG-APSi-FFR-Pd, GG-APSi-FFR-Pd2+; GG-APSi-SAAL, GG-APSi-salicylaldehyde; GG-APSi-SAAL-Cu, GG-APSi-SAAL-Cu2+; GG-LPEI, LPEI grafted GG; GG-g-LPEI/pDNA, GG-g-LPEI/pDNA coacervate; GG-GMA, glycidyl methacrylate guar gum; GG-GMA-g-P(AA-*co*-DMAAm), AA-*co*-DMAAm grafted GG-GMA; GG-GMA-g-P(AA-*co*-DMAAm)/HCS, HCS-encapsulated GG-GMA-g-P(AA-*co*-DMAAm); GG-g-PAA, acrylic acid grafted guar gum; GG-g-PAAm, AAm grafted GG; GG-g-PAGA, AGA grafted GG; GG-g-PCL, PCL grafted GG; GG-g-PEA, EA grafted GG; GG-g-PHEMA, HEMA grafted GG; GG-g-PHEMA/ASA, ASA-encapsulated GG-g-PHEMA; GGH, GG hydrolysate; GGH-DDSA, GGH-dodecenyl succinic acid; GGH-OSA, GGH-*n*-octenyl succinic acid; GGH-S-L, GGH-sulfonic acid by Larm method; GGH-S-O, GGH-sulfonic acid by O'Neill method; GG-IA, GG indole acetate; GG-MA, GG-maleic acid; GG-N, aminated GG-NH_2; GG-O-Sn(C≡CPh)3, alkoxy-tin(IV) of GG; GG-P, GG-phosphonic acid; GG-PU, GG-based polyurethanes; GG-RDA, GG-ricinoleic dimer acid; GG-SL, guar gum-soya lecithin; GG-S-L, GG-sulfonic acid by Larm method; GG-S-O, GG-sulfonic acid by O'Neill method; GG-X, GG xanthate; GG-X/CuS, GG-X/CuS nanocomposite; GH, galacylhydrazine; glyoxal-cl-GG/activated C, glyoxal-cross-linked GG/activated C; GMA, glycidyl methacrylate; GMS, gentamicin sulphate; GO, graphene oxide; GS, gentamicin sulfate; GTE, green tea extract; GTMAC, glycidyltrimethylammonium chloride; GY, grafting yield; h, hour; H^+, proton; H_2AA, ascorbic acid; HCS, hydrocortisone; HDGG, 6-O-(3-hexadecyloxy-2-hydroxypropyl)-GG; HDGG/AmB, AmB-encapsulated HDGG; HDGG/AmB/Pip, AmB and Pip-encapsulated HDGG; HEK-293, human embryonic kidney 293; HEMA, 2-hydroxy ethyl methacrylate; ^{1}H NMR, proton nuclear magnetic resonance; $HO^\bullet$, hydroxyl radicals; HOMO, highest occupied molecular orbital; HOS, human osteosarcoma; HPGG, hydroxypropyl GG; HSO_5^-, S-centered bisulfite free radicals; HSO_3, bisulfite; HSO_4, bisulfate; HTPB, hydroxyl-terminated polybutadiene; hydrazine-cl-DAGG-MBAAm-cl-P(AA-*co*-MMA), hydrazine-cross-linked DAGG-MBAAm-cl-P(AA-*co*-MMA); I2959, Irgacure 2959; IO_4, periodate; IPA, isopropyl alcohol; IPDI, isophorone diisocyanate; *K. pneumonia, Klebsiella pneumonia*; $K_2S_2O_8$ or KPS, potassium persulfate; KSPA, potassium 3-sulfopropyl acrylate; LCME, ʟ-cysteine methyl ester; LGG, linoleic guar gum; LiCl, lithium chloride; LPEI, low-molecular-weight polyethylenimine; LUMO, lowest unoccupied molecular orbital; MA, maleic anhydride; Man, mannose; MB, methylene blue; MBAAm, N,N'-methylenebisacrylamide; MBAAm-cl-AGG-g-P(AA-*co*-KSPA), MBAAm-cross-linked AA-*co*-KSPA grafted AGG; MBAAm-cl-AGG-g-P(AA-*co*-KSPA)/GMS, GMS-encapsulated MBAAm-cl-AGG-g-P(AA-*co*-KSPA); MBAAm-cl-CMGG-g-PAA, MBAAm-cross-linked AA grafted CMGG; MBAAm-cl-CMGG-g-P(AA-*co*-AAm), MBAAm-cross-linked AA-*co*-AAm grafted CMGG; MBAAm-cl-CMGG-g-PAAm, MBAAm-cross-linked AAm grafted CMGG; MBAAm-cl-GG-g-PAA, MBAAm-cross-linked GG-g-PAA; MBAAm-cl-GG-g-PAA/Ag NPs, MBAAm-cl-GG-g-PAA/Ag NPs nanocomposite; MBAAm-cl-GG-g-P(AA-*co*-AAm), MBAAm-cross-linked AA-*co*-AAm grafted GG; MBAAm-cl-GG-g-P(AA-*co*-AN), MBAAm-cross-linked AA-*co*-AN grafted GG; MBAAm-cl-GG-g-P(AA-*co*-AN)/TQ, TQ-encapsulated MBAAm-cl-GG-g-P(AA-*co*-AN); MBAAm-cl-GG-g-P(AA-*co*-NIPAAm), MBAAm-cross-linked AA-*co*-NIPAAm grafted GG; MBAAm-cl-GG-g-P(AA-*co*-NIPAAm-*co*-NIPAAmPA), MBAAm-cross-linked AA-*co*-NIPAAm-*co*-NIPAAmPA grafted GG; MBAAm-cl-GG-g-P(AAm-*co*-AMPS), MBAAm-cross-linked AAm-*co*-AMPS grafted GG; MBAAm-cl-GG-g-P(AAm-*co*-AGA)/Ag NPs, MBAAm-cross-linked AAm-*co*-AGA grafted GG/Ag NPs nanocomposite; MBAAm-cl-GG-g-PAMPS, MBAAm-cross-linked AMPS grafted GG; MBAAm-cl-P(AA-*co*-MMA), MBAAm cross-linked copolymer of acrylic acid and methyl methacrylate; MBAAm-cl-GG-SL/Fe^0, MBAAm-cross-linked GG-SL/Fe^0; MBAAm-cl-GG/SLS-g-PAA, MBAAm-cross-linked AA grafted GG/SLS; MBAAm, Fe^{3+}-cl-CMGG-g-PAA, MBAAm, Fe^{3+}-cross-linked CMGG-g-PAA; MCA, monochloroacetic acid; MDCK, Madin-Darby canine kidney; MeO, methyl orange; MeOH, methanol; *meta*-BPDM, *meta*-benziporphodimethene; MG, malachite green; MGG, methylated GG; MGG/nanoclays, MGG/nanoclays nanocomposite; MIL, Materials of Institute Lavoisier; MnO_2, manganese dioxide; MnO_4^-, permanganate(VII); MnO_4^{2-}, manganate(VI); MS, degree of molar substitution; MW, microwave; $NaBH_4$, sodium borohydride; $NaBH_4$-cl-GG-g-PAGA/Ag NPs, $NaBH_4$-cross-linked GG-g-PAGA/Ag NPs; $NaBH_4$-cl-GG/CNC/Pd NPs, $NaBH_4$-cross-linked GG/CNC/Pd NPs nanocomposite; $NaBH_4$-cl-GG-PVA/Ag NPs, $NaBH_4$-cross-linked GG-PVA/Ag NPs; $NaBO_2$, sodium metaborate; $Na_2B_4O_7$, anhydrous sodium tetraborate; $Na_2B_4O_7$·$5H_2O$, sodium tetraborate pentahydrate; $Na_2B_4O_7$·$10H_2O$ or $Na_2[B_4O_5(OH)_4]$·$8H_2O$, sodium tetraborate decahydrate; NaBr, sodium bromide; $NaClO_2$, sodium chlorite; $NaIO_4$, sodium periodate; NaOCl, sodium hypochlorite; NaOH, sodium hydroxide; $Na_2S_2O_8$ or SPS, sodium persulfate; NBA, 4-bromo-1,8-naphthalic anhydride; -NCO, isocyanate; NHS, N-hydroxysuccinimide; -NH_2, amino; NH_2-C_2H_4-NH_2, ethylenediamine; $(NH_4)_2$[Ce $(NO_3)_6$] or CAN, ceric(IV) ammonium nitrate; $(NH_4)_2S_2O_8$ or APS, ammonium persulfate; NIPAAm, *N*-isopropylacrylamide; NIPAAmPA, 3-(*N*-isopropylacrylamido) propanoic acid; NTP, non-thermal plasma; OCGG, oxidized CGG; OGG, oxidized guar gum; -OH, hydroxyl; OH-, hydroxide; OlGG, oleic guar gum; O/N, overnight; O-O, peroxide bond; OSA, *n*-octenyl succinic anhydride; P(AA-*co*-AN), poly(acrylic acid)-P(AA-*co*-acrylonitrile); PAAm, polyacrylamide; *P. aeruginosa, Pseudomonas aeruginosa*; PBA, phenylboronic acid; PBA-cl-HPGG-g-P(AAm-*co*-AAPBA), PBA-cross-linked AAm-*co*-AAPBA grafted HPGG; PBS, phosphate-buffered saline; PCL, poly(ε-caprolactone); PCLD, poly(ε-caprolactone) diol; PDA, polydopamine; PDA-rGO, polydopamine-coated reduced graphene oxide; PDA-STMS/GA, PDA-coated GA-loaded STMS; PDI, polydispersity index; pDNA, EGFP-N1 plasmid DNA; Pd NPs, Pd nanoparticles; PEG, polyethylene glycol; PHGG, partially hydrolyzed GG; Pip, piperine; PO, propylene oxide; P_2O_5, phosphorus pentoxide; $POCl_3$, phosphorus oxychloride; PPE, pomegranate peel extract; PVA, polyvinyl alcohol; PVP, polyvinylpyrrolidone; py, pyridine; QGG, quaternized GG; RB19, reactive blue 19; RDA, ricinoleic dimer acid; RhB, rhodamine B; ROP, ring-opening polymerization; rt, room temperature; s, second; SA, succinic acid; SAAL, salicylaldehyde; *S. aureus, Staphylococcus aureus*; SAP, self-assembly peptide; SAL, sodium alginate; SBS, sodium bisulfite; SF, silk fibroin; SGP, step-growth polymerization; SH, salicylhydrazine; -NH_2, amino; NH_2-C_2H_4-NH_2, ethylenediamine; $(NH_4)_2$[Ce simulated intestinal fluid; SiO_2, silicon dioxide; $SiO_2@Au$, SiO_2 core-Au shell; SL, soya lecithin; SLS, sodium lignosulfonate; SMA, stearyl methacrylate; S_N, nucleophilic substitution; S_N2, bimolecular nucleophilic substitution; Sn(C≡CPh)4 or SnAK, tetra(phenylethynyl)tin; SO_3, sulfur trioxide; $SO_3^{\bullet-}$, S-centered sulfite radical anions; $SO_4^{\bullet-}$, sulfate radical anions; SO_4^{2-}, sulfate; $SO_5^{\bullet-}$, peroxymonosulfate radical anions; $S_2O_5^{\bullet-}$, S-centered metabisulfite radical anions; $S_2O_5^{2-}$, metabisulfite; $S_2O_8^{2-}$, peroxydisulfate or persulfate; SSD, silver sulfadiazine; STMP, sodium trimetaphosphate; STMP-cl-GG/orange oil, STMP-cross-linked orange oil-incorporated GG/orange oil; STMS, stellate mesoporous silica; STPP, sodium tripolyphosphate; TBHP, *tert*-butyl hydroperoxide; TEGDA, tetra(ethyleneglycol)diacrylate; TEGDA-cl-GG-g-PAAm, TEGDA-cross-linked GG-g-PAAm; TEMPO, 2,2,6,6-tetramethylpiperidine-1-oxyl radical; TEMPO+, 2,2,6,6-tetramethylpiperidine-1-oxoammonium; TEMPOH, 1-Hydroxy-2,2,6,6-tetramethylpiperidine; TEOS, tetraethyl orthosilicate; TEOS-cl-CMGG-CS, TEOS-cross-linked CMGG-CS; TEOS-cl-CMGG-CS@, NTP-treated TEOS-cross-linked CMGG-CS; TEOS-cl-CMGG-CS@Ar, Ar NTP-treated TEOS-cross-linked CMGG-CS; TEOS-cl-CMGG-CS@O_2, O_2 NTP-treated TEOS-cross-linked CMGG-CS; TEOS-cl-CMGG-CS@O_2+Ar, O_2 and Ar NTP-treated TEOS-cross-linked CMGG-CS; TEOS-cl-CMGG-PVA, TEOS-cross-linked CMGG-PVA; TEOS-cl-CMGG-PVA@/chrysin, chrysin-encapsulated NTP-treated TEOS-cl-CMGG-PVA; TEOS-cl-GG-g-ARX, TEOS-cross-linked GG-ARX; TEOS-cl-GG-ARX/SSD, SSD-encapsulated TEOS-cl-GG-ARX; TEOS-cl-GG-CS-PEG/CED, TEOS-cross-linked CED-encapsulated GG-CS-PEG/CED; TEOS-cl-GG-CS-PVA, TEOS-cross-linked GG-CS-PVA; TEOS-cl-GG-CS-PVA/paracetamol, paracetamol-loaded TEOS-cl-GG-CS-PVA; TEOS-cl-GG-g-PNIPAAm, TEOS-cross-linked NIPAAm grafted GG; TEOS-cl-GG-g-PNIPAAm/β-CD/FU, β-CD/FU-loaded TEOS-cl-GG-g-PNIPAAm; THF, tetrahydrofuran; TMEDA or TEMED, N,N,N',N'-tetramethylethylenediamine; TNBC, triple negative breast cancer; TOC, total organic carbon; TQ, thymoquinone; TsOH, tosylic acid; UO_2^{2+}, uranyl ions; v/v, volume by volume; wt%, weight percentage; w/v, weight by volume; w/w, weight by weight; Zr^{4+}-cl-HPGG, Zr^{4+}-cross-linked HPGG.
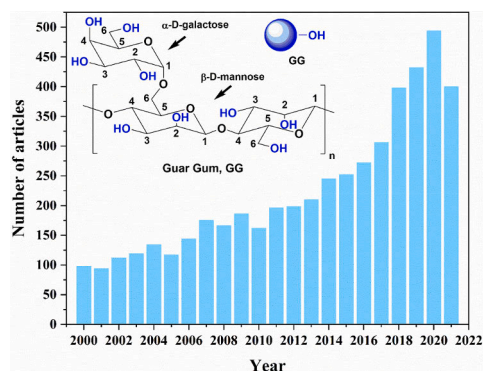
Fig. 1. Published articles per year based on "guar gum" keyword from Web of Science search engine on June 5, 2022 and chemical structure of GG repeating unit.

chemical synthetic techniques [9–21]. GG is obtained naturally from seeds of cluster bean *(Cyamopsis tetragonolobus)*. Endosperm of guar seed contains more than 80 % of non-ionic galactomannan polysaccharide, as well as some amount of water, protein, ash, and fat [22]. GG has been widely used as stabilizers for soil treatment,[23–25] concrete additives

[26], corrosion inhibitors in metal protection [27,28], promoters for tetrahydrofuran (THF) hydrate formation [29], inhibitors for methane hydrate formation [30,31], precursors in carbon dot synthesis and single-atom catalysts [32,33], binders for Li-ion batteries [34–36], electrolytes in zinc-ion batteries [37,38], perovskite-based zinc-air batteries [39], and dye-sensitized solar cells [40], biomaterials in food industry [41–47], bio-ink in 3D printing [48], as well as components in photocatalysts [49–51], wound dressing, healing and drug delivery [52–60]. Besides numerous fascinating properties of pristine GG, in order to extend its applicability and overcome remaining limitations, namely, uncontrollable swelling, susceptibility to bacterial contamination and rapid biodegradation, etc. further studies on chemical modification of GG are highly motivated [10].

Herein, latest approaches in the chemical functionalization and potential applications of GG and its derivatives are discussed and highlighted. Even though polymer blending offers great simplicity to modify properties of materials including GG [61–63], this approach, however, is not covered in detail here since direct chemical modifications of GG are rarely performed. In addition, partial hydrolysis of native GG can also be carried out to depolymerize the polysaccharide chain, hence, decreasing the molecular weight and viscosity of GG [64,65]. In this review, chemical modifications on partially hydrolyzed GG (PHGG) or GG hydrolysate (GGH) are also covered and treated equivalently to GG due to their similar repeating units in the polymer structure.
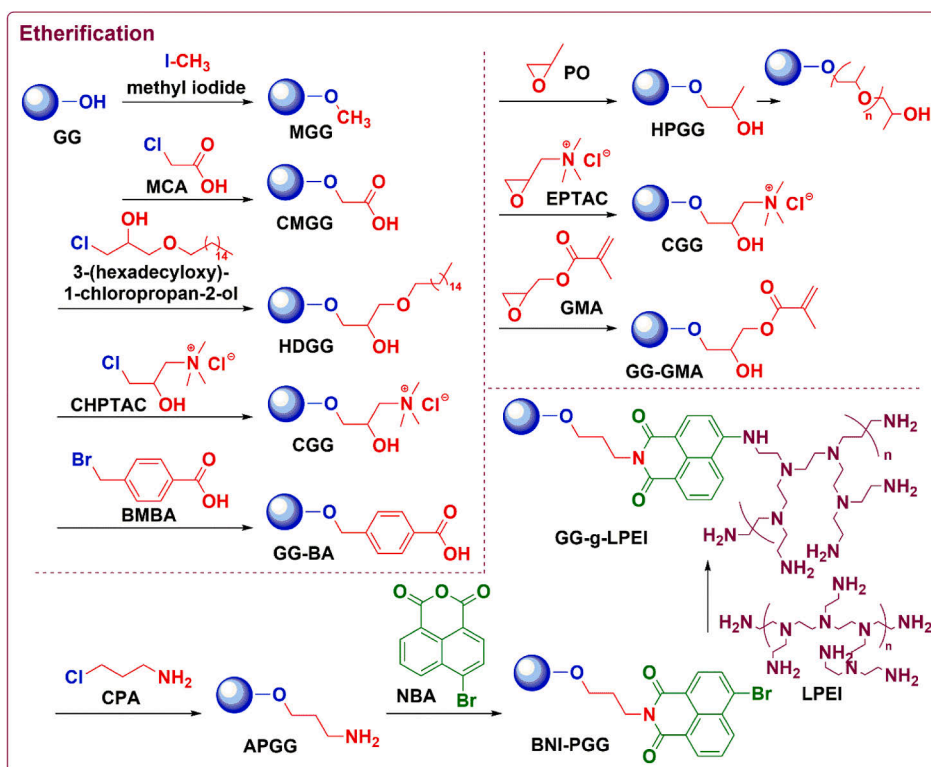
Fig. 2. Etherification of GG by different alkylating agents.

Table 1
Reaction conditions for graft polymerization of GG and its derivatives.

Entry	Reaction condition								Product			Ref.
	Polymer	Monomer	Cross-linker	Initiator	Atm[a]	Solvent	T [°C]	t[b]	Abbreviation	GE	GY [%]	
Acrylic acid (AA) monomer												
54	GG	AA	Ala	APS	N₂	H₂O	rt	15 m	Ala-cl-GG-g-PAA	N/A	N/A	[256]
55	GG	AA	MBAAm	APS	N/A	H₂O	30	N/A	MBAAm-cl-GG-g-PAA	N/A	N/A	[258]
56	GG	AA	MBAAm	APS	N₂	H₂O	60–70	3 h	MBAAm-cl-GG-g-PAA	N/A	N/A	[259]
57	GG	AA	None	APS	N/A	H₂O	50	N/A	GG-g-PAA	N/A	N/A	[260]
58	GG, SLS	AA	MBAAm	APS	N/A	H₂O	60–80	1 h	MBAAm-cl-GG/SLS-g-PAA	N/A	N/A	[261]
59	GG	AA, AN	MBAAm	MW	N/A	H₂O	N/A	90 s	MBAAm-cl-GG-g-P(AA-co-AN)	N/A	50–86.6	[262]
60	GG	AA, AAm	MBAAm	APS	N₂	H₂O	68–70	3–4 h	MBAAm-cl-GG-g-P(AA-co-AAm)	N/A	N/A	[263]
61	GG	AA, AAm	None	MW	N/A	H₂O	N/A	120 s	GG-g-P(AA-co-AAm)	N/A	N/A	[264]
62	GG	AA, NIPAAm	MBAAm	KPS, SBS	amb	H₂O	25	34 m	MBAAm-cl-GG-g-P(AA-co-NIPAAm), MBAAm-cl-GG-g-P(AA-co-NIPAAm-co-NIPAAmPA)	N/A	76	[265]
2	CMGG	AA and/or AAm	MBAAm	KPS	N/A	H₂O	60–65	2.5 h	MBAAm-cl-CMGG-g-PAA, MBAAm-cl-CMGG-g-PAAm, MBAAm-cl-CMGG-g-P(AA-co-AAm)	N/A	N/A	[82]
4	CMGG	AA	MBAAm, Fe³⁺	KPS, TEMED	N₂	H₂O	50	12 h	MBAAm, Fe³⁺-cl-CMGG-g-PAA	N/A	N/A	[84]
15	CGG	AA, SMA	CTAB	APS	inert	H₂O	60	7 h	CTAB-cl-CGG-g-P(AA-co-SMA)	N/A	N/A	[121]
20	GG-GMA	AA	DMAAm	SPS	N/A	H₂O	50, rt	30 m	GG-GMA-g-P(AA-co-DMAAm)	N/A	N/A	[132]
29	AGG	AA, KSPA	MBAAm	APS	N/A	H₂O	60	3 h	MBAAm-cl-AGG-g-P(AA-co-KSPA)	N/A	N/A	[150]
Acrylamide (AAm) monomer												
63	GG	AAm	TEGDA	KPS	N₂	H₂O	65	4 h	TEGDA-cl-GG-g-PAAm	N/A	91	[269]
64	GG	AAm	Borax	CAN, MW	N/A	H₂O	N/A	30 s × 3	borax-cl-GG-g-PAAm	79.5	795.6	[270]
65	GG	AAm, AMPS	MBAAm	KPS	N₂	H₂O	70	3 h	MBAAm-cl-GG-g-P(AAm-co-AMPS)	N/A	N/A	[271]
66	GG	AAm, AGA	MBAAm	APS	N/A	H₂O	60	10 m	MBAAm-cl-GG-g-P(AAm-co-AGA)	N/A	N/A	[272]
3	CMGG	AAm	MBAAm	KPS	N/A	H₂O, acetone	60	N/A	MBAAm-cl-CMGG-g-PAAm	N/A	N/A	[83]
9	HPGG	AAm	AAPBA	I2959 (UV at 360 nm)	N/A	H₂O	rt	3 h	PBA-cl-HPGG-g-P(AAm-co-AAPBA)	N/A	N/A	[97]
Other monomers												
67	GG	NIPAAm	TEOS	APS, TEMED	N₂	H₂O	rt	N/A	TEOS-cl-GG-g-PNIPAAm	N/A	N/A	[273]
68	GG	AGA	NaBH₄	APS	N₂	H₂O	60	2 h	NaBH₄-cl-GG-g-PAGA	N/A	N/A	[274]
69	GG	AMPS	MBAAm	KPS	N₂	H₂O	70	3 h	MBAAm-cl-GG-g-PAMPS	N/A	N/A	[276]
70	GG	EA	None	KPS, H₂AA	N/A	H₂O	35	1 h	GG-g-PEA	N/A	N/A	[277]
71	GG	HEMA	None	CAN, MW	amb	H₂O		40 s × 3	GG-g-PHEMA	114.22	1142	[278]

[a] Atm: atmosphere, amb: ambient, N/A: not available.
[b] m: minute.

2. Chemical structure and properties of GG

Galactomannan polysaccharide of GG is composed of mannose (Man) backbones and galactose (Gal) side chains with an average Man: Gal ratio varying between 1.8:1 and 2:1. Natural GG exhibits a significantly high molecular weight, which can be found up to millions of Da [66]. While Man moieties are linked via β-1,4-glycosidc bonds to establish the polymer backbone, Gal side chains are connected to the Man backbones by α-1,6-glycosidic bonds (insert of Fig. 1). Due to the unique structure of galactomannan chain and numerous remaining hydroxyl (-OH) functional groups, hydrophilic GG has high solubility even in cold water even though it is least hygroscopic among different types of gums [67–69]. Moreover, because of the rich chemistry of these -OH functional groups, further chemical functionalization and derivatization of original GG can be easily performed [70–72]. On an average, each GG monomer contains three anhydroglucose units (AGU), while each AGU contains approximately three -OH groups, and therefore, the degree of derivatization or substitution (DS) for each AGU might be up to three. Additionally, the nucleophilicity of these -OH groups vary, i.e., less bulky primary -OH groups are more nucleophilic than secondary -OH groups [73].

3. Chemical functionalization and potential applications of GG and its derivatives

3.1. Nucleophilic reactions

3.1.1. Etherification (GG-O-)

Etherification is one of the most common synthetic routes to chemically modify GG due to its synthetic simplicity. Typically, GG is activated in N₂-purged alkaline solutions, followed by an addition of electrophilic alkylating agents to carry out nucleophilic substitution (S_N) reactions. A summary of reported etherification reactions on GG can be found in Fig. 2 and Table 2.

3.1.1.1. Carboxymethyl GG (CMGG) and its derivatives.
Carboxymethylation of GG has been reported via S_N of GG with monochloroacetic acid (MCA) or sodium chloroacetate in aqueous solutions [70,74], lithium chloride/dimethylsulfoxide (LiCl/DMSO) solvent system [75], or using dry method.[76] Carboxymethyl GG (CMGG) products can be found as valuable starting materials to develop novel hydrogels and coacervates for drug delivery [77–80].

In the recent past, Dalei et al. reported a similar procedure for the carboxymethylation of GG using MCA in a solvent mixture of isopropyl

Table 2
Reaction conditions for chemical modifications of GG and its derivatives.

Entry	Reaction	Reaction condition						Product			Ref.
		Reactant	Catalyst	Atm	Solvent	T [°C]	t	Abbreviation	DS	Yield [%]	
Nucleophilic reactions											
Etherfication											
Carboxymethyl GG (CMGG) and its derivatives											
1	Carboxymethylation	(1) GG, NaOH	None	N/A	IPA, H_2O	rt	2 h	CMGG	N/A	N/A	[81]
		(2) MCA	None	N/A	IPA, H_2O	60	8 h		N/A	N/A	
	Cross-linking	CMGG, CS, TEOS	None	N/A	H_2O	rt	brief	TEOS-cl-CMGG-CS	–	N/A	
	NTP treatment	CMGG-TEOS-cl-CS, O_2 and/or Ar	None	0.5 mbar	None	N/A	30 s	TEOS-cl-CMGG-CS@O_2, TEOS-cl-CMGG-CS@Ar, TEOS-cl-CMGG-CS@O_2 + Ar	–	N/A	
	Drug encapsulation	CMGG-TEOS-cl-CS or CMGG-TEOS-cl-CS@, diclofenac sodium	None	N/A (dark)	EtOH	N/A	48 h	–	–	N/A	
2	Carboxymethylation	(1) GG, NaOH	None	inert	H_2O	rt	15 m	CMGG	N/A	N/A	[82]
		(2) MCA	None	inert	H_2O	50	4 h		N/A	N/A	
	FRGP and cross-linking	(1) CMGG, NaOH, AA and/or AAm, KPS	None	N/A	H_2O	60	30 m	MBAAm-cl-CMGG-g-PAA, MBAAm-cl-CMGG-g-PAAm, MBAAm-cl-CMGG-g-P(AA-co-AAm)	–	N/A	
		(2) MBAAm	None	N/A	H_2O	65	2 h		–	N/A	
3	FRGP and cross-linking	CMGG, AAm, MBAAm, meta-BPDM, KPS	None	N/A	H_2O, acetone	60	N/A	MBAAm-cl-CMGG-g-PAAm/meta-BPDM	–	N/A	[83]
4	FRGP and cross-linking	CMGG, AA, MBAAm, $FeCl_3 \cdot 6H_2O$, KPS, TEMED	None	N_2	H_2O	50	12 h	MBAAm, Fe^{3+}-cl-CMGG-g-PAA	–	N/A	[84]
5	Cross-linking	CMGG, CA	None	N/A	None	140	5 m	CA-cl-CMGG	–	N/A	[85]
6	Cross-linking	CMGG, PVA, TEOS	None	N/A	H_2O	N/A	brief	TEOS-cl-CMGG-PVA	–	N/A	[86]
	NTP treatment	TEOS-cl-CMGG-PVA, N_2 or N_2 + NH_3	None	0.5 mbar	None	N/A	30 s	TEOS-cl-CMGG-PVA@N_2, TEOS-cl-CMGG-PVA@N_2 + NH_3	–	N/A	
	Drug encapsulation	TEOS-cl-CMGG-PVA@, chrysin	None	N/A	EtOH	37	24 h	TEOS-cl-CMGG-PVA@/chrysin	–	N/A	
Hydroxypropyl GG (HPGG) and its derivatives											
7	Hydroxypropylation	(1) GG, NaOH	None	N_2	H_2O	rt	0.5 h	HPGG	0–1.2[c]	N/A	[95]
		(2) PO	None	N_2	H_2O	rt	0–30 h				
	Cross-linking	(1) HPGG, $Na_2S_2O_3$, Na_2CO_3	None	N/A	H_2O	25	N/A	boric acid-cl-HPGG, Zr^{4+}-cl-HPGG	–	N/A	
		(2) H_3BO_3 or sodium zirconium lactate	None	N/A	H_2O	25	N/A				
8	Hydroxypropylation	(1) GG, NaOH	None	N/A	H_2O	25	15 m	HDGG	N/A	N/A	[96]
		(2) 3-(hexadecyloxy)-1-chloropropan-2-ol (THF)	None	N/A	H_2O, THF	50	24 h		N/A	N/A	
	Drug encapsulation	HDGG, AmB (DMSO)	None	N/A (dark)	H_2O, DMSO	25	16 h	HDGG/AmB	–	92	
	Drug encapsulation	HDGG, AmB, Pip (DMSO)	None	N/A (dark)	H_2O, DMSO	25	16 h	HDGG/AmB/Pip	–	54	
	Drug encapsulation and coating	HDGG, AmB (DMSO), Eu	None	N/A (dark)	H_2O, DMSO	25	16 h	Eu-coated-HDGG/AmB	–	87	
	Drug encapsulation and coating	HDGG, AmB, Pip (DMSO), Eu	None	N/A (dark)	H_2O, DMSO	25	16 h	Eu-coated-HDGG/AmB/Pip	–	80	
9	FRGP and cross-linking	HPGG, AAm, AAPBA	I2959 (UV at 360 nm)	N/A	H_2O	rt	3 h	PBA-cl-HPGG-g-P(AAm-co-AAPBA)	–	N/A	[97]

(continued on next page)

Table 2 (*continued*)

Entry	Reaction	Reaction condition						Product			Ref.
		Reactant	Catalyst	Atm	Solvent	T	t	Abbreviation	DS	Yield [%]	
						[°C]					
10	Cross-linking	(1) HPGG, PDA-rGO, FeCl$_3$·6H$_2$O	None	N/A	H$_2$O, glycerol	rt	N/A	borax, Fe^{3+}-cl-HPGG-PDA-rGO	–	N/A	[98]
		(2) borax	None	N/A	H$_2$O	45	N/A		–	N/A	
Methylated GG (MGG) and its derivatives											
11	Methylation	GG, NaOH, CH$_3$I	None	N$_2$	H$_2$O	25	2.5	MGG	0.4	94	[100]
12	Methylation	GG, NaOH, CH$_3$I	None	N$_2$	H$_2$O	25	2.5	MGG	0.4	94	[101]
	Nanocomposite	MGG, nanoclays, glycerol	None	N/A	H$_2$O	N/A	O/N	MGG/nanoclays		N/A	
Cationic GG (CGG) and its derivatives											
13	Quaternization	(1) GG, NaOH	None	N/A	H$_2$O, EtOH	N/A	N/A	CGG	0.158	N/A	[118]
		(2) EPTAC	None	N/A	H$_2$O, EtOH	55	3 h				
14	Quaternization	(1) GG, NaOH	None	N/A	H$_2$O, MeOH	rt	15 *m*	CGG	0.49	N/A	[119]
		(2)CHPTAC	None	N/A	H$_2$O, MeOH	30	2 h				
15	FRGP and cross-linking	CGG, AA, SMA, CTAB, APS	None	inert	H$_2$O	60	7 h	CTAB-cl-CGG-g-P(AA-*co*-SMA)	–	N/A	[121]
16	Partial oxidation and cross-linking	CGG, CS, NaIO$_4$	None	N/A (dark)	H$_2$O	rt	24 h	cl-OCGG-CS	–	N/A	[122]
17	Quaternization	GG, CHPTAC, NaOH	None	N/A	H$_2$O	50	3 h	CGG	0.21	N/A	[123]
	Partial oxidation	CGG, NaIO$_4$	None	N/A (dark)	H$_2$O	rt	24 h	OCGG	4.8[d]	N/A	
	Cross-linking	OCGG, CMCS	None	N/A	H$_2$O	rt	N/A	cl-OCGG-CMCS		N/A	
Other GG derivatives											
18	Nucleophilic substitution	(1) GG, NaOH	None	N/A	H$_2$O, IPA	50	1 h	APGG	N/A	N/A	[130]
		(2) CPA(IPA)	None	N/A	H$_2$O, IPA	50	4.5 h				
	Condensation	APGG, NBA	None	N$_2$	DMSO	80	3 h	BNI-PGG	N/A	N/A	
	Nucleophilic substitution	BNI-PGG, LPEI	None	N$_2$	H$_2$O	80	3 h	GG-g-LPEI	42.9–56.6 %[e]	N/A	
	Complex coacervation	GG-g-LPEI (acetate buffer), pDNA (sodium sulfate solution)	None	N/A	H$_2$O	55	10 *m*	GG-g-LPEI/pDNA		N/A	
19	Nucleophilic substitution	(1) GG, NaOH	None	N$_2$	H$_2$O	rt	30 *m*	GG-BA	0.164	83.1	[131]
		(2) 4-(bromomethyl) benzoic acid	None	N$_2$	H$_2$O	rt	O/N				
20	Nucleophilic substitution	GG, NaOH, GMA	None	N/A	H$_2$O	60	24 h	GG-GMA	N/A	N/A	[132]
	FRGP and cross-linking	GG-GMA, sodium acrylate, DMAAm, SPS	None	N/A	H$_2$O	50, rt	30 *m*	GG-GMA-g-P(AA-*co*-DMAAm)	N/A	N/A	
	Drug loading	GG-GMA-g-P(AA-*co*-DMAAm), HCS	None	N/A	H$_2$O	rt	20 h	GG-GMA-g-P(AA-*co*-DMAAm)/HCS	–	N/A	
Esterification											
21	Esterification (microwave)	GG, DA, NaOH, DBSA	TsOH	N/A	None (Solvent free)	N/A	N/A	GG-RDA	N/A	N/A	[136,137]
	Cross-linking and drug loading	GG-RDA, PVA, GA, glycerol, GS or AX	HCl	N/A	H$_2$O	60	5 h	GA-cl-GG-RDA-PVA/GS or AX	–	N/A	
22	Steglich esterification	GG, FA, DCC	DMAP	N/A (dark)	DMSO	rt	48 h	FA-GG	N/A	N/A	[138]
	Esterification	FA-GG, succinic anhydride	DMAP	N/A	H$_2$O	rt	24 h	FA-GG-SA	N/A	N/A	
	Condensation	(1) FITC-SiO$_2$@Au, LCME	None	N/A	DMSO	rt	12 h	FA-GG-SA-FITC-SiO$_2$@Au-DOX	N/A	N/A	
		(2) FA-GG-SA, EDC	NHS	N/A	DMSO	rt	12 h				
		(3) hydrazine	None	N/A	DMSO	rt	3 h				
		(4) DOX	None	N/A	DMSO	rt	24 h				
23	Esterification	GGH, DDSA	NaHCO$_3$	N/A	H$_2$O, EtOH	45	2 h	GGH-DDSA	0.029	N/A	[140]
	Esterification	GGH, OSA	NaHCO$_3$	N/A	H$_2$O, EtOH	85	2 h	GGH-OSA	0.07	N/A	
24	Esterification	GG, MA	Et$_3$N	N/A	DCM	40	3–4 h	GG-MA	N/A	N/A	[141]
25	Esterification	GG, MA	DMAP	N/A	ACN	25	12 h	GG-MA	N/A	N/A	[142]

Table 2 (*continued*)

Entry	Reaction	Reactant	Catalyst	Atm	Solvent	T [°C]	t	Abbreviation	DS	Yield [%]	Ref.
	aza-Michael addition	GG-MA, CS-g-PCL	None	N/A	H$_2$O	60	24 h	cl-GG-MA-CS-g-PCL	N/A	N/A	
	Drug encapsulation	(1) GG-MA/CS-g-PCL, rifampicin	None	N/A	H$_2$O, DMSO	rt	30 *m*	cl-GG-MA-CS-g-PCL/ rifampicin	–	N/A	
		(2) ultrasonication	None	N/A	H$_2$O, DMSO	~ 0	5 *m*				
26	Esterification	GG, oleic/ linoleic/ erucic acyl chlorides, NaOH	None	N/A	acetone	50	12 h	OGG, LGG, EGG	0.01–0.08	90.2–94.4	[143]
27	Esterification	GG, cinnamoyl chloride	DMAP	N$_2$	LiCl/ DMSO	30	4 h	GG-C	0.79–1.40	N/A	[144]
	Ouzo nanoprecipitation (nanonization)	GG-C (DMSO)	None	N/A	H$_2$O, DMSO	rt	30 h	GG-C-N	–	N/A	
28	Esterification	GG, 2-(1H-indol-3-yl)acetyl chloride	DMAP	N$_2$	LiCl/ DMSO	30	3 h	GG-IA	0.61	N/A	[149]
	Cross-linking and solvent-casting	GG-IA, keratin, GA, glycerol	None	inert	H$_2$O	42	18 h	GA-cl-GG-IA-keratin	–	N/A	
29	Esterification	(1) GG, NaOH	None	N/A	H$_2$O	N/A	N/A	AGG	N/A	N/A	[150]
		(2)acryloyl chloride	None	N/A	N/A	ice	N/A				
	FRGP and cross-linking	AGG, AA, KSPA, MBAAm, APS	None	N/A	H$_2$O	60	3 h	MBAAm-cl-AGG-g-P(AA-*co*-KSPA)	–	N/A	
	Drug loading	MBAAm-cl-AGG-g-P(AA-*co*-KSPA), GMS	None	N/A	H$_2$O	37	8 h	MBAAm-cl-AGG-g-P(AA-*co*-KSPA)/GMS	–	N/A	
Xanthation											
30	Xanthation	(1) GG, NaOH	None	N$_2$	H$_2$O	rt	30 *m*	GG-X	0.132	87.23	[161]
		(2)CS$_2$	None	N$_2$	H$_2$O	rt	2.5 h				
	Surfactant-assisted precipitation	GG-X, CuCl$_2$, Na$_2$S	None	N$_2$	H$_2$O	85	2 h	GG-X/CuS	–	N/A	
Silanization/ Silylation											
31	Silylation	GG, APTES	None	N/A	toluene	100	48 h	GG-APS	N/A	N/A	[169]
	Schiff-base condensation	GG-APS, FFR	None	N/A	MeOH	reflux	72 h	GG-APS-FFR	N/A	N/A	
	Metal complexation	GG-APS-FFR, Na$_2$PdCl$_4$	None	N/A	H$_2$O	rt	5 h	GG-APS-FFR-Pd	–	N/A	
32	Silylation	GG, APTMS	None	N$_2$	H$_2$O	100	24 h	GG-APS	N/A	N/A	[170]
	Schiff-base condensation	GG-APS, SA	None	N$_2$	EtOH	80	24 h	GG-APS-SA	N/A	N/A	
	Metal complexation	GG-APS-SA, Cu (OAc)$_2$	None	N/A	EtOH	80	24 h	GG-APS-SA-Cu	–	N/A	
Phosphorylation											
33	Phosphorylation, metal dispersion and cross-linking	GG, SL, DCC, Fe(0), MBAAm	None	N/A	CHCl$_3$	60	3 h	MBAAm-cl-GG-SL/Fe^0	N/A	78	[178]
34	Phosphorylation	(1) GG, urea	None	N/A	DMF	110	1 h	GG-P	N/A	95	[180]
		(2) H$_3$PO$_4$	None	N/A	DMF	150	3 h				
	Cross-linking	(1) GG-P, CS, Fe$_3$O$_4$	None	N/A	H$_2$O	50	1 h	ECH-cl-GG-P-CS/Fe$_3$O$_4$	–	N/A	
		(2) ECH(dioxane)	None	N/A	H$_2$O, 1,4-dioxane	60	3 h				
Sulfation											
35	Sulfation (O'Neill method)	GG or GGH, py, chlorosulfonic acid	None	N/A	HCHO	0 / 40	1 h / 6 h	GG-S-O, GGH-S-O	1.26, 1.21	N/A	[184]
	Sulfation (Larm method)	GG or GGH, SO$_3$·py	None	N/A	DMF	25	6 h	GG-S-L, GGH-S-L	0.38, 1.91	N/A	
36	Sulfation	GG, chlorosulfonic acid	None	N/A	1,4-dioxane	60	2.9 h	GG-S	0.91	N/A	[185]
37	Sulfation	GG, urea, sulfamic acid	None	N/A	1,4-dioxane	80	3 h	GG-S	0.78	N/A	[186]
Amination											
38	Amination	(1) GG, ethylenediamine	None	N/A	H$_2$O	rt	O/N	GG-N	N/A	N/A	[190]
		(2) HCl	None	N/A	H$_2$O	rt	30 *m*				
	Cross-linking	GG-N, GO, borax	None	N/A	H$_2$O	rt	3 h	borax-cl-GG-*N*-GO	–	N/A	

Partial oxidation
TEMPO-mediated oxidation

Table 2 (*continued*)

Entry	Reaction	Reaction condition						Product			Ref.
		Reactant	Catalyst	Atm	Solvent	T [°C]	t	Abbreviation	DS	Yield [%]	
39	TEMPO oxidation	GG, NaOCl	NaBr, TEMPO	N_2	H_2O	3	N/A	OGG	1.2[d]	71	[199]
40	Enzymatic TEMPO oxidation and self-cross-linking	GG, O_2	Laccase, TEMPO	N/A	H_2O	35 rt	3 h 24 h	OGG	N/A	N/A	[200]
Periodate-mediated oxidation											
41	Periodate oxidation and self-cross-linking	GG, $NaIO_4$	None	N/A	H_2O	N/A	N/A	cl-DAGG	N/A	N/A	[208]
42	Periodate oxidation, self-cross-linking and nanocomposite	GG, Ag NPs@MIL-100(Fe), $NaIO_4$	None	N/A	H_2O	rt	N/A	cl-DAGG/Ag NPs@MIL-100 (Fe)	N/A	N/A	[209]
43	Periodate oxidation	GG, $NaIO_4$	None	N/A (dark)	H_2O	rt	6 h	DAGG	78 %	N/A	[210]
	Cross-linking and incorporation	DAGG, gelatin, GTE, ethylene glycol	None	N/A	H_2O	40 rt	45 *m* 24 h	cl-DAGG-gelatin/GTE	–	N/A	
44	Periodate oxidation	GG, $NaIO_4$	None	N/A (dark)	H_2O	rt	6 h	DAGG	72 %	N/A	[211]
	Cross-linking and incorporation	DAGG, CS, PPE	None	N/A	H_2O	rt	24 h	cl-DAGG-CS/PPE	–	N/A	
45	Periodate oxidation	GG, $NaIO_4$	None	N/A (dark)	H_2O	25	24 h	DAGG	56.3 %	N/A	[212]
	Cross-linking	DAGG, CMCS	None	N/A	H_2O	37	30 *m*	cl-DAGG-CMCS	–	N/A	
	Drug loading	cl-DAGG-CMCS, DOX	None	N/A	H_2O	N/A	48 h	cl-DAGG-CMCS/DOX	–	N/A	
46	Periodate oxidation	GG, $NaIO_4$	None	N/A (dark)	H_2O	N/A	2 h	DAGG	N/A	N/A	[213]
	Cross-linking and drug loading	DAGG, Cur-zein NPs, SF	None	N/A	H_2O	N/A	N/A	cl-DAGG-SF/Cur-zein NPs	–	N/A	
47	Periodate oxidation	GG, $NaIO_4$	None	N/A	H_2O	40	4 h	DAGG	N/A	N/A	[218]
	Schiff-base condensation	DAGG, GH	None	N/A	EtOH	45	72 h	DAGG-GH	N/A	N/A	
48	Schiff-base condensation	DAGG, SH	TsOH	N/A	EtOH	45	72 h	DAGG-SH	N/A	N/A	[219]
49	Periodate oxidation	GG, $NaIO_4$	None	N/A (dark)	H_2O	40	8 h	DAGG	67.6 %	N/A	[220]
	Nucleophilic acyl substitution	MBAAm-cl-P(AA-*co*-MMA), hydrazine-H_2O	None	N/A	H_2O	80	3 h	MBAAm-cl-P (AA-*co*-MMASH)	N/A	N/A	
	Cross-linking	DAGG, MBAAm-cl-P(AA-*co*-MMASH)	AcOH	N/A	EtOH	85	4 h	hydrazine-cl-DAGG MBAAm-cl-P(AA-*co*-MMA)	–	N/A	
50	Periodate oxidation	GG, $NaIO_4$	None	N/A (dark)	H_2O	40	24 h	DAGG	0.59–1.79[d] (30.12–60.63 %)	77.5	[221]
	Chlorite oxidation	DAGG, $NaClO_2$	AcOH	N/A	H_2O	30	48 h	DCGG	0.49–1.62[d]	82	
	Cross-linking	DCGG, $FeSO_4$,	None	N_2	H_2O	30	24 h	Fe^{2+}-cl-DCGG	None	64	
Graft polymerization											
51	SGP	GG, HTPB, IPDI, BDO	DBTDL	N_2	None	90	N/A	GG-PU	–	N/A	[225]
52	SGP	(1) PCLD, DMBA, IPDI	None	N_2	None	80	2 h	GG-PU	–	N/A	[226]
		(2) GG, TEA	None	N_2	None	80	1 h				
		(3) BD	None	N_2	None	80	1 h				
53	ROP	GG, ε-cL	SnAK	amb	None	rt 120	2 h 15–20 *m*	GG-g-PCL	–	92–94 %	[232,233]
54	FRGP	GG, AA, Ala, APS	None	N_2	H_2O	rt	15 *m*	Ala-cl-GG-g-PAA	–	N/A	[256]
	Drug loading	GG-g-PAA, levofloxacin (PBS)	None	N/A	H_2O	N/A	2 h	Ala-cl-GG-g-PAA/levofloxacin	–	65–75 %	
55	FRGP	GG, AA, MBAAm, APS	None	N/A	H_2O	30	N/A	MBAAm-cl-GG-g-PAA	–	N/A	[258]
	Drug loading	MBAAm-cl-GG-g-PAA, vitamin B6	None	N/A	H_2O	37	48 h	MBAAm-cl-GG-g-PAA/vitamin B6	–	94 %	
57	FRGP	GG, AA, APS	None	N/A	H_2O	50	N/A	GG-g-PAA	–	N/A	[260]
	Nanocomposite	GG-g-PAA, $AgNO_3$, $NaBH_4$, MBAAm	None	N/A	H_2O	N/A	10 *m*	MBAAm-cl-GG-g-PAA/Ag NPs	–	N/A	

Table 2 (*continued*)

Entry	Reaction	Reaction condition						Product			Ref.
		Reactant	Catalyst	Atm	Solvent	T [°C]	t	Abbreviation	DS	Yield [%]	
59	FRGP	GG, AA, AN, MBAAm, MW	None	N/A	H_2O	N/A	90 s	MBAAm-cl-GG-g-P(AA-*co*-AN)	–	50–86.6 %	[262]
	Drug encapsulation	MBAAm-cl-GG-g-P(AA-*co*-AN), TQ	None	N/A	H_2O	25	60 m	MBAAm-cl-GG-g-P(AA-*co*-AN)/TQ	–	N/A	
66	FRGP	GG, AAm, AGA, MBAAm, APS	None	N/A	H_2O	60	10 m	MBAAm-cl-GG-g-P(AAm-*co*-AGA)	–	N/A	[272]
	Incorporation	(1) MBAAm-cl-GG-g-P(AAm-*co*-AGA), AgNO$_3$	None	N/A	H_2O	25	24 h	MBAAm-cl-GG-g-P(AAm-*co*-AGA)/Ag NPs	–	N/A	
		(2) rhubarb extract	None	N/A (dark)	H_2O	25	12 h				
67	Hot-guess complexation	(1) β-CD, FU (1:1)	None	N/A	H_2O	N/A	24 h	β-CD/FU	–	N/A	[273]
		(2) freeze-drying	None	N/A	N/A	−55	48 h				
	FRGP, cross-linking and drug loading	(1) GG, NIPAAm, APS, TEMED	None	N_2	H_2O	rt	N/A	TEOS-cl-GG-g-PNIPAAm-FU or TEOS-cl-GG-g-PNIPAAm-β-CD/FU	–	N/A	
		(2) TEOS	None	N_2	H_2O	rt	24 h				
		(3) FU or β-CD/FU	None	N_2	H_2O	rt	brief				
68	FRGP	GG, AGA, APS	None	N_2	H_2O	60	2 h	GG-g-PAGA	–	N/A	[274]
	Nanocomposite and cross-linking	GG-g-PAGA, AgNO$_3$, NaBH$_4$	None	N/A	H_2O	N/A	N/A	NaBH$_4$-cl-GG-g-PAGA/Ag NPs	–	N/A	
71	FRGP	GG, HEMA, CAN (MW)	None	N/A	H_2O	N/A	40 s × 3	GG-g-PHEMA	–	N/A	[278]
	Drug loading	(1) GG-g-PHEMA, PVP, ASA	None	N/A	EtOH	50	N/A	GG-g-PHEMA/ASA	–	N/A	
		(2) magnesium stearate, SiO$_2$	None	N/A	None	N/A	N/A				

Cross-linking

B-O-

Entry	Reaction	Reactant	Catalyst	Atm	Solvent	T [°C]	t	Abbreviation	DS	Yield [%]	Ref.
72	Cross-linking	GG, peptide, borax	None	N/A	H_2O	rt	15 m	borax-cl-GG-SAP	–	N/A	[288]
73	Cross-linking	GG, GelG, borax	None	N/A	H_2O	80	1 h	borax-cl-GG-GelG	–	N/A	[289]
74	Cross-linking	GG, borax	None	N/A	H_2O	rt	4.5 h	borax-cl-GG	–	N/A	[290]
	Nanocomposite	KMnO$_4$, NaOH, borax-cl-GG	None	N/A	H_2O	rt	O/N	borax-cl-GG/MnO$_2$	–	N/A	
75	Nanocomposite	CNC, PdCl$_2$, NaBH$_4$	None	N/A	H_2O	rt	2 h	CNC/Pd NPs	–	N/A	[291]
	Cross-linking	GG, CNC/Pd, NaBH$_4$	None	N/A	H_2O	N/A	N/A	NaBH$_4$-cl-GG/CNC/Pd NPs	–	N/A	
76	Nanocomposite	Cur (DMSO), K$_2$CO$_3$, AgNO$_3$	None	N/A	H_2O	100	1 h	Cur-Ag NPs	–	N/A	[292]
	Cross-linking	GG, Cur-Ag NPs, NaOH, borax	None	N/A	H_2O	N/A	N/A	borax-cl-GG/Cur-Ag NPs	–	N/A	
77	Cross-linking	GG, PVA, AgNO$_3$, NaBH$_4$	None	N/A	H_2O	rt	48 h	NaBH$_4$-cl-GG-PVA/Ag NPs	–	N/A	[293]

C-O-

Entry	Reaction	Reactant	Catalyst	Atm	Solvent	T [°C]	t	Abbreviation	DS	Yield [%]	Ref.
78	Coprecipitation	(1) FeCl$_3$, FeCl$_2$, NH$_3$	None	N_2	H_2O	70	15 m	Fe$_3$O$_4$ NPs	–	N/A	[295]
		(2) CA	None	N_2	H_2O	70	1 h				
	Cross-linking	GG, Fe$_3$O$_4$ NPs, GA, NaOH	None	N_2	IPA	60	3 h	GA-cl-GG/Fe$_3$O$_4$ NPs	–	N/A	
79	Encapsulation	(1) STMS, GA	None	N/A	EtOH	rt	48 h	PDA-STMS/GA	–	N/A	[296]
		(2) DA-HCl, Tris·HCl	None	N/A	EtOH	rt	36 h				
	Cross-linking and nanocomposite	PDA-STMS/GA, Fe^{3+}, GG, SAL	None	N/A	H_2O	rt	2 h	GA, Fe^{3+}-cl-GG/SAL/DA-STMS/GA	–	N/A	
80	Cross-linking and nanocomposite	GG, activated C, glyoxal	None	N/A	H_2O	60	24 h	glyoxal-cl-GG/activated C	–	N/A	[297]

Si-O-

Entry	Reaction	Reactant	Catalyst	Atm	Solvent	T [°C]	t	Abbreviation	DS	Yield [%]	Ref.
81	Drug loading and cross-linking	GG, CS, PEG, CED, TEOS	None	N/A	H_2O	60	2 h	TEOS-cl-GG-CS-PEG/CED	–	N/A	[298]
82	Drug loading and cross-linking	GG, ARX, SSD (MeOH), TEOS	None	N/A	H_2O	60	3 h	TEOS-cl-GG-ARX/SSD	–	N/A	[299]

Table 2 (*continued*)

Entry	Reaction	Reaction condition						Product			Ref.
		Reactant	Catalyst	Atm	Solvent	T	t	Abbreviation	DS	Yield [%]	
						[°C]					
83	Drug loading and cross-linking	GG, CS, PVA, paracetamol, TEOS	None	N/A	H_2O	55	3 h	TEOS-cl-GG-CS-PVA/paracetamol	–	N/A	[300]
P-O-84	Cross-linking	GG, SL, glycerol, orange oil, NaOH, STMP	None	N/A	H_2O	N/A	2 h	STMP-cl-GG/orange oil	–	N/A	[301]

[c] degree of molar substitution (MS).
[d] mmol g^{-1}.
[e] degree of amination.

alcohol (IPA) and water [81]. The obtained CMGG product was then cross-linked with chitosan (CS) using tetraethyl orthosilicate (TEOS) to give TEOS-cl-CMGG-CS hydrogels. Due to the presence of carboxylic acid (-CO_2H) and amino (-NH_2) functional groups from CMGG and CS respectively, TEOS-cl-CMGG-CS hydrogels are responsive to a wide range of pH values, which plays an important role in swelling and drug delivery properties of hydrogels. Further surface modification of the hydrogels was then performed in a direct current glow discharge plasma reactor, using Ar, O_2 or a mixture of Ar and O_2 gases. The non-thermal plasma (NTP)-treated TEOS-cl-CMGG-CS (TEOS-cl-CMGG-CS@) hydrogels show a significant decrease in contact angles with water, hence, a significant increase in wettability of the hydrogel surface. The TEOS-cl-CMGG-CS@ hydrogels are promising candidates for the delivery of diclofenac sodium non-steroidal anti-inflammatory medication to human colon. They also possess good biocompatibility to human blood cells, as well as excellent biodegradability.

In order to study surface topography, roughness and swelling properties of CMGG by atomic force microscopy, Hasan and coworkers also used MCA in an aqueous alkaline solution to modify GG (see Table 1) [82]. Free-radical graft polymerization (FRGP) was then employed on CMGG with pH-responsive acrylic acid (AA) and/or thermo-responsive acrylamide (AAm) monomers, potassium persulfate (KPS) free-radical initiator, N,N'-methylenebis(acrylamide) (MBAAm) cross-linker to prepare MBAAm-cross-linked AA grafted CMGG (MBAAm-cl-CMGG-g-PAA), MBAAm-cross-linked AAm grafted CMGG (MBAAm-cl-CMGG-g-PAAm) and MBAAm-cross-linked AA-*co*-AAm grafted CMGG [MBAAm-cl-CMGG-g-P(AA-*co*-AAm)] hydrogels.

In addition, FRGP of CMGG with AAm monomer and MBAAm cross-linker was reported by Chauhan et al. to fabricate a hydrophilic polymeric platform with embedded hydrophobic *meta*-benzyporphodimethene (*meta*-BPDM), namely, MBAAm-cl-CMGG-g-PAAm/*meta*-BPDM [83]. The newly fabricated hydrogel can be employed in colorimetric sensing of aqueous d^{10}-metal ions such as Zn^{2+}, Cd^{2+} and Hg^{2+}. Upon the exposure to these ions, metal complexation with embedded *meta*-BPDM in the hydrogel allows a color change from red to blue-green, while no color change is observed with other interfering alkali, alkaline and transition metal ions such as Na^+, K^+, Ca^{2+}, Mg^{2+}, Cr^{3+}, Fe^{3+}, Fe^{2+}, Mn^{2+}, Co^{2+}, Ni^{2+}, Cu^{2+} and Pb^{2+}.

Moreover, CMGG-based hydrogels can be prepared by combining FRGP of AA monomers and Fe^{3+} cross-linking process in an aqueous solution of CMGG as reported by Chen and coworkers [84]. N,N,N',N'-tetramethylethylenediamine (TMEDA or TEMED) was chosen to initiate KPS for the grafting reaction. The obtained MBAAm, Fe^{3+}-cross-linked CMGG-g-PAA (MBAAm, Fe^{3+}-cl-CMGG-g-PAA) hydrogels possess dynamic, reversible hydrogen bonding and coordinate covalent bonding between -CO_2H groups from CMGG and PAA, resulting in strong, stretchable and self-healing ionic conductive hydrogels. These hydrogels can also be fabricated into strain sensors to monitor human body

motions e.g. joint bending, swallowing and speaking, with great sensitivity and repeatability.

Citric acid (CA) was chosen by Orsu and Matta to cross-link CMGG at high temperature through several continuous steps of forming cyclic carboxylic acid anhydride, followed by esterification reactions with remaining -OH groups on CMGG [85]. The prepared CA-cross-linked CMGG (CA-cl-CMGG) scaffold films show good hemocompatibility to human blood and great potential for wound healing and drug release of ciprofloxacin up to 60 % over 60 min under physiological pH and temperature.

Dalei et al. incorporated pH-responsive CMGG and polyvinyl alcohol (PVA) due to its good capacity in forming films, stability towards pH and temperature [86]. The two polymers were cross-linked by TEOS to obtain TEOS-cross-linked CMGG-PVA (TEOS-cl-CMGG-PVA) hydrogels with good mechanical integrity and pH-responsivity. Surface properties of the TEOS-cl-CMGG-PVA hydrogels such as wettability, energy, topography were of great interest to enhance their biocompatibility. NTP modification was also carried out using N_2 or a mixture of N_2 and NH_3 to improve surface wettability and to induce topographical changes of hydrogels. NTP-treated TEOS-cl-CMGG-PVA (TEOS-cl-CMGG-PVA@) hydrogels show good antibacterial activity against *Escherichia coli* (*E. coli*), hemocompatibility, biodegradability, as well as great potential for the delivery of chrysin (5,7-dihydroxyflavone) as a natural anticancer bioflavonoid to colon.

3.1.1.2. Hydroxypropyl GG (HPGG) and its derivatives. Over the years, hydroxypropyl GG (HPGG) has been well-known as a more hydrophobic derivative of native GG [87]. HPGG and its similar compounds can be found in fracturing fluids [88–90], fragile surface cleaning [91], stabilization of fly ash suspensions [92], as a binder in lithium-ion batteries [93], detection of NH_3 [94], etc.

In order to modify the hydrophilicity, water dissolution and temperature resistance of native GG, Gao and Grady recently studied in detail the kinetics of hydroxypropylation of GG in aqueous solution [95]. After the activation of GG by sodium hydroxide (NaOH), propylene oxide (PO) was used to carry out nucleophilic reaction in a polymerization reaction manner to obtain oligomeric PO chains linked to GG. Under the chosen reaction conditions, the reaction was found to be first and zeroth order with respect to the concentration of GG and PO respectively. Proton nuclear magnetic resonance (^{1}H NMR) was employed to quantify the amount of PO repeating units on GG. However, because different oligomeric chains of PO units might be attached onto each AGU of GG, the degree of molar substitution (MS) based on the average number of moles was reported instead. The reported MS values of HPGG vary from 0 to 1.2, depending on the reaction time. In addition, boric acid (H_3BO_3) and Zr^{4+} ions were used to create boric acid-cross-linked HPGG and Zr^{4+}-cross-linked HPGG (boric acid-cl-HPGG and Zr^{4+}-cl-HPGG respectively) to get viscoelastic gels. Rheological studies

suggest that Zr^{4+} ions can provide much better cross-linking than borates in the same concentration range between 20 and 200 ppm at pH above 9.5.

To further explore the drug delivery behavior of HPGG, Ray et al. employed the hydroxypropylation of GG using 3-(hexadecyloxy)-1-chloropropan-2-ol electrophiles to prepare a new derivative of GG, namely 6-O-(3-hexadecyloxy-2-hydroxypropyl)-GG (HDGG) [96]. HDGG was used to encapsulate polyene antibiotic amphotericin B (AmB) and piperine (Pip) due to their potential antileishmanial activity and ability to enhance the bioavailability of various drugs respectively. In addition, the encapsulated HDGG nanoparticles were also coated with eudragit L30D (Eu) for oral medication administration. In vitro and in vivo studies of the final nanoparticle products were performed to show good controlled drug release at the designated organs, great drug bioavailability, antileishmanial activity and non-nephrotoxic nature.

From HPGG starting material, Lu et al. recently reported a novel FRGP of GG using AAm, 3-acrylamidophenylboronic acid (AAPBA) monomers and Irgacure 2959 (I2959) photo-initiator [97]. The AAPBA monomers offer both double bonds for copolymerization and boric acid moieties for cross-linking with remaining hydroxyl groups on HPGG via phenylboronic acid (PBA)-diol ester bonds. These ester bonds are responsive to pH changes and therefore, acid-base chemistry can be employed to tune mechanical properties of the self-healing PBA-cross-linked AAm-*co*-AAPBA grafted HPGG [PBA-cl-HPGG-g-P(AAm-*co*-AAPBA)] hydrogel products. Rheological results indicate a significant improvement in mechanical behaviors of the hydrogels when pH varies from acidic to neutral and alkaline conditions (4.00, 7.00, 8.15 and 9.00).

Besides taking advantage of hydrogen bonding and boron-based cross-linkers, Sun and coworkers also explored the mussel-inspired chemistry of catechol and Fe^{3+} to form hydrogels between HPGG and polydopamine-coated reduced graphene oxide (PDA-rGO) [98]. The obtained borax, Fe^{3+}-cross-linked HPGG-PDA-rGO (borax, Fe^{3+}-cl-HPGG-PDA-rGO) hydrogels possess numerous dynamic, reversible and pH-sensitive cross-linkers between hydroxyl groups on HPGG and catechol groups from PDA-rGO through boron and Fe^{3+}, resulting in good self-healing and mechanical properties. While PDA-rGO offers more flexibility and electrical conductivity to the hydrogel, glycerol also enhances the freeze resistance and moisture retention of the material. Borax, Fe^{3+}-cl-HPGG-PDA-rGO hydrogels might be employed to fabricate flexible sensors, which can detect different types of human motion over a wide temperature range (-20 to 30 °C) with good stability and repeatability.

3.1.1.3. Methylated GG (MGG) and its derivatives. Methylation of GG can be carried out to decrease the hydrophilicity of GG, hence, enhancing barrier and mechanical properties, as well as sealability against humidity of GG-based biodegradable films [99].

Recently, Tripathi et al. carried out the methylation of GG using methyl iodide in an aqueous solution of NaOH to yield methylated GG (MGG) [100]. The obtained product shows improvements in crystallinity, hydrophobicity, thermal stability, mechanical and barrier properties to water vapor transmission, hence, the MGG product can be used as biodegradable food packaging films. In addition, the mechanical and barrier properties against humidity transmission can be further enhanced by incorporating nanoclays, e.g. inorganic bentonite nanofil 116 and organically modified bentonite cloisite 20A, into MGG to create nanocomposite films [101]. Beneficial effects of these nanoclays were observed as the concentration of nanoclays increased up to 20 % w/w, while no significant change in the opacity of the nanocomposite films was reported.

3.1.1.4. Quaternized/ cationic GG (QGG/CGG) and its derivatives. The introduction of quaternary ammonium groups (quaternization) to GG is one of the most common approaches to obtain cationic GG (CGG) [102].

In the past, nucleophilic reactions between GG and etherifying reagents such as N-(3-chloro-2-hydroxypropyl)-trimethyl ammonium chloride (CHPTAC) in aqueous medium [103,104], aqueous IPA solution [105], 2,3-epoxypropyltrimethylammonium chloride (EPTAC, glycidyltrimethylammonium chloride, GTMAC) in aqueous EtOH medium [106], etc. were reported. Since CGG shows no harmful effect on natural environment or human health, it has been found in cosmetic products [107,108], protein drug release [109], and liposome encapsulation [110]. Moreover, CGG can also be employed in developing complex membranes and films for oil/water separation [111], antibacterial packaging [112–114], as depressants in flotation separation,[115] and stabilizers for zirconia suspensions as well as plasma emulsion [116,117].

In the recent time, Nakamura and coworkers used EPTAC (GTMAC) cationizing reagent in an aqueous EtOH solution to introduce positive charge to non-ionic GG [118]. The CGG product was used as a flocculant for negatively charged bentonite aqueous suspensions. In order to optimize the reaction conditions for the quaternization of GG, Tyagi et al. recently employed the well-known Taguchi's statistical methodology in designing and optimizing experimental conditions [119,120]. Due to the instability, toxicity, and high cost of EPTAC, CHPTAC was used to quaternize GG instead. Under alkaline condition, CHPTAC might easily be converted into EPTAC in situ, followed by nucleophilic reaction with activated GG. Several reaction factors were tested, namely, concentration of alkali and cationizing reagent, reaction time and temperature, using Taguchi L_{16} orthogonal array (4^5). The optimized experimental condition was reported that GG was dispersed in aqueous MeOH (80 % v/v) with a GG:solvent ratio of 1:20, together with 3.24 mol of NaOH and 2.04 mol of CHPTAC per each mole of GG AGU for 2 h at 30 °C. Among different experimental factors, the reaction time and amount of NaOH play a crucial role in the quaternization of GG.

FRGP was employed by Jing et al. to develop ultra-stretchable, self-healing hydrogels based on hexadecyl trimethyl ammonium bromide (CTAB)-cross-linked AA-*co*-stearyl methacrylate (SMA) grafted CGG [CTAB-cl-CGG-g-P(AA-*co*-SMA)] [121]. The quaternary amine groups in CGG offer hydrogen bonding and ionic interaction with carboxylate moieties in AA, hence, enhancing the mechanical strength of the hydrogel product. In addition, CTAB cross-linker was chosen to reinforce physical intermolecular interaction of the hydrogel by ionic attraction between positively charged ammonium groups and carboxylate groups from AA, as well as hydrophobic dispersion force between aliphatic hexadecyl chains and stearyl chains from SMA. Due to the presence of various dynamic intermolecular interaction in CTAB-cl-CGG-g-P(AA-*co*-SMA), the hydrogel shows self-healing capacity, ionic conductivity and can be used to develop strain electronic sensors.

Besides the quaternization of GG, partial oxidation of CGG has also been considered to broaden the applicability of CGG. Dai et al. reported a simple procedure to cross-link oxidized CGG (OCGG) and CS without employing extraneous cross-linking agents [122]. Several hydroxyl groups on CGG and CS were partially oxidized by sodium periodate ($NaIO_4$) first to yield aldehyde functional groups. These aldehyde groups subsequently reacted with remaining -OH groups on OCGG, -OH and/or -NH_2 groups from CS to form a cross-linked hydrogel via acetal and imine chemical bonds. The received cross-linked OCGG-CS (cl-OCGG-CS) hydrogel responds to pH changes due to the chemistry of acetal and imine bonds. In addition, cl-OCGG-CS possesses thermal responsiveness within the temperature range between 25 and 80 °C, and adhesiveness towards various surfaces e.g. metal, glass, plastic, wood and human skin. The gel is also an efficient adsorbent for the removal of phosphate in wastewater treatment and the obtained phosphate-adsorbed hydrogel can be utilized to fabricate N,P-doped carbon aerogel electrodes in supercapacitors.

Moreover, Yu et al. proposed an idea of cross-linking OCGG and carboxymethyl CS (CMCS) to create hydrogels for wound dressing [123]. Criteria for hydrogel properties in wound dressing can be found from some of these excellent reviews [124–128]. While CGG can offer
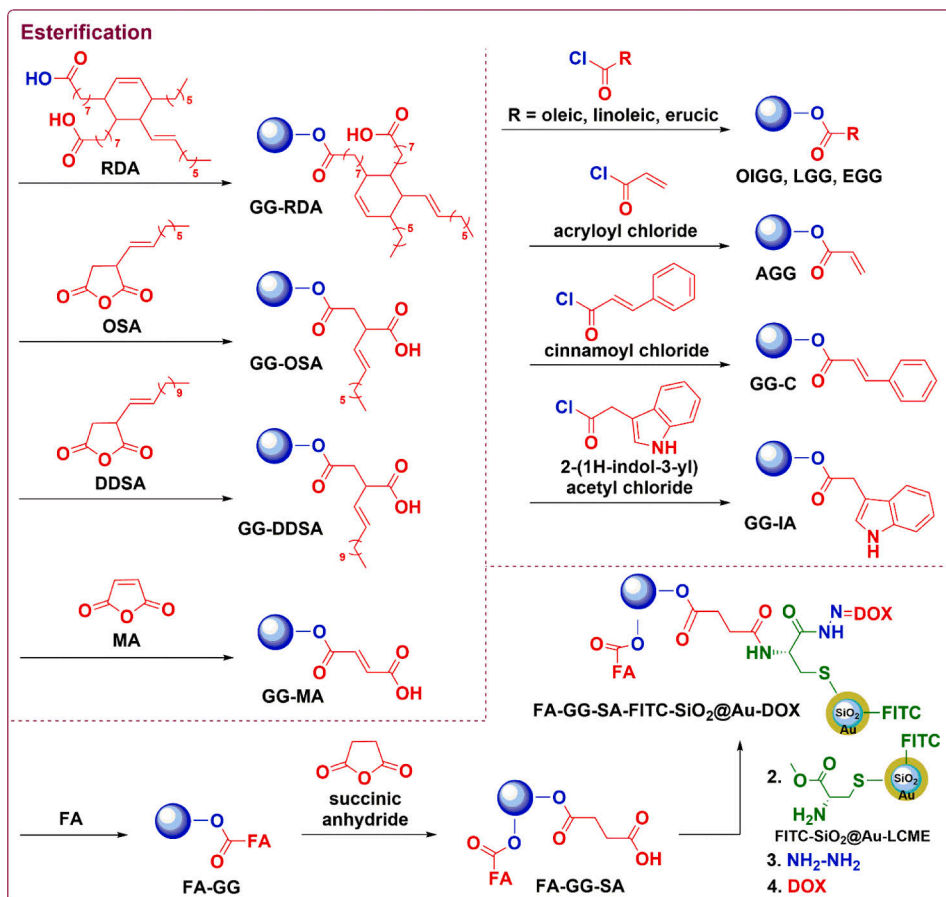
Fig. 3. Esterification of GG by carboxylic acids, acid anhydrides and acyl halides.

antibacterial activity due to the presence of quaternary ammonium groups [129], remaining -OH groups of CGG can also be partially oxidized to yield aldehyde groups for further cross-linking with CMCS. The cross-linked OCGG-CMCS (cl-OCGG-CMCS) hydrogel product has excellent antibacterial activity against *E. coli* and *Staphylococcus aureus* (*S. aureus*), hemostatic, cytocompatible, self-healing, injectable properties and great potential in wound dressing and healing.

3.1.1.5. Other derivatives of GG. Etherification remains as one of the most convenient approaches to modify GG. To create a novel non-viral, receptor-targeted gene delivery vector system for gene therapy against triple negative breast cancer (TNBC), Jana et al. performed several consecutive chemical transformations on GG [130]. GG was conjugated with low-molecular-weight polyethylenimine (LPEI), which has been reported as a non-viral carrier due to its high transfection efficiency, by using 4-bromo-1,8-naphthalic anhydride coupling agent. In the first step, S_N reaction was carried out between GG and 3-chloropropylamine (CPA) to form 3-aminopropyl GG (APGG). LPEI was then grafted to APGG via naphthalimide moieties to yield the final cationic LPEI grafted GG (GG-g-LPEI) product. Finally, complex coacervation between

cationic GG-g-LPEI and anionic EGFP-N1 plasmid DNA (pDNA) was performed to form GG-g-LPEI/pDNA final coacervate product. The synthesized GG-g-LPEI has excellent blood and cyto-compatibility towards cervical HeLa and triple negative breast MDA-MB-231 cancer cells. GG-g-LPEI with 10 % the concentration of LPEI shows the highest in vitro transfection efficiency in TNBC, comparing to other concentrations of LPEI. Higher transfection efficiency in MDA-MB 231 cell line comparing to HeLa cell line has been reported and suggested due to the overexpression of mannose receptors in MDA-MB-231 cells.

Recently, Le and coworkers introduced benzoic acid (BA) moieties onto GG to yield GG-benzoic acid (GG-BA) [131]. After activating GG by NaOH in aqueous solution, 4-(bromomethyl)benzoic acid (BMBA) was used to provide BA moieties to the S_N reaction on GG. BA can offer rich coordination chemistry due to the presence of carboxylic acid functional groups, as well as hydrophobicity and π stacking intermolecular interaction from aromatic rings. Density functional theory (DFT) was employed to study electronic properties and visualize molecular orbitals of GG-BA. GG-BA with the concentration up to 4000 µg mL^{-1} shows good biocompatibility to mouse embryonic fibroblasts, human mammary epithelial cells and can potentially be used to develop novel

biomaterials such as bioadhesives, hydrogels, and coacervates.

In addition, Reis and coworkers also chemically introduced vinyl moieties onto GG via etherification reaction with epoxide groups from glycidyl methacrylate (GMA) [132]. The obtained glycidyl methacrylate guar gum (GG-GMA) was grafted with AA (in the sodium acrylate salt form) and N,N-dimethylacrylamide (DMAAm) spacer to yield AA-co-DMAAm grafted GG-GMA [GG-GMA-g-P(AA-co-DMAAm)] hydrogels as colon-targeting drug carriers. The obtained GG-GMA-g-P(AA-co-DMAAm) hydrogels show pH-responsiveness and swelling at intestinal pH 6.8 comparing to gastric pH 1.2, due to the presence of carboxylic acid functional groups. The hydrogel possesses low cytotoxicity to 3T3 cells line murine with hydrogel concentration up to 1000 μg mL^{-1} and can be used for the controlled release of hydrocortisone (HCS) model drug.

3.1.2. Esterification (GG-O-CO-)

Esterification of -OH groups on GG can be carried out using carboxylic acids and their reactive derivatives such as carboxylic acid anhydrides and acyl halides (Fig. 3, Table 2) [133–135].

To increase the hydrophobicity of GG, Bajpai and Raj used ricinoleic dimer acid (RDA) to esterify GG in the presence of dodecylbenzene-sulfonic acid (DBSA) and catalytic amount of tosylic acid (TsOH), under microwave (MW) irradiation condition [136,137]. GG-ricinoleic dimer acid (GG-RDA) ester product is less susceptible to microbial growth than original GG and can be cross-linked with PVA by glutaraldehyde (GA) to form GA-cross-linked GG-RDA-PVA (GA-cl-GG-RDA-PVA) biofilms. Hydrophilic antibiotic gentamicin sulfate (GS) and hydrophobic amoxicillin (AX) medications were successfully loaded into GA-cl-GG-RDA-PVA films for wound dressing and drug delivery applications. These films show good biodegradability, resistance toward microbial growth of *E. coli*, *S. aureus* and *Candida albicans* (*C. albicans*), moisture-retention, wound exudate absorption capacity and wound healing properties.

Recently, Rajkumar and Prabaharan have reported complex chemical transformations of GG to prepare muti-functional nanoparticles for simultaneous cancer imaging and therapy [138]. Folic acid (FA) was first conjugated to GG as a tumor-targeting ligand to assist the drug delivery process to tumor sites, i.e. better cellular uptake and cytotoxicity for cancer cells via folate receptor-mediated endocytosis [139]. Steglich esterification with N,N'-dicyclohexylcarbodiimide (DCC) and 4-dimethylaminopyridine (DMAP) catalyst was chosen to provide a mild reaction condition for FA and GG at room temperature in DMSO. FA-conjugated GG (FA-GG) product was further esterified with succinic anhydride to introduce succinic acid (SA) moieties onto FA-GG to yield FA-GG-succinic acid (FA-GG-SA). Meanwhile, fluorescein isothiocyanate-SiO$_2$ core-Au shell-L-cysteine methyl ester (FITC-SiO$_2$@Au-LCME) nanoparticles was synthesized for fluorescence-computed tomography of cancer cells. SiO$_2$ core-Au shell (SiO$_2$@Au) nanoparticles offer good mesoporous structure, large surface area, biocompatibility and photostability. While conjugated fluorescein isothiocyanate (FITC) can exhibit emission spectrum peak wavelengths of around 490 nm corresponding to green fluorescence, L-cysteine methyl ester (LCME) linkers can connect FITC-SiO$_2$@Au via Au-S bonds, FA-GG-SA via amide bonds based on remaining SA moieties, and doxorubicin (DOX) chemotherapy medication via acid-cleavable hydrazone bonds. The acid-sensitive hydrazone bonds allow the controlled release of DOX at pH 5.6 inside Hela cancer cells, while remain stable at physiological pH 7.4. EDC/NHS coupling chemistry based on 1-ethyl-3-(3-dimethylaminopropyl)carbodiimide (EDC) and N-hydroxysuccinimide (NHS) was employed to form amide bonds between FA-GG-SA and FITC-SiO$_2$@Au-LCME, resulting in FA-GG-SA-FITC-SiO$_2$@Au-DOX final product.

In addition, Soni et al. carried out esterification of GGH by hydrophobic carboxylic acid anhydrides to enhance emulsifying and micro-encapsulant properties of GGH [140]. GGH and NaHCO$_3$ were dispersed in aqueous EtOH (95 % v/v) solutions of dodecenyl succinic anhydride (DDSA) or n-octenyl succinic anhydride (OSA). 45 °C and 2 h were reported as the optimized reaction temperature and time to obtain

DS of 0.029 for GGH-dodecenyl succinic acid (GGH-DDSA) product. Meanwhile, GGH-n-octenyl succinic acid (GGH-OSA) product was obtained with DS of 0.07. GGH-DDSA was reported as a promising alternative to gum arabic for the emulsification and microencapsulation of soybean oil in food engineering.

Besides, Zhang and coworkers employed maleic anhydride (MA) to prepare anionic GG [141]. GG was dispersed in a dichloromethane (DCM) solution of maleic anhydride and triethylamine (Et$_3$N) catalyst to yield GG-maleic acid (GG-MA). The obtained GG-MA product has better water solubility, elasticity and great potential as a fracturing fluid with good temperature resistance between 120 and 150 °C, as indicated by rheology. Moreover, Yuan et al. has used maleic anhydride to cross-link GG and poly(ε-caprolactone) (PCL) grafted chitosan (CS-g-PCL) to form hydrogels for drug delivery [142]. Acetonitrile (ACN) solvent was chosen to disperse GG in the presence of DMAP catalyst for esterification reaction between GG and MA to yield GG-MA. Then, aza-Michael addition was allowed between double bonds on maleic acid moieties of GG-MA and free amine groups from CS-g-PCL to yield cross-linked cl-GG-MA-CS-g-PCL hydrogels. Noncytotoxic cl-GG-MA-CS-g-PCL shows anti-microbial activity against *S. aureus* (ATCC 27661), *Klebsiella pnumoniae* (*K. pnumoniae*) (ATCC 13883) and can be used to develop micelles for the delivery of rifampicin medication, which has low water solubility, in tuberculosis treatment.

A wide range of acyl halides has also been employed for esterification of GG. Zhang et al. has prepared acyl chlorides from oleic, linoleic, erucic acids and phosphorous trichloride [143]. These hydrophobic unsaturated acyl chlorides were then added to dispersions of GG and NaOH in acetone to yield new derivatives of GG, namely oleic guar gum (OlGG), linoleic guar gum (LGG) and erucic guar gum (EGG). Rheological studies indicate that aqueous solutions of these GG derivatives are non-Newtonian shear-thinning fluids and possess hydrophobic interaction.

Recently, Das and coworkers reported an esterification of GG using cinnamoyl chloride to modify the hydrophobicity and antibacterial activity of GG [144]. LiCl/DMSO solvent system was used as a medium for this reaction with catalytic amount of DMAP to yield GG cinnamate (GG-C). Beneficial effects of LiCl in polar aprotic solvents such as DMSO have been well-known for the dissolution of polysaccharides due to its ability to disrupt and prevent the reformation of hydrogen bonds [145–147]. Nanoprecipitation based on ouzo effects of GG-C hydrophobic solute, DMSO polar organic solvent and water non-solvent, was employed to yield GG-C nanoparticles (GG-C-N) [148]. The obtained GG-C-N have hydrodynamic size of around 289 nm and polydispersity index (PDI) of 0.43 from dynamic light scattering (DLS) measurements. Antibacterial activity of GG-C and GG-C-N was studied on E. coli (MTCC 44) and S. aureus (MTCC 160) strains to show that GG-C has better activity comparing to ciprofloxacin antibiotic control. Moreover, GG-C-N exhibit nearly-two times higher the antibacterial activity of GG-C and this was attributed to strong hydrophobic, aromatic interaction and high surface area of GG-C-N, resulting in better cell membrane perforations and cell death.

Similarly, Das and coworkers carried out esterification of GG with 2-(1H-indol-3-yl)acetyl chloride also in the LiCl/DMSO solvent system to form GG indole acetate (GG-IA) [149]. GA was then chosen to cross-link GG-IA and hydrolyzed fibrous keratin protein, which was extracted from chicken feather wastes, and subsequently solvent-casted into GA-cross-linked GG-IA-keratin (GA-cl-GG-IA-keratin) film scaffolds. These scaffolds are noncytotoxic and biocompatible to human dermal fibroblast cells. Both GG-IA and GA-cl-GG-IA-keratin films possess antimicrobial activity against gram-positive (*S. aureus* MTCC160), gram-negative (*E. coli* MTCC44) bacteria and show great potentials in skin tissue engineering.

Additionally, Bhattacharyya and Chowdhury introduced vinyl moieties to GG via esterification of NaOH-activated GG and acryloyl chloride, resulting in acryloyl GG (AGG) [150]. AGG was then grafted with AA and potassium 3-sulfopropyl acrylate (KSPA) to develop a novel pH-
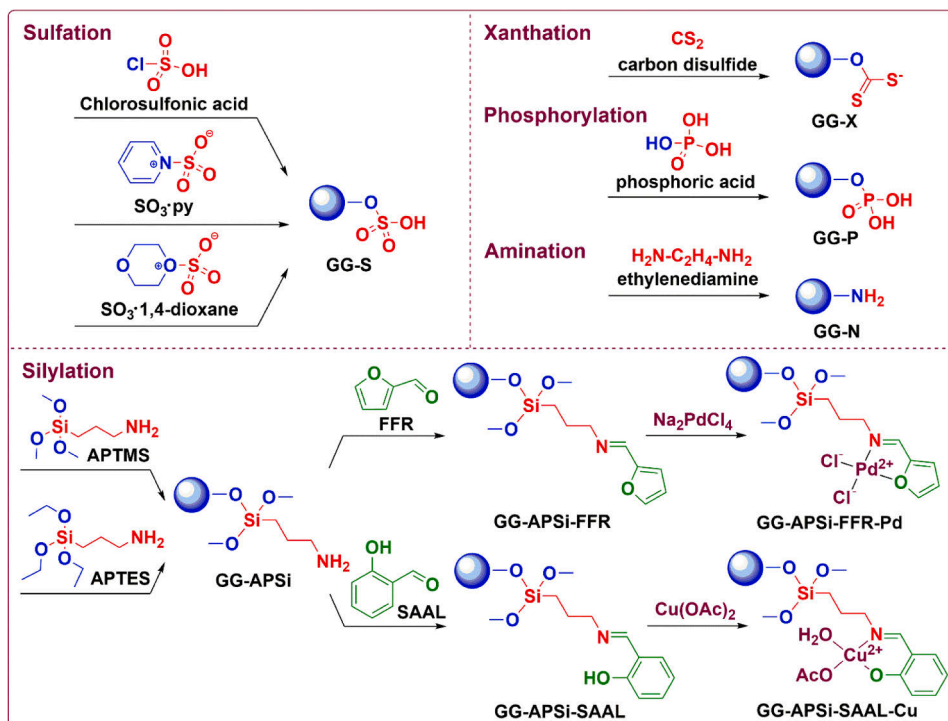
Fig. 4. Xanthation, silylation, phosphorylation, sulfation and amination of GG.

responsive MBAAm-cross-linked AA-*co*-KSPA grafted AGG [MBAAm-cl-AGG-g-P(AA-*co*-KSPA)] drug delivery system. Gentamicin sulphate (GMS) medication, which is used for the treatment of colorectal and anal fistula surgical site infections, can be adsorbed or desorbed from MBAAm-cl-AGG-g-P(AA-*co*KSPA) hydrogels via reversible hydrogen bonding. Under physiological pH, deprotonation of carboxylic acid groups in the hydrogels increases the electrostatic repulsion between the polymer chains, hence, enhancing the release of GMS.

3.1.3. Xanthation (GG-O-CS₂)

According hard-soft acid-base (HSAB) theory, hydroxyl functional groups of native GG are considered as hard bases and possess strong affinity towards hard acids [151]. The coordination chemistry of -OH groups on GG, therefore, remains limited mainly to hard metal ions. Meanwhile, a wide range of transition and heavy metal ions is soft acids and tend to interact more strongly with soft bases such as S-containing thiol, sulfide, xanthate and dithiocarbamate functional groups [152–154]. While dithiocarbamate can be easily introduced onto polysaccharides that contain amino groups such as chitosan [155–158], xanthate functional groups are of great interest to polysaccharides possessing hydroxyl groups [159,160].

To broaden coordination chemistry of GG to a wider range of metal ions, especially heavy metal ions, Le and coworkers have reported a facile aqueous xanthation protocol (Fig. 4) [161]. Nucleophilic hydroxyl groups on GG were first activated by NaOH, followed by an addition of electrophilic carbon disulfide (CS_2) to yield GG xanthate (GG-X) product. N_2 purging to remove dissolved O_2 was found crucial to avoid further oxidation of xanthate groups. Under alkaline condition, while hard -OH groups of GG have good coordinating capacity towards hard

metal ions, e.g. Al^{3+}, GG-X with soft xanthate moieties can easily form gels with various borderline and soft metal ions, e.g. Co^{2+}, Fe^{2+}, Cu^{2+}, Ni^{2+}, Pb^{2+}, Pt^{2+} and Cd^{2+}. GG-X, therefore, exhibits great potentials for heavy metal ion extraction, removal, and hydrogel formation. In addition, GG-X was employed to fabricate nanocomposites with CuS covellite (GG-X/CuS). GG-X not only can act as a capping agent for the aqueous dispersion of CuS nanoparticles, but also provides beneficial effects on the crystallite size of CuS. The application of GG-X/CuS nanocomposite in humidity sensing was also explored, in which hydrophilic GG-X matrix allows the interaction with humidity while CuS semiconductor contributes the electrical sensitivity to the nanocomposite. As a result, reversible linear responses of GG-X/CuS to relative humidity changes between 10 and 80 % were recorded.

3.1.4. Silylation/ Silanization (GG-O-Si-)

Over the years, silylation has been a popular process to covalently modify hydroxyl functional groups of chemical molecules or on different surfaces for various applications [162–167]. Si has high affinity towards O and Si-O bonds are particularly stable, hence the silylation of -OH groups can be carried out readily [168].

To construct Pd-based catalytic sites onto GG, Baran and coworkers have carried out several chemical modification steps on GG (Fig. 4) [169]. (3-aminopropyl)triethoxysilane (APTES) was first used to silylate hydroxyl groups and introduce free -NH₂ groups on GG. Schiff-base condensation between amino groups of GG-(3-aminopropyl)silane (GG-APSi) product and aldehyde groups from furfural (FFR) was then performed with refluxing MeOH to yield GG-APSi-furfural (GG-APSi-FFR). Finally, metal complexation between FFR, aldimine moieties on GG-APSi-FFR and Pd^{2+} metal cations were carried out to complete GG-

APSi-FFR-Pd catalytic sites for Suzuki solvent-free cross-coupling reactions between phenylboronic acid and different aryl halides under green reaction conditions (microwave radiation in 5 min and ambient atmosphere). The newly developed GG-APSi-FFR-Pd heterogeneous catalyst shows good catalytic activity and recyclability.

Moreover, (3-aminopropyl)trimethoxysilane (APTMS) was employed by Kumari et al. to also silylate and introduce amino groups on GG for developing a new Cu-based heterogeneous catalyst [170]. Silylated GG-APSi product was then refluxed with salicylaldehyde (SAAL) in EtOH to receive GG-APSi-salicylaldehyde (GG-APSi-SAAL) via Schiff-base condensation reaction. Final GG-APSi-SAAL-Cu heterogeneous catalyst was then obtained by metal complexation of GG-APSi-SAAL and copper(II) acetate [$Cu(OAc)_2$]. Catalytic activity of GG-APSi-SAAL-Cu was demonstrated based on selective oxidation reactions of diarylmethanes, resulting in different benzophenone derivatives. ACN solvent and *tert*-butyl hydroperoxide (TBHP) oxidant at 70 °C were found as the best condition for this catalytic reaction to give a reaction yield up to 90 % with good turnover number and frequency.

3.1.5. Phosphorylation (GG-O-P-)

Mimicking nature in developing new materials has been one of the most sustainable approaches in modern materials science. While discussions on the reasons why nature chooses phosphate and similar derivatives have long been of great interest to the science community [171–173], much effort has also been devoted to introducing phosphate moieties onto various materials to explore their properties and potential applications [174–176]. Over the years, phosphorylation of polysaccharides using phosphorylating agents such as phosphorus oxychloride ($POCl_3$), phosphorus pentoxide (P_2O_5), sodium trimetaphosphate (STMP), sodium tripolyphosphate (STPP), phosphoric acid and its anhydride, has been reported as a convenient chemical modification pathway to alter biological activities of natural polysaccharides [177].

In order to enhance hydrophobicity, emulsifying properties and homogenization of GG, Sharma and coworkers linked GG and soya lecithin (SL) via C-O-P bonds [178]. DCC was used to couple phosphate ester groups of SL and hydroxyl groups from GG, resulting in guar gum-soya lecithin (GG-SL). Then, MBAAm-cross-linked GG-SL/Fe^0 (MBAAm-cl-GG-SL/Fe^0) nanocomposites were prepared from GG-SL and zero-valent iron (Fe^0) in the presence of MBAAm cross-linker for the photocatalytic degradation of methyl violet dye. The Fe^0 photocatalyst can absorb solar energy to yield photogenerated electrons and holes, followed by the formation of reactive oxygen species and the degradation, mineralization of organic dyes. Detailed studies on the degradation of methyl violet, total organic carbon (TOC) removal efficiency and reusability of MBAAm-cl-GG-SL/Fe^0, have also been performed to show that MBAAm-cl-GG-SL/Fe^0 is an efficient photocatalytic system.

Phosphate and its derivatives are ones of the most commonly used coordinating functional groups in U(VI) removal due to their high affinity towards uranyl (UO_2^{2+}) ions [179]. In an effort of developing new materials for the removal of U(VI) in wastewater treatment, Hamza et al. have performed phosphorylation of GG to introduce phosphonic acid (or phosphonate groups) onto GG (Fig. 4) [180]. The phosphorylation of GG was carried out by using urea and H_3PO_4 reactants in 1,4-dioxane solvent at high temperature. New insights into the phosphorylation reaction mechanism by urea and H_3PO_4 have been presented recently [181]. Urea was suggested as a chemical source for the in-situ generation of NH_3 real catalyst, while phosphoramidate was proposed as the reaction intermediate. The obtained GG-phosphonic acid (GG-P) was then cross-linked with CS via epichlorohydrin (ECH), while magnetic Fe_3O_4 could also be added to the mixture to introduce magnetic properties for better separation and recovery of ECH-cross-linked GG-P-CS/Fe_3O_4 (ECH-cl-GG-P-CS/Fe_3O_4) nanocomposite product. The ECH-cl-GG-P-CS/Fe_3O_4 nanocomposite is pH-responsive due to the presence of both amino and phosphonate groups, resulting in the pH-dependence of metal cation sorption and desorption. This nanocomposite also possesses good

selectivity towards UO_2^{2+} and Nd^{3+} comparing to other tested alkali-earth metals ions (e.g. Ca^{2+} and Mg^{2+}). In addition, ECH-cl-GG-P-CS/Fe_3O_4 can also offer antibacterial activity towards gram-positive [*Bacillus subtilis* (*B. subtilis*), *S. aureus*] and -negative [*E. coli, Pseudomonas aeruginosa* (*P. aeruginosa*)] bacteria.

3.1.6. Sulfation (GG-O-S-)

Recently, the introduction of sulfate functional groups to polysaccharides has drawn much attention as a convenient and efficient approach to alter the physicochemical properties of polysaccharides, especially their antioxidant, anticoagulant and antitumor activity [182,183].

To explore anticoagulant and antithrombotic effects of GG derivatives, de Oliveira Barddal and coworkers have carried out sulfation reactions on GG and GGH (Fig. 4) [184]. Chlorosulfonic acid-pyridine (py) (O'Neill method) and sulfur trioxide (SO$_3$)-pyridine (Larm method) sulfating reagents were employed to yield GG-sulfonic acid (GG-S-O, GG-S-L) and GGH-sulfonic acid (GGH-S-O, GGH-S-L respectively) with good DS. Further hydrolysis of GG products was also noticed and suggested due to the acidic reaction media. Degradation of GG-S-O was observed over the time while GG-S-L and GGH-S-L remained more stable. In vitro anticoagulant activity studies were performed to correlate the anticoagulant activity to the presence of sulfate groups and also indicate that GGH-S-L is a promising alternative to heparin, which is a glycosaminoglycan anticoagulant and antithrombotic medication. In addition, GGH-S-L has good antithrombotic activity from in vivo studies on male Wistar rats and good bioavailability when administered subcutaneously.

Kazachenko et al. combined chlorosulfonic acid and 1,4-dioxane at 20 °C to prepare SO$_3$·1,4-dioxane sulfating complex for the sulfation of GG [185]. GG-S product with DS of 0.91 was obtained after dispersing GG with SO$_3$·1,4-dioxane complex in 1,4-dioxane solvent at 60 °C for 2.9 h. Gel permeation chromatography has indicated a decrease in the molecular weight from 600 to 176 kDa after the sulfation. Moreover, computational chemistry was also carried out by DFT using Gaussian 09W software with B3PW91/6-31 + G(d, p) basis set to provide insights into electronic properties of GG-S.

Besides traditional sulfating agents, e.g. chlorosulfonic acid-pyridine, sulfur trioxide-pyridine and concentrated sulfuric acid-*n*-butanol, Kazachenko and coworkers have explored a novel milder sulfation pathway on GG using sulfamic acid and urea-based activators in 1,4-dioxane solvent [186]. It was suggested that urea and its similar compounds could activate sulfamic acid by creating Lewis acid-base complexes with S atom, hence, weakening S-N bonds in sulfamic acid to yield SO$_3$. Urea appears to be the best activator comparing to thiourea, methyl urea, ethyl urea, hydroxyethylurea and biuret. Among the tested polar aprotic solvents, namely, diglyme, 1,4-dioxane, DMF, piperidine, py and morpholine, 1,4-dioxane was also reported as the best solvent in terms of sulfur content for this bimolecular nucleophilic substitution (S$_N$2) sulfation reaction. While the experimental optimal reaction condition was obtained at 80 °C in 3 h using 25 mmol sulfamic acid per 1 g GG, the calculated optimal condition was suggested at 85 °C in 2.6 h with 34 mmol sulfamic acid for every 1 g of GG. In addition, depolymerization of GG chain was also observed, resulting in a molecular weight reduction by a factor of 2.7.

3.1.7. Amination (GG-NH$_2$)

Amino groups can be introduced to pristine polysaccharides via several pathways, resulting in chemical and biological property changes of polysaccharides [187]. For instance, polyamines have been conjugated to polysaccharide chains via condensation reaction with carboxylic acids [188], naphthalic anhydride coupling chemistry [130], and aza-Michael addition with oxidized polysaccharides [189].

In addition, direct replacement of hydroxyl groups on polysaccharides by amino groups is also another alternative and was recently performed on GG by Gopi et al. to prepare cross-linked hydrogels with
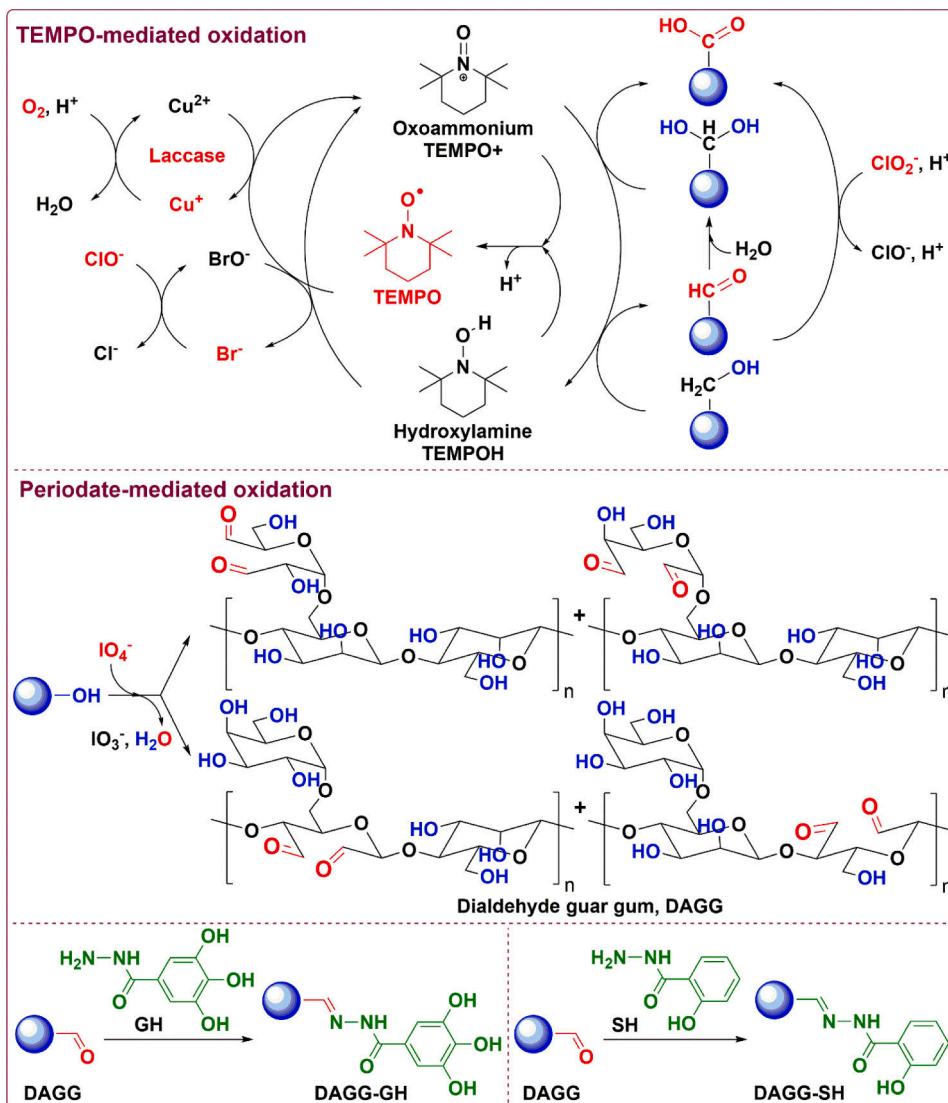
Fig. 5. Partial oxidation mechanism of GG using O_2-Laccase-TEMPO and NaOCl-NaBr-TEMPO systems (top). Regioselective oxidation of GG using periodate and further functionalization of DAGG products (bottom).

graphene oxide (GO) (Fig. 4) [190]. Nucleophilic substitution by ethylenediamine (NH_2-C_2H_4-NH_2) was first carried out to replace hydroxyl groups on GG (GG-OH to GG-NH-C_2H_4-NH_2), followed by reduction of GG-NH-C_2H_4-NH_2 by HCl to yield aminated GG-NH_2 (GG-N). GG-N was then cross-linked with GO by borax to yield borax-cross-linked GG-N-GO (borax-cl-GG-N-GO) hydrogels. The borax-cl-GG-N-GO hydrogel product possesses high surface area and abundant remaining -OH and -CO_2H functional groups. These contribute to the adsorption capability of pH-responsive borax-cl-GG-N-GO hydrogel towards inorganic and organic pollutants (e.g. Cu^{2+}, malachite green (MG), methylene blue (MB) and rhodamine B (RhB) cationic dyes).

3.2. Partial oxidation (GG-CHO, GG-CO_2H)

Over the years, partial oxidation of alcohol functional groups on polysaccharides to aldehydes has been regarded as convenient chemical synthesis approaches to diversify chemical properties of native polysaccharides [191,192]. While hydroxyl groups in general behave as nucleophiles, the presence of aldehyde and/or carboxylic acid groups on polysaccharide structures can offer electrophilic reactive sites as well as

condensation and cross-linking reaction pathways.

3.2.1. TEMPO-mediated oxidation

Oxidation of alcohol groups can be performed regioselectively on primary C6-OH groups of GG via 2,2,6,6-tetramethylpiperidine-1-oxyl radical (TEMPO)-mediated oxidation route [193,194]. In the past, TEMPO and sodium bromide (NaBr) were employed as catalysts for the oxidation of primary alcohol groups on GG derivatives to carboxylic acid groups using sodium hypochlorite (NaOCl) oxidant (NaOCl-NaBr-TEMPO system) in water [195]. C6-OH groups on Man backbone were suggested to be more accessible to TEMPO-catalyzed oxidation than C6-OH groups on Gal side chains of GG, due to possible intramolecular hydrogen bonding between C6-OH from Gal and C3-OH from adjacent Man [196,197]. In addition, enzymatic oxidation of primary alcohol groups using fungal laccase enzymes and TEMPO mediator was also reported (Fig. 5) [198].

Recently, de Seixas-Junior and coworkers prepared oxidized guar gum (OGG) by TEMPO-mediated oxidation as a reference to highlight the importance of primary alcohol groups of GG in the interaction with sodium lauryl ether sulfate anionic surfactant for the development of pharmaceutical or cosmetic products [199]. Primary alcohol groups of GG were selectively oxidized by NaOCl-NaBr-TEMPO system into carboxylic acids (1.2 mmol -CO_2H groups per g of GG). Moreover, Ponzini et al. have tested the enzymatic TEMPO-oxidation of several galactomannan polysaccharides, including GG [200]. Laccase enzyme was coupled to the catalytic oxidation of alcohol groups using O_2 oxidant and TEMPO mediator (O_2-Laccase-TEMPO system) in water [201,202]. Mass spectrometry analysis on the oxidation of primary alcohol groups based on this oxidation system indicated that both aldehyde and carboxylic acid groups are possible products from the oxidation reaction. OGG product was obtained as a hydrogel due to self-cross-linking via hemiacetal, ester bonds and could be further lyophilized to form aerogels. Interestingly, among three tested galactomannans, obtained aerogels from fenugreek gum exhibit the greatest mechanical stability comparing to aerogels from sesbania and guar gums, even though fenugreek gum has the lowest relative amount of Man comparing to Gal (Man:Gal ratios of 1:1, 1.3:1, and 1.5:1 in fenugreek, sesbania and guar gums respectively).

3.2.2. Periodate-mediated oxidation

Periodate (IO_4^-) has been well-known as an oxidizing agent for oxidative cleavage of vicinal 1,2-diols [203]. Over the years, much effort to employ periodate-mediated oxidation of vicinal alcohol groups located on equatorial-equatorial and equatorial-axial positions in polysaccharides has also been devoted [204–206]. Oxidation of galactomannan polysaccharide by periodate can be carried out on C2-OH and C3-OH of mannose backbone, as well as C2-OH, C3-OH and C4-OH of galactose side groups to yield dialdehyde products (Fig. 5) [207].

Recently, several research groups have performed periodate-mediated oxidation of GG to obtain dialdehyde GG (DAGG). Typically GG and periodate are dissolved in water solvent at room temperature and the oxidation is allowed in the dark for several hours and quenched by adding ethylene glycol. For instance, Dai and coworkers utilized this reaction pathway to prepare DAGG, followed by self-cross-linking between remaining alcohol groups and newly formed aldehyde groups via acetal bonds in DAGG, without the assistance of any external cross-linkers [208]. The obtained cross-linked-DAGG (cl-DAGG) hydrogels have great potential for oil–water separation in harsh alkaline (pH 11), salty environments (NaCl 5 wt%), with good separation efficiency (up to 99.47 %) and recyclability.

Duan et al. also carried out the oxidation and self-cross-linking of GG by periodate in the presence of Ag nanoparticles (Ag NPs) dispersed in porous iron(III) carboxylate of MIL (Materials of Institute Lavoisier, a type of metal–organic framework materials) [Ag NPs@MIL-100(Fe)] to enhance photocatalytic and antibacterial activity [209]. Photocatalytic degradation of MB dye by cl-DAGG/Ag NPs@MIL-100(Fe) hydrogel

product was demonstrated with good performance (up to 100 % MB can be degraded within 100 min) and recyclability. The hydrogel also possesses injectability, self-healing, antibacterial properties against *E. coli* and can be employed in water–oil separation with a separation efficiency up to 99.1 %.

In addition, a wide range of materials has been cross-linked with DAGG to synergize properties of these materials. For instance, Maroufi et al. reported periodate-mediated oxidation of GG to yield DAGG, followed by cross-linking with amino groups in fish gelatin to form cross-linked DAGG-gelatin (cl-DAGG-gelatin) food packaging films [210]. The cl-DAGG-gelatin film products possess lower water solubility, moisture content, water vapor permeability, better tensile strength and thermal stability than GG/gelatin reference films. Green tea extract (GTE) was also incorporated into the films (cl-DAGG-gelatin/GTE) to provide antioxidant and antibacterial activities on gram-positive *S. aureus* bacteria. Moreover, DAGG was also cross-linked with amino groups from CS in the presence of pomegranate peel extract (PPE) as a chemically active component to yield antioxidant and antibacterial cross-linked DAGG-CS/PPE (cl-DAGG-CS/PPE) hydrogels for food packaging applications [211].

Pandit and coworkers recently performed Schiff-base condensation between aldehyde groups in DAGG, which were obtained from periodate-mediated oxidation of GG, and remaining amino groups on CMCS to produce cross-linked DAGG-CMCS (cl-DAGG-CMCS) hydrogels [212]. These hydrogels show good self-healing properties, injectability, biocompatibility to human embryonic kidney 293 (HEK-293) cells up to a 100 µg mL^{-1} concentration of cl-DAGG-CMCS, blood compatibility and biodegradability. These cl-DAGG-CMCS hydrogels can also be used for drug loading and delivery from their study on DOX as a model anticancer medication.

Moreover, Mokhtari et al. carried out the cross-linking between newly synthesized DAGG and amino groups in silk fibroin (SF), followed by an incorporation of curcumin (Cur)-loaded zein nanoparticles (Cur-zein NPs) to obtain a novel cross-linked DAGG-SF/Cur-zein NPs (cl-DAGG-SF/Cur-zein NPs) hydrogel scaffold [213]. Applications of SF in materials science, flexible electronics, wound dressings, drug carriers, etc. have attracted great attention recently [214–217]. Cur was added to the hydrogel scaffold to enhance anti-inflammatory, antioxidant, antimicrobial properties of the system. Due to the hydrophobic polyphenolic nature, Cur has low water-solubility, bioavailability and can be encapsulated by protein carriers to enhance the drug delivery capacity. The synthesized hydrogel scaffold can promote viability, proliferation of mouse embryonic fibroblast (NIH-3T3) cells, and possesses antimicrobial activity against gram-positive (*Bacillus*) as well as gram-negative (*E. coli*) bacteria. DAGG/SF-Cur-zein-NPs, therefore, is a promising candidate for wound dressings and healing.

In the recent time, hydrazine was used as a linker to introduce new organic functional moieties to DAGG. Schiff-base condensation between DAGG and galacylhydrazine (GH) or salicylhydrazine (SH) was carried out by Duan and Ma et al. respectively to extend applicability of GG in wastewater treatment [218,219]. While phenolic moieties in DAGG-GH can enhance the reversible adsorption of cationic dyes [bromophenol blue (BrB), methyl orange (MeO), MB, RhB] via ionic and π stacking interaction, SH moieties in DAGG-SH are efficient adsorptive sites for metal cations such as Ni^{2+}, Co^{2+} and Cr^{3+}. In addition, Wen et al. also used hydrazine to conjugate DAGG and MBAAm cross-linked copolymer of acrylic acid and methyl methacrylate [MBAAm-cl-P(AA-*co*-MMA)] to prepare a novel adsorbent [220]. Oxidation of GG was first carried out by periodate to yield DAGG with the degree of oxidation of 67.62 %. MBAAm-cl-P(AA-*co*-MMA) was prepared using KPS initiator and MBAAm cross-linker to take advantage of carboxylic acid groups from AA for interaction with cations, and ester groups of MMA for further conjugation with DAGG. Then, MBAAm-cl-P(AA-*co*-MMA) and DAGG were linked together by using hydrazine, nucleophilic acyl substitution in water and Schiff-base condensation reaction in refluxing EtOH. Hydrazine-cross-linked DAGG-MBAAm-cl-P(AA-*co*-MMA) [hydrazine-
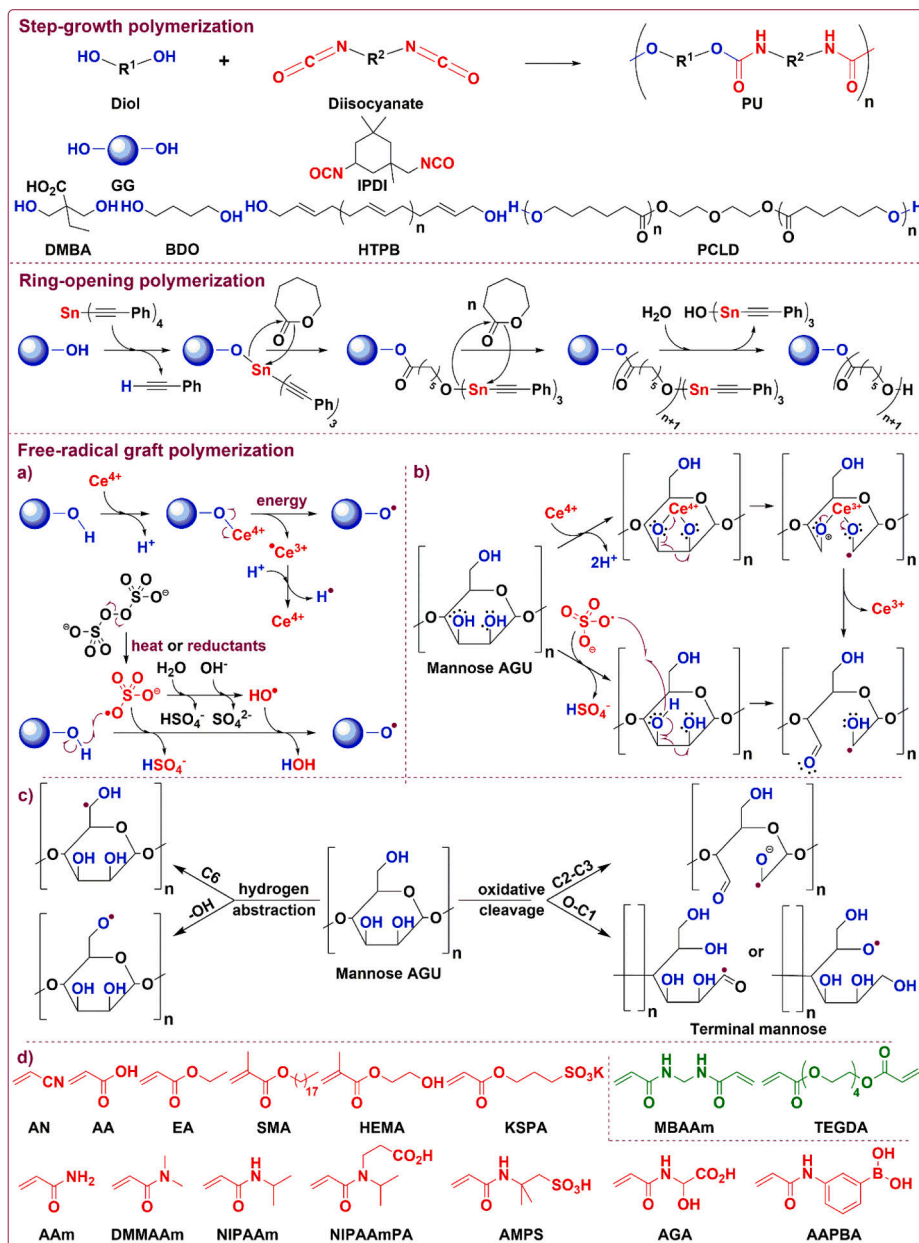
Fig. 6. Reported step-growth (top) and ring-opening (middle) polymerization of GG. Initiation mechanism of FRGP on GG and its derivatives (bottom). a) Formation of O-centered free-radicals. b) Formation of C-centered free-radicals. c) Formation of free-radicals via hydrogen abstraction and oxidative cleavage. d) Reported vinyl-containing monomers (red) and cross-linkers (green) for FRGP of GG and its derivatives. (For interpretation of the references to color in this figure legend, the reader is referred to the web version of this article.)

cl-DAGG-MBAAm-cl-P(AA-*co*-MMA)] product shows great capacity for removal of cationic organic dyes (MB, MG), Cu^{2+} metal ions from wastewater and also for water–oil separation with good efficiency and reusability.

In addition, aldehyde groups in DAGG can also be transformed into carboxylic acid groups. For instance, Ganie and coworkers used sodium chlorite ($NaClO_2$) under acidic condition [acetic acid (AcOH)] to further oxidize aldehyde groups in DAGG to dicarboxylic acid GG (DCGG) [221]. Coordination reactions between Fe^{2+} and $-CO_2H$ groups from DCGG were employed to yield Fe^{2+}-cross-linked DCGG (Fe^{2+}-cl-DCGG), which was eventually formulated with other polymeric materials (ethyl cellulose (EC), polyvinylpyrrolidone (PVP) and PVA) to form tablets for the controlled release of Fe^{2+}. In vitro studies indicate a faster release of iron in simulated intestinal fluid (pH 4.5) than in simulated gastric fluid (pH 1.5). Antianemic activity of Fe^{2+}-cl-DCGG tablets was also tested on male albino rats to show an overall health improvement.

3.3. Graft polymerization

3.3.1. Step-growth polymerization (SGP)

Step-growth polymerization (SGP) is one of the most common synthetic approaches in polymer science. Typically, chemical reactions between bi- or multi-functional monomers are performed to fabricate step-growth polymers [222–224].

To synthesize GG-based polyurethanes (GG-PU) as potential natural polysaccharide-based stabilizer, thickener, emulsifier or binding agent, Anjum and coworkers performed SGP between -OH groups of GG, hydroxyl-terminated polybutadiene (HTPB), and isocyanate (-NCO) functional groups of isophorone diisocyanate (IPDI) (Fig. 6) [225]. Firstly, GG was mixed with HTPB as a homogenous mixture, followed by reactions with IPDI to form GG-PU pre-polymers. Remaining -NCO groups of pre-polymers were finally allowed to react with 1,4-butanediol (BDO) as chain extender. Dibutyltin dilaurate (DBTDL) catalyst was also employed in this SGP of GG. Comparing to GG, GG-PU has better thermal stability, which was suggested due to an increase in intermolecular hydrogen bonding.

In addition, Ma et al. used -OH groups from GG and BD as chain extenders to further modify PU with -NCO terminating functional groups [226]. The synthesized PU was first fabricated from IPDI, poly(ε-caprolactone) diol (PCLD), and 2,2-dimethylolbutyric (DMBA) acid as hard, soft segments and anionic internal emulsifier respectively. Then, cross-linking of the obtained PU was carried out by GG and BD to yield GG-PU final product. The employment of GG up to 0.3 wt% results in an increase in the tensile strength, thermal stability and water resistance of GG-PU, which can be used as finishing and coating layers.
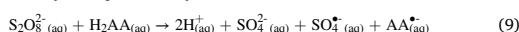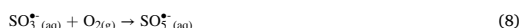
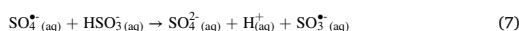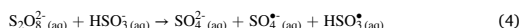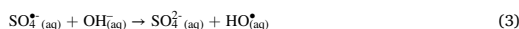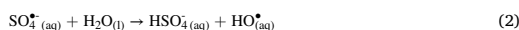#### 3.3.2. Ring-opening polymerization (ROP)

Over the years, ring-opening polymerization (ROP) has been of great interest to prepare and graft polymers from cyclic monomer starting materials [227–231]. Recently, El Assimi and coworkers employed ROP to prepare PCL grafted GG (GG-g-PCL) (Fig. 6) [232]. Tetra(phenyl-ethynyl)tin [Sn(C≡CPh)₄ or SnAK] was used to initiate -OH groups on GG into alkoxy-tin(IV) (GG-O-Sn(C≡CPh)₃) moieties at room temperature in ambient atmosphere, followed by ROP of ε-caprolactone (ε-CL) onto GG. GG-g-PCL products with 1, 3 and 5 % w/w has lower hydrophilicity than native GG, which was confirmed by contact angle measurements, and can be well-dispersed in DCM solvent over a long period of time. The dispersity and reaction yield of grafted PCL was approximated of 1.75–1.86 and 92–94 % respectively. GG-g-PCL was successfully employed as a coating agent to formulate slow-release fertilizer of diammonium phosphate [233].

3.3.3. Free-radical graft polymerization (FRGP)

Free-radical polymerization is ubiquitous in polymer synthesis and modification [234,235]. The reaction is normally initiated by chemicals and/or radiation to yield free-radicals, followed by polymerization with different vinyl monomers and multifunctional cross-linkers [222].

In the recent past, a wide range of chemical initiators has been employed in free-radical graft polymerization. For instance, ceric(IV) ammonium nitrate [$(NH_4)_2[Ce(NO_3)_6]$ or CAN] is a common oxidizing agent and radical initiator in chemical synthesis. In water, CAN dissociates to hexanitratocerate(IV) [$[Ce(NO_3)_6]^{2-}$], while further dissociation and hydrolysis of Ce^{4+} ions might occur depending on pH conditions. Besides acting as a one-electron oxidant, oxo-bridged dinuclear cerium(IV) complexes [$[Ce^{IV}$-O-$Ce^{IV}]^{6+}$] can also behave as two-electron oxidizing agents [236]. Moreover, peroxydisulfate or persulfate ($S_2O_8^{2-}$) can also be used as a free-radical initiator due to the presence of peroxide O-O bond [237]. Commercially available forms of peroxydisulfate can be found with different counter-cations such as NH_4^+ [ammonium persulfate, $(NH_4)_2S_2O_8$ or APS], Na^+ (sodium persulfate, $Na_2S_2O_8$ or SPS) and K^+ (potassium persulfate, $K_2S_2O_8$ or KPS). Physical (thermal) activation of peroxydisulfate is normally carried out to yield sulfate radical anions ($SO_4^{\bullet-}$) and/or hydroxyl radicals ($HO^{\bullet}$) in aqueous media [Eq. (1) to (3)] [238]. In addition, chemical reactions between peroxydisulfate and reducing agents such as bisulfite (HSO_3^-) and metabisulfite [$S_2O_5^{2-}$, a precursor of HSO_3^-, Eq. (6)] also allow the formation of $SO_4^{\bullet-}$, S-centered bisulfite free radicals ($HSO_3^{\bullet}$) and S-centered metabisulfite radical anions ($S_2O_5^{\bullet-}$) [Eq. (4), (5)] [239]. Further reactions between $SO_4^{\bullet-}$ and excess HSO_3^- might proceed to yield $HSO_3^{\bullet}$, which dissociates into proton (H^+) and S-centered sulfite radical anions ($SO_3^{\bullet-}$) [Eq. (7)] [240,241]. Moreover, $SO_3^{\bullet-}$ can react with dissolved O_2 to form peroxymonosulfate radical anions ($SO_5^{\bullet-}$) [Eq. (8)], which might result in more complex free-radical reactions [242]. Organic amines, such as TMEDA or TEMED, can also be used to initiate the formation of free-radicals via chemical reactions between nucleophilic N and O from peroxide O-O bonds of persulfates [243–245]. In addition, ascorbic acid (H_2AA) might also initiate the transformation of persulfate into $SO_4^{\bullet-}$ free-radicals with ascorbic acid radical anion ($AA^{\bullet-}$) by products for graft polymerization [Eq. (9)] [246–248].

$$S_2O_8^{2-}{}_{(aq)} \rightarrow 2\ SO_4^{\bullet-}{}_{(aq)} \tag{1}$$

$$SO_4^{\bullet-}{}_{(aq)} + H_2O_{(l)} \rightarrow HSO_4^-{}_{(aq)} + HO^{\bullet}{}_{(aq)} \tag{2}$$

$$SO_4^{\bullet-}{}_{(aq)} + OH^-{}_{(aq)} \rightarrow SO_4^{2-}{}_{(aq)} + HO^{\bullet}{}_{(aq)} \tag{3}$$

$$S_2O_8^{2-}{}_{(aq)} + HSO_3^-{}_{(aq)} \rightarrow SO_4^{2-}{}_{(aq)} + SO_4^{\bullet-}{}_{(aq)} + HSO_3^{\bullet}{}_{(aq)} \tag{4}$$

$$S_2O_8^{2-}{}_{(aq)} + S_2O_5^{2-}{}_{(aq)} \rightarrow SO_4^{2-}{}_{(aq)} + SO_4^{\bullet-}{}_{(aq)} + S_2O_5^{\bullet-}{}_{(aq)} \tag{5}$$

$$S_2O_5^{2-}{}_{(aq)} + H_2O_{(l)} \rightarrow 2\ HSO_3^-{}_{(aq)} \tag{6}$$

$$SO_4^{\bullet-}{}_{(aq)} + HSO_3^-{}_{(aq)} \rightarrow SO_4^{2-}{}_{(aq)} + H^+{}_{(aq)} + SO_3^{\bullet-}{}_{(aq)} \tag{7}$$

$$SO_3^{\bullet-}{}_{(aq)} + O_{2(g)} \rightarrow SO_5^{\bullet-}{}_{(aq)} \tag{8}$$

$$S_2O_8^{2-}{}_{(aq)} + H_2AA_{(aq)} \rightarrow 2H^+{}_{(aq)} + SO_4^{2-}{}_{(aq)} + SO_4^{\bullet-}{}_{(aq)} + AA^{\bullet-}{}_{(aq)} \tag{9}$$

In the presence of radical initiators, different carbon-centered and/or oxygen-centered free-radicals of polysaccharides can be formed (Fig. 6a, 6b). Electron spin resonance (ESR) studies suggest that Ce^{4+} can chelate to two adjacent -OH groups, possibly at C2 and C3 positions on AGUs of polysaccharides. Then, an electron transfer from the AGU to Ce^{4+} occurs, resulting in the reduction of Ce^{4+} to Ce^{3+}, pyranose ring opening due to C2-C3 bond cleavage and formation of a carbon-centered radical species [249,250]. Moreover, $S_2O_8^{2-}$ can be activated to yield $SO_4^{\bullet-}$ and $HO^{\bullet}$. These free radicals can approach -OH groups on polysaccharides and subsequently convert them into oxygen-centered radical sites for grafting polymerization [251]. In addition, other free-radical initiation pathways of polysaccharides have been proposed such as hydrogen abstraction on C6, oxidative cleavage of O-C1 bond in terminal AGU of polysaccharide chain, etc. (Fig. 6c) [252]. Once free-radicals are formed, propagation of FRGP can occur with various vinyl-containing monomers and cross-linkers (Fig. 6d).

3.3.3.1. Acrylic acid (AA) monomer.

Among various polymers, poly (acrylic acid) (PAA) has been commonly used in the fabrication of numerous biocompatible and biodegradable gel systems to enhance the pH-responsiveness of materials due to numerous carboxylic acid groups on the polymer backbone [253–255].

Recently, several research groups have tried to graft AA onto GG to fabricate acrylic acid grafted guar gum (GG-g-PAA) polymers by varying the composition of GG, PAA, free-radical initiators and different cross-linkers. For instance, L-alanine (Ala) cross-linker was used by Sharma and coworkers to prepared Ala-cross-linked GG-g-PAA (Ala-cl-GG-g-PAA) in order to enhance the hydrogen bonding network, self-healing properties and to study the controlled release of levofloxacin hydrophilic medication under physiological pH and temperature [256]. Concentration of Ala was varied from 0.4 to 1 % w/v to show that Ala-cl-GG-g-PAA with 1 % w/v Ala possesses good thermal stability from 30 to 90 °C, the best mechanical and swelling properties (3350 % at pH 9). The obtained GG-g-PAA gels also show drug-loading efficiency of around 65 and 75 %, while the drug release can reach up to 98 % with varying release time up to 130 h, due to changes in the concentration of Ala.

Bifunctional MBAAm has been widely employed as a vinyl-containing cross-linker for GG and other polymeric systems [257]. Recently, Shamanta et al. studied the swelling and mechanical strength of MBAAm-cross-linked GG-g-PAA (MBAAm-cl-GG-g-PAA) hydrogels, which was prepared from an optimized system of 1 wt% APS, 1 wt% MBAAm, 25 wt% AA and 4 wt% GG [258]. Pyridoxine hydrochloride (vitamin B6) was chosen as model medication to examine the gradual drug release of the synthesized MBAAm-cl-GG-g-PAA hydrogel. Under physiological pH, carboxylic acid groups of MBAAm-cl-GG-g-PAA hydrogels get deprotonated into negatively charged carboxylates, leading to electrostatic repulsion between functional groups with the same charge, hence, swelling of the gels. This allows the physical desorption and release of vitamin B6 from the MBAAm-cl-GG-g-PAA hydrogels up to 95 % over 30 h. Moreover, MBAAm was also chosen by HaqAsif et al. to develop drug delivery systems for curcumin with the cumulative release up to 100 % over 12 h [259].

Besides using MBAAm to cross-link GG-g-PAA polymers, Singh and Dhaliwal also incorporated Ag NPs into MBAAm-cl-GG-g-PAA polymer matrix to fabricate a new MBAAm-cl-GG-g-PAA/Ag NPs adsorbent for removal of MB dye [260]. The Ag NPs with an average size of 100 nm, offer large specific surface area and surface energy to the matrix, resulting in an improvement in MB adsorption capacity of the polymer matrix. Meanwhile, Li and coworkers incorporated GG and sodium lignosulfonate (SLS) together to develop novel MBAAm-cross-linked AA grafted GG/SLS (MBAAm-cl-GG/SLS-g-PAA) hydrogel adsorbents [261]. Due to the presence of various coordinating functional groups such as alcohols, phenols, sulfonic acid and carboxylic acid, the MBAAm-cl-GG/SLS-g-PAA hydrogels show good chelating and adsorption capacity towards Cu^{2+} and Co^{2+} metal ions (709 mg g^{-1} and 601 mg g^{-1} respectively). Under neutral pH, deprotonation of acidic functional groups allows stronger adsorption of metal ions, while acidic pH can also be exploited for desorption and recovery of metal ions, resulting in good reversibility and reusability of the hydrogel adsorbents.

In the recent time, copolymers between AA and other vinyl-containing monomers have also been explored. Pal et al. reported the grafting of GG with poly(AA-co-acrylonitrile) [P(AA-co-AN)] copolymer to yield MBAAm-cross-linked AA-co-AN grafted GG [MBAAm-cl-GG-g-P(AA-co-AN)] [262]. While AA enhances pH-responsiveness of GG, AN is expected to improve physiochemical properties of the polysaccharide. Microwave was employed to initiate grafting polymerization in the absence of free-radical initiators. Different reaction parameters were optimized to achieve the best reaction conditions in terms of grafting yield (GY) (0.03 mol/L AA, 1.0 mol/L AN, 2000W microwave power under 100 s to receive 82.84 % grafting yield). Encapsulation of antioxidant and anti-inflammatory thymoquinone (TQ) by MBAAm-cl-GG-P(AA-co-AN) was carried out to demonstrate potential applications of

the novel grafted GG, and to increase the low bioavailability of TQ in aqueous media. Under physiological pH condition, swelling of MBAAm-cl-GG-g-P(AA-co-AN) can be observed due to the formation of carboxylate groups from deprotonation of AA or hydrolysis of AN, resulting in the maximum release of TQ up to 78 % over 6 h. Moreover, this drug delivery system also shows hemocompatibility and no cytotoxicity against the tested monkey normal kidney Vero cell line.

In addition, grafting of AA and AAm onto GG was chosen to fabricate MBAAm-cross-linked AA-co-AAm grafted GG [MBAAm-cl-GG-g-P(AA-co-AAm)] by Karnakar and Gite for the gradual release of $ZnSO_4$ as a micronutrient for plant growth [263]. The release kinetics of $ZnSO_4$ from MBAAm-cl-GG-g-P(AA-co-AAm) into water fits Korsmeyer-Peppas and Peppas-Sahlin mathematical models. MBAAm-cl-GG-g-P(AA-co-AAm) was found degradable under hydrolytic and soil burial conditions (pH 7.4–7.5, 37 °C). Moreover, Gihar et al. also prepared GG-g-P(AA-co-AAm) via microwave-assisted graft polymerization for the removal of Hg^{2+} ions from aqueous solutions [264]. Hg^{2+} adsorption by the obtained GG-g-P(AA-co-AAm) shows best performance at pH 6, while acidic pH less than 3 reduces the adsorption capacity of GG-g-P(AA-co-AAm). This might be attributed to the deprotonation and protonation of carboxylic acid functional groups.

Mitra and coworkers recently prepared MBAAm-cross-linked AA-co-N-isopropylacrylamide grafted GG [MBAAm-cl-GG-g-P(AA-co-NIPAAm)] using AA and N-isopropylacrylamide (NIPAAm) [265]. The employed FRGP was initiated by chemical reaction between KPS and sodium bisulfite (SBS) at mild temperature (25 °C). Under the reported synthetic condition, in-situ reactions between grafted NIPAAm and free AA yield 3-(N-isopropylacrylamido)propanoic acid (NIPAAmPA) moieties also occurred, resulting in MBAAm-cross-linked AA-co-NIPAAm-co-NIPAAmPA grafted GG [MBAAm-cl-GG-g-P(AA-co-NIPAAm-co-NIPAAmPA)] as non-aromatic clusteroluminogenic polymers. MBAAm-cl-GG-g-P(AA-co-NIPAAm-co-NIPAAmPA) absorbs mainly in the UV radiation range between 200 and 350 nm depending on solvents of choice, while fluorescent emission maxima of the polymer between 400 and 450 nm were recorded. Computational studies by DFT reveal effects of NIPAmPA moieties on electronic transitions between highest occupied molecular orbital (HOMO) and lowest unoccupied molecular orbital (LUMO). MBAAm-cl-GG-g-P(AA-co-NIPAAm-co-NIPAAmPA) shows biocompatibility to normal mammalian Madin-Darby canine kidney (MDCK) cells and a certain degree of cytotoxicity against human osteosarcoma (HOS) cancer cells. The obtained polymer can also be exploited for fluorescent sensing of Pb^{2+}, based on reversible fluorescence quenching of the polymer due to the disruption of hydrogen bonding network and breakdown of polymer aggregates in the presence of Pb^{2+} metal ions.

3.3.3.2. Acrylamide (AAm) monomer.

Nonionic biocompatible poly-acrylamide (PAAm) and its derivatives have been widely found in various industries, clinical and environmental systems [266–268].

Recently, AAm monomers have also been employed to fabricate new AAm grafted GG (GG-g-PAAm) materials. For instance, Sand and Vyas reported the grafting reaction in the presence of tetra(ethyleneglycol) diacrylate (TEGDA) cross-linker to yield TEGDA-cross-linked GG-g-PAAm (TEGDA-cl-GG-g-PAAm) absorbent [269]. 0.8 wt% of KPS initiator was found as an optimum concentration in terms of reaction yield and water absorbing capacity of the obtained material. Varying concentrations of TEGDA cross-linkers from 0.4 to 1.2 wt% shows no significant effect on the reaction yield but decreases the water absorbing capacity. The optimized TEGDA-cl-GG-g-PAAm has swelling capacities of 80 g g^{-1} for deionized water and 22 g g^{-1} for 0.8 wt% sodium chloride solution.

In addition, Mahto and Mishra prepared borax-cross-linked GG-g-PAAm (borax-cl-GG-g-PAAm) with grafting yield and efficiency up to 795.6 %, 79.5 % respectively, and tested the material as an adsorbent for removal of reactive blue 19 (RB19) textile dye [270]. The optimized
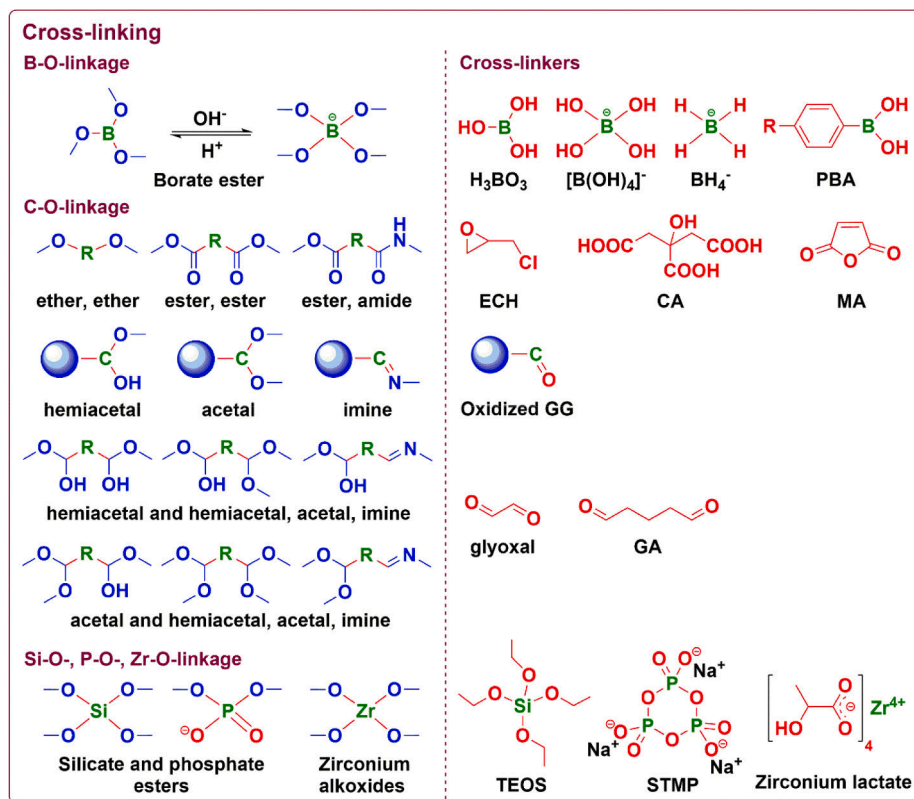
Fig. 7. Cross-linking of GG and its derivatives via B-O-, C-O-, Si-O-, P-O-, Zr-O-linkages (left) and reported cross-linkers (right).

borax-cl-GG-g-PAAm can adsorb up to 1073.84 mg g^{-1} with removal percentage of 80 %. Mildly acidic pH around 6.0 allows the best electrostatic interaction between sulfonate groups of RB19 and amide functional groups from borax-cl-GG-g-PAAm.

Meanwhile, Elsaeed and coworkers fabricated MBAAm-cross-linked AAm-*co*-2-acrylamido-2-methyl-1-propane sulfonic acid (AMPS) grafted GG [MBAAm-cl-GG-g-P(AAm-*co*-AMPS)] hydrogel and further modified this into a composite with biochar carbonic material [MBAAm-cl-GG-g-P(AAm-*co*-AMPS)/biochar] for enhanced oil recovery via polymer flooding under highly saline reservoir conditions [271]. AMPS contains both nonionic and ionic moieties, which can enhance salt tolerance, swelling capacity of the polymer and oil displacement from the sandstone surface during the secondary oil recovery process up to around 12 %, with the optimum polymer concentration of 5 g L^{-1}. Incorporating hydrophobic biochar into the polymer matrix offers high surface area and an enhancement in secondary oil recovery process of around 6 % with lower optimum polymer concentration of 2 g L^{-1}.

Recently, Palem et al. developed multifunctional nanocomposite hydrogels, which consist of MBAAm-cross-linked AAm-*co*-2-acrylamidoglycolic acid (AGA) grafted GG and Ag nanoparticles (Ag NPs) [MBAAm-cl-GG-g-P(AAm-*co*-AGA)/Ag NPs], for various applications [272]. Ag NPs were incorporated into the polymer matrix via diffusion of free Ag$^+$ ions, followed by reduction of Ag$^+$ by active components

such as quinones, emodin and rhein in rhubarb-stem extract *(Rheum rhabarbarum)* bio-reductants. MBAAm-cl-GG-g-P(AAm-*co*-AGA) shows pH-responsiveness due to the presence of carboxylic acids, and better biodegradability than its nanocomposite with Ag NPs, which can be attributed to the antimicrobial activity of Ag NPs. Further confirmation on antimicrobial activity of the nanocomposites against *B. subtilis* (ATCC 6633) and *E. coli* (ATCC 25922) has also been reported. Moreover, the introduction of Ag NPs into the polymer matrix increases the matrix porosity, resulting in better drug encapsulation of 5-fluorouracil (FU), which was chosen as an anticancer model medication to study the drug release behavior of MBAAm-cl-GG-g-P(AAm-*co*-AGA)/Ag NPs. Under physiological pH, FU can be released due to the deprotonation of carboxylic acid groups and swelling of the polymer. Furthermore, the developed composite also shows catalytic potential for the reduction of p-nitrophenol to p-aminophenol using sodium borohydride (NaBH$_4$) reducing agent in aqueous solution.

3.3.3.3. Other monomers. Das and Subuddhi grafted NIPAAm, which is a thermo-responsive derivative of AAm, onto GG using APS and TEMED activator [273]. While NIPAAm has a low critical solution temperature of around 33 °C, its low mechanical stability, biocompatibility and sustained drug-releasing ability can be improved by combining with GG.

The obtained graft polymer was further cross-linked by TEOS to yield TEOS-cross-linked NIPAAm grafted GG (TEOS-cl-GG-g-PNIPAAm) hydrogel to show good biocompatibility towards L-929 rat fibroblasts. FU was also chosen to study drug release behavior of the hydrogel. By increasing weight percentage of GG comparing to NIPAAm, longer drug release time and slower drug release rate of the hydrogel can be obtained. In addition, host-guess complexation between β-cyclodextrin (β-CD) and FU was also carried out to form β-CD/FU complex, therefore, enhancing the aqueous stability, solubility and bioavailability of the medication.

Besides, AGA was grafted to GG by Palem and coworkers to obtain AGA grafted GG (GG-g-PAGA) polymer [274]. Ag$^+$ ions were then dispersed in the polymer system and reduced to Ag NPs of around 5.4 nm by NaBH$_4$, which also allowed the cross-linking of GG-g-PAGA to form NaBH$_4$-cross-linked GG-g-PAGA/Ag NPs (NaBH$_4$-cl-GG-g-PAGA/Ag NPs) nanocomposite. The prepared nanocomposite possesses self-healing property, stretchability, antibacterial activity against *E. coli*, *S. aureus*, *P. aeruginosa*, cytocompatibility to human skin fibroblast (CCD-986sk) cell lines and therefore, a promising candidate for wound dressing and drug release [275].

Singh et al. recently prepared MBAAm-cross-linked AMPS grafted GG (MBAAm-cl-GG-g-PAMPS) as a corrosion inhibitor for copper in NaCl media [276]. The corrosion inhibition efficiency of GG-g-PAMPS was evaluated by electrochemistry and reported up to 95 % at 600 mg L^{-1} concentration. In addition, they also fabricated ethyl acrylate (EA) grafted GG (GG-g-PEA) using KPS and H$_2$AA activator at mild temperature (35 °C) [277]. The obtained GG-g-PEA graft polymer was tested as a corrosion inhibitor to reduce P110 steel corrosion in acidic environment. The spontaneous adsorption of GG-EEA onto P110 steel surface was found both physical and chemical. Molecular dynamic simulations were performed and indicated an improvement in adsorption capacity of GG-g-PEA onto the steel surface, comparing to pristine GG. The corrosion inhibition efficiency of GG and GG-g-PEA for P110 steel was reported as 77.5 and 92.3 % respectively at 500 mg L^{-1} concentration.
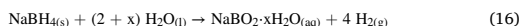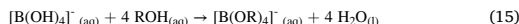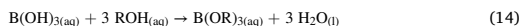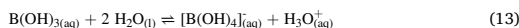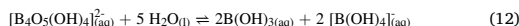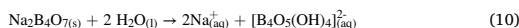
Moreover, CAN and microwave irradiation was used by Mahto and Mishra to graft 2-hydroxyl ethyl methacrylate (HEMA) to GG (GG-g-PHEMA) via three cycles of MW irradiation and cooling in ice bath [278]. Molar ratio of GG, HEMA and CAN was optimized to obtain the grafting percentage of 1142 % and grafting efficiency (GE) of 114.22. To demonstrate the drug delivery capacity of GG-g-PHEMA, the graft polymer together with PVP binder, 5-aminosalicylic acid (ASA) medication, silicon dioxide (SiO$_2$) and magnesium stearate were physically mixed and formulated into GG-g-PHEMA/ASA tablets. Swelling of GG-g-PHEMA was observed under all tested pH of 1.2, 6.8, 7.4, allowing the gradual release of ASA from the tablets under these pH conditions.

3.4. Cross-linking

3.4.1. B-O-linkage

Borate esters have been widely employed as cross-linkers for polyol compounds and various polymers [279–281]. Commercially available borax [anhydrous sodium tetraborate (Na$_2$B$_4$O$_7$), sodium tetraborate pentahydrate (Na$_2$B$_4$O$_7$·5H$_2$O), sodium tetraborate decahydrate [Na$_2$B$_4$O$_7$·10H$_2$O or Na$_2$[B$_4$O$_5$(OH)$_4$]·8H$_2$O]] is normally used as a source of boron for cross-linking. In aqueous media, borax dissociates to hydrated tetraborate [[B$_4$O$_5$(OH)$_4$]$_{(aq)}^{2-}$, Eq. (10), (11)], followed by further hydrolysis to yield a mixture of boric acid [B(OH)$_{3(aq)}$, pK$_a$ ≈ 9.14] and tetrahydroxyborate conjugate base, [[B(OH)$_4$]$_{(aq)}^-$, Eq. (12)]. The molar ratio between boric acid and tetrahydroxyborate varies accordingly to pH of the media [Eq. (13)], and they can also react with alcohol groups to form borate ester linkages [Eq. (14), (15)]. Moreover, sodium borohydride (NaBH$_4$) is also exploited as a common source of

boron. In aqueous media, NaBH$_4$ hydrolyzes to form hydrated sodium metaborate [NaBO$_2$, Eq. (16)], especially in the presence of catalysts [282,283]. Further hydrolysis of NaBO$_2$ yields [B(OH)$_4$]$^-$ [Eq. (17)], which allows the cross-linking with vicinal diol groups via the formation of borate ester bonds (Fig. 7).[284].

$$Na_2B_4O_{7(s)} + 2\ H_2O_{(l)} \rightarrow 2Na_{(aq)}^+ + [B_4O_5(OH)_4]_{(aq)}^{2-} \tag{10}$$

$$Na_2[B_4O_5(OH)_4]\cdot 8H_2O_{(s)} \rightarrow 2Na_{(aq)}^+ + [B_4O_5(OH)_4]_{(aq)}^{2-} \tag{11}$$

$$[B_4O_5(OH)_4]_{(aq)}^{2-} + 5\ H_2O_{(l)} \rightleftharpoons 2B(OH)_{3(aq)} + 2\ [B(OH)_4]_{(aq)}^- \tag{12}$$

$$B(OH)_{3(aq)} + 2\ H_2O_{(l)} \rightleftharpoons [B(OH)_4]_{(aq)}^- + H_3O_{(aq)}^+ \tag{13}$$

$$B(OH)_{3(aq)} + 3\ ROH_{(aq)} \rightarrow B(OR)_{3(aq)} + 3\ H_2O_{(l)} \tag{14}$$

$$[B(OH)_4]_{(aq)}^- + 4\ ROH_{(aq)} \rightarrow [B(OR)_4]_{(aq)}^- + 4\ H_2O_{(l)} \tag{15}$$

$$NaBH_{4(s)} + (2 + x)\ H_2O_{(l)} \rightarrow NaBO_2\cdot xH_2O_{(aq)} + 4\ H_{2(g)} \tag{16}$$

$$NaBO_{2(s)} + 2\ H_2O_{(l)} \rightarrow Na_{(aq)}^+ + [B(OH)_4]_{(aq)}^- \tag{17}$$

Boron-based cross-linkers can be introduced to the GG polymeric structures by simple dissolution and mixing of borax, boric acid or sodium borohydride with GG in aqueous media [285–287]. Recently, Pugliese and Gelain prepared and cross-linked a self-assembly peptide (SAP) NH$_2$-FAQRVPPGGGLDLKLDLKLDLK-CONH$_2$ and GG using borax at pH 8.5 to form self-healing borax-cross-linked GG-SAP (borax-cl-GG-SAP) composite hydrogel [288]. GG was combined with SAP to enhance elasticity, mechanical strength and thermo-responsiveness of SAP. Meanwhile, Cao and coworkers used borax to cross-link GG in the presence of gellan gum (GelG) to form borax-cross-linked GG-GelG (borax-cl-GG-GelG) composite hydrogel [289]. At room temperature, GelG adopts hard and brittle double helix conformation with good compatibility to GG. The borax-cl-GG-GelG hydrogel exhibits electrical conductivity due to the presence of borate ions, as well as self-healing properties because of dynamic borate and hydrogen bonds. Mechanical deformation of the hydrogel can produce electrical signals, allowing the fabrication of flexible hydrogel-based strain sensors for detecting and monitoring human motions with good repeatability and reliability.

Additionally, a wide range of inorganic particles has been incorporated into GG-based polymeric matrices to form composites. For example, Dassanayake et al. recently cross-linked GG by borax to yield borax-cross-linked GG (borax-cl-GG) [290]. Then, permanganate(VII) (MnO$_4^-$) precursor ions were allowed to diffuse into the borax-cl-GG polymeric structure and oxidize -OH groups of GG. Meanwhile, MnO$_4^-$ was reduced into manganate(VI) (MnO$_4^{2-}$) ions, and eventually to manganese dioxide (MnO$_2$) nanoparticles under alkaline pH, resulting in the formation of borax-cl-GG/MnO$_2$ brownish nanocomposite. Potential applications of B-cl-GG/MnO$_2$ were demonstrated based on oxidative decolorization of MB dye. Comparing to MnO$_2$ nanoparticle reference, the borax-cl-GG/MnO$_2$ photocatalyst has a much better oxidative decolorization capacity under the tested pH of 4, 7 and 10.

Moreover, Wang and coworkers employed NaBH$_4$ to cross-link GG with a composite of Pd heterogeneous catalyst nanoparticles (Pd NPs) and cellulose nanocrystal (CNC) system (CNC/Pd NPs) [291]. A homogeneous mixture of PdCl$_2$ and CNC was firstly prepared, followed by the reduction of Pd^{2+} to Pd NPs by NaBH$_4$ reducing agent to form CNC/Pd NPs nanocomposite. Then, the obtained CNC/Pd NPs nanocomposite was mixed with GG and NaBH$_4$ to yield NaBH$_4$-cross-linked GG/CNC/Pd NPs (NaBH$_4$-cl-GG/CNC/Pd NPs) nanocomposite. The boron-based cross-linkers are temperature-sensitive, which allows the sol–gel transition by changing the temperature of NaBH$_4$-cl-GG/CNC/Pd NPs, hence, the catalytic reactions and recycling of Pd NPs. The catalytic activity of NaBH$_4$-cl-GG/CNC/Pd NPs was tested on Suzuki cross coupling reactions between various aryl halides and aryl boronic acids
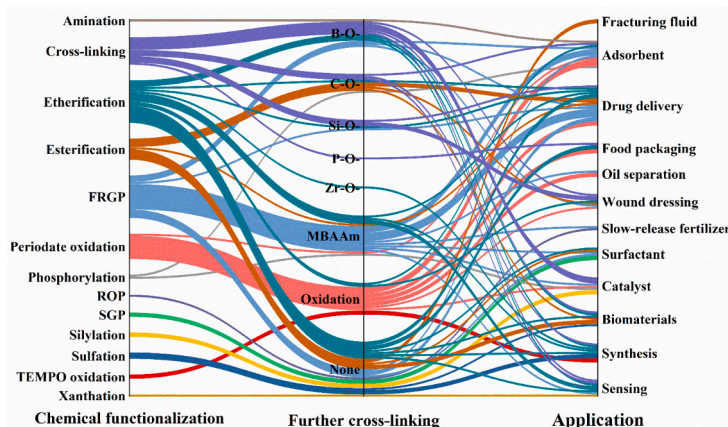
Fig. 8. Summary on different chemical functionalization, further cross-linking approaches and potential applications of GG and its derivatives.

and showed promising efficiency and recyclability.

Recently, Talodthaisong and coworkers cross-linked Cur-stabilized Ag NPs (Cur-Ag NPs) and GG to develop borax-cross-linked GG/Cur-Ag NPs (borax-cl-GG/Cur-Ag NPs) nanocomposite [292]. Borax was used to cross-link GG in the presence of Cur-stabilized Ag NPs, which were obtained from thermal decomposition of $AgNO_3$, resulting in injectable self-healing borax-cl-GG/Cur-Ag NPs hydrogel. The hydrogel is also pH- and temperature-responsive due to the responsiveness of borate ester cross-linkers present in the hydrogel structure. In addition, borax-cl-GG/ Cur-Ag NPs also possesses antibacterial activity, with greater inhibition capacity against gram-positive bacteria (*E. coli, P. aeruginosa*) compared to gram-negative bacteria (*S. Aureus*).

Meanwhile, Deka et al. employed $NaBH_4$ as a reducing agent for the preparation of Ag NPs from $AgNO_3$, and a cross-linker for GG and PVA polymeric matrix [293]. The fabricated $NaBH_4$-cross-linked GG/PVA/ Ag NPs ($NaBH_4$-cl-GG-PVA/Ag NPs) nanocomposite also shows pH-responsiveness, injectability, improved mechanical strength and antibacterial activity against *E. coli*. Moreover, $NaBH_4$-cl-GG-PVA/Ag NPs is a promising catalyst for reduction of nitrobenzene to aniline using $NaBH_4$ reductant.

3.4.2. C-O-linkage

Various C-based functional groups have been employed in the cross-linking of GG and its derivatives (Fig. 7). For example, epoxide and chloro groups on ECH can easily form ether groups for cross-linking [180]. Moreover, carboxylic acid anhydrides can be used for cross-linking via the formation of ester, amide bonds, and/or aza-Michael addition reaction [85,142]. Aldehyde functional groups, which might be found directly on oxidized GG and its derivatives, or from external cross-linkers such as GA, have also shown efficient cross-linking with other polysaccharides via the formation of hemiacetal, acetal and/or imine linkages [122,123,136,137,149,200,208–213,294].

Additionally, Bag and coworkers employed GA to cross-link GG into a polymeric structure in the presence of iron oxide nanoparticles (Fe_3O_4 NPs) for the fabrication of GA-cross-linked GG/Fe_3O_4 NPs (GA-cl-GG/ Fe_3O_4 NPs) nanocomposite [295]. Firstly, Fe_3O_4 NPs were synthesized by coprecipitation method with an assistance of citric acid surfactant. Then, GG was cross-linked in the presence of the Fe_3O_4 NPs to obtain the nanocomposite final product, which shows no genotoxic effects on Drosophila melanogaster fruit flies.

To enhance mechanical strength and self-healing properties of natural polysaccharide-based hydrogels, Rao et al. combined two self-

healing mechanisms, namely, covalent cross-linking between GG, sodium alginate (SAL) by GA, and coordination bonds between SAL, dopamine (DA) and Fe^{3+} [296]. Stellate mesoporous silica (STMS) nanoparticles with high specific surface area and large pore volume, were chosen to store GA cross-linking agent for its gradual release, and to offer a surface for the preparation of polydopamine. The obtained PDA-coated GA-loaded STMS (PDA-STMS/GA) nanoparticles were dispersed in a mixture of Fe^{3+}, GG and SAL to fabricate GA, Fe^{3+}-cross-linked GG/SAL/DA-STMS/GA (GA, Fe^{3+}-cl-GG/SAL/DA-STMS/GA) nanocomposite. The nanocomposite product possesses excellent self-healing properties, tensile strength (up to 7.0 MPa) and can also be used to develop strain electronic sensors.

Besides GA, glyoxal can also be employed as a cross-linker and was used by Gupta et al. to develop glyoxal-cross-linked GG/activated C (glyoxal-cl-GG/activated C) nanocomposite [297]. The obtained nanocomposite has been found as a promising dye adsorbent for wastewater treatment, with adsorption capacity of 831.82 mg g^{-1} at 30 °C and good recyclability.

3.4.3. Si-O-linkage

TEOS is a typical Si-containing precursor for cross-linking GG and its derivatives [81,86,273]. Recently, Butt el al. blended a mixture of GG, CS, polyethylene glycol (PEG), cephradine (CED) antibiotic medication in water and chemically cross-linked these polymers by TEOS to develop a novel pH-sensitive TEOS-cross-linked GG-CS-PEG/CED (TEOS-cl-GG-CS-PEG/CED) hydrogel for controlled drug release of CED [298]. Better swelling behavior of the prepared hydrogels was recorded under acidic environment (pH around 4), comparing to neutral and alkaline pH. This might be attributed to the protonation of -NH_2 functional groups in CS, resulting in electrostatic repulsion and swelling of the polymeric matrix. The loaded CED can be released from the hydrogels in a controlled manner, up to 85 % in PBS and 82.4 % in simulated intestinal fluid (SIF) over 130 min.

Meanwhile, Khan and coworkers also used TEOS in cross-linking GG and arabinoxylan (ARX) to fabricate TEOS-cross-linked GG-ARX (TEOS-cl-GG-ARX) hydrogels, as well as GG, CS and PVA to prepare TEOS-cross-linked GG-CS-PVA (TEOS-cl-GG-CS-PVA) hydrogels for wound dressing [299,300]. Maximum swelling of TEOS-cl-GG-ARX and TEOS-cl-GG-CS-PVA hydrogels were reported at pH 7 and 4 respectively. Silver sulfadiazine (SSD) antibiotic was incorporated into TEOS-cl-GG-ARX (TEOS-cl-GG-ARX/SSD) hydrogel. This drug release hydrogel shows antimicrobial activity against skin disease-causing bacteria such as

gram-negative *P. aeruginosa*, gram-positive *S. aureus*, and noncytotoxic responses towards mouse MC3T3-E1 cell line. Besides, paracetamol was loaded into TEOS-cl-GG-CS-PVA (TEOS-cl-GG-CS-PVA/paracetamol) and could be released up to 98 % in PBS medium at pH 7.4. The TEOS-cl-GG-CS-PVA/paracetamol hydrogels also possess antibacterial activity against gram-negative (*E. coli*, *P. aeruginosa*) and gram-positive (*B. cereus*, *S. aureus*) bacteria.

3.4.4. P-O-linkage

Aydogdu and coworkers recently demonstrated the cross-linking of GG in the presence of SL emulsion stabilizer, glycerol plasticizer, orange oil, using non-toxic, FDA-approved STMP cross-linker under alkaline condition (pH 12) [301]. The fabricated STMP-cross-linked GG/orange oil (STMP-cl-GG/orange oil) films were tested for food packaging. Incorporation of orange oil into the films and crosslinking of GG decrease the water dissolvability and surface water wettability of these films, hence, enhancing their hydrophobicity. In addition, the films also show antimicrobial activity against gram-negative (*E. coli*) and gram-positive (*B. subtilis*) bacteria.

4. Conclusions

In the recent past, various chemical modification approaches of natural GG polysaccharide and its derivatives have been explored to alter their properties and extend their applicability in numerous fields (Fig. 8). Among the reported functionalization methods, etherification, esterification, FRGP, periodate-mediated oxidation and cross-linking have been ones of the most commonly used chemical reactions, while other reaction pathways such as amination, phosphorylation, ROP, SGP, silylation, sulfation, TEMPO-mediated oxidation and xanthation are also promising for future research. Moreover, further cross-linking of chemically modified GG has also been of profound interest and can be done by employing different chemical cross-linking methods. Chemical derivatives of natural GG are versatile polysaccharides that can be used in numerous fields, from biomedicine, wound dressing, drug delivery, to catalysis, sensing, food packaging, surfactant, slow-release fertilizer, metal corrosion inhibition, waste treatment, oil separation and recovery. With a fascinating increase in the amount of published work on GG, this review can be used as a library of choice for readers who are searching for chemical modification approaches of GG and its derivatives to develop and explore novel properties and applications of GG-based advanced materials (Table 2).

CRediT authorship contribution statement

Trung-Anh Le: Conceptualization, Methodology, Investigation, Writing – original draft, Writing – review & editing. **Tan-Phat Huynh:** Conceptualization, Supervision, Writing – review & editing.

Declaration of Competing Interest

The authors declare the following financial interests/personal relationships which may be considered as potential competing interests: Tan-Phat Huynh reports financial support was provided by Abo Akademi University Faculty of Science and Engineering. Tan-Phat Huynh reports financial support was provided by Academy of Finland. Trung-Anh Le reports was provided by Magnus Ehrnrooth foundation. Tan-Phat Huynh reports financial support was provided by Liv och Hälsa Foundation.

Data availability

The authors do not have permission to share data.

References

[1] J. Rogelj, O. Geden, A. Cowie, A. Reisinger, Net-zero emissions targets are vague: three ways to fix, Nature 591 (2021) 365–368, https://doi.org/10.1038/d41586-021-00662-3.

[2] L. Jeffry, M.Y. Ong, S. Nomanbhay, M. Mofijur, M. Mubashir, P.L. Show, Greenhouse gases utilization: A review, Fuel 301 (2021), 121017, https://doi.org/10.1016/j.fuel.2021.121017.

[3] J. González-Martín, N.J.R. Kraakman, C. Pérez, R. Lebrero, R. Muñoz, A state–of–the-art review on indoor air pollution and strategies for indoor air pollution control, Chemosphere 262 (2021), 128376, https://doi.org/10.1016/j.chemosphere.2020.128376.

[4] P. Li, X. Wang, M. Su, X. Zou, L. Duan, H. Zhang, Characteristics of Plastic Pollution in the Environment: A Review, Bull. Environ. Contam. Toxicol. 107 (2021) 577–584, https://doi.org/10.1007/s00128-020-02820-1.

[5] T. Le, T. Huynh, The Combination of Hydrogen and Methanol Production through Artificial Photosynthesis—Are We Ready Yet? ChemSusChem 11 (2018) 2654–2672, https://doi.org/10.1002/cssc.201800731.

[6] R.K. Goswami, S. Mehariya, P.K. Obulisamy, P. Verma, Advanced microalgae-based renewable biohydrogen production systems: A review, Bioresour. Technol. 320 (2021), 124301, https://doi.org/10.1016/j.biortech.2020.124301.

[7] A.-E.-L. Hesham, T. Kaur, R. Devi, D. Kour, S. Prasad, N. Yadav, et al., Current Trends in Microbial Biotechnology for Agricultural Sustainability: Conclusion and Future, Challenges (2021) 555–572, https://doi.org/10.1007/978-981-15-6949-4_22.

[8] P. Horton, S.P. Long, P. Smith, S.A. Banwart, D.J. Beerling, Technologies to deliver food and climate security through agriculture, Nat. Plants 7 (2021) 250–255, https://doi.org/10.1038/s41477-021-00877-2.

[9] Jana S, Maiti S, Jana S, Sen KK, Nayak AK. Guar gum in drug delivery applications. Natural Polysaccharides in Drug Delivery and Biomedical Applications, Elsevier; 2019, p. 187–201. 10.1016/B978-0-12-817055-7.00007-8.

[10] A. George, P.A. Shah, P.S. Shrivastav, Guar gum: Versatile natural polymer for drug delivery applications, Eur. Polym. J. 112 (2019) 722–735, https://doi.org/10.1016/j.eurpolymj.2018.10.042.

[11] Q. Huang, S. Liu, G. Wang, B. Wu, Y. Zhang, Coalbed methane reservoir stimulation using guar-based fracturing fluid: A review, J. Nat. Gas Sci. Eng. 66 (2019) 107–125, https://doi.org/10.1016/j.jngse.2019.03.027.

[12] A.K. Nayak, M.S. Hasnain, K. Pal, I. Banerjee, D. Pal, Gum-based hydrogels in drug deliveryBiopolymer-Based Formulations, Elsevier (2020) 605–645, https://doi.org/10.1016/B978-0-12-816897-4.00025-4.

[13] M. Dehghani Soltani, H. Meftahizadeh, M. Barani, A. Rahdar, S.M. Hosseinikhah, M. Hatami, et al., Guar (Cyamopsis tetragonoloba L.) plant gum: From biological applications to advanced nanomedicine, Int. J. Biol. Macromol. 193 (2021) 1972–1985, https://doi.org/10.1016/j.ijbiomac.2021.11.028.

[14] L. Saya, V. Malik, A. Singh, S. Singh, G. Gambhir, W.R. Singh, et al., Guar gum based nanocomposites: Role in water purification through efficient removal of dyes and metal ions, Carbohydr. Polym. 261 (2021), 117851, https://doi.org/10.1016/j.carbpol.2021.117851.

[15] D. Verma, S.K. Sharma, Recent advances in guar gum based drug delivery systems and their administrative routes, Int. J. Biol. Macromol. 181 (2021) 653–671, https://doi.org/10.1016/j.ijbiomac.2021.03.087.

[16] M.-E.-S. Abdel-raouf, A. Sayed, M. Mostafa, Application of Guar Gum and Its Derivatives, in, Agriculture (2022) 1–17, https://doi.org/10.1007/978-3-030-76523-1_5-1.

[17] V. Adimule, S.S. Kerur, S. Chinnam, B.C. Yallur, S.S. Nandi, Guar Gum and its Nanocomposites as Prospective Materials for Miscellaneous Applications: A Short Review, Top. Catal. (2022), https://doi.org/10.1007/s11244-022-01587-5.

[18] S. Kaur, S. Santra, Recent Progress in Chemical Modification of the Natural Polysaccharide Guar Gum, Curr. Org. Synth. 19 (2022) 197–219, https://doi.org/10.2174/1570179418666211109105416.

[19] G. Sharma, S. Sharma, A. Kumar, A.H. Al-Muhtaseb, M.u. Naushad, A.A. Ghfar, et al., Guar gum and its composites as potential materials for diverse applications: A review, Carbohydr. Polym. 199 (2018) 534–545, https://doi.org/10.1016/j.carbpol.2018.07.053.

[20] S. Thakur, B. Sharma, A. Verma, J. Chaudhary, S. Tamulevicius, V.K. Thakur, Recent approaches in guar gum hydrogel synthesis for water purification, Int. J. Polym. Anal. Charact. 23 (2018) 621–632, https://doi.org/10.1080/1023666X.2018.1488661.

[21] A.M.A. Hasan, M.E. Abdel-Raouf, Applications of guar gum and its derivatives in petroleum industry: A review, Egypt. J. Pet. 27 (2018) 1043–1050, https://doi.org/10.1016/j.ejpe.2018.03.005.

[22] R.J. Chudzikowski, Guar gum and its applications, J. Soc. Cosmet. Chem. 22 (1971) 43–60.

[23] E.R. Sujatha, S. Saisree, Geotechnical behaviour of guar gum-treated soil, Soils Found. 59 (2019) 2155–2166, https://doi.org/10.1016/j.sandf.2019.11.012.

[24] S. Anandha Kumar, E.R. Sujatha, A. Pugazhendi, M.T. Jamal, Guar gum-stabilized soil: a clean, sustainable and economic alternative liner material for landfills, Clean Techn. Environ. Policy (2021), https://doi.org/10.1007/s10098-021-02032-z.

[25] A.A.B. Moghal, K.V. Vydehi, State-of-the-art review on efficacy of xanthan gum and guar gum inclusion on the engineering behavior of soils, Innov. Infrastr. Sol. 6 (2021) 108, https://doi.org/10.1007/s41062-021-00462-8.

[26] T. Radvand, V. Toufigh, Properties of concrete containing Guar gum, Eur. J. Environ. Civ. Eng. 26 (2022) 2736–2752, https://doi.org/10.1080/19648189.2020.1767217.

[27] G. Palumbo, K. Berent, E. Proniewicz, J. Banaś, Guar Gum as an Eco-Friendly Corrosion Inhibitor for Pure Aluminium in 1-M HCl Solution, Materials 12 (2019) 2620, https://doi.org/10.3390/ma12162620.

[28] K.O. Shamsheera, A.R. Prasad, P.K. Jaseela, A. Joseph, Effect of surfactant addition to Guar Gum and protection of mild steel in hydrochloric acid at high temperatures: Experimental and theoretical studies, J. Mol. Liq. 331 (2021), 115807, https://doi.org/10.1016/j.molliq.2021.115807.

[29] S.E. Atakoohi, P. Naeiji, K. Peyvandi, S.S. Mollashahi, The experimental study and molecular dynamic simulation of THF hydrate growth kinetics in the presence of Arabic and Guar gum: New approaches in promotion of THF hydrate formation, J. Mol. Liq. 325 (2021), 115249, https://doi.org/10.1016/j.molliq.2020.115249.

[30] S. Mollashahi Sanatgar, K. Peyvandi, New edible additives as green inhibitors for preventing methane hydrate formation, J. Environ. Chem. Eng. 7 (2019), 103172, https://doi.org/10.1016/j.jece.2019.103172.

[31] P. Gupta, V.C. Nair, J.S. Sangwai, Phase Equilibrium of Methane Hydrate in Aqueous Solutions of Polyacrylamide, Xanthan Gum, and Guar Gum, J. Chem. Eng. Data 64 (2019) 1650–1661, https://doi.org/10.1021/acs.jced.8b01194.

[32] S.K. Bajpai, A. D'Souza, B. Suhail, Carbon dots from Guar Gum: Synthesis, characterization and preliminary in vivo application in plant cells, Mater. Sci. Eng. B 241 (2019) 92–99, https://doi.org/10.1016/j.mseb.2019.02.014.

[33] Y. Cheng, H. Guo, X. Li, X. Wu, X. Xu, L. Zheng, et al., Rational design of ultrahigh loading metal single-atoms (Co, Ni, Mo) anchored on in-situ pre-crosslinked guar gum derived N-doped carbon aerogel for efficient overall water splitting, Chem. Eng. J. 410 (2021), 128359, https://doi.org/10.1016/j.cej.2021.128359.

[34] L.-H. Huang, C.-C. Li, Effects of interactions between binders and different-sized silicons on dispersion homogeneity of anodes and electrochemistry of lithium-silicon batteries, J. Power Sources 409 (2019) 38–47, https://doi.org/10.1016/j.jpowsour.2018.10.087.

[35] Z.-W. Yin, T. Zhang, S.-J. Zhang, Y.-P. Deng, X.-X. Peng, J.-Q. Wang, et al., Understanding the role of water-soluble guar gum binder in reducing capacity fading and voltage decay of Li-rich cathode for Li-ion batteries, Electrochim. Acta 351 (2020), 136401, https://doi.org/10.1016/j.electacta.2020.136401.

[36] S. Kaur, S. Santra, Application of Guar Gum and its Derivatives as Green Binder/Separator for Advanced Lithium-Ion Batteries, ChemistryOpen 11 (2022), https://doi.org/10.1002/open.202100209.

[37] Y. Huang, J. Zhang, J. Liu, Z. Li, S. Jin, Z. Li, et al., Flexible and stable quasi-solid-state zinc ion battery with conductive guar gum electrolyte, Mater. Today Energy 14 (2019), 100349, https://doi.org/10.1016/j.mtener.2019.100349.

[38] R. Xu, J. Zhou, H. Gong, L. Qiao, Y. Li, D. Li, et al., Environment-friendly degradable zinc-ion battery based on guar gum-cellulose aerogel electrolyte, Biomater. Sci. 10 (2022) 1476–1485, https://doi.org/10.1039/D1BM01747K.

[39] U. Bhardwaj, A. Sharma, A. Mathur, A. Halder, H.S. Kushwaha, Novel guar-gum electrolyte to aggrandize the performance of LaMnO₃ perovskite-based zinc-air batteries. Electrochem.Sci.Adv. 2 (2022) https://doi.org/10.1002/elsa.202100056.

[40] A. Gunasekaran, A. Sorrentino, A.M. Asiri, S. Anandan, Guar gum-based polymer gel electrolyte for dye-sensitized solar cell applications, Sol. Energy 208 (2020) 160–165, https://doi.org/10.1016/j.solener.2020.07.084.

[41] D. Mudgil, S. Barak, B.S. Khatkar, Guar gum: processing, properties and food applications—A Review, J. Food Sci. Technol. 51 (2014) 409–418, https://doi.org/10.1007/s13197-011-0522-x.

[42] Gupta S, Variyar PS. Guar Gum: A Versatile Polymer for the Food Industry. Biopolymers for Food Design, Elsevier; 2018, p. 383–407. 10.1016/B978-0-12-811449-0.00012-8.

[43] F. Liu, W. Chang, M. Chen, F. Xu, J. Ma, F. Zhong, Film-forming properties of guar gum, tara gum and locust bean gum, Food Hydrocoll. 98 (2020), 105007, https://doi.org/10.1016/j.foodhyd.2019.03.028.

[44] E. Kirtil, A. Aydogdu, T. Svitova, C.J. Radke, Assessment of the performance of several novel approaches to improve physical properties of guar gum based biopolymer films, Food Packag. Shelf Life 29 (2021), 100687, https://doi.org/10.1016/j.fpsl.2021.100687.

[45] T. Gasti, V.D. Hiremani, S.S. Kesti, V.N. Vanjeri, N. Goudar, S.P. Masti, et al., Physicochemical and Antibacterial Evaluation of Poly (Vinyl Alcohol)/Guar Gum/Silver Nanocomposite Films for Food Packaging Applications, J. Polym. Environ. 29 (2021) 3347–3363, https://doi.org/10.1007/s10924-021-02123-4.

[46] R.K. Deshmukh, K. Akhila, D. Ramakanth, K.K. Gaikwad, Guar gum/carboxymethyl cellulose based antioxidant film incorporated with halloysite nanotubes and litchi shell waste extract for active packaging, Int. J. Biol. Macromol. 201 (2022) 1–13, https://doi.org/10.1016/j.ijbiomac.2021.12.198.

[47] A. Theocharidou, I. Mourtzinos, C. Ritzoulis, The role of guar gum on sensory perception, on food function, and on the development of dysphagia supplements – A review, Food Hydrocolloid Health 2 (2022), 100053, https://doi.org/10.1016/j.fhfh.2022.100053.

[48] A. Indurkar, P. Bangde, M. Gore, P. Reddy, R. Jain, P. Dandekar, Optimization of guar gum-gelatin bioink for 3D printing of mammalian cells, Bioprinting 20 (2020) e00101.

[49] M.Y. Rezk, M. Zeitoun, A.N. El-Shazly, M.M. Omar, N.K. Allam, Robust photoactive nanoadsorbents with antibacterial activity for the removal of dyes, J. Hazard. Mater. 378 (2019), 120679, https://doi.org/10.1016/j.jhazmat.2019.05.072.

[50] J. Balachandramohan, T. Sivasankar, M. Sivakumar, Facile sonochemical synthesis of Ag₂O-guar gum nanocomposite as a visible light photocatalyst for the organic transformation reactions, J. Hazard. Mater. 385 (2020), 121621, https://doi.org/10.1016/j.jhazmat.2019.121621.

[51] J. Balachandramohan, R. Singh, T. Sivasankar, S. Manickam, Sonochemical synthesis of highly efficient Ag₃PO₄-Guar gum nanocomposite with photo-oxidation property under visible light irradiation, Chem. Eng. Process. - Process Intesif. 168 (2021), 108549, https://doi.org/10.1016/j.cep.2021.108549.

[52] T.M. Aminabhavi, M.N. Nadagouda, S.D. Joshi, U.A. More, Guar gum as platform for the oral controlled release of therapeutics, Expert Opin. Drug Deliv. 11 (2014) 753–766, https://doi.org/10.1517/17425247.2014.897326.

[53] Seeli DS, Prabaharan M. Prospects of Guar Gum and its Derivatives as Biomaterials. Handbook of Polymers for Pharmaceutical Technologies, Hoboken, NJ, USA: John Wiley & Sons, Inc.; 2015, p. 413–31. 10.1002/9781119041375.ch13.

[54] D.S. Seeli, M. Prabaharan, Guar Gum and Its Derivatives: Versatile Materials for Controlled Drug Delivery, in: Handbook of Sustainable Polymers, Jenny Stanford Publishing, 2016, pp. 261–287, https://doi.org/10.1201/b19948-11.

[55] A. Martín-Illana, R. Cazorla-Luna, F. Notario-Pérez, L.M. Bedoya, R. Ruiz-Caro, M. D. Veiga, Freeze-dried bioadhesive vaginal bigels for controlled release of Tenofovir, Eur. J. Pharm. Sci. 127 (2019) 38–51, https://doi.org/10.1016/j.ejps.2018.10.013.

[56] S. Das, D. Bera, K. Pal, D. Mondal, P. Karmakar, S. Das, et al., Guar gum micro-vehicle mediated delivery strategy and synergistic activity of thymoquinone and piperine: An in vitro study on bacterial and hepatocellular carcinoma cells, J. Drug Delivery Sci. Technol. 60 (2020), 101994, https://doi.org/10.1016/j.jddst.2020.101994.

[57] H.D. Jhundoo, T. Siefen, A. Liang, C. Schmidt, J. Lokhnauth, B. Moulari, et al., Anti-inflammatory effects of acacia and guar gum in 5-amino salicylic acid formulations in experimental colitis, Int. J. Pharm.: X 3 (2021), 100080, https://doi.org/10.1016/j.ijpx.2021.100080.

[58] B. Mukherjee, L. Kumari, I. Ehsan, P. Ghosh, S. Banerjee, S. Chakraborty, et al., Guar gum-based nanomaterials in drug delivery and biomedical applicationsBiopolymer-Based Nanomaterials in Drug Delivery and Biomedical Applications, Elsevier (2021) 143–164, https://doi.org/10.1016/B978-0-12-820874-8.00016-6.

[59] S. Das, U. Subuddhi, Potential of guar gum hydrogels in drug deliveryPlant and Algal Hydrogels for Drug Delivery and Regenerative Medicine, Elsevier (2021) 143–180, https://doi.org/10.1016/B978-0-12-821649-1.00006-4.

[60] M. Caldera-Villalobos, D.A. Cabrera-Munguía, J.J. Becerra-Rodríguez, J. A. Claudio-Rizo, Tailoring biocompatibility of composite scaffolds of collagen/guar gum with metal–organic frameworks, RSC Adv. 12 (2022) 3672–3686, https://doi.org/10.1039/D1RA08824F.

[61] Z.H. Ghauri, A. Islam, M.A. Qadir, N. Gull, B. Haider, R.U. Khan, et al., Development and evaluation of pH-sensitive biodegradable ternary blended hydrogel films (chitosan/guar gum/PVP) for drug delivery application, Sci. Rep. 11 (2021) 21255, https://doi.org/10.1038/s41598-021-00452-x.

[62] J. Wang, Y. Huang, B. Liu, Z. Li, J. Zhang, G. Yang, et al., Flexible and anti-freezing zinc-ion batteries using a guar-gum/sodium-alginate/ethylene-glycol hydrogel electrolyte, Energy Storage Mater. 41 (2021) 599–605, https://doi.org/10.1016/j.ensm.2021.06.034.

[63] M. Mofradi, H. Karimi, K. Dashtian, M. Ghaedi, Processing Guar Gum into polyester fabric based promising mixed matrix membrane for water treatment, Carbohydr. Polym. 254 (2021), 116806, https://doi.org/10.1016/j.carbpol.2020.116806.

[64] J.L. Slavin, N.A. Greenberg, Partially hydrolyzed guar gum, Nutrition 19 (2003) 549–552, https://doi.org/10.1016/S0899-9007(02)01032-8.

[65] D. Mudgil, Partially Hydrolyzed Guar Gum: Preparation and Properties. Polymers for Food Applications, Springer International Publishing, Cham, 2018, pp. 529–549.

[66] A.I. Bourbon, A.C. Pinheiro, C. Ribeiro, C. Miranda, J.M. Maia, J.A. Teixeira, et al., Characterization of galactomannans extracted from seeds of Gleditsia triacanthos and Sophora japonica through shear and extensional rheology: Comparison with guar gum and locust bean gum, Food Hydrocoll. 24 (2010) 184–192, https://doi.org/10.1016/j.foodhyd.2009.09.004.

[67] M. Prabaharan, Prospective of guar gum and its derivatives as controlled drug delivery systems, Int. J. Biol. Macromol. 49 (2011) 117–124, https://doi.org/10.1016/j.ijbiomac.2011.04.022.

[68] M.D. Torres, R. Moreira, F. Chenlo, M.J. Vázquez, Water adsorption isotherms of carboxymethyl cellulose, guar, locust bean, tragacanth and xanthan gums, Carbohydr. Polym. 89 (2012) 592–598, https://doi.org/10.1016/j.carbpol.2012.03.055.

[69] N. Thombare, U. Jha, S. Mishra, M.Z. Siddiqui, Guar gum as a promising starting material for diverse applications: A review, Int. J. Biol. Macromol. 88 (2016) 361–372, https://doi.org/10.1016/j.ijbiomac.2016.04.001.

[70] G. Dodi, D. Hritcu, M.I. Popa, Carboxymethylation of guar gum: synthesis and characterization, Cellul. Chem. Technol. 45 (2011) 171–176.

[71] K.P. Chandrika, A. Singh, A. Rathore, A. Kumar, Novel cross linked guar gum-g-poly(acrylate) porous superabsorbent hydrogels: Characterization and swelling

behaviour in different environments, Carbohydr. Polym. 149 (2016) 175–185, https://doi.org/10.1016/j.carbpol.2016.04.077.

[72] N. Thombare, U. Jha, S. Mishra, M.Z. Siddiqui, Borax cross-linked guar gum hydrogels as potential adsorbents for water purification, Carbohydr. Polym. 168 (2017) 274–281, https://doi.org/10.1016/j.carbpol.2017.03.086.

[73] N. Thombare, S. Mishra, M.Z. Siddiqui, U. Jha, D. Singh, G.R. Mahajan, Design and development of guar gum based novel, superabsorbent and moisture retaining hydrogels for agricultural applications, Carbohydr. Polym. 185 (2018) 169–178, https://doi.org/10.1016/j.carbpol.2018.01.018.

[74] S. Pal, Carboxymethyl guar: Its synthesis and macromolecular characterization, J. Appl. Polym. Sci. 111 (2009) 2630–2636, https://doi.org/10.1002/app.29338.

[75] S. Kundu, A. Das, A. Basu, D. Ghosh, P. Datta, A. Mukherjee, Carboxymethyl guar gum synthesis in homogeneous phase and macroporous 3D scaffolds design for tissue engineering, Carbohydr. Polym. 191 (2018) 71–78, https://doi.org/10.1016/j.carbpol.2018.03.007.

[76] H. Gong, M. Liu, J. Chen, F. Han, C. Gao, B. Zhang, Synthesis and characterization of carboxymethyl guar gum and rheological properties of its solutions, Carbohydr. Polym. 88 (2012) 1015–1022, https://doi.org/10.1016/j.carbpol.2012.01.057.

[77] R.T. Thimma, S. Tammishetti, Barium chloride crosslinked carboxymethyl guar gum beads for gastrointestinal drug delivery, J. Appl. Polym. Sci. 82 (2001) 3084–3090, https://doi.org/10.1002/app.2164.

[78] R.T. Thimma, S. Tammishetti, Study of complex coacervation of gelatin with sodium carboxymethyl guar gum: Microencapsulation of clove oil and sulphamethoxazole, J. Microencapsul. 20 (2003) 203–210, https://doi.org/10.3109/02652040309178062.

[79] S.K. Ghosh, A. Das, A. Basu, A. Halder, S. Das, S. Basu, et al., Semi-interpenetrating hydrogels from carboxymethyl guar gum and gelatin for ciprofloxacin sustained release, Int. J. Biol. Macromol. 120 (2018) 1823–1833, https://doi.org/10.1016/j.ijbiomac.2018.09.212.

[80] G. Dalei, S. Das, Carboxymethyl guar gum: A review of synthesis, properties and versatile applications, Eur. Polym. J. 176 (2022), 111433, https://doi.org/10.1016/j.eurpolymj.2022.111433.

[81] G. Dalei, S. Das, S.P. Das, Non-thermal plasma assisted surface nano-textured carboxymethyl guar gum/chitosan hydrogels for biomedical applications, RSC Adv. 9 (2019) 1705–1716, https://doi.org/10.1039/C8RA09161G.

[82] A.M.A. Hasan, M. Keshawy, M.-E.-S. Abdel-Raouf, Atomic force microscopy investigation of smart superabsorbent hydrogels based on carboxymethyl guar gum: Surface topography and swelling properties, Mater. Chem. Phys. 278 (2022), 125521, https://doi.org/10.1016/j.matchemphys.2021.125521.

[83] D. Chauhan, A. Kumar, S.G. Warkar, Synthesis, characterization and metal ions sensing applications of *meta*-benziporphodimethene-embedded polyacrylamide/carboxymethyl guargum polymeric hydrogels in water, Environ. Technol. 43 (2022) 991–1002, https://doi.org/10.1080/09593330.2020.1812730.

[84] W. Chen, Y. Bu, D. Li, Y. Liu, G. Chen, X. Wan, et al., Development of high-strength, tough, and self-healing carboxymethyl guar gum-based hydrogels for human motion detection, J. Mater. Chem. C 8 (2020) 900–908, https://doi.org/10.1039/C9TC05797H.

[85] P. Orsu, S. Matta, Fabrication and characterization of carboxymethyl guar gum nanocomposite for application of wound healing, Int. J. Biol. Macromol. 164 (2020) 2267–2276, https://doi.org/10.1016/j.ijbiomac.2020.07.322.

[86] G. Dalei, S. Das, S.P. Das, Low-pressure nitrogen and ammonia plasma treatment on carboxymethyl guar gum/PVA hydrogels: impact on drug delivery, biocompatibility and biodegradability, Int. J. Polym. Mater. Polym. Biomater. 70 (2021) 75–89, https://doi.org/10.1080/00914037.2019.1695204.

[87] M.A. Shenoy, D.J. D'Melo, Evaluation of mechanical properties of unsaturated polyester-guar gum/hydroxypropyl guar gum composites, Express Polym. Lett. 1 (2007) 622–628, https://doi.org/10.3144/expresspolymlett.2007.85.

[88] H. Fan, Z. Gong, Z. Wei, H. Chen, H. Fan, J. Geng, et al., Understanding the temperature–resistance requirement of a borate cross-linked hydroxypropyl guar gum fracturing fluid based on a facile evaluation method, RSC Adv. 7 (2017) 53290–53300, https://doi.org/10.1039/C7RA11687J.

[89] L. Qiu, Y. Shen, T. Wang, C. Wang, Rheological and fracturing characteristics of a novel sulfonated hydroxypropyl guar gum, Int. J. Biol. Macromol. 117 (2018) 974–982, https://doi.org/10.1016/j.ijbiomac.2018.05.072.

[90] Y. Li, S. Wang, J. Guo, R. Chen, F. Zhao, Y. Liu, Reducing adsorption of hydroxypropyl guar gum on sandstone by silicon nanoparticles, Carbohydr. Polym. 219 (2019) 21–28, https://doi.org/10.1016/j.carbpol.2019.05.016.

[91] C. Berlangieri, G. Poggi, S. Murgia, M. Monduzzi, L. Dei, E. Carretti, Structural, rheological and dynamics insights of hydrogels in hydroxypropyl guar gel-like systems, Colloids Surf. BBiointerfaces 168 (2018) 178–186, https://doi.org/10.1016/j.colsurfb.2018.02.025.

[92] Q. Shi, B. Qin, Q. Bi, B. Qu, Fly ash suspensions stabilized by hydroxypropyl guar gum and xanthan gum for retarding spontaneous combustion of coal, Combust. Sci. Technol. 190 (2018) 2097–2110, https://doi.org/10.1080/00102202.2018.1491845.

[93] D. Carvalho, N. Loeffler, G.-T. Kim, S. Passerini, High Temperature Stable Separator for Lithium Batteries Based on SiO2 and Hydroxypropyl Guar Gum, Membranes (Basel) 5 (2015) 632–645, https://doi.org/10.3390/membranes5040632.

[94] Y. Meng, H. Luo, C. Dong, C. Zhang, Z. He, Z. Long, et al., Hydroxypropyl Guar/Cellulose Nanocrystal Film with Ionic Liquid and Anthocyanin for Real-Time and Visual Detection of NH₃, ACS Sustain. Chem. Eng. 8 (2020) 9731–9741, https://doi.org/10.1021/acssuschemeng.0c01833.

[95] J. Gao, B.P. Grady, Hydroxypropylation of Guar Splits: Kinetics and Rheology, Ind. Eng. Chem. Res. 58 (2019) 11673–11679, https://doi.org/10.1021/acs.iecr.9b01674.

[96] L. Ray, K. Karthik, V. Srivastava, S.P. Singh, A.B. Pant, N. Goyal, et al., Efficient antileishmanial activity of amphotericin B and piperine entrapped in enteric coated guar gum nanoparticles, Drug Deliv. Transl. Res. 11 (2021) 118–130, https://doi.org/10.1007/s13346-020-00712-9.

[97] X. Lu, Y. Li, W. Feng, S. Guan, P. Guo, Self-healing hydroxypropyl guar gum/poly (acrylamide-co-3-acrylamidophenyl boronic acid) composite hydrogels with yield phenomenon based on dynamic PBA ester bonds and H-bond, Colloids Surf. A Physicochem. Eng. Asp. 561 (2019) 325–331, https://doi.org/10.1016/j.colsurfa.2018.10.071.

[98] Z. Sun, L. Wang, X. Jiang, L. Bai, W. Wang, H. Chen, et al., Self-healing, sensitive and antifreezing biomass nanocomposite hydrogels based on hydroxypropyl guar gum and application in flexible sensors, Int. J. Biol. Macromol. 155 (2020) 1569–1577, https://doi.org/10.1016/j.ijbiomac.2019.11.134.

[99] D. Risica, M. Dentini, V. Crescenzi, Guar gum methyl ethers. Part I., Synthesis and macromolecular characterization, Polymer (Guildf) 46 (2005) 12247–12255, https://doi.org/10.1016/j.polymer.2005.10.083.

[100] J. Tripathi, R. Ambolikar, S. Gupta, D. Jain, J. Bahadur, P.S. Variyar, Methylation of guar gum for improving mechanical and barrier properties of biodegradable packaging films, Sci. Rep. 9 (2019) 14505, https://doi.org/10.1038/s41598-019-50991-7.

[101] J. Tripathi, R. Ambolikar, S. Gupta, P.S. Variyar, Preparation and characterization of methylated guar gum based nano-composite films, Food Hydrocoll. 124 (2022), 107312, https://doi.org/10.1016/j.foodhyd.2021.107312.

[102] H.J. Prado, M.C. Matulewicz, Cationization of polysaccharides: A path to greener derivatives with many industrial applications, Eur. Polym. J. 52 (2014) 53–75, https://doi.org/10.1016/j.eurpolymj.2013.12.011.

[103] S. Pal, D. Mal, R.P. Singh, Synthesis and characterization of cationic guar gum: A high performance flocculating agent, J. Appl. Polym. Sci. 105 (2007) 3240–3245, https://doi.org/10.1002/app.26440.

[104] Y. Huang, H. Yu, C. Xiao, pH-sensitive cationic guar gum/poly (acrylic acid) polyelectrolyte hydrogels: Swelling and in vitro drug release, Carbohydr. Polym. 69 (2007) 774–783, https://doi.org/10.1016/j.carbpol.2007.02.016.

[105] C. Banerjee, S. Ghosh, G. Sen, S. Mishra, P. Shukla, R. Bandopadhyay, Study of algal biomass harvesting using cationic guar gum from the natural plant source as flocculant, Carbohydr. Polym. 92 (2013) 675–681, https://doi.org/10.1016/j.carbpol.2012.09.022.

[106] X. Wan, C. Guo, J. Feng, T. Yu, X.-S. Chai, G. Chen, et al., Determination of the Degree of Substitution of Cationic Guar Gum by Headspace-Based Gas Chromatography during Its Synthesis, J. Agric. Food Chem. 65 (2017) 7012–7016, https://doi.org/10.1021/acs.jafc.7b03144.

[107] T. Bujak, Z. Nizioł-Łukaszewska, A. Ziemlewska, Amphiphilic cationic polymers as effective substances improving the safety of use of body wash gels, Int. J. Biol. Macromol. 147 (2020) 973–979, https://doi.org/10.1016/j.ijbiomac.2019.10.064.

[108] R.L. McMullen, D. Laura, G. Zhang, B. Kroon, Investigation of the interactions of cationic guar with human hair by electrokinetic analysis, Int. J. Cosmet. Sci. 43 (2021) 375–390, https://doi.org/10.1111/ics.12704.

[109] L. Dai, T. Cheng, Y. Wang, H. Lu, S. Nie, H. He, et al., Injectable all-polysaccharide self-assembling hydrogel: a promising scaffold for localized therapeutic proteins, Cellulose 26 (2019) 6891–6901, https://doi.org/10.1007/s10570-019-02579-7.

[110] C. Pu, W. Tang, X. Li, M. Li, Q. Sun, Stability enhancement efficiency of surface decoration on curcumin-loaded liposomes: Comparison of guar gum and its cationic counterpart, Food Hydrocoll. 87 (2019) 29–37, https://doi.org/10.1016/j.foodhyd.2018.07.039.

[111] H. Yagoub, L. Zhu, M.H.M.A. Shibraen, X. Xu, D.M.D. Babiker, J. Xu, et al., Complex membrane of cellulose and chitin nanocrystals with cationic guar gum for oil/water separation, J. Appl. Polym. Sci. 136 (2019) 47947, https://doi.org/10.1002/app.47947.

[112] M.F. Abdullah, S.K. Ghosh, S. Basu, A. Mukherjee, Guar gum orchestrated environmental synthesis for silver nano-bio-composite films, Carbohydr. Polym. 134 (2015) 30–37, https://doi.org/10.1016/j.carbpol.2015.06.029.

[113] M. Chu, N. Feng, H. An, G. You, C. Mo, H. Zhong, et al., Design and validation of antibacterial and pH response of cationic guar gum film by combining hydroxyethyl cellulose and red cabbage pigment, Int. J. Biol. Macromol. 162 (2020) 1311–1322, https://doi.org/10.1016/j.ijbiomac.2020.06.198.

[114] M.H.M.A. Shibraen, O.M. Ibrahim, R.A.M. Asad, S. Yang, M.R. El-Aassar, Interpenetration of metal cations into polyelectrolyte-multilayer-films via layer-by-layer assembly: Selective antibacterial functionality of cationic guar gum/polyacrylic acid- Ag+ nanofilm against resistant E. coli, Colloids Surf. A Physicochem. Eng. Asp. 610 (2021) 125921, https://doi.org/10.1016/j.colsurfa.2020.125921.

[115] X. Tan, Y. Zhu, C. Sun, X. Zhang, J. Su, Adding cationic guar gum after collector: A novel investigation in flotation separation of galena from sphalerite, Miner. Eng. 157 (2020), 106542, https://doi.org/10.1016/j.mineng.2020.106542.

[116] E. Grządka, J. Matusiak, E. Godek, U. Maciołek, Mixtures of cationic guar gum and anionic surfactants as stabilizers of zirconia suspensions, J. Mol. Liq. 343 (2021), 117677, https://doi.org/10.1016/j.molliq.2021.117677.

[117] W. Zou, S. Tang, Q. Li, G. Hu, L. Liu, Y. Jin, et al., Addition of cationic guar-gum and oleic acid improved the stability of plasma emulsions prepared with enzymatically hydrolyzed egg yolk, Food Hydrocoll. 105 (2020) 105827, https://doi.org/10.1016/j.foodhyd.2020.105827.

[118] A. Nakamura, M. Ozaki, K. Murakami, Elucidation of the aggregation mechanism of bentonite with cationic guar gum as flocculant and application to filtration,

Colloids Surf. A Physicochem. Eng. Asp. 596 (2020), 124660, https://doi.org/10.1016/j.colsurfa.2020.124660.

[119] R. Tyagi, P. Sharma, R. Nautiyal, A.K. Lakhera, V. Kumar, Synthesis of quaternised guar gum using Taguchi L(16) orthogonal array, Carbohydr. Polym. 237 (2020), 116136, https://doi.org/10.1016/j.carbpol.2020.116136.

[120] R. Jeyapaul, P. Shahabudeen, K. Krishnaiah, Quality management research by considering multi-response problems in the Taguchi method – a review, Int. J. Adv. Manuf. Technol. 26 (2005) 1331–1337, https://doi.org/10.1007/s00170-004-2102-y.

[121] H. Jing, J. Feng, J. Shi, L. He, P. Guo, S. Guan, et al., Ultra-stretchable, self-recovering, self-healing cationic guar gum/poly(stearyl methacrylate-co-acrylic acid) hydrogels, Carbohydr. Polym. 256 (2021), 117563, https://doi.org/10.1016/j.carbpol.2020.117563.

[122] L. Dai, Y. Wang, Z. Li, X. Wang, C. Duan, W. Zhao, et al., A multifunctional self-crosslinked chitosan/cationic guar gum composite hydrogel and its versatile uses in phosphate-containing water treatment and energy storage, Carbohydr. Polym. 244 (2020), 116472, https://doi.org/10.1016/j.carbpol.2020.116472.

[123] X. Yu, C. Cheng, X. Peng, K. Zhang, X. Yu, A self-healing and injectable oxidized quaternized guar gum/carboxymethyl chitosan hydrogel with efficient hemostatic and antibacterial properties for wound dressing, Colloids Surf. BBiointerfaces 209 (2022), 112207, https://doi.org/10.1016/j.colsurfb.2021.112207.

[124] E.A. Kamoun, E.-R.S. Kenawy, X. Chen, A review on polymeric hydrogel membranes for wound dressing applications: PVA-based hydrogel dressings, J. Adv. Res. 8 (2017) 217–233, https://doi.org/10.1016/j.jare.2017.01.005.

[125] D. Simões, S.P. Miguel, M.P. Ribeiro, P. Coutinho, A.G. Mendonça, I.J. Correia, Recent advances on antimicrobial wound dressing: A review, Eur. J. Pharm. Biopharm. 127 (2018) 130–141, https://doi.org/10.1016/j.ejpb.2018.02.022.

[126] A. Gupta, M. Kowalczuk, W. Heaselgrave, S.T. Britland, C. Martin, I. Radecka, The production and application of hydrogels for wound management: A review, Eur. Polym. J. 111 (2019) 134–151, https://doi.org/10.1016/j.eurpolymj.2018.12.019.

[127] Y. Liang, J. He, B. Guo, Functional Hydrogels as Wound Dressing to Enhance Wound Healing, ACS Nano 15 (2021) 12687–12722, https://doi.org/10.1021/acsnano.1c04206.

[128] Q. Zeng, X. Qi, G. Shi, M. Zhang, H. Haick, Wound Dressing: From Nanomaterials to Diagnostic Dressings and Healing Evaluations, ACS Nano 16 (2022) 1708–1733, https://doi.org/10.1021/acsnano.1c08411.

[129] M.C. Jennings, K.P.C. Minbiole, W.M. Wuest, Quaternary Ammonium Compounds: An Antimicrobial Mainstay and Platform for Innovation to Address Bacterial Resistance, ACS Infect. Dis. 1 (2015) 288–303, https://doi.org/10.1021/acsinfecdis.5b00047.

[130] P. Jana, S. Ghosh, K. Sarkar, Low molecular weight polyethyleneimine conjugated guar gum for targeted gene delivery to triple negative breast cancer, Int. J. Biol. Macromol. 161 (2020) 1149–1160, https://doi.org/10.1016/j.ijbiomac.2020.06.090.

[131] T.-A. Le, Y. Guo, J.-N. Zhou, J. Yan, H. Zhang, T.-P. Huynh, Synthesis, characterization and biocompatibility of guar gum-benzoic acid, Int. J. Biol. Macromol. 194 (2022) 110–116, https://doi.org/10.1016/j.ijbiomac.2021.11.180.

[132] A.C. Reis, L.v. dos Santos, K.R. Santos, M.K. Lima-Tenório, K.S. Paludo, M.R. Maurício, et al., Chemically crosslinked guar gum hydrogels: An investigation on the water transport and its relationship with hydrocortisone release, Int. J. Pharm. 617 (2022), 121626, https://doi.org/10.1016/j.ijpharm.2022.121626.

[133] S. Sarkar, R.S. Singhal, Esterification of guar gum hydrolysate and gum Arabic with n-octenyl succinic anhydride and oleic acid and its evaluation as wall material in microencapsulation, Carbohydr. Polym. 86 (2011) 1723–1731, https://doi.org/10.1016/j.carbpol.2011.07.003.

[134] H. Kono, F. Otaka, M. Ozaki, Preparation and characterization of guar gum hydrogels as carrier materials for controlled protein drug delivery, Carbohydr. Polym. 111 (2014) 830–840, https://doi.org/10.1016/j.carbpol.2014.05.050.

[135] C. Lacroix, E. Sultan, E. Fleury, A. Charlot, Functional galactomannan platform from convenient esterification in imidazolium-based ionic liquids, Polym. Chem. 3 (2012) 538–546, https://doi.org/10.1039/C2PY00512C.

[136] V. Raj, A. Bajpai, Synthesis of hydrophobically modified guar gum film for packaging materials, Mater. Today: Proc. 29 (2020) 1132–1142, https://doi.org/10.1016/j.matpr.2020.05.339.

[137] A. Bajpai, V. Raj, Hydrophobically modified guar gum films for wound dressing, Polym. Bull. 78 (2021) 4109–4128, https://doi.org/10.1007/s00289-020-03302-4.

[138] S. r, m. p., Multi-functional FITC-silica@gold nanoparticles conjugated with guar gum succinate, folic acid and doxorubicin for CT/fluorescence dual imaging and combined chemo/PTT of cancer, Colloids Surf. BBiointerfaces 186 (2020), 110701, https://doi.org/10.1016/j.colsurfb.2019.110701.

[139] S. Kunjiappan, P. Pavadai, S. Vellaichamy, S. Ram Kumar Pandian, V. Ravishankar, P. Palanisamy, et al., Surface receptor-mediated targeted drug delivery systems for enhanced cancer treatment: A state-of-the-art review, Drug Dev. Res. 82 (2021) 309–340, https://doi.org/10.1002/ddr.21758.

[140] N. Soni, N.N. Shah, R.S. Singhal, Dodecenyl succinylated guar gum hydrolysate as a wall material for microencapsulation: Synthesis, characterization and evaluation, J. Food Eng. 242 (2019) 133–140, https://doi.org/10.1016/j.jfoodeng.2018.08.030.

[141] Z. Zhang, J. Mao, B. Yang, X. Yang, W. Zhang, C. Zhang, et al., Experimental evaluation of a novel modification of anionic guar gum with maleic anhydride for fracturing fluid, Rheol. Acta 58 (2019) 173–181, https://doi.org/10.1007/s00397-019-01131-5.

[142] X. Yuan, R. Amarnath Praphakar, M.A. Munusamy, A.A. Alarfaj, S. Suresh Kumar, M. Rajan, Mucoadhesive guargum hydrogel inter-connected chitosan-g-polycaprolactone micelles for rifampicin delivery, Carbohydr. Polym. 206 (2019) 1–10, https://doi.org/10.1016/j.carbpol.2018.10.098.

[143] M. Zhang, J. He, M. Deng, P. Gong, X. Zhang, M. Fan, et al., Rheological behaviours of guar gum derivatives with hydrophobic unsaturated long-chains, RSC Adv. 10 (2020) 32050–32057, https://doi.org/10.1039/D0RA04322B.

[144] A. Das, S. Kundu, S.K. Ghosh, A. Basu, M. Gupta, A. Mukherjee, Guar gum cinnamate ouzo nanoparticles for bacterial contact killing in water environment, Carbohydr. Res. 491 (2020), 107983, https://doi.org/10.1016/j.carres.2020.107983.

[145] L. Petruš, D.G. Gray, J.N. BeMiller, Homogeneous alkylation of cellulose in lithium chloride/dimethyl sulfoxide solvent with dimsyl sodium activation. A proposal for the mechanism of cellulose dissolution in LiCl/Me2SO, Carbohydr. Res. 268 (1995) 319–323, https://doi.org/10.1016/0008-6215(94)00330-I.

[146] Z. Liu, C. Zhang, R. Liu, W. Zhang, H. Kang, P. Li, et al., Dissolution of cellobiose in the aqueous solutions of chloride salts: Hofmeister series consideration, Cellulose 23 (2016) 295–305, https://doi.org/10.1007/s10570-015-0827-4.

[147] S. Kundu, A. Das, A. Basu, M.F. Abdullah, A. Mukherjee, Guar gum benzoate nanoparticle reinforced gelatin films for enhanced thermal insulation, mechanical and antimicrobial properties, Carbohydr. Polym. 170 (2017) 89–98, https://doi.org/10.1016/j.carbpol.2017.04.056.

[148] E. Lepeltier, C. Bourgaux, P. Couvreur, Nanoprecipitation and the "Ouzo effect": Application to drug delivery devices, Adv. Drug Deliv. Rev. 71 (2014) 86–97, https://doi.org/10.1016/j.addr.2013.12.009.

[149] A. Das, A. Das, A. Basu, P. Datta, M. Gupta, A. Mukherjee, Newer guar gum ester/chicken feather keratin interact films for tissue engineering, Int. J. Biol. Macromol. 180 (2021) 339–354, https://doi.org/10.1016/j.ijbiomac.2021.03.034.

[150] R. Bhattacharyya, P. Chowdhury, Hydrogels of Acryloyl guar gum-g-(acrylic acid-co-3sulfopropylacrylate) for high-performance adsorption and release of gentamicin sulphate, J. Polym. Res. 28 (2021) 286, https://doi.org/10.1007/s10965-021-02633-8.

[151] R.G. Pearson, Hard and soft acids and bases, HSAB, part 1: Fundamental principles, J. Chem. Educ. 45 (1968) 581, https://doi.org/10.1021/ed045p581.

[152] X. Li, W. Ma, H. Li, Q. Zhang, H. Liu, Sulfur-functionalized metal-organic frameworks: Synthesis and applications as advanced adsorbents, Coord. Chem. Rev. 408 (2020), 213191, https://doi.org/10.1016/j.ccr.2020.213191.

[153] A. Pohl, Removal of Heavy Metal Ions from Water and Wastewaters by Sulfur-Containing Precipitation Agents, Water Air Soil Pollut. 231 (2020) 503, https://doi.org/10.1007/s11270-020-04863-w.

[154] J. Chen, The interaction of flotation reagents with metal ions in mineral surfaces: A perspective from coordination chemistry, Miner. Eng. 171 (2021), 107067, https://doi.org/10.1016/j.mineng.2021.107067.

[155] Y. Qin, S. Liu, R. Xing, H. Yu, K. Li, X. Meng, et al., Synthesis and characterization of dithiocarbamate chitosan derivatives with enhanced antifungal activity, Carbohydr. Polym. 89 (2012) 388–393, https://doi.org/10.1016/j.carbpol.2012.03.018.

[156] V.N. Mehta, H. Basu, R.K. Singhal, S.K. Kailasa, Simple and sensitive colorimetric sensing of Cd2+ ion using chitosan dithiocarbamate functionalized gold nanoparticles as a probe, Sens. Actuators B 220 (2015) 850–858, https://doi.org/10.1016/j.snb.2015.05.105.

[157] E. Doustkhah, S. Rostamnia, B. Gholipour, B. Zeynizadeh, A. Baghban, R. Luque, Design of chitosan-dithiocarbamate magnetically separable catalytic nanocomposites for greener aqueous oxidations at room temperature, Mol. Catal. 434 (2017) 7–15, https://doi.org/10.1016/j.mcat.2017.01.031.

[158] J. Hao, J. Liu, D. Yang, X. Qin, H. Gao, X. Bai, et al., Application of a new depressant dithiocarbamate chitosan in separation of chalcopyrite and molybdenite, Colloids Surf. A Physicochem. Eng. Asp. 634 (2022), 127920, https://doi.org/10.1016/j.colsurfa.2021.127920.

[159] B.M. Córdova, R. Venâncio, M. Olivera, R.G. Huamani-Palomino, A.C. Valderrama, Xanthation of alginate for heavy metal ions removal. Characterization of xanthate-modified alginates and its metal derivatives, Int. J. Biol. Macromol. 169 (2021) 130–142, https://doi.org/10.1016/j.ijbiomac.2020.12.022.

[160] A.D. Gupta, K.P. Rawat, V. Bhadauria, H. Singh, Recent trends in the application of modified starch in the adsorption of heavy metals from water: A review, Carbohydr. Polym. 269 (2021), 117763, https://doi.org/10.1016/j.carbpol.2021.117763.

[161] T.-A. Le, E. Zouheir, K. Nikiforow, M. Khatib, O. Zohar, H. Haick, et al., Synthesis, characterization, and humidity-responsiveness of guar gum xanthate and its nanocomposite with copper sulfide covellite, Int. J. Biol. Macromol. 206 (2022) 105–114, https://doi.org/10.1016/j.ijbiomac.2022.02.132.

[162] S.C. Richter, M. Oestreich, Emerging Strategies for C-H Silylation, Trends in Chemistry 2 (2020) 13–27, https://doi.org/10.1016/j.trechm.2019.07.003.

[163] A. Tyagi, N. Yadav, J. Khan, S. Singh, H.C. Kumar, Transition-Metal-Free C–H Silylation: An Emerging Strategy, Asian J. Org. Chem. 10 (2021) 334–354, https://doi.org/10.1002/ajoc.202000584.

[164] M.A. Ashraf, Z. Liu, C. Li, D. Zhang, Recent advances in catalytic silylation of hydroxyl-bearing compounds: A green technique for protection of alcohols using Si–O bond formations, Appl. Organomet. Chem. 35 (2021), https://doi.org/10.1002/aoc.6131.

[165] S. Ghosh, D. Lai, A. Hajra, Visible-light-induced silylation: an update, Org. Biomol. Chem. 19 (2021) 2399–2415, https://doi.org/10.1039/D1OB00082A.

[166] F. Yan, Y. Jiang, X. Sun, Z. Bai, Y. Zhang, X. Zhou, Surface modification and chemical functionalization of carbon dots: a review, Microchim. Acta 185 (2018) 424, https://doi.org/10.1007/s00604-018-2953-9.

[167] S.-L. Bee, M.A.A. Abdullah, S.-T. Bee, L.T. Sin, A.R. Rahmat, Polymer nanocomposites based on silylated-montmorillonite: A review, Prog. Polym. Sci. 85 (2018) 57–82, https://doi.org/10.1016/j.progpolymsci.2018.07.003.

[168] K. Kuciński, H. Stachowiak-Dłużyńska, G. Hreczycho, Catalytic silylation of O–nucleophiles via Si–H or Si–C bond cleavage: A route to silyl ethers, silanols and siloxanes, Coord. Chem. Rev. 459 (2022), 214456, https://doi.org/10.1016/j.ccr.2022.214456.

[169] T. Baran, N. Yılmaz Baran, A. Menteş, Highly active and recyclable heterogeneous palladium catalyst derived from guar gum for fabrication of biaryl compounds, Int. J. Biol. Macromol. 132 (2019) 1147–1154, https://doi.org/10.1016/j.ijbiomac.2019.04.042.

[170] KumariS. Krishna, D. Yadav, S.K.Cu Sharma, (II), Schiff base complex grafted guar gum: Catalyst for benzophenone derivatives synthesis, Appl. Catal. A: Gen. 601 (117529) (2020), https://doi.org/10.1016/j.apcata.2020.117529.

[171] F.H. Westheimer, Why Nature Chose Phosphates, Science 1987 (235) (1979) 1173–1178, https://doi.org/10.1126/science.2434996.

[172] T. Hunter, Why nature chose phosphate to modify proteins, Philos. Trans. R. Soc., B 367 (2012) 2513–2516, https://doi.org/10.1098/rstb.2012.0013.

[173] S.C.L. Kamerlin, P.K. Sharma, R.B. Prasad, A. Warshel, Why nature really chose phosphate, Q. Rev. Biophys. 46 (2013) 1–132, https://doi.org/10.1017/S0033583512000157.

[174] C.-P. Li, H. Enomoto, Y. Hayashi, H. Zhao, T. Aoki, Recent advances in phosphorylation of food proteins: A review, LWT Food Sci. Technol. 43 (2010) 1295–1300, https://doi.org/10.1016/j.lwt.2010.03.016.

[175] N. Sbei, G.M. Martins, B. Shirinfar, N. Ahmed, Electrochemical Phosphorylation of Organic Molecules, Chem. Rec. 20 (2020) 1530–1552, https://doi.org/10.1002/tcr.202000096.

[176] K.W. Knouse, D.T. Flood, J.C. Vantourout, M.A. Schmidt, I.M. Mcdonald, M. D. Eastgate, et al., Nature Chose Phosphates and Chemists Should Too: How Emerging P(V) Methods Can Augment Existing Strategies, ACS Cent. Sci. 7 (2021) 1473–1485, https://doi.org/10.1021/acscentsci.1c00487.

[177] S. Xia, Y. Zhai, X. Wang, Q. Fan, X. Dong, M. Chen, et al., Phosphorylation of polysaccharides: A review on the synthesis and bioactivities, Int. J. Biol. Macromol. 184 (2021) 946–954, https://doi.org/10.1016/j.ijbiomac.2021.06.149.

[178] G. Sharma, A. Kumar, S. Sharma, A.H. Al-Muhtaseb, M.u. Naushad, A.A. Ghfar, et al., Fabrication and characterization of novel Fe0@Guar gum-crosslinked-soya lecithin nanocomposite hydrogel for photocatalytic degradation of methyl violet dye, Sep. Purif. Technol. 211 (2019) 895–908, https://doi.org/10.1016/j.seppur.2018.10.028.

[179] J. Wang, S. Zhuang, Extraction and adsorption of U(VI) from aqueous solution using affinity ligand-based technologies: an overview, Rev. Environ. Sci. Bio/Technol. 18 (2019) 437–452, https://doi.org/10.1007/s11157-019-09507-y.

[180] M.F. Hamza, A. Fouda, K.Z. Elwakeel, Y. Wei, E. Guibal, N.A. Hamad, Phosphorylation of Guar Gum/Magnetite/Chitosan Nanocomposites for Uranium (VI) Sorption and Antibacterial Applications, Molecules 26 (2021) 1920, https://doi.org/10.3390/molecules26071920.

[181] D. Belosinschi, A. Benkaddour, B.-M. Tofanica, T. Ngo, Phosphorylation of Cellulose in the Presence of Urea, Mech. React. Reagent Impact. (2022), https://doi.org/10.21203/rs.3.rs-862264/v1.

[182] Y. Xu, Y. Wu, P. Sun, F. Zhang, R.J. Linhardt, A. Zhang, Chemically modified polysaccharides: Synthesis, characterization, structure activity relationships of action, Int. J. Biol. Macromol. 132 (2019) 970–977, https://doi.org/10.1016/j.ijbiomac.2019.03.213.

[183] L. Xie, M. Shen, Y. Hong, H. Ye, L. Huang, J. Xie, Chemical modifications of polysaccharides and their anti-tumor activities, Carbohydr. Polym. 229 (2020), 115436, https://doi.org/10.1016/j.carbpol.2019.115436.

[184] H.P. de Oliveira Barddal, F.A.M. Faria, A.V. Nogueira, M. Iacomini, T.R. Cipriani, Anticoagulant and antithrombotic effects of chemically sulfated guar gum, Int. J. Biol. Macromol. 145 (2020) 604–610, https://doi.org/10.1016/j.ijbiomac.2019.12.210.

[185] A.S. Kazachenko, F. Akman, A. Sagaama, N. Issaoui, Y.N. Malyar, N.Y. Vasilieva, et al., Theoretical and experimental study of guar gum sulfation, J. Mol. Model. 27 (5) (2021), https://doi.org/10.1007/s00894-020-04645-5.

[186] A.S. Kazachenko, Y.N. Malyar, N.Y. Vasilyeva, V.S. Borovkova, N. Issaoui, Optimization of guar gum galactomannan sulfation process with sulfamic acid, Biomass Convers. Biorefin. (2021), https://doi.org/10.1007/s13399-021-01895-y.

[187] M. Simsek, T.T. Asiyanbi-Hammed, N. Rasaq, A.M. Hammed, Progress in Bioactive Polysaccharide-Derivatives: A Review, Food Rev. Intl. (2021) 1–16, https://doi.org/10.1080/87559129.2021.1935998.

[188] P. Jana, T. Mitra, T.K.R. Selvaraj, A. Gnanamani, Kundu pp., Preparation of guar gum scaffold film grafted with ethylenediamine and fish scale collagen, cross-linked with ceftazidime for wound healing application, Carbohydr. Polym. 153 (2016) 573–581, https://doi.org/10.1016/j.carbpol.2016.07.053.

[189] Y. Zhang, M. Chen, J. Zhang, J. Li, S.Q. Shi, Q. Gao, A High-Performance Bio-Adhesive Using Hyperbranched Aminated Soybean Polysaccharide and Bio-Based Epoxide, Adv. Mater. Interfaces 7 (2020) 2000148, https://doi.org/10.1002/admi.202000148.

[190] E. Jsc, S. Gopi, A, R, G, S, A. Pius, Highly crosslinked 3-D hydrogels based on graphene oxide for enhanced remediation of multi contaminant wastewater, J. Water Proc. Eng. 31 (2019), https://doi.org/10.1016/j.jwpe.2019.100850.

[191] I. Cumpstey, Chemical Modification of Polysaccharides, ISRN Org. Chem. 2013 (2013) 1–27, https://doi.org/10.1155/2013/417672.

[192] S. Coseri, G. Biliuta, B.C. Simionescu, K. Stana-Kleinschek, V. Ribitsch, V. Harabagiu, Oxidized cellulose—Survey of the most recent achievements, Carbohydr. Polym. 93 (2013) 207–215, https://doi.org/10.1016/j.carbpol.2012.03.086.

[193] G. Pierre, C. Punta, C. Delattre, L. Melone, P. Dubessay, A. Fiorati, et al., TEMPO-mediated oxidation of polysaccharides: An ongoing story, Carbohydr. Polym. 165 (2017) 71–85, https://doi.org/10.1016/j.carbpol.2017.02.028.

[194] A. Isogai, TEMPO-catalyzed oxidation of polysaccharides, Polym. J. 54 (2022) 387–402, https://doi.org/10.1038/s41428-021-00580-1.

[195] B. Ding, Y. Ye, qing, J. Cheng, K. Wang, J. Luo, B. Jiang, TEMPO-mediated selective oxidation of substituted polysaccharides—an efficient approach for the determination of the degree of substitution at C-6, Carbohydr. Res. 343 (2008) 3112–3116, https://doi.org/10.1016/j.carres.2008.09.005.

[196] C.N. Sakakibara, M.R. Sierakowski, N. Lucyszyn, R.A. de Freitas, TEMPO-mediated oxidation on galactomannan: Gal/Man ratio and chain flexibility dependence, Carbohydr. Polym. 153 (2016) 371–378, https://doi.org/10.1016/j.carbpol.2016.07.114.

[197] C.L.O. Petkowicz, F. Reicher, K. Mazeau, Conformational analysis of galactomannans: from oligomeric segments to polymeric chains, Carbohydr. Polym. 37 (1998) 25–39, https://doi.org/10.1016/S0144-8617(98)00051-4.

[198] M. Lavazza, C. Formantici, V. Langella, D. Monti, U. Pfeiffer, Y.M. Galante, Oxidation of galactomannan by laccase plus TEMPO yields an elastic gel, J. Biotechnol. 156 (2011) 108–116, https://doi.org/10.1016/j.jbiotec.2011.08.029.

[199] C.H. de Seixas-Junior, M.M. de Carvalho, J. Jacumazo, R.D. Piazza, G.P. Parchen, R.A. de Freitas, Interaction of guar gum galactomannans with the anionic surfactant sodium lauryl ether sulphate, Int. J. Biol. Macromol. 165 (2020) 713–721, https://doi.org/10.1016/j.ijbiomac.2020.09.216.

[200] E. Ponzini, A. Natalello, F. Usai, M. Bechmann, F. Peri, N. Müller, et al., Structural characterization of aerogels derived from enzymatically oxidized galactomannans of fenugreek, sesbania and guar gums, Carbohydr. Polym. 207 (2019) 510–520, https://doi.org/10.1016/j.carbpol.2018.11.100.

[201] S. Witayakran, A.J. Ragauskas, Synthetic Applications of Laccase in Green Chemistry, Adv. Synth. Catal. 351 (2009) 1187–1209, https://doi.org/10.1002/adsc.200800775.

[202] S.A. Tromp, I. Matijošytė, R.A. Sheldon, I.W.C.E. Arends, G. Mul, M.T. Kreutzer, et al., Mechanism of Laccase-TEMPO-Catalyzed Oxidation of Benzyl Alcohol, ChemCatChem 2 (2010) 827–833, https://doi.org/10.1002/cctc.201000068.

[203] A. Sudalai, A. Khenkin, R. Neumann, Sodium periodate mediated oxidative transformations in organic synthesis, Org. Biomol. Chem. 13 (2015) 4374–4394, https://doi.org/10.1039/C5OB00238A.

[204] K.A. Kristiansen, A. Potthast, B.E. Christensen, Periodate oxidation of polysaccharides for modification of chemical and physical properties, Carbohydr. Res. 345 (2010) 1264–1271, https://doi.org/10.1016/j.carres.2010.02.011.

[205] T. Nypelö, B. Berke, S. Spirk, J.A. Sirviö, Review: Periodate oxidation of wood polysaccharides—Modulation of hierarchies, Carbohydr. Polym. 252 (2021), 117105, https://doi.org/10.1016/j.carbpol.2020.117105.

[206] L. Münster, M. Fojtů, Z. Capáková, M. Muchová, L. Musilová, T. Vaculovič, et al., Oxidized polysaccharides for anticancer-drug delivery: What is the role of structure? Carbohydr. Polym. 257 (2021), 117562 https://doi.org/10.1016/j.carbpol.2020.117562.

[207] W. Ding, Y. Wu, Sustainable dialdehyde polysaccharides as versatile building blocks for fabricating functional materials: An overview, Carbohydr. Polym. 248 (2020), 116801, https://doi.org/10.1016/j.carbpol.2020.116801.

[208] L. Dai, T. Cheng, Y. Wang, B. Wang, C. Duan, H. Ke, et al., A self-assembling guar gum hydrogel for efficient oil/water separation in harsh environments, Sep. Purif. Technol. 225 (2019) 129–135, https://doi.org/10.1016/j.seppur.2019.05.070.

[209] C. Duan, C. Liu, X. Meng, K. Gao, W. Lu, Y. Zhang, et al., Facile synthesis of Ag NPs@ MIL-100(Fe)/ guar gum hybrid hydrogel as a versatile photocatalyst for wastewater remediation: Photocatalytic degradation, water/oil separation and bacterial inactivation, Carbohydr. Polym. 230 (2020), 115642, https://doi.org/10.1016/j.carbpol.2019.115642.

[210] L. Yavari Maroufi, M. Ghorbani, M. Tabibiazar, A Gelatin-Based Film Reinforced by Covalent Interaction with Oxidized Guar Gum Containing Green Tea Extract as an Active Food Packaging System, Food Bioproc. Tech. 13 (2020) 1633–1644, https://doi.org/10.1007/s11947-020-02509-7.

[211] L.Y. Maroufi, M. Tabibiazar, M. Ghorbani, A. Jahanban-Esfahlan, Fabrication and characterization of novel antibacterial chitosan/dialdehyde guar gum hydrogels containing pomegranate peel extract for active food packaging application, Int. J. Biol. Macromol. 187 (2021) 179–188, https://doi.org/10.1016/j.ijbiomac.2021.07.126.

[212] A.H. Pandit, S. Nisar, K. Imtiyaz, M. Nadeem, N. Mazumdar, M.M.A. Rizvi, et al., Injectable, Self-Healing, and Biocompatible N, O -Carboxymethyl Chitosan/Multialdehyde Guar Gum Hydrogels for Sustained Anticancer Drug Delivery, Biomacromolecules 22 (2021) 3731–3745, https://doi.org/10.1021/acs.biomac.1c00537.

[213] P. Nezhad-Mokhtari, M. Ghorbani, N. Abdyazdani, Reinforcement of hydrogel scaffold using oxidized-guar gum incorporated with curcumin-loaded zein nanoparticles to improve biological performance, Int. J. Biol. Macromol. 167 (2021) 59–65, https://doi.org/10.1016/j.ijbiomac.2020.11.103.

[214] L.-D. Koh, Y. Cheng, C.-P. Teng, Y.-W. Khin, X.-J. Loh, S.-Y. Tee, et al., Structures, mechanical properties and applications of silk fibroin materials, Prog. Polym. Sci. 46 (2015) 86–110, https://doi.org/10.1016/j.progpolymsci.2015.02.001.

[215] D.-L. Wen, D.-H. Sun, P. Huang, W. Huang, M. Su, Y. Wang, et al., Recent progress in silk fibroin-based flexible electronics, Microsyst. Nanoeng. 7 (2021) 35, https://doi.org/10.1038/s41378-021-00261-2.

[216] M. Farokhi, F. Mottaghitalab, Y. Fatahi, A. Khademhosseini, D.L. Kaplan, Overview of Silk Fibroin Use in Wound Dressings, Trends Biotechnol. 36 (2018) 907–922, https://doi.org/10.1016/j.tibtech.2018.04.004.

[217] M. Farokhi, F. Mottaghitalab, R.L. Reis, S. Ramakrishna, S.C. Kundu, Functionalized silk fibroin nanofibers as drug carriers: Advantages and challenges, J. Control. Release 321 (2020) 324–347, https://doi.org/10.1016/j.jconrel.2020.02.022.

[218] M. Duan, J. Ma, S. Fang, Synthesis of hydrazine-grafted guar gum material for the highly effective removal of organic dyes, Carbohydr. Polym. 211 (2019) 308–314, https://doi.org/10.1016/j.carbpol.2019.01.112.

[219] J. Ma, S. Fang, P. Shi, M. Duan, Hydrazine-Functionalized guar-gum material capable of capturing heavy metal ions, Carbohydr. Polym. 223 (2019), 115137, https://doi.org/10.1016/j.carbpol.2019.115137.

[220] Y. Wen, Z. Xie, S. Xue, W. Li, H. Ye, W. Shi, et al., Functionalized polymethyl methacrylate-modified dialdehyde guar gum containing hydrazide groups for effective removal and enrichment of dyes, ion, and oil/water separation, J. Hazard. Mater. 426 (2022), 127799, https://doi.org/10.1016/j.jhazmat.2021.127799.

[221] S.A. Ganie, R.A. Naik, A. Ali, T.A. Mir, N. Mazumdar, Preparation, characterization, release and antianemic studies of guar gum functionalized Iron complexes, Int. J. Biol. Macromol. 183 (2021) 1495–1504, https://doi.org/10.1016/j.ijbiomac.2021.05.125.

[222] T.-P. Huynh, T.A. Le, CHAPTER 2, Synthetic Chemistry for Molecular Imprinting (2018) 28–64, https://doi.org/10.1039/9781788010474-00028.

[223] A. Bossion, K.v. Heifferon, L. Meabe, N. Zivic, D. Taton, J.L. Hedrick, et al., Opportunities for organocatalysis in polymer synthesis via step-growth methods, Prog. Polym. Sci. 90 (2019) 164–210, https://doi.org/10.1016/j.progpolymsci.2018.11.003.

[224] G. Yilmaz, Y. Yagci, Light-induced step-growth polymerization, Prog. Polym. Sci. 100 (2020), 101178, https://doi.org/10.1016/j.progpolymsci.2019.101178.

[225] A. Anjum, M. Zuber, K.M. Zia, M.N. Anjum, W. Aftab, Preparation and characterization of guar gum based polyurethanes, Int. J. Biol. Macromol. 183 (2021) 2174–2183, https://doi.org/10.1016/j.ijbiomac.2021.06.025.

[226] J. Ma, J. Zhou, G. Liu, Z. Luo, K. Yan, H. Yao, et al., Synthesis and Properties of Waterborne Polyurethane Modified with Guar Gum Polysaccharide, ChemistrySelect 5 (2020) 2348–2353, https://doi.org/10.1002/slct.201904054.

[227] J. Gao, D. Zhu, W. Zhang, G.A. Solan, Y. Ma, W.-H. Sun, Recent progress in the application of group 1, 2 & 13 metal complexes as catalysts for the ring opening polymerization of cyclic esters, Inorg. Chem. Front. 6 (2019) 2619–2652, https://doi.org/10.1039/C9QI00855A.

[228] D.M. Lyubov, A.O. Tolpygin, A.A. Trifonov, Rare-earth metal complexes as catalysts for ring-opening polymerization of cyclic esters, Coord. Chem. Rev. 392 (2019) 83–145, https://doi.org/10.1016/j.ccr.2019.04.013.

[229] A. Rasines Mazo, S. Allison-Logan, F. Karimi, N.-J.-A. Chan, W. Qiu, W. Duan, et al., Ring opening polymerization of α-amino acids: advances in synthesis, architecture and applications of polypeptides and their hybrids, Chem. Soc. Rev. 49 (2020) 4737–4834, https://doi.org/10.1039/C9CS00738E.

[230] H. Li, R.M. Shakaroun, S.M. Guillaume, J. Carpentier, Recent Advances in Metal-Mediated Stereoselective Ring-Opening Polymerization of Functional Cyclic Esters towards Well-Defined Poly(hydroxy acid)s: From Stereoselectivity to Sequence-Control. Chemistry – A, Eur. J. 26 (2020) 128–138, https://doi.org/10.1002/chem.201904108.

[231] S.A. Kedzior, J.O. Zoppe, R.M. Berry, E.D. Cranston, Recent advances and an industrial perspective of cellulose nanocrystal functionalization through polymer grafting, Curr. Opin. Solid State Mater. Sci. 23 (2019) 74–91, https://doi.org/10.1016/j.cossms.2018.11.005.

[232] T. el Assimi, R. Blažic, A. el Kadib, M. Raihane, R. Beniazza, G.A. Luinstra, et al., Synthesis of poly(ε-caprolactone)-grafted guar gum by surface-initiated ring-opening polymerization, Carbohydr. Polym. 220 (2019) 95–102, https://doi.org/10.1016/j.carbpol.2019.05.049.

[233] T. el Assimi, M. Chaib, M. Raihane, A. el Meziane, M. Khouloud, R. Benhida, et al., Poly(ε-caprolactone)-g-Guar Gum and Poly(ε-caprolactone)-g-Halloysite Nanotubes as Coatings for Slow-Release DAP Fertilizer, J. Polym. Environ. 28 (2020) 2078–2090, https://doi.org/10.1007/s10924-020-01750-7.

[234] R. Kumar, R.K.r. Sharma, A.P. Singh, Grafted cellulose: a bio-based polymer for durable applications, Polym. Bull. 75 (2018) 2213–2242, https://doi.org/10.1007/s00289-017-2136-6.

[235] D. Kumar, S. Gihar, M.K. Shrivash, P. Kumar, P.P. Kundu, A review on the synthesis of graft copolymers of chitosan and their potential applications, Int. J. Biol. Macromol. 163 (2020) 2097–2112, https://doi.org/10.1016/j.ijbiomac.2020.09.060.

[236] T.J. Demars, M.K. Bera, S. Seifert, M.R. Antonio, R.J. Ellis, Revisiting the Solution Structure of Ceric Ammonium Nitrate, Angew. Chem. Int. Ed. 54 (2015) 7534–7538, https://doi.org/10.1002/anie.201502336.

[237] J. Lee, U. von Gunten, J.-H. Kim, Persulfate-Based Advanced Oxidation: Critical Assessment of Opportunities and Roadblocks, Environ. Sci. Tech. 54 (2020) 3064–3081, https://doi.org/10.1021/acs.est.9b07082.

[238] S. Wacławek, H.v. Lutze, K. Grübel, V.V.T. Padil, M. Černík, D. Dionysiou, Dionysiou, Chemistry of persulfates in water and wastewater treatment: A review, Chem. Eng. J. 330 (2017) 44–62, https://doi.org/10.1016/j.cej.2017.07.132.

[239] A.S. Sarac, Redox polymerization, Prog. Polym. Sci. 24 (1999) 1149–1204, https://doi.org/10.1016/S0079-6700(99)00026-X.

[240] C.G. Gutierrez, G. Cáceres Montenegro, R.J. Minari, J.R. Vega, L.M. Gugliotta, Scale Inhibitor and Dispersant Based on Poly(Acrylic Acid) Obtained by Redox-Initiated Polymerization, Macromol. React. Eng. 13 (2019) 1900007, https://doi.org/10.1002/mren.201900007.

[241] M. Bühl, T. Hutson, A. Missio, J.C. Walton, Sulfur and Phosphorus Oxyacid Radicals, J. Phys. Chem. A 126 (2022) 760–771, https://doi.org/10.1021/acs.jpca.1c10455.

[242] D. Zhou, L. Chen, J. Li, F. Wu, Transition metal catalyzed sulfite auto-oxidation systems for oxidative decontamination in waters: A state-of-the-art minireview, Chem. Eng. J. 346 (2018) 726–738, https://doi.org/10.1016/j.cej.2018.04.016.

[243] X.D. Feng, X.Q. Guo, K.Y. Qiu, Studies on the initiation mechanism of persulfate/aliphatic secondary amine system in vinyl polymerization, Polym. Bull. (1987) 18, https://doi.org/10.1007/BF00255817.

[244] X.-D. Feng, The role of amine in vinyl radical polymerization, Makromol. Chem. Macromol. Sympos. 63 (1992) 1–18, https://doi.org/10.1002/masy.19920630105.

[245] V. Nikolic, S. Velickovic, A. Popovic, Amine activators influence on grafting reaction between methacrylic acid and starch, Carbohydr. Polym. 88 (2012) 1407–1413, https://doi.org/10.1016/j.carbpol.2012.02.027.

[246] U.D.N. Bajpai, V. Mishra, S. Rai, Grafting of poly(acrylonitrile) onto guar gum using potassium persulfate/ascorbic acid redox initiating system, J. Appl. Polym. Sci. 47 (1993) 717–722, https://doi.org/10.1002/app.1993.070470415.

[247] Y.-J. Tu, D. Njus, H.B. Schlegel, A theoretical study of ascorbic acid oxidation and HOO/O$_2^-$ radical scavenging, Org. Biomol. Chem. 15 (2017) 4417–4431, https://doi.org/10.1039/C7OB00791D.

[248] X. Hou, G. Zhan, X. Huang, N. Wang, Z. Ai, L. Zhang, Persulfate activation induced by ascorbic acid for efficient organic pollutants oxidation, Chem. Eng. J. 382 (2020), 122355, https://doi.org/10.1016/j.cej.2019.122355.

[249] J.C. Arthur, P.J. Baugh, O. Hinojosa, ESR study of reactions of cellulose initiated by the ceric ion method, J. Appl. Polym. Sci. 10 (1966) 1591–1606, https://doi.org/10.1002/app.1966.070101015.

[250] M.S. Bains, Inorganic redox systems in graft polymerization onto cellulosic materials, J. Polym. Sci., Part C: Polym. Symp. 37 (2007) 125–151, https://doi.org/10.1002/polc.5070370108.

[251] S. Iftekhar, V. Srivastava, A. Casas, M. Sillanpää, Synthesis of novel GA-g-PAM/SiO$_2$ nanocomposite for the recovery of rare earth elements (REE) ions from aqueous solution, J. Clean. Prod. 170 (2018) 251–259, https://doi.org/10.1016/j.jclepro.2017.09.166.

[252] M. Kumar, P.S. Gehlot, D. Parihar, P.K. Surolia, G. Prasad, Promising grafting strategies on cellulosic backbone through radical polymerization processes – A review, Eur. Polym. J. 152 (2021), 110448, https://doi.org/10.1016/j.eurpolymj.2021.110448.

[253] S.S. Halacheva, D.J. Adlam, E.K. Hendow, T.J. Freemont, J. Hoyland, B.R. Saunders, Injectable Biocompatible and Biodegradable pH-Responsive Hollow Particle Gels Containing Poly(acrylic acid): The Effect of Copolymer Composition on Gel Properties, Biomacromolecules 15 (2014) 1814–1827, https://doi.org/10.1021/bm5002069.

[254] S. Bazban-Shotorbani, M.M. Hasani-Sadrabadi, A. Karkhaneh, V. Serpooshan, K.I. Jacob, A. Moshaverinia, et al., Revisiting structure-property relationship of pH-responsive polymers for drug delivery applications, J. Control. Release 253 (2017) 46–63, https://doi.org/10.1016/j.jconrel.2017.02.021.

[255] G. Sennakesavan, M. Mostakhdemin, L.K. Dkhar, A. Seyfoddin, S.J. Fatihhi, Acrylic acid/acrylamide based hydrogels and its properties - A review, Polym. Degrad. Stab. 180 (2020), 109308, https://doi.org/10.1016/j.polymdegradstab.2020.109308.

[256] S. Sharma, S. Afgan, K.A. Deepak, R. Kumar, l-Alanine induced thermally stable self-healing guar gum hydrogel as potential drug vehicle for sustained release of hydrophilic drug, Mater. Sci. Eng. C 99 (2019) 1384–1391, https://doi.org/10.1016/j.msec.2019.02.074.

[257] M. Dinari, M.A. Shirani, M.H. Maleki, R. Tabatabaeian, Green cross-linked bionanocomposite of magnetic layered double hydroxide/guar gum polymer as an efficient adsorbent of Cr(VI) from aqueous solution, Carbohydr. Polym. 236 (2020), 116070, https://doi.org/10.1016/j.carbpol.2020.116070.

[258] H.S. Samanta, S.K. Ray, Synthesis of interpenetrating network (IPN) hydrogels based on acrylic acid (AAc) and guar gum and its application as drug delivery for pyridoxine hydrochloride (vitamin B6), J. Polym. Res. 28 (2021) 479, https://doi.org/10.1007/s10965-021-02848-9.

[259] A. HaqAsif, R.R. Karnakar, N. Sreeharsha, V. Gite, N. Borane, B.E. Al-Dhubiab, et al., pH and Salt Responsive Hydrogel based on Guar Gum as a Renewable Material for Delivery of Curcumin: A Natural Anti-Cancer Drug, J. Polym. Environ. 29 (2021) 1978–1989, https://doi.org/10.1007/s10924-020-01934-1.

[260] J. Singh, A.S. Dhaliwal, Effective Removal of Methylene Blue Dye Using Silver Nanoparticles Containing Grafted Polymer of Guar Gum/Acrylic Acid as Novel Adsorbent, J. Polym. Environ. 29 (2021) 71–88, https://doi.org/10.1007/s10924-020-01859-9.

[261] X. Li, X. Wang, T. Han, C. Hao, S. Han, X. Fan, Synthesis of sodium lignosulfonate-guar gum composite hydrogel for the removal of Cu2+ and Co2+, Int. J. Biol. Macromol. 175 (2021) 459–472, https://doi.org/10.1016/j.ijbiomac.2021.02.018.

[262] R.R. Pal, D. Kumar, V. Raj, V. Rajpal, P. Maurya, S. Singh, et al., Synthesis of pH-sensitive crosslinked guar gum-g-poly(acrylic acid-co-acrylonitrile) for the delivery of thymoquinone against inflammation, Int. J. Biol. Macromol. 182 (2021) 1218–1228, https://doi.org/10.1016/j.ijbiomac.2021.05.072.

[263] R.R. Karnakar, V. Gite, v., Eco-friendly slow release of ZnSO$_4$ as a micronutrient from poly (acrylic acid: acrylamide) and guar gum based crosslinked

biodegradable hydrogels, Polymer-Plastics Technology and Materials 61 (2022) 691–708.

[264] S. Gihar, D. Kumar, P. Kumar, Facile synthesis of novel pH-sensitive grafted guar gum for effective removal of mercury (II) ions from aqueous solution, Carbohyd. Polym. Technol. Appl. 2 (2021), 100110, https://doi.org/10.1016/j.carpta.2021.100110.

[265] M. Mitra, M. Mahapatra, A. Dutta, M. Deb, S. Dutta, P.K. Chattopadhyay, et al., Fluorescent Guar Gum-*g*-Terpolymer via In Situ Acrylamido-Acid Fluorophore-Monomer in Cell Imaging, Pb(II) Sensor, and Security Ink, ACS Appl. Bio Mater. 3 (2020) 1995–2006, https://doi.org/10.1021/acsabm.9b01146.

[266] S. Awasthi, J.K. Gaur, M.S. Bobji, C. Srivastava, Nanoparticle-reinforced polyacrylamide hydrogel composites for clinical applications: a review, J. Mater. Sci. 57 (2022) 8041–8063, https://doi.org/10.1007/s10853-022-07146-3.

[267] J.K. Koh, C.W. Lai, M.R. Johan, S.S. Gan, W.W. Chua, Recent advances of modified polyacrylamide in drilling technology, J. Pet. Sci. Eng. 215 (2022) 110566, https://doi.org/10.1016/j.petrol.2022.110566.

[268] B. Xiong, R.D. Loss, D. Shields, T. Pawlik, R. Hochreiter, A.L. Zydney, et al., Polyacrylamide degradation and its implications in environmental systems, Npj Clean Water 1 (2018) 17, https://doi.org/10.1038/s41545-018-0016-8.

[269] A. Sand, A. Vyas, Superabsorbent polymer based on guar gum-graft-acrylamide: synthesis and characterization, J. Polym. Res. 27 (2020) 43, https://doi.org/10.1007/s10965-019-1951-x.

[270] A. Mahto, S. Mishra, The removal of textile industrial Dye-RB-19 using Guar gum-based adsorbent with thermodynamic and kinetic evaluation parameters, Polym. Bull. 79 (2022) 3353–3378, https://doi.org/10.1007/s00289-021-03663-4.

[271] E. ShimaaM, E.G. Zaki, W.A.E. Omar, A. Ashraf Soliman, A.M. Attia, Guar Gum-Based Hydrogels as Potent Green Polymers for Enhanced Oil Recovery in High-Salinity Reservoirs. ACS, Omega 6 (2021) 23421–23431, https://doi.org/10.1021/acsomega.1c03352.

[272] R.R. Palem, G. Shimoga, T.J. Kang, S.-H. Lee, Fabrication of multifunctional Guar gum-silver nanocomposite hydrogels for biomedical and environmental applications, Int. J. Biol. Macromol. 159 (2020) 474–486, https://doi.org/10.1016/j.ijbiomac.2020.05.041.

[273] S. Das, U. Subuddhi, Guar gum–poly(N-isopropylacrylamide) smart hydrogels for sustained delivery of 5-fluorouracil, Polym. Bull. 76 (2019) 2945–2963, https://doi.org/10.1007/s00289-018-2526-4.

[274] R.R. Palem, K. Madhusudana Rao, T.J. Kang, Self-healable and dual-functional guar gum-grafted-polyacrylamidoglycolic acid-based hydrogels with nano-silver for wound dressings, Carbohydr. Polym. 223 (2019), 115074, https://doi.org/10.1016/j.carbpol.2019.115074.

[275] R.R. Palem, G. Shimoga, K.S.V.K. Rao, S.-H. Lee, T.J. Kang, Guar gum graft polymer-based silver nanocomposite hydrogels: synthesis, characterization and its biomedical applications, J. Polym. Res. 27 (2020) 68, https://doi.org/10.1007/s10965-020-2026-8.

[276] A. Singh, M. Liu, E. Ituen, Y. Lin, Anti-Corrosive Properties of an Effective Guar Gum Grafted 2-Acrylamido-2-Methylpropanesulfonic Acid (GG-AMPS) Coating on Copper in a 3.5% NaCl Solution, Coatings (2020;10:241.), https://doi.org/10.3390/coatings10030241.

[277] A. Singh, K.R. Ansari, M.A. Quraishi, S. Kaya, S. Erkan, Chemically modified guar gum and ethyl acrylate composite as a new corrosion inhibitor for reduction in hydrogen evolution and tubular steel corrosion protection in acidic environment, Int. J. Hydrogen Energy 46 (2021) 9452–9465, https://doi.org/10.1016/j.ijhydene.2020.12.103.

[278] A. Mahto, S. Mishra, Design, development and validation of guar gum based pH sensitive drug delivery carrier via graft copolymerization reaction using microwave irradiations, Int. J. Biol. Macromol. 138 (2019) 278–291, https://doi.org/10.1016/j.ijbiomac.2019.07.063.

[279] B. Marco-Dufort, M.W. Tibbitt, Design of moldable hydrogels for biomedical applications using dynamic covalent boronic esters, Mater. Today Chem. 12 (2019) 16–33, https://doi.org/10.1016/j.mtchem.2018.12.001.

[280] J.A.L. da Silva, Borate esters of polyols: Occurrence, applications and implications, Inorg. Chim. Acta 520 (2021), 120307, https://doi.org/10.1016/j.ica.2021.120307.

[281] M. Maseda, Y. Miyazaki, T. Takamuku, Thermodynamics for complex formation of boric acid and borate with hydroxy acids and diols, J. Mol. Liq. 341 (2021), 117343, https://doi.org/10.1016/j.molliq.2021.117343.

[282] U.B. Demirci, O. Akdim, J. Andrieux, J. Hannauer, R. Chamoun, P. Miele, Sodium Borohydride Hydrolysis as Hydrogen Generator: Issues, State of the Art and Applicability Upstream from a Fuel Cell, Fuel Cells 10 (2010) 335–350, https://doi.org/10.1002/fuce.200800171.

[283] H.N. Abdelhamid, A review on hydrogen generation from the hydrolysis of sodium borohydride, Int. J. Hydrogen Energy 46 (2021) 726–765, https://doi.org/10.1016/j.ijhydene.2020.09.186.

[284] L. Dai, B. Nadeau, X. An, D. Cheng, Z. Long, Y. Ni, Silver nanoparticles-containing dual-function hydrogels based on a guar gum-sodium borohydride system, Sci. Rep. 6 (2016) 36497, https://doi.org/10.1038/srep36497.

[285] H. Wei, H. Gao, X. Wang, Development of novel guar gum hydrogel based media for abrasive flow machining: Shear-thickening behavior and finishing performance, Int. J. Mech. Sci. 157–158 (2019) 758–772, https://doi.org/10.1016/j.ijmecsci.2019.05.022.

[286] Y. Cheng, K. Pang, X. Xu, P. Yuan, Z. Zhang, X. Wu, et al., Borate crosslinking synthesis of structure tailored carbon-based bifunctional electrocatalysts directly from guar gum hydrogels for efficient overall water splitting, Carbon N Y 157 (2020) 153–163, https://doi.org/10.1016/j.carbon.2019.10.024.

[287] J. Liu, S. Wang, C. Wang, F. Zhao, S. Lei, H. Yi, et al., Influence of nanomaterial morphology of guar-gum fracturing fluid, physical and mechanical properties, Carbohydr. Polym. 234 (2020), 115915, https://doi.org/10.1016/j.carbpol.2020.115915.

[288] R. Pugliese, F. Gelain, Characterization of elastic, thermo-responsive, self-healable supramolecular hydrogel made of self-assembly peptides and guar gum, Mater. Des. 186 (2020), 108370, https://doi.org/10.1016/j.matdes.2019.108370.

[289] D. Cao, Y. Lv, Q. Zhou, Y. Chen, X. Qian, Guar gum/gellan gum interpenetrating-network self-healing hydrogels for human motion detection, Eur. Polym. J. 151 (2021), 110371, https://doi.org/10.1016/j.eurpolymj.2021.110371.

[290] R.S. Dassanayake, E. Rajakaruna, N. Abidi, Borax-Cross-Linked Guar Gum-Manganese Dioxide Composites for Oxidative Decolorization of Methylene Blue, J. Nanomater. 2019 (2019) 1–11, https://doi.org/10.1155/2019/7232715.

[291] B. Wang, L. Dai, G. Yang, G. Bendrich, Y. Ni, G. Fang, A highly efficient thermo responsive palladium nanoparticles incorporated guar gum hydrogel for effective catalytic reactions, Carbohydr. Polym. 226 (2019), 115289, https://doi.org/10.1016/j.carbpol.2019.115289.

[292] C. Talodthaisong, W. Boonta, S. Thammawithan, R. Patramanon, N. Kamonsutthipaijit, J.A. Hutchison, et al., Composite guar gum-silver nanoparticle hydrogels as self-healing, injectable, and antibacterial biomaterials, Mater. Today Commun. 24 (2020), 100992, https://doi.org/10.1016/j.mtcomm.2020.100992.

[293] R. Deka, S. Sarma, P. Patar, P. Gogoi, J.K. Sarmah, Highly stable silver nanoparticles containing guar gum modified dual network hydrogel for catalytic and biomedical applications, Carbohydr. Polym. 248 (2020), 116786, https://doi.org/10.1016/j.carbpol.2020.116786.

[294] A. Indurkar, P. Bangde, M. Gore, A.K. Agrawal, R. Jain, P. Dandekar, Fabrication of guar gum-gelatin scaffold for soft tissue engineering, Carbohyd. Polym. Technol. Appl. 1 (2020), 100006, https://doi.org/10.1016/j.carpta.2020.100006.

[295] J. Bag, S. Mukherjee, S.K. Ghosh, A. Das, A. Mukherjee, J.K. Sahoo, et al., Fe$_3$O$_4$ coated guargum nanoparticles as non-genotoxic materials for biological application, Int. J. Biol. Macromol. 165 (2020) 333–345, https://doi.org/10.1016/j.ijbiomac.2020.09.144.

[296] Z. Rao, S. Liu, R. Wu, G. Wang, Z. Sun, L. Bai, et al., Fabrication of dual network self-healing alginate/guar gum hydrogels based on polydopamine-type microcapsules from mesoporous silica nanoparticles, Int. J. Biol. Macromol. 129 (2019) 916–926, https://doi.org/10.1016/j.ijbiomac.2019.02.089.

[297] V.K. Gupta, S. Agarwal, R. Ahmad, A. Mirza, J. Mittal, Sequestration of toxic congo red dye from aqueous solution using ecofriendly guar gum/ activated carbon nanocomposite, Int. J. Biol. Macromol. 158 (2020) 1310–1318, https://doi.org/10.1016/j.ijbiomac.2020.05.025.

[298] A. Butt, S. Jabeen, N. Nisar, A. Islam, N. Gull, S.K. Iqbal, et al., Controlled release of cephradine by biopolymers based target specific crosslinked hydrogels, Int. J. Biol. Macromol. 121 (2019) 104–112, https://doi.org/10.1016/j.ijbiomac.2018.10.018.

[299] M.U.A. Khan, M.A. Raza, S.I.A. Razak, M.R. Abdul Kadir, A. Haider, S.A. Shah, et al., Novel functional antimicrobial and biocompatible arabinoxylan/guar gum hydrogel for skin wound dressing applications, J. Tissue Eng. Regen. Med. 14 (2020) 1488–1501, https://doi.org/10.1002/term.3115.

[300] M.U.A. Khan, I. Iqbal, M.N.M. Ansari, S.I.A. Razak, M.A. Raza, A. Sajjad, et al., Development of Antibacterial, Degradable and pH-Responsive Chitosan/Guar Gum/Polyvinyl Alcohol Blended Hydrogels for Wound Dressing, Molecules 26 (2021) 5937, https://doi.org/10.3390/molecules26195937.

[301] A. Aydogdu, C.J. Radke, S. Bezci, E. Kirtil, Characterization of curcumin incorporated guar gum/orange oil antimicrobial emulsion films, Int. J. Biol. Macromol. 148 (2020) 110–120, https://doi.org/10.1016/j.ijbiomac.2019.12.255.

Synthesis, characterization, and humidity-responsiveness of guar gum xanthate and its nanocomposite with copper sulfide covellite

Trung-Anh Le, Morad Zouheir, Kostiantyn Nikiforow, Muhammad Khatib, Orr Zohar, Hossam Haick, and Tan-Phat Huynh*

III

Synthesis, characterization, and humidity-responsiveness of guar gum xanthate and its nanocomposite with copper sulfide covellite

Trung-Anh Le [a], Morad Zouheir [a,b], Kostiantyn Nikiforow [c], Muhammad Khatib [d], Orr Zohar [d], Hossam Haick [d], Tan-Phat Huynh [a,*]

[a] *Laboratory of Molecular Sciences and Engineering, Åbo Akademi University, Henrikinkatu 2, 20500 Turku, Finland*
[b] *Laboratoire de Matériaux, Procédés, Catalyse et Environnement (LMPCE), Université Sidi Mohammed Ben Abdellah, Fès, Route d'Imouzzer, BP 2427 Fès, Morocco*
[c] *Institute of Physical Chemistry, Polish Academy of Sciences, 44/52 Kasprzaka, 01-224 Warsaw, Poland*
[d] *The Department of Chemical Engineering, Technion – Israel Institute of Technology, Haifa 3200003, Israel*

ARTICLE INFO

ABSTRACT

A novel conjugation of guar gum with xanthate groups via facile aqueous xanthation reaction has been reported. Density of grafted xanthate on guar gum product (GG-X) is as high as 4.4%, thus GG-X is conceivably characterized and confirmed by various spectrometric, electrochemical, thermogravimetric, and microscopic methods. Complexation of GG-X with numerous borderline and soft metal ions (e.g. Fe^{2+}, Co^{2+}, Ni^{2+}, Cu^{2+}, Pb^{2+}, Pt^{2+} and Cd^{2+}) yields hydrophilic gel-like materials and shows good agreement with hard and soft acid and base (HSAB) theory. This indicates tremendous potential of GG-X in metal ion extraction, removal and hydrogel cross-linking. GG-X is also employed to formulate an aqueous colloidal dispersion of copper sulfide covellite (GG-X/CuS) nanocomposites. GG-X therefore behaves as a surfactant, allowing formation of electronically conductive nanocomposites. XRD indicates apparent beneficial effects of GG-X in the synthesis of CuS with a crystallite size of 15.6 nm. This novel nanocomposite is a promising material for humidity sensing, showing reversible linear responses to relative humidity changes within 10 to 80% range. The interaction between GG-X and water might cause changes in electrical permittivity of GG-X/CuS nanocomposite and/or electrical hopping conductivity between CuS nanoparticles.

1. Introduction

Guar gum (GG) is a natural non-ionic galactomannan polysaccharide with a large molecular weight up to $2 \cdot 10^6$ Da, depending on the natural sources [1,2]. GG is composed of a mannose (M) backbone and galactose (G) side chains with a M/G ratio of around 1.8:1 (Fig. 1a). In GG, β-1,4-glycosidic bonds are found between M monomers, while G monomers are linked to the M backbone via α-1,6-glycosidic bonds. Due to the existence of numerous hydroxyl (–OH) groups on polysaccharide backbone, GG is highly hydrophilic and viscous solutions of GG can be obtained easily even in cold water [3]. Moreover, these –OH groups also act as reactive sites for diverse chemical functionalization and derivatization approaches of the original GG towards novel advanced materials [4–10]. Possessing the nontoxicity, biocompatibility, biodegradability, abundant availability and low cost, GG has attracted great attention as a promising material in various research fields, e.g. hydraulic fracturing, water purification, food and petroleum industry, cosmetics and drug delivery [11–15]. Despite numerous advantages that GG can offer, challenges in the usage of GG in the development of new materials remain due to its susceptibility to microbial contamination

and fast biodegradation. It is, therefore, important to chemically modify GG in order to enhance its stability, functionality and extend its applicability [11].

Over the years, xanthate (X) functional group has been well-known for its various applications in chemistry and materials science. While O- and N-based functional groups such as alkoxide, ether, carboxylic acid, sulfonic acid and amine, are typically regarded as hard bases, S-based xanthate functional group can be considered as a soft base from the hard and soft acid and base (HSAB) theory [16]. Xanthate, therefore, has been a popular functional group to chelate soft acids due to its strong binding capacity to a wide range of metal ions especially heavy metal ions, and therefore, an ideal functional group for metal ion removal and extraction [17–22], surface capping and synthesis of nanoparticles [23–25]. The selective tumor-killing capacity of platinum or non-platinum xanthate complexes was also reported, showing promising bioactivity of xanthate towards tumor cells [26–29]. In addition, xanthate moieties also act as important intermediates in organic transformations such as the synthesis of organofluorine derivatives [30], amines, anilines, and other nitrogen compounds [31], or in reversible addition-–fragmentation chain transfer (RAFT) and macromolecular design via the interchange of xanthates (MADIX) polymerization [32–34].

In this study, GG polymer backbone is xanthated for the first time to give guar gum xanthate (GG-X), which would enhance the chelating ability of original GG towards different metal ions. Characterization of GG-X has been carried out using various techniques. In addition, potential applications of GG-X are explored and demonstrated through the complexation of metal ions (Section 3.3) and the formation of copper sulfide nanocomposites for humidity sensing (Section 3.4) with GG-X. Traditionally, the complexation of molecular xanthate derivatives and

metal ions in aqueous solutions yields nonpolar metal xanthate complex products [35]. Due to polymeric structure and remaining -OH groups of GG-X, however, the complexation of metal ions via GG-X can result in hydrophilic gel-like materials. This allows a convenient and environmentally friendly approach for metal ion extraction and removal, since organic solvents are not required and resultant gel-like materials can be easily separated or recovered. Moreover, hydrophilic GG-X can be used to formulate nanocomposites with semiconductors such as copper sulfide for humidity sensing. Among different types of copper sulfide phase structures, copper sulfide covellite (CuS) stands out because of its simple synthesis at ambient conditions, metallic-like conductivity, numerous potential applications in photocatalysis, solar cells and electronics [36–38]. The chelating effect of xanthate functional groups in GG-X can assist the formation and stabilization of CuS nanoparticles dispersed in GG-X matrix, which cannot be obtained without the presence of xanthate groups by using GG solely. Once GG-X/CuS nanocomposites are formed and employed as humidity sensors, hydrophilicity of GG-X might allow humidity interaction while CuS can act as a filler in the GG-X matrix to form electronically conductive composites, which are potential materials for chemical and biological sensing. The interaction between GG-X and water might cause changes in electrical permittivity of GG-X/CuS nanocomposite and/or electrical hopping conductivity between CuS nanoparticles, resulting in humidity sensing capacity of the nanocomposite [39,40].
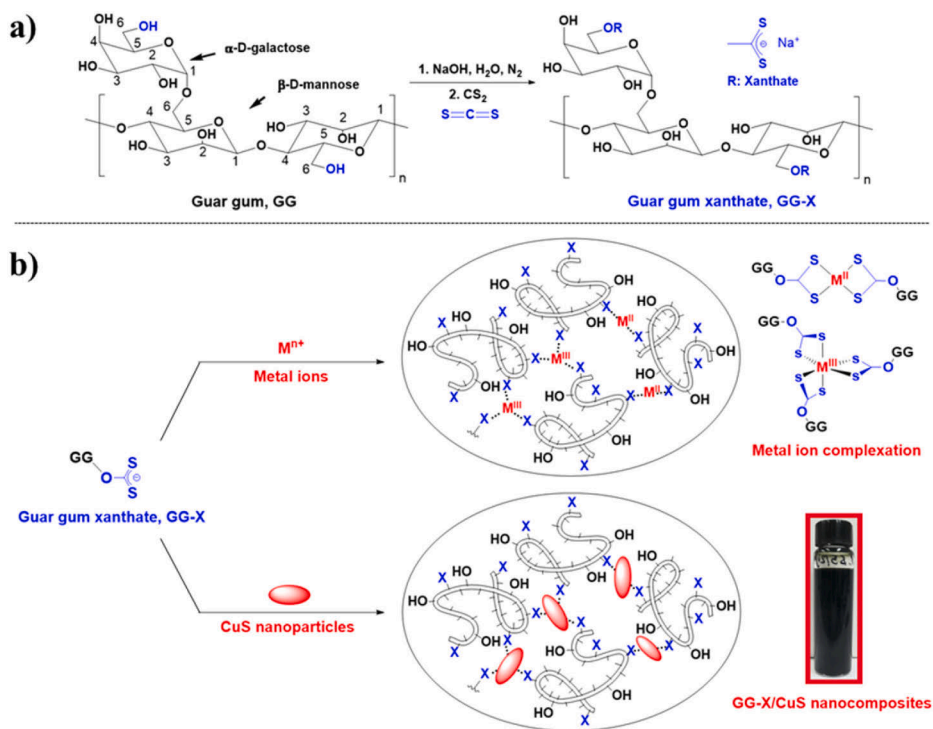

Fig. 1. Xanthation of GG in aqueous solution (a), metal ion complexation of GG-X and GG-X/CuS preparation (b).

2. Experimental

2.1. Chemicals and reagents

Guar gum (MW = 220 kDa), carbon disulfide (CS_2), $AlCl_3$, $CdCl_2$, $CoCl_2.6H_2O$, $CuCl_2$, $FeCl_2.4H_2O$, $FeCl_3.6H_2O$, $Ni(NO_3)_2.6H_2O$, Na_2S, $PbCl_2$, $PtCl_2$, $SnCl_2$, $ZnCl_2$, potassium ethyl xanthogenate $C_2H_5OCS_2K$ (Et-X), $NaHCO_3$, Na_2CO_3, acetone, ethanol (EtOH), hexanol, methanol (MeOH), toluene are purchased from Sigma-Aldrich. All chemicals are reagent-grade and used as received without further purification.

2.1.1. Carbonate-bicarbonate buffer solution

Carbonate-bicarbonate buffer (pH 10.5) was prepared by dissolving 1.05 g of $NaHCO_3$ and 9.28 g of Na_2CO_3 in 1.00 L of distilled water.

2.2. Material synthesis and device fabrication

2.2.1. GG-X

12.22 g NaOH was added to 200 mL N_2-purged H_2O. Then, 2.00 g GG was added gradually to NaOH solution and the solution was stirred in 30 min. 4.455 mL CS_2 was then added to the solution and the reaction was carried out for 2.5 h at room temperature. MeOH was added to quench the reaction and precipitate GG-X products. The products were washed intensively by MeOH to remove inorganic xanthates byproducts until highly pure GG-X products were confirmed by UV–Vis spectroscopy. GG-X final product was dried in vacuum to give a reaction yield of 87.23%.

2.2.2. GG-X/CuS nanocomposite

600 mg of GG-X (0.452 mmol X) powder was dissolved in 32.0 mL distilled water at 40 °C to obtain a homogenous yellow solution. Meanwhile, 608 mg of $CuCl_2$ (4.386 mmol) powder was dissolved in 8.0 mL water. The two solutions were mixed together under vigorous stirring to get a viscous mixture of GG-X and Cu^{2+}. Finally, 61.5 mL of Na_2S 0.1 M (6.15 mmol) was added dropwise to the GG-X and Cu^{2+} mixture under vigorous stirring for 15 min to allow the formation of copper sulfide and the liquefaction of the gel. This solution was then sonicated for 15 min and concentrated by a hotplate at 85 °C for 2 h to get 48.0 mL of a homogeneous solution. The resultant product was purified by solvent precipitation (H_2O and EtOH antisolvent) and then redissolved in water.

2.2.3. Reference materials

(1) inorganic xanthate (Inorg-X) control solution: 30.0 μL CS_2 was added to 2.0 mL of NaOH 1 M under N_2 atmosphere. The solution was stirred within 2.5 h to give a reference Inorg-X solution composed of different forms of inorganic xanthates for UV–vis spectrophotometry. (2) CuS references: CuS (S^{2-}) reference was obtained by the typical synthetic route of CuS, in which Cu^{2+} was added into an alkaline solution of S^{2-} (pH 10.5). Meanwhile, CuS (OH^-) reference was prepared by adding S^{2-} to a slightly alkaline Cu^{2+} solution at pH 10.5, to mimic the preparation of GG-X/CuS but without GG-X, hence, examining the effect of alkaline pH on the formation of CuS. (3) GG/CuS reference: GG/CuS reference was also prepared by using 600 mg of GG, instead of GG-X at the same alkaline pH 10.5, to study the effect of GG-X in the formation of CuS.

2.2.4. Metal complexation for demonstration

Different metal ion solutions of the same molar concentrations 37.68 mM (Al^{3+}, Cr^{3+}, Fe^{3+}), and 56.52 mM (Zn^{2+}, Sn^{2+}, Fe^{2+}, Co^{2+}, Ni^{2+}, Cu^{2+}, Pb^{2+}, Cd^{2+}, Pt^{2+}) were prepared in acidified H_2O. 15.0 mg GG-X was dissolved completely in 1000 μL neutral H_2O in different vials. Then 100 μL of different metal ion solutions was added to those GG-X vials to give complexation reactions. pH of final gel-like products was measured to be in the range of 9.5–10.5.

2.2.5. Sensor fabrication

5-μm gap platinum-interdigitated electrodes (IDEs) (Micrux, Spain) were washed with water and ethanol. Then tape was applied onto the electrodes to control the coating area. The electrodes were then placed in plasma cleaner for 3 min. 20.0 μL of following solutions: GG, GG-X, GG/CuS, GG-X/CuS was drop-coated on the clean electrodes using micropipettes and the electrodes were then dried in vacuum for 4 h before testing.

2.3. Characterization

2.3.1. UV–Visible (UV–Vis) spectrophotometry

UV–Vis spectra of all compounds in carbonate-bicarbonate buffer solutions (pH 10.5) were recorded on Shimadzu UV 2501PC spectrophotometer (Shimadzu Inc., Kyoto, Japan) in the range of 260–700 nm with a resolution of 0.5 nm, in quartz cells (1 × 1 cm) at room temperature.

2.3.2. Cyclic voltammetry (CV)

Measurements were performed using a portable electrochemical interface and impedance analyzer (CompactStat, Ivium Technologies, The Netherlands). The experiments were carried out with a three-electrode setup including 1-mm diameter Pt disk working electrode, Pt wire counter electrode, and Ag/AgCl reference electrode. Cyclic voltammograms were recorded under potentiodynamic conditions over the potential range of −0.5 to 0.8 *V* (vs. Ag/AgCl) at the potential scan rate of 50 mV/s.

2.3.3. Fourier-transform infrared spectroscopy - Attenuated total reflectance (FTIR-ATR) spectroscopy

IR spectra were measured by Nicolet™ iS50 FTIR spectrometer (Thermo Scientific Inc., Waltham, MA, USA). The spectra were recorded from 400 to 4000 cm^{-1} with a resolution of 4.0 cm^{-1} and averaged from 64 scans. The instrument was equipped with a diamond crystal and a pressure gauge.

2.3.4. Powder X-ray diffraction (XRD)

Bruker D8 Discover diffractometer (Bruker Inc., Billerica, MA, USA) was employed to measure XRD spectra of samples in a diffraction angle range between 10 to 80° with resolution of 0.04° at room temperature. X-ray K780 (Cu Kα anode, λ = 1.5418 Å) generator was used at 40 kV voltage and 40 mA current.

2.3.5. Scanning electron microscopy - energy dispersive X-ray spectroscopy (SEM-EDS)

Morphology of materials was studied by LEO Gemini 1530 scanning electron microscopy (Leo Electron Microscopy Inc., Thornwood, NY, USA) while elemental mapping was done by energy dispersive X-ray spectroscopy (thermo scientific ultradry silicon drift detector). Resultant SEM images of GG-X/CuS were analyzed and CuS particle size was examined using Image J software. The particle size distribution curve of CuS was plotted based on 200 particles of CuS in GG-X/CuS.

2.3.6. X-ray photoelectron spectroscopy (XPS)

PHI 5000 VersaProbe (ULVAC-PHI Inc., Hagisono, Chigasaki, Kanagawa, Japan) spectrometer was used to conduct XPS measurements under following conditions: monochromatic Al Kα radiation (h*ν* = 1486.6 eV), an X-ray source operating at 25 W, 15 kV, 100 μm spot, pass energy of 23.5 eV, energy step of 0.1 eV. Obtained XPS spectra were analyzed in CasaXPS software using the set of the sensitivity factors native for the hardware. Shirley background and Gaussian-Lorentzian peak shape were used for deconvolution of all spectra.

2.3.7. Thermogravimetric analysis - differential scanning calorimetry (TGA-DSC)

TGA-DSC measurements were carried out by a Netzch STA 449 F1

Jupiter thermogravimetric analyzer (Netzsch Instruments Inc., Featherstone, Wolverhampton, UK) under N_2 inert atmosphere from 30 to 600 °C with a heating rate of 10 °C min^{-1}. Dry samples of 2–10 mg were placed in aluminium DSC pans, while N_2 flow rate was maintained at 20 mL min^{-1}.
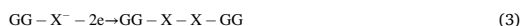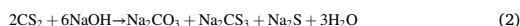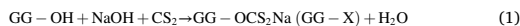
2.3.8. Humidity and electrical resistance studies

Two procedures, one is without and another is with vacuum applied for desorption step, have been adopted for gas and humidity sensing. The experimental setup for the former procedure has been reported by Zouheir et al. [41] In short, a wireless and portable data acquisition hardware (DAQ) device was built from the Arduino and 16-bit analog-to-digital converter to acquire data from resistive sensors. LabVIEW VI was programmed to plot and save voltage outputs acquired by the prototype through Bluetooth communication. The reference and coated sensors were set inside a chamber to monitor relative humidity (RH) by adjusting the humid air or the dry air via an inlet. Room-temperature (25 °C) air with varying humidity levels was generated using an ultrasonic humidifier (Wilfa), without affecting the temperature inside the humidity chamber. In the latter procedure, the sensors were loaded into a stainless-steel chamber and exposed to cycles of vacuum and N_2 with varying concentrations of gases or water vapor, while measuring their resistance. A computer-controlled bubbler was filled with the corresponding liquid, and then N_2 was bubbled through. The resulting gas mixture (N_2 and organic compounds/water) was diluted to obtain the desired concentrations. The normalized resistance was calculated according to the following equation: $R_{Normalized} = (R-R_0) / R_0$, where R_0 is the initial resistance value.

3. Results and discussion

3.1. Synthesis, metal ion complexation of GG-X and preparation of GG-X/CuS nanocomposites

Hydroxyl groups of GG were first activated by using an excess amount of sodium hydroxide. Carbon disulfide was then added to the solution to yield xanthated guar gum GG-X (Fig. 1a). N_2 purging was crucial to avoid further oxidation of xanthates. Since the xanthation was carried out in aqueous media, complex equilibria between the main reaction to produce GG-X and side reactions to create Inorg-X byproducts, were quickly established (e.g. Eqs. (1) and (2)) [42]. Meanwhile, a control solution for Inorg-X byproducts was also prepared under similar conditions without addition of GG for comparison purposes. In addition, complexation between various metal ions and GG-X was carried out effortlessly in aqueous solutions by controlling the molar ratio between metal ions and xanthate groups as 1:2 or 1:3 (Fig. 1b). To prepare GG-X/CuS nanocomposites, Cu^{2+} was first dispersed in GG-X aqueous solution, followed by a precipitation reaction between Cu^{2+} and S^{2-} to give a homogenous dispersion of CuS nanoparticles in GG-X aqueous matrix (Fig. 1b). Other samples such as CuS (S^{2-}), CuS (OH$^-$), GG/CuS were also studied to highlight beneficial effects of GG-X on the formation of CuS.

$$GG - OH + NaOH + CS_2 \rightarrow GG - OCS_2Na \ (GG - X) + H_2O \qquad (1)$$

$$2CS_2 + 6NaOH \rightarrow Na_2CO_3 + Na_2CS_3 + Na_2S + 3H_2O \qquad (2)$$

$$GG - X^- - 2e \rightarrow GG - X - X - GG \qquad (3)$$

3.2. Characterization

3.2.1. UV–vis spectrophotometry

GG-X was characterized by UV–Vis spectrophotometry with ethyl xanthogenate (Et-X) as a reference compound to confirm the xanthation of GG. Similar absorption bands of around 302.5 and 300.5 nm from GG-X and Et-X reference are observed, while different Inorg-X impurities in

the control solution possess a collective absorption band of around 334.5 nm (Fig. 2a). Based on different absorption bands at 302.5 and 334.5 nm, the purity of GG-X product can be monitored and confirmed (Fig. S1). The degree of substitution (DS) and grafting density (GD) of xanthate on guar gum are approximated as 0.132 (number of xanthate moieties per each anhydroglucose unit (AGU)) and 4.4% (percentage of -OH groups which have been xanthated out of three -OH groups in one AGU) respectively, based on the molar absorption coefficient of Et-X (supplementary data, SD). While CuS is insoluble in water, a green, transparent and homogeneous aqueous colloidal dispersion of GG-X/CuS was easily studied by UV–Vis spectrophotometry (Fig. 2a) because of the stabilization effect of GG-X as a surfactant. GG-X/CuS shows a typical absorption spectrum of CuS that ranges from UV to visible light and near IR radiation [43].
.

3.2.2. Cyclic voltammetry (CV)

The presence of xanthate on GG is also confirmed by CV with Et-X reference compound, since xanthate can be oxidized electrochemically [44]. CV of the blank buffer (Fig. S7) shows a cathodic peak, corresponding to the reduction of buffer solution. In the presence of Et-X and GG-X, anodic peaks of xanthate oxidation at 0.7 and 0.5 V (vs. Ag/AgCl) respectively are recorded and therefore, suggesting a possible electrochemical cross-linking approach of GG-X via covalent disulfide bonds (Eq. (3)). In addition, the cathodic peak of the buffer solution is not observed, and this might be due to the adsorption of Et-X or GG-X on the electrode surface, hence, inhibiting the charge transfer process to the buffer.

3.2.3. FTIR spectroscopy

IR spectra of GG, CuS (S^{2-}), GG-X, GG-X/CuS were recorded and shown in Fig. 2b, c. Typical IR absorption bands of galactomannan backbone appear in all three spectra of GG, GG-X and GG-X/CuS. The O—H stretching vibration from hydroxyl groups and C—H stretching of CH_2 groups can be found in the wavenumber range of 3000–3600 and 2800–3000 cm^{-1} respectively. Meanwhile, absorption bands of around 1640 cm^{-1} due to ring stretching, strong absorption peaks at 1143, 1064 and 1014 cm^{-1} from C-OH bond, CH_2OH stretching and CH_2 twisting vibrations respectively, and typical peaks at 874 cm^{-1} for galactose and mannose are also observed [45–47].

IR spectrum of GG-X was compared to that of GG to emphasize new absorption bands at 1149 cm^{-1} (S-C-S stretching) and 1057 cm^{-1} (C=S stretching), ([18]; Y [22].) indicating the successful xanthation of GG. The employment of inert gases in the synthesis of GG-X is also crucial for xanthation process since in the presence of O_2, oxidation of xanthate functional groups might occur. Fig. S8 compares IR spectra of GG-X samples prepared in aerobic and anaerobic conditions. GG-X synthesized under aerobic atmosphere also possesses similar absorption bands around 1149 and 1057 cm^{-1}. Nevertheless, a new intensive absorption band around 1437 cm^{-1} due to the stretching of S=O bonds can be easily detected [48], suggesting the further oxidation of xanthate groups under aerobic synthesis. In addition, IR spectrum of CuS (S^{2-}) reference shows no significant signals, while similar absorption bands of GG-X (especially at 1057 cm^{-1} due to C=S stretching) can also be found in GG-X/CuS, confirming the presence of GG-X.

3.2.4. Powder X-ray diffraction (XRD)

X-ray diffractograms of newly synthesized materials and their references are shown in Fig. 2d to confirm their phase structures and purity. Both GG and GG-X possess broad peaks at similar 2θ values of around 18°, indicating the amorphous phase structure of GG and GG-X. XRD peaks of GG-X/CuS are identified at 2θ = 10.72, 27.20, 27.72, 29.32, 31.84, 32.84, 38.88, 43.20, 44.40, 48.00, 52.76, 57.28, 59.40, and correspond to lattice plane indices (002), (100), (101), (102), (103), (006), (105), (106), (008), (110), (108), (202), (116), respectively, of covellite CuS (JCPDS file no. 79-2321) [49,50], hence CuS in GG-X/CuS
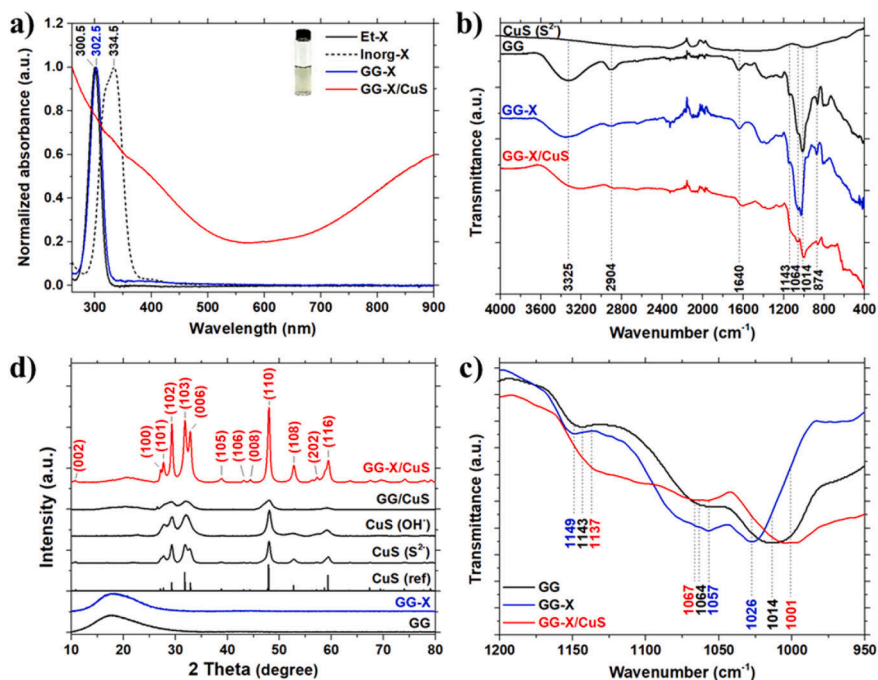
Fig. 2. UV–Vis spectra (a) of Et-X, Inorg-X, GG-X and GG-X/CuS (greenish homogeneous solution in the vial) in carbonate-bicarbonate buffer solution at pH 10.5. IR spectra (b, c) of GG, CuS (S^{2-}) references, GG-X synthesized under anaerobic atmosphere, and GG-X/CuS. XRD patterns (d) of GG, GG-X, stick pattern of CuS covellite (JCPDS file no. 79–2321), CuS (S^{2-}), CuS (OH^-), GG/CuS and GG-X/CuS.

exists in covellite phase. A broad signal at 2θ of 20.56° is attributed to amorphous GG-X in GG-X/CuS. The XRD spectrum of GG-X/CuS shows strong and sharp diffraction peaks, suggesting its high crystallinity and purity.

In addition, several reference samples prepared in the same reaction condition as that of GG-X/CuS were characterized by XRD to determine whether beneficial effects of GG-X on the formation of CuS covellite are due to the alkaline pH, the presence of guar gum and/or xanthate functional groups of GG-X. The crystallite size D of these samples was calculated from the (110) peak width through the well-known Scherrer eq. (SD) and is used to correlate the effects of GG-X on the formation of crystalline CuS covellite. X-ray diffractograms of CuS (S^{2-}) shows a more distinct XRD pattern of CuS than those of CuS (OH^-). CuS (S^{2-}) also has a larger crystallite size of 11.7 nm than 9.1 nm of CuS (OH^-), hence, excluding beneficial effect of OH^- on the formation of CuS in this particular synthetic pathway. Additionally, GG/CuS prepared in alkaline pH possesses broad peaks of CuS and much smaller crystallite size of 5.1 nm, therefore, also disproving any beneficial effects of GG and OH^- on the formation of crystalline CuS. Among these X-ray diffractograms, GG-X/CuS has the most distinctly sharp XRD peaks of CuS and largest crystallite size of 15.6 nm, correlating the advantageous presence of GG-X in the formation of highly crystalline, hence highly electrical conductivity of CuS [51].

3.2.5. Scanning electron microscopy - energy dispersive X-ray spectroscopy (SEM-EDS)

SEM analysis on GG, GG-X and GG-X/CuS (Fig. 3a, b and g respectively) shows irregular morphology of the three samples with particle size of around 30–90 μm. Meanwhile, aggregation of large-sized

particles is observed in electron micrographs of GG-X and GG-X/CuS. This could be explained due to the presence of electrically charged xanthate functional groups in GG-X, hence, enhancing electrostatic interaction between particles. In addition, elemental mapping based on EDS was also employed to confirm the success of xanthation process, as well as the formation and distribution of CuS in GG-X/CuS nano-composite. Fig. 3c, d, e, f show a uniform distribution of C, O and S elements in GG-X, while Fig. 3h, i, j, k and l also show well-distributed C, O, S and Cu elements in GG-X/CuS nanocomposite. CuS particles in GG-X/CuS possess rod-like morphology and are distributed uniformly throughout GG-X structure (Fig. S9). The particle size distribution of CuS particles was plotted and fitted by Gaussian function to give an average length of 230 ± 31 nm (Fig. S10).

3.2.6. X-ray photoelectron spectroscopy (XPS)

XPS measurements were carried out on GG, Et-X, CuS (S^{2-}), GG/CuS, GG-X/CuS, to confirm the presence of xanthate functional groups in GG-X and to study the interaction between GG-X and CuS in GG-X/CuS. The high-resolution XPS spectrum of sulfur S 2p for Et-X reference is shown in Fig. 4a. Two types of S 2p states are observed on the spectrum and due to spin-orbit coupling, these S 2p signals are present as doublets (S 2p 3/2 and S 2p 1/2, separated by 1.2 eV). The high-intensity doublet at lower energy (S 2p 3/2 at 161.9 eV, S 2p 1/2 at 163.1 eV) is most likely from xanthate functional groups, while the low-intensity doublet at higher energy (S 2p 3/2 at 167.8 eV, S 2p 1/2 at 169.0 eV) could be attributed to sulfur in higher oxidation states, whose presence could have been caused by the oxidation of xanthate groups [52].

XPS spectra of GG-X sample were compared to those of GG reference sample to show that the main differences can be correlated to the
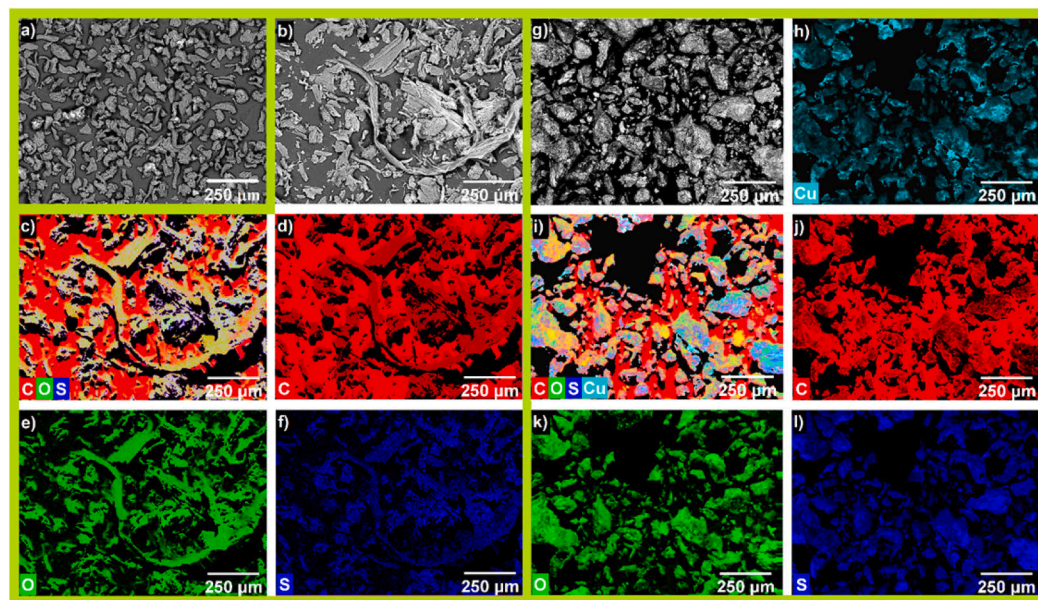
Fig. 3. Electron micrographs of GG (a), GG-X and its elemental mapping (b-f), GG-X/CuS and its elemental mapping (g-l).

presence of sulfur in GG-X. The S 2p spectrum of GG-X possesses two similar groups of peaks to those of Et-X (Fig. 4b). The first doublet at lower energy (S 2p 3/2 at 162.2 eV, S 2p 1/2 at 163.4 eV) confirms the presence of xanthate functional groups in GG-X. The atomic concentration of sulfur from xanthate groups is also determined to be around 0.2% (Table S6). Meanwhile, the second doublet of higher energy (S 2p 3/2 at 167.7 eV, S 2p 1/2 at 168.9 eV) has a greater intensity than the lower energy doublet, suggesting the further oxidation of xanthate groups on the sample surface.

XPS spectra of GG/CuS also indicate the presence of copper(II) (Cu^{2+}) and sulfide (S^{2-}) covellite in the sample (Fig. 4c for S-XPS, Table S7). The binding energy of Cu 2p 3/2 peak (932.7 eV), the general shape of the Cu 2p spectra, as well as the S 2p spectra (S 2p 3/2 at 162.1 eV) agree with literature data on the presence of CuS copper(II) sulfide covellite [53–55]. XPS analysis of GG-X/CuS sample also confirms the presence of copper(II) sulfide (Cu^{2+} and S^{2-}) covellite (Fig. 4d for S-XPS, Table S8). S 2p and Cu 2p spectra of GG/CuS and GG-X/CuS show peaks in the similar range. More interestingly, while the atomic concentrations of Cu^{2+} and S^{2-} in GG/CuS are measured as 0.67 and 0.81% respectively, the atomic concentrations of Cu^{2+} and S^{2-} in GG-X/CuS are found approximately five times greater, of 3.45 and 4.54% respectively. As CuS in GG/CuS and in GG-X/CuS was synthesized in the same reaction conditions, this implies a much stronger interaction between CuS and GG-X than between CuS and GG due to the presence of xanthate groups.

3.2.7. Thermogravimetric analysis - differential scanning calorimetry (TGA-DSC)

Thermal properties of GG-X, GG-X/CuS, as well as GG and CuS (S^{2-}) references were studied by TGA-DSC. TGA and derivative of weight loss (DTG) thermograms of these materials are shown in Fig. 4e and f. Both GG and GG-X possess an initial endothermic weight loss of 8.61% and 8.41% due to water desorption at around 78 and 72 °C respectively. Thermal degradation of galactomannan chains in GG is detected in the temperature range of 225–425 °C, with the largest weight loss at 314 °C

based on DTG and three endothermic events at around 246 °C, 315 °C, 396 °C on the DSC thermogram (Fig. S11a). This decomposition temperature range is commonly found in galactomannan polysaccharides under N_2 inert atmosphere [45]. Meanwhile, a similar endothermic degradation of galactomannan chains is also observed in GG-X within a lower temperature range between 150 and 375 °C, with the largest weight loss at 251 °C from DTG and two major endothermic events at around 244 °C, 366 °C from DSC (Fig. S11c). These temperature ranges are also in good agreement with typical decomposition temperature ranges of compounds which contain xanthate functional groups, hence, confirming the presence of xanthate in GG-X [56]. The lower thermal stability of GG-X comparing to GG might be attributed to the loss of -OH functional groups during the xanthation process, resulting in the disruption of the original hydrogen bonding system in GG [57,58].

Thermograms of CuS (S^{2-}) reference (Fig. S11b) show an initial weight loss of 1.88% at around 105 °C due to the endothermic desorption of water. Two other endothermic events are also observed within the temperature range of 180 and 300 °C, corresponding to a total weight loss of 10.85%, because of the removal of lattice water in the crystalline structure of CuS. Thermal decomposition of CuS gradually into Cu_xS ($1 < x \leq 2$) and vaporization of S also occurs endothermically at around 409 °C to give a weight loss of 6.20% [59,60]. The endothermic water desorption of GG-X/CuS occurs at temperature above 100 °C and reaches its greatest weight loss of 9.04% at around 161 °C according to DTG (Fig. S11d). A significant weight loss of 10.66% is also observed within the temperature range of 200–300 °C, which can be attributed mainly to the thermal decomposition of xanthate functional groups and/or the removal of lattice water in GG-X/CuS. Above 300 °C, another weight loss of 9.68% is detected and could be due to the thermal degradation of xanthate functional groups, galactomannan backbone and/or CuS into Cu_xS ($1 < x \leq 2$).
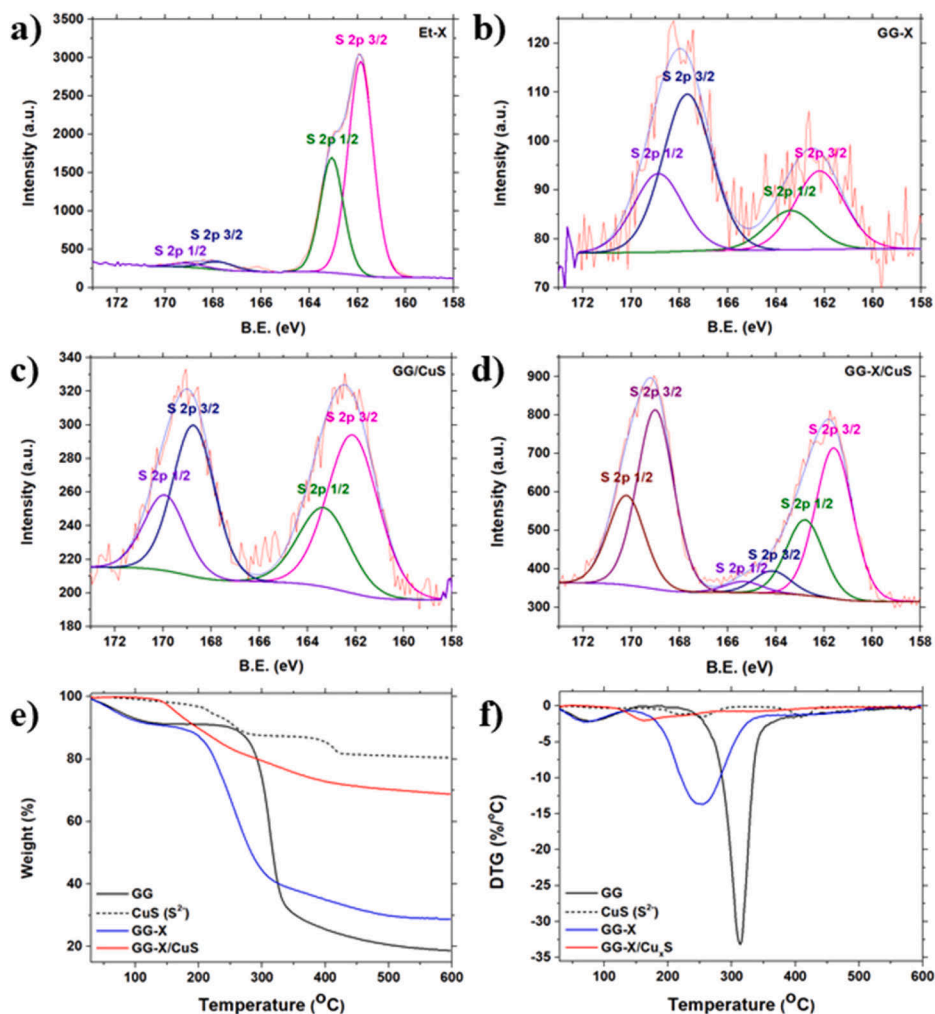
Fig. 4. Sulfur XPS spectra of Et-X (a), GG-X (b), GG/CuS (c), GG-X/CuS (d); TGA (e) and DTG (f) thermograms of GG, CuS (S^{2-}), GG-X and GG-X/CuS.

3.3. Metal ion complexation of GG-X

Potential applications of GG-X in metal ion complexation are demonstrated with various metal ions of 2+ and 3+ electrical charges to form gel-like materials (Fig. 1b). Using the hard and soft acid and base (HSAB) theory, metal ions of interest can be classified as hard (Al^{3+}, Cr^{3+}, Fe^{3+}), borderline (Zn^{2+}, Sn^{2+}, Fe^{2+}, Co^{2+}, Ni^{2+}, Cu^{2+}, Pb^{2+}), and soft (Cd^{2+}, Pt^{2+}) acids, while S-based xanthate functional group is a soft base. The obtained gel-like products formed by different metal ions have good agreements with HSAB theory as the coordinating capacity of soft xanthate bases becomes stronger towards softer acids (Fig. 5a, S5 in SI) [16]. In addition, control experiments on the complexation of original unxanthated GG were done to show a reverse behavior of GG-based gel-like materials (Fig. S6). Under similar pH condition of around 10, -OH groups on GG can be deprotonated partially to become alkoxides. These

O-based alkoxide chelating moieties are classified as hard bases and therefore, interacting more strongly with hard (Al^{3+}) and borderline (Pb^{2+}) acids rather than soft (Cd^{2+}) ones.

3.4. Sensing application of GG-X/CuS

In order to explore the chemical sensing capability of GG-X/CuS, electrical responses of GG-X/CuS to relative humidity (RH) was first studied and compared to other reference materials, namely, the bare IDE, GG, GG-X, CuS (S^{2-}) and GG/CuS (Figs. S13), using a low-cost wireless Arduino platform, which was manually assembled in our lab [41]. At RH of around 5%, all bare-IDE, GG and GG-X reference sensors show high resistance of 500–600 kΩ. As the RH increases from 5 to 100%, the resistance of these decreases significantly to around 15–30 kΩ. Several cycles of changing RH were performed to show good
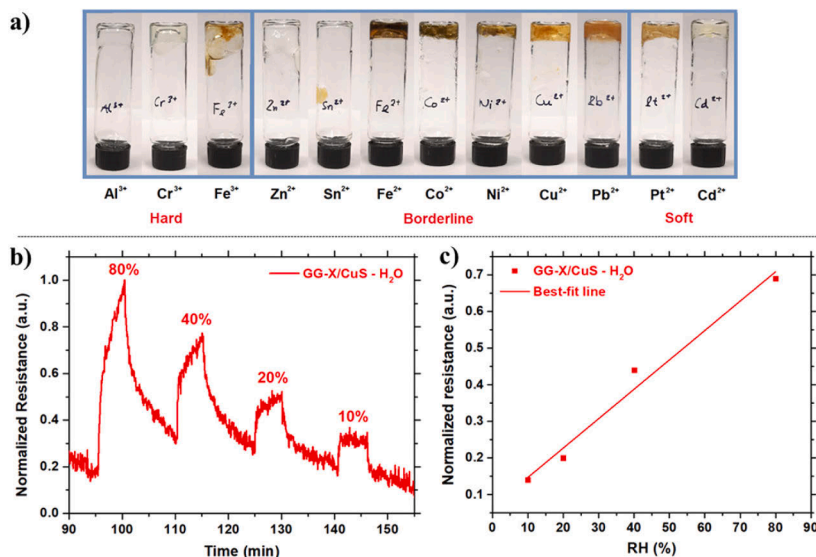
Fig. 5. Photographs of gel-like materials formed by complexing GG-X with different metal ions, which can be classified as hard, borderline, and soft acids (a). Normalized electrical resistance of GG-X/CuS sensors to various RH changes (b) and its best-fit line (c).

reversibility of these reference electrodes. Meanwhile, the CuS (S^{2-}) reference sensor shows a much lower resistance, of around 81 Ω, and its resistance is independent of RH changes. In the presence of GG, the GG/CuS nanocomposite reference sensors, on the contrary, show responses to RH variation with good reversibility. The resistance of GG/CuS sensors varies within the range of 57–95 Ω as the RH changes between 5 and 100%. More interestingly, when GG-X is used to form the nanocomposites with CuS instead (GG-X/CuS), not only reversible responses of GG-X/CuS to RH changes are observed, but also a greater range of resistance changes (98–301 Ω) is recorded, indicating higher sensitivity comparing to GG/CuS. These results confirm the importance of employing GG-X in the fabrication of CuS-based humidity sensors.

Fig. 5b shows the responses of GG-X/CuS sensors to RH changes under vacuum-exposure cycles in terms of normalized resistance. The sensors were first exposed to vacuum to establish the baseline of the graph, and RH = 80% was then chosen to normalize the electrical resistance. When the RH decreases from 80 to 10%, a linear decrease in the normalized resistance is obtained (y = 0.00803× + 0.06652, Fig. 5b). During these vacuum-exposure cycles, even though some degree of hysteresis might be observed, the sensors still show good reversible responses towards RH changes. These electrical behaviors of GG-X/CuS nanocomposite share similarities with other reported composites, which are also made of CuS nanoparticles and carrageenan polysaccharides containing O-based sulfonic functional groups [40]. The varying resistance of GG-X/CuS sensor with respect to changes in RH might be due to changes in electrical permittivity of GG-X/CuS nanocomposite and/or the swelling of hydrophilic GG-X component in the composite, which results in an increase in the distance and the hopping conductivity between CuS nanoparticles, hence, changing the overall electrical properties of GG-X/CuS nanocomposite upon water exposure. ([61,62].

Further investigations on the sensing capability of GG-X/CuS nanocomposite to volatile organic compounds (VOCs) of different polarity such as toluene, acetone, hexanol were also carried out (Fig. S14). GG-X/CuS does not show positive responses to a wide concentration range of the tested VOCs, which might be attributed to the hydrophilic nature of

GG-X.

4. Conclusion

In this work, GG has been chemically conjugated by xanthate functional groups via a simple aqueous xanthation reaction to yield GG-X. This newly functionalized polysaccharide possesses great potentials in developing numerous novel materials due to the polymeric hydrophilic nature of GG as well as the rich coordination chemistry of xanthate. The presence of conjugated xanthate moieties in GG-X product has been confirmed and studied by UV–Vis, CV, FTIR, XRD, SEM-EDS, XPS and TGA-DSC. Demonstrations on the complexation of GG-X with various metal ions have shown good agreements with HSAB theory, indicating that GG-X can be used not only for metal ion extraction and removal, but also the preparation of gel-like materials and hydrophilic nanocomposites. As a result, the GG-X/CuS nanocomposites were prepared and characterized to highlight the significance of GG-X in developing metal sulfide semiconductor-based humidity sensors. Due to the hydrophilic, polymeric properties and xanthate groups of GG-X, a homogeneous aqueous dispersion of CuS can be easily obtained, allowing a simple fabrication of future electrical sensors and device. More importantly, GG-X is the essential component that gives good electrical responses to humidity changes in CuS-based humidity sensors. In order to realize GG-X/CuS nanocomposites as a fully functioning, commercial humidity sensors, further optimization of the preparation and fabrication of GG-X/CuS sensors is of great interest for future research.

CRediT authorship contribution statement

T.-A.L.: Conceptualization, Methodology, Investigation, Writing - Original Draft, Writing - Review & Editing. M.Z.: Methodology, Investigation, Writing - Review & Editing. K.N.: Methodology, Investigation, Writing - Review & Editing. M.K.: Methodology, Investigation, Writing - Review & Editing. O.Z.: Methodology, Investigation, Writing - Review & Editing. H.H.: Methodology, Writing - Review & Editing. T.-P.H.: Conceptualization, Supervision, Writing - Review & Editing, Project

administration.

Declaration of competing interest

All authors reviewed and approved the final manuscript. The authors declare that they have no known competing financial interests or personal relationships that could have appeared to influence the work reported in this paper.

Acknowledgment

Appendix A. Supplementary data

Supplementary data to this article can be found online at https://doi.org/10.1016/j.ijbiomac.2022.02.132.

References

[1] A.I. Bourbon, A.C. Pinheiro, C. Ribeiro, C. Miranda, J.M. Maia, J.A. Teixeira, A. A. Vicente, Characterization of galactomannans extracted from seeds of Gleditsia triacanthos and Sophora japonica through shear and extensional rheology: comparison with guar gum and locust bean gum, Food Hydrocoll. 24 (2) (2010) 184–192.

[2] S. Kesavan, R.K. Prud'homme, Rheology of guar and (hydroxypropyl) guar crosslinked by borate, Macromolecules 25 (7) (1992) 2026–2032.

[3] D. Mudgil, S. Barak, B.S. Khatkar, Guar gum: processing, properties and food applications—a review, J. Food Sci. Technol. 51 (3) (2014) 409–418.

[4] K.S.V.P. Chandrika, A. Singh, A. Rathore, A. Kumar, Novel cross linked guar gum-g-poly(acrylate) porous superabsorbent hydrogels: characterization and swelling behaviour in different environments, Carbohydr. Polym. 149 (2016) 175–185.

[5] G. Dodi, D. Hritcu, I.M. Popa, Carboxymethylation of guar gum: synthesis and characterization, Cell. Chem. Technol. 45 (2011) 171–176.

[6] K. Dutta, B. Das, J.T. Orasugh, D. Mondal, A. Adhikari, D. Rana, D. Chattopadhyay, Bio-derived cellulose nanofibril reinforced poly(N-isopropylacrylamide)-g-guar gum nanocomposite: an avant-garde biomaterial as a transdermal membrane, Polymer 135 (2018) 85–102.

[7] M. Mitra, M. Mahapatra, A. Dutta, M. Deb, S. Dutta, P.K. Chattopadhyay, N. R. Singha, Fluorescent guar gum-g-terpolymer via in situ acrylamido-acid fluorophore-monomer in cell imaging, Pb(II) sensor, and security ink, ACS Appl. Bio Mater. 3 (4) (2020) 1995–2006.

[8] M. Mitra, M. Mahapatra, A. Dutta, J.S.D. Roy, M. Karmakar, M. Deb, N.R. Singha, Carbohydrate and collagen-based doubly-grafted interpenetrating terpolymer hydrogel via N-H activated in situ allocation of monomer for superadsorption of Pb (II), Hg(II), dyes, vitamin-C, and p-nitrophenol, J. Hazard. Mater. 369 (2019) 746–762.

[9] R.T. Thimma, S. Tammishetti, Study of complex coacervation of gelatin with sodium carboxymethyl guar gum: microencapsulation of clove oil and sulphamethoxazole, J. Microencapsul. 20 (2) (2003) 203–210.

[10] N. Thombare, U. Jha, S. Mishra, M.Z. Siddiqui, Borax cross-linked guar gum hydrogels as potential adsorbents for water purification, Carbohydr. Polym. 168 (2017) 274–281.

[11] A. George, P.A. Shah, P.S. Shrivastav, Guar gum: versatile natural polymer for drug delivery applications, Eur. Polym. J. 112 (2019) 722–735.

[12] A.M.A. Hasan, M.E. Abdel-Raouf, Applications of guar gum and its derivatives in petroleum industry: a review, Egypt. J. Pet. 27 (4) (2018) 1043–1050.

[13] M. Prabaharan, Prospective of guar gum and its derivatives as controlled drug delivery systems, Int. J. Biol. Macromol. 49 (2) (2011) 117–124.

[14] G. Sharma, S. Sharma, A. Kumar, A.A.H. Al-Muhtaseb, M. Naushad, A.A. Ghfar, F. J. Stadler, Guar gum and its composites as potential materials for diverse applications: a review, Carbohydr. Polym. 199 (2018) 534–545.

[15] N. Thombare, U. Jha, S. Mishra, M.Z. Siddiqui, Guar gum as a promising starting material for diverse applications: a review, Int. J. Biol. Macromol. 88 (2016) 361–372.

[16] R.G. Pearson, Hard and soft acids and bases, HSAB, part 1: fundamental principles, J. Chem. Educ. 45 (9) (1968) 581.

[17] Z. Li, Y. Kong, Y. Ge, Synthesis of porous lignin xanthate resin for Pb2+ removal from aqueous solution, Chem. Eng. J. 270 (2015) 229–234.

[18] S. Liang, X. Guo, N. Feng, Q. Tian, Application of orange peel xanthate for the adsorption of Pb2+ from aqueous solutions, J. Hazard. Mater. 170 (1) (2009) 425–429.

[19] W.S. Ng, L.A. Connal, E. Forbes, G.V. Franks, Xanthate-functional temperature-responsive polymers as selective flocculants and collectors for fines recovery, Miner. Eng. 96–97 (2016) 73–82.

[20] N. Sankararamakrishnan, A. Dixit, L. Iyengar, R. Sanghi, Removal of hexavalent chromium using a novel cross linked xanthated chitosan, Bioresour. Technol. 97 (18) (2006) 2377–2382.

[21] G. Zhu, J. Liu, J. Yin, Z. Li, B. Ren, Y. Sun, Y. Liu, Functionalized polyacrylamide by xanthate for Cr (VI) removal from aqueous solution, Chem. Eng. J. 288 (2016) 390–398.

[22] Y. Zhu, J. Hu, J. Wang, Competitive adsorption of Pb(II), Cu(II) and Zn(II) onto xanthate-modified magnetic chitosan, J. Hazard. Mater. 221–222 (2012) 155–161.

[23] M. Al-Shakban, P.D. Matthews, G. Deogratias, P.D. McNaughter, J. Raftery, I. Vitorica-Yrezabal, P. O'Brien, Novel xanthate complexes for the size-controlled synthesis of copper sulfide nanorods, Inorg. Chem. 56 (15) (2017) 9247–9254.

[24] Y. Mikhlin, S. Vorobyev, S. Saikova, Y. Tomashevich, O. Fetisova, S. Kozlova, S. Zharkov, Preparation and characterization of colloidal copper xanthate nanoparticles, New J. Chem. 40 (4) (2016) 3059–3065.

[25] O. Tzhayik, P. Sawant, S. Efrima, E. Kovalev, J.T. Klug, Xanthate capping of silver, copper, and gold colloids, Langmuir 18 (8) (2002) 3364–3369.

[26] E. Amtmann, G. Sauer, Selective killing of tumor cells by xanthates, Cancer Lett. 35 (3) (1987) 237–244.

[27] C.N. Banti, N. Kourkoumelis, C.G. Tsiafoulis, S. Skoulika, S.K. Hadjikakou, Silver(I) complexes of methyl xanthate against human adenocarcinoma breast cancer cells, Polyhedron 121 (2017) 115–122.

[28] W. Friebolin, G. Schilling, M. Zöller, E. Amtmann, Synthesis and structure–activity relationship of novel antitumoral platinum xanthate complexes, J. Med. Chem. 47 (9) (2004) 2256–2263.

[29] W. Friebolin, G. Schilling, M. Zöller, E. Amtmann, Antitumoral activity of non-platinum xanthate complexes, J. Med. Chem. 48 (25) (2005) 7925–7931.

[30] S.Z. Zard, The xanthate route to organofluorine derivatives.A brief account, Org. Biomol. Chem. 14 (29) (2016) 6891–6912.

[31] B. Quiclet-Sire, S.Z. Zard, The xanthate route to amines, anilines, and other nitrogen compounds. A brief account, Synlett 27 (05) (2016) 680–701.

[32] M. Destarac, W. Bzducha, D. Taton, I. Gauthier-Gillaizeau, S.Z. Zard, Xanthates as chain-transfer agents in controlled radical polymerization (MADIX): structural effect of the O-alkyl group, Macromol. Rapid Commun. 23 (17) (2002) 1049–1054.

[33] K. Hakobyan, T. Gegenhuber, C.S.P. McErlean, M. Müllner, Visible-light-driven MADIX polymerisation via a reusable, low-cost, and non-toxic bismuth oxide photocatalyst, Angew. Chem. Int. Ed. 58 (6) (2019) 1828–1832.

[34] S. Perrier, P. Takolpuckdee, Macromolecular design via reversible addition–fragmentation chain transfer (RAFT)/xanthates (MADIX) polymerization, J. Polym. Sci. A Polym. Chem. 43 (22) (2005) 5347–5393.

[35] E.M. Donaldson, Solvent extraction of metal xanthates, Talanta 23 (6) (1976) 417–426.

[36] S. Deb, P.K. Kalita, Green synthesis of copper sulfide (CuS) nanostructures for heterojunction diode applications, J. Mater. Sci. Mater. Electron. 32 (2021) 24125–24137.

[37] K. Diwate, S. Rondia, A. Mayabadi, A. Rokade, R. Waykar, H. Borate, S. Jadkar, Chemical spray pyrolysis synthesis of covellite copper sulphide (CuS) thin films for economical counter electrode for DSSCs, J. Mater. Sci. Mater. Electron. 29 (6) (2018) 4940–4947.

[38] M. Masar, M. Urbanek, P. Urbanek, Z. Machovska, J. Maslik, R.S. Yadav, I. Kuritka, Synthesis, characterization and examination of photocatalytic performance of hexagonal covellite CuS nanoplates, Mater. Chem. Phys. 237 (2019) 121823.

[39] T.-P. Huynh, Chemical and biological sensing with nanocomposites prepared from nanostructured copper sulfides, Nano Futures 4 (3) (2020), 032001.

[40] M. Zouheir, T.-A. Le, J. Torop, K. Nikiforow, M. Khatib, O. Zohar, T.-P. Huynh, CuS-carrageenan composite grown from the gel/liquid interface, ChemSystemsChem 3 (2021), e2000063.

[41] M. Zouheir, M. Zniber, S. Qudsia, T.-P. Huynh, Real-time humidity sensing by integration of copper sulfide nanocomposite with low-cost and wireless Arduino platform, Sens. Actuators A 319 (2021), 112541.

[42] S.C. Gondhalekar, P.J. Pawar, S.S. Dhumal, S.S. Thakre, Mechanism of xanthation reaction in viscose process, Cellulose 26 (3) (2019) 1595–1604.

[43] Y. Xie, A. Riedinger, M. Prato, A. Casu, A. Genovese, P. Guardia, L. Manna, Copper sulfide nanocrystals with tunable composition by reduction of covellite nanocrystals with Cu+ ions, J. Am. Chem. Soc. 135 (46) (2013) 17630–17637.

[44] R. Woods, Oxidation of ethyl xanthate on platinum, gold, copper, and galena electrodes. Relation to the mechanism of mineral flotation, J. Phys. Chem. 75 (3) (1971) 354–362.

[45] M.A. Cerqueira, B.W.S. Souza, J. Simões, J.A. Teixeira, M.R.M. Domingues, M. A. Coimbra, A.A. Vicente, Structural and thermal characterization of galactomannans from non-conventional sources, Carbohydr. Polym. 83 (1) (2011) 179–185.

[46] Z. Movasaghi, S. Rehman, D.I. ur Rehman, Fourier transform infrared (FTIR) spectroscopy of biological tissues, Appl. Spectrosc. Rev. 43 (2) (2008) 134–179.

[47] D. Mudgil, S. Barak, B.S. Khatkar, X-ray diffraction, IR spectroscopy and thermal characterization of partially hydrolyzed guar gum, Int. J. Biol. Macromol. 50 (4) (2012) 1035–1039.

[48] R.J. Gillespie, E.A. Robinson, The sulphur–oxygen bond in sulphuryl and thionyl compounds: correlation of stretching frequencies and force constants with bond lengths, bond angles, and bond orders, Can. J. Chem. 41 (8) (1963) 2074–2085.

[49] S.S. Kalanur, S.Y. Chae, O.S. Joo, Transparent Cu1.8S and CuS thin films on FTO as efficient counter electrode for quantum dot solar cells, Electrochim. Acta 103 (2013) 91–95.

[50] P. Kumar, M. Gusain, R. Nagarajan, Synthesis of Cu1.8S and CuS from copper-thiourea containing precursors; anionic (Cl−, NO3−, SO42−) influence on the product stoichiometry, Inorg. Chem. 50 (7) (2011) 3065–3070.

[51] H. Grijalva, M. Inoue, S. Boggavarapu, P. Calvert, Amorphous and crystalline copper sulfides, CuS. J. Mater. Chem. 6 (7) (1996) 1157–1160.

[52] J.F. Moulder, W.F. Stickle, K.D. Bomben, Handbook of X-Ray Photoelectron Spectroscopy, Perkin Elmer Corporation, Eden Prairie, MN, 1992.

[53] M.C. Biesinger, Advanced analysis of copper X-ray photoelectron spectra, Surf. Interface Anal. 49 (13) (2017) 1325–1334.

[54] S.W. Goh, A.N. Buckley, R.N. Lamb, R.A. Rosenberg, D. Moran, The oxidation states of copper and iron in mineral sulfides, and the oxides formed on initial exposure of chalcopyrite and bornite to air, Geochim. Cosmochim. Acta 70 (9) (2006) 2210–2228.

[55] C.D. Wagner, A.V. Naumkin, A. Kraut-Vass, J.W. Allison, C.J. Powell, J.R.R. Jr, NIST Standard Reference Database 20. Ver. 3.4, 2006. http://srdata.nist.gov/xps/index.htm.

[56] J.G. Dunn, A.C. Chamberlain, N.G. Fisher, J. Avraamides, The influence of activated carbon on the thermal decomposition of sodium ethyl xanthate, J. Therm. Anal. 49 (3) (1997) 1399–1408.

[57] N.R. Singha, A. Dutta, M. Mahapatra, M. Karmakar, H. Mondal, P. K. Chattopadhyay, D.K. Maiti, Guar gum-grafted terpolymer hydrogels for ligand-selective individual and synergistic adsorption: effect of comonomer composition, ACS Omega 3 (1) (2018) 472–494.

[58] A. Srivastava, V. Mishra, P. Singh, A. Srivastava, R. Kumar, Comparative study of thermal degradation behavior of graft copolymers of polysaccharides and vinyl monomers, J. Therm. Anal. Calorim. 107 (1) (2012) 211–223.

[59] Y.L. Auyoong, P.L. Yap, X. Huang, S.B. Abd Hamid, Optimization of reaction parameters in hydrothermal synthesis: a strategy towards the formation of CuS hexagonal plates, Chem. Cent. J. 7 (1) (2013) 67.

[60] B. Brunetti, V. Piacente, P. Scardala, Study on sulfur vaporization from covellite (CuS) and anilite (Cu1.75S), J. Alloys Compd. 206 (1) (1994) 113–119.

[61] D. Adkar, A. Hake, S. Jadkar, P. Adhyapak, U. Mulik, D. Amalnerkar, Humidity sensing performance of in-situ fabricated Cu/Cu2O/Cu2S-polymer nanocomposite via polyphenylene sulphide cyclisation route, J. Nanosci. Nanotechnol. 11 (8) (2011) 6815–6822.

[62] D.Y. Godovski, V.Y. Sukharev, A.V. Volkov, M.A. Moskvina, Absorption induced response of electrophysical characteristics of filled polymer-composite, J. Phys. Chem. Solids 54 (11) (1993) 1613–1620.

Supplementary data

Synthesis, characterization, and humidity-responsiveness of guar gum xanthate and its nanocomposite with copper sulfide covellite

Trung-Anh Le[1], Morad Zouheir[1,2], Kostiantyn Nikiforow[3], Muhammad Khatib[4], Orr Zohar[4], Hossam Haick[4], Tan-Phat Huynh[1]*

[1]Laboratory of Molecular Sciences and Engineering, Åbo Akademi University 20500 Turku, Finland

[2]Laboratoire de Matériaux, Procédés, Catalyse et Environnement (LMPCE), Université Sidi Mohammed Ben Abdellah, Fès, Route d'Imouzzer, BP 2427, Fès, Morocco

[3]Institute of Physical Chemistry, Polish Academy of Sciences, 44/52 Kasprzaka, 01-224 Warsaw, Poland

[4]The Department of Chemical Engineering, Technion – Israel Institute of Technology, Haifa 3200003, Israel

E-mail address: tan.huynh@abo.fi

1. Purity of GG-X products
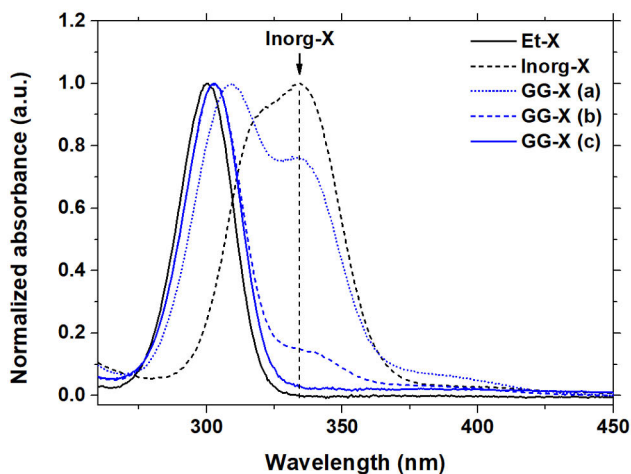
Figure S1. Normalized absorbance of Et-X, Inorg-X reference solutions, GG-X solutions before

(a), during (b) and after (c) purification by intensive washing with MeOH. All were prepared in

aqueous solution at pH 10

2. Calibration curve for Et-X

17.10 mg Potassium ethyl xanthogenate (Et-X) 97% was first dissolved in 50.00 mL carbonate-bicarbonate 0.1 M buffer solution (solution 1). The solution 1 was then diluted 10 times by adding 9.00 mL of buffer solution to 1.00 mL of the solution 1 to give solution 2. Different volumes of Et-X in solution 2 were diluted to give Et-X solutions of different concentrations for the UV-Vis measurements (**Table S1**). Absorbance of those solutions at 300 nm was recorded.

$$n_{Et-X} = \frac{17.10 \text{ mg} \quad 0.97}{160.30 \text{ gmol}^{-1}} = 103.475 \quad \text{mol}$$

$$[Et-X_{\text{solution 1}}] = \frac{103.475 \quad \text{mol}}{50 \text{ mL}} = 2.069 \text{ mM}$$

$$[Et-X_{\text{solution 2}}] = \frac{2.069 \text{ mM}}{10} = 0.2069 \text{ mM}$$

Table S1. Absorbance of several reference solutions for the calibration curve of Et-X

$V_{Et-X\ (solution\ 2)}$ [mL]	1.00	2.00	3.00	4.00	5.00	6.00
V_{buffer}, [mL]	19.00	18.00	17.00	16.00	15.00	14.00
$C_{M\ (Et-X)}10^5$, [M]	1.034	2.069	3.014	4.138	5.172	6.207
Absorbance	0.17992	0.35997	0.53955	0.71947	0.89902	1.07921

Equation	y = a + b*x
Plot	Absorbance
Weight	No Weighting
Intercept	--
Slope	--
Residual Sum of Squares	1.94216E-4
Pearson's r	0.99983
R-Square (COD)	0.99966
Adj. R-Square	0.99957
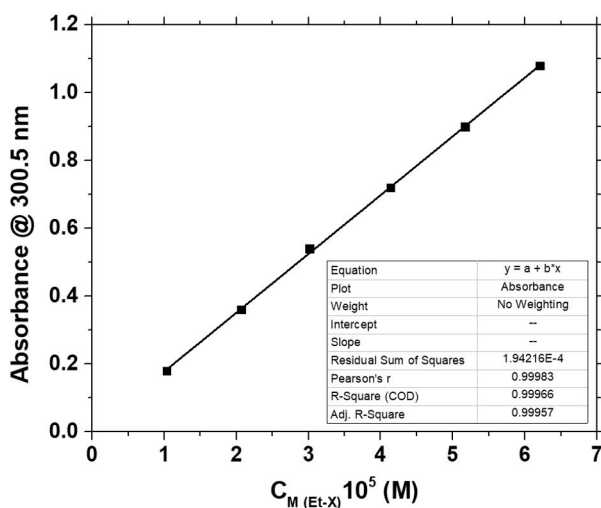
Figure S2. Calibration curve at 300 nm for Et-X

Calibration curve equation: $A_{@300} = 17382 \cdot [Et\text{-}X] + 1.94511 \cdot 10^{-4}$.

3. Degree of substitution DS, grafting density GD and reaction yield for GG-X

15.10 mg of GG was dissolved in 50.00 mL carbonate-bicarbonate 0.1 M buffer solution to give a GG stock solution. The GG stock solution was subsequently diluted 5 times to give a GG reference solution for UV-Vis measurements (Figure S3). Meanwhile, 15.12 mg of GG-X was dissolved completely in also 50.00 mL carbonate-bicarbonate 0.1 M buffer solution. This GG-X stock solution is then diluted 5 times to give $A_{@300}$ of 0.79019, corresponding to $[X] = 4.545 \cdot 10^{-5}$ M. Assuming Et-

X and GG-X have similar molar absorption coefficient at 300nm, the concentration of xanthates in stock solution is approximated as $[X] = 2.272 \cdot 10^{-4}$ M.

$$n_{X\,(GG-X)} = 2.272 \ 10^{-4} \text{ M} \ \ 50.000 \text{ mL} = 1.136 \ 10^{-5} \text{ mol}$$

$$M_{X\,(GG-X)} = M_{CS2} + M_{Na} = 99.13 \text{ gmol}^{-1}$$

$$m_{X\,(GG-X)} = 1.136 \ 10^{-5} \text{ mol} \ \ 99.13 \text{ gmol}^{-1} \approx 1.13 \text{ mg}$$

$$\%m_{X\,(GG-X)} = \frac{1.13 \text{ mg}}{15.12 \text{ mg}} \approx 7.47 \ \%$$

$$m_{\,GG\,(GG-X)} = m_{GG-X} - m_{X\,(GG-X)} = 15.12 \text{ mg} - 1.13 \text{ mg} = 13.99 \text{ mg}$$
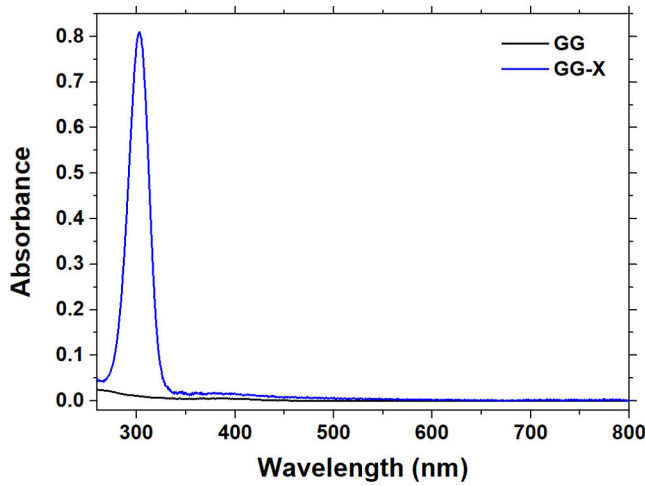
Figure S3. Absorption spectra of GG and GG-X at pH 10 in water

Each guar gum monomer consists of 2 mannose and 1 galactose molecules to give 2 primary and 7 secondary –OH groups. This monomer can be approximated as a combination of 3 anhydroglucose units (AGU) and each AGU has 3 –OH groups, molecular formula as $C_6H_{10}O_5$ and molecular mass of 162.14 gmol^{-1}. Then, the calculation of DS and grafting density can be performed on one AGU to give similar results for guar gum monomers.

$$m_{\,AGU\,(GG-X)} = m_{\,GG\,(GG-X)} = 13.99 \text{ mg}$$

$$n_{\,AGU\,(GG-X)} = \frac{13.99 \text{ mg}}{162.14 \text{ gmol}^{-1}} = 8.628 \ 10^{-5} \text{ mol}$$

$$\frac{N_{X\ (GG-X)}}{N_{AGU\ (GG-X)}} = \frac{n_{X\ (GG-X)}}{n_{AGU\ (GG-X)}} = \frac{1.136 \cdot 10^{-5}\ mol}{8.628 \cdot 10^{-5}\ mol} \approx 0.132$$

Hence, DS for each AGU or guar gum monomer is 0.132. The molecular formula of AGU can be approximated as $C_6H_{9.868}O_5(CS_2Na)_{0.132}$.

$$\overline{M}_{AGU\ (GG-X)} = 162.14\ gmol^{-1} - 0.132\ gmol^{-1} + 0.132 \cdot 99.13\ gmol^{-1} \approx 175.09\ gmol^{-1}$$

Each AGU has 0.132 out of 3 -OH groups is xanthated, hence,

$$GD = \frac{0.132}{3} \cdot 100\% = 4.4\ \%$$

From 2.000g GG starting material, 1.884 g of GG-X product is obtained. The reaction yield for xanthation of GG is calculated as the molar ratio between AGU of original GG ($C_6H_{10}O_5$) and AGU of GG-X ($C_6H_{9.868}O_5(CS_2Na)_{0.132}$).

$$n_{AGU\ (GG\ reactant)} = \frac{2.000\ g}{162.14\ gmol^{-1}} = 12.335\ mmol$$

$$n_{AGU\ (GG-X\ product)} = \frac{1.884\ g}{175.09\ gmol^{-1}} = 10.760\ mmol$$

$$\%\ yield = \frac{n_{AGU\ (GG-X\ product)}}{n_{AGU\ (GG\ reactant)}} \cdot 100\ \% = \frac{10.760\ mmol}{12.335\ mmol} \cdot 100\ \% \approx 87.23\%$$

4. Metal ion complexation of GG-X and GG

15.0 mg GG-X is dissolved in 1000 µL of neutral H_2O at room temperature.

$$m_{X\ (GG-X)} = \%m_{X\ (GG-X)} \cdot m_{GG-X} = 7.47\ \% \cdot 15.0\ mg \approx 1.1205\ mg$$

$$n_{X\ (GG-X)} = \frac{m_{X\ (GG-X)}}{M_{X\ (GG-X)}} = \frac{1.1205\ mg}{99.13\ gmol^{-1}} = 11.303\ \mu mol$$

100 µL of M^{3+} solution of

$$n_{M^{3+}} = \frac{n_{X\ (GG-X)}}{3} = \frac{11.303\ \mu mol}{3} = 3.768\ \mu mol$$

$$[M^{3+}] = \frac{3.768\ \mu mol}{100\ \mu L} = 37.68\ mM$$

$$n_{M^{2+}} = \frac{n_{X\ (GG-X)}}{2} = \frac{11.303\ \mu mol}{2} = 5.652\ \mu mol$$

$$[M^{2+}] = \frac{5.652 \quad mol}{100 \quad L} = 56.52 \text{ mM}$$
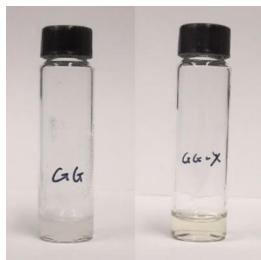

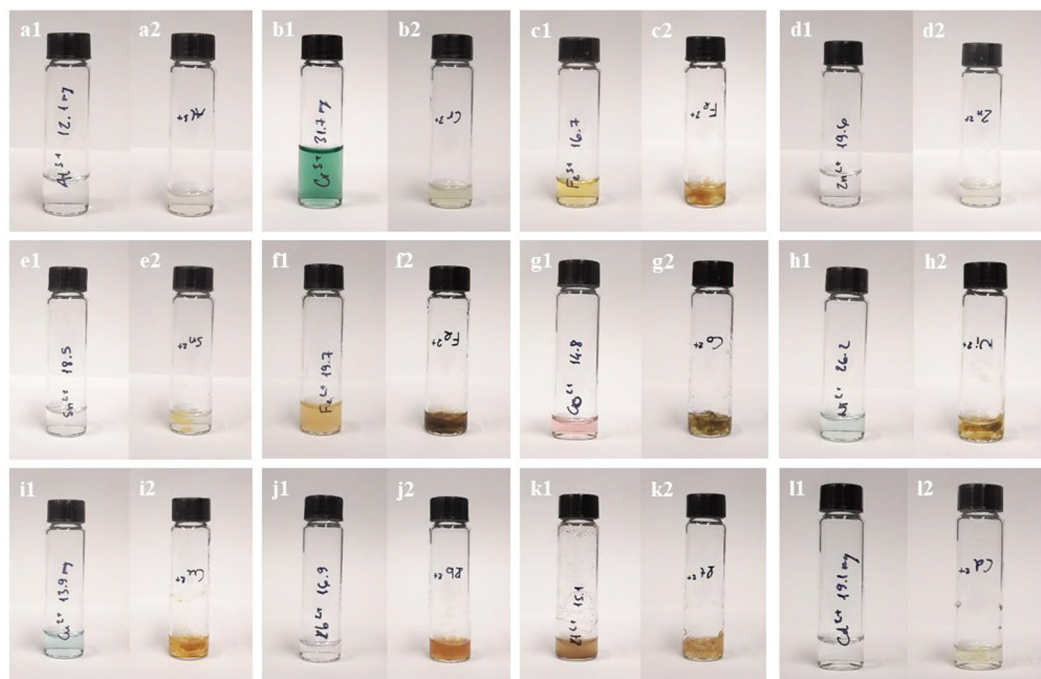**Figure S4.** GG (left) and GG-X (right) aqueous solutions

Figure S5. Al^{3+} solution (a1) and Al-GG-X gel-like product (a2), Cr^{3+} solution (b1) and Cr-GG-X gel-like product (b2), Fe^{3+} solution (c1) and Fe^{III}-GG-X gel-like product (c2), Zn^{2+} solution (d1) and Zn-GG-X gel-like product (d2), Sn^{2+} solution (e1) and Sn-GG-X gel-like product (e2), Fe^{2+} solution (f1) and Fe^{II}-GG-X gel-like product (f2), Co^{2+} solution (g1) and Co-GG-X gel-like product (g2), Ni^{2+} solution (h1) and Ni-GG-X gel-like product (h2), Cu^{2+} solution (i1) and Cu-GG-X gel-like product (i2), Pb^{2+} solution (j1) and Pb-GG-X gel-like product (j2), Pt^{2+} solution (k1) and Pt-GG-X gel-like product (k2), Cd^{2+} solution (l1) and Cd-GG-X gel-like product (l2)

Control experiments on original unxanthated GG are carried out using similar procedure. pH of the final solutions is adjusted around 10 by NaOH to allow the formation of metal ion complexes.
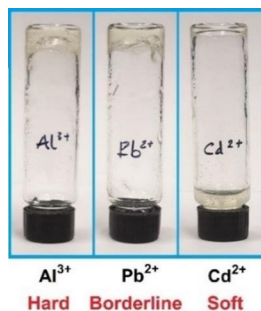
Figure S6. Control experiments for metal ion complexation with unmodified GG at pH 10

5. Cyclic voltammetry (CV)
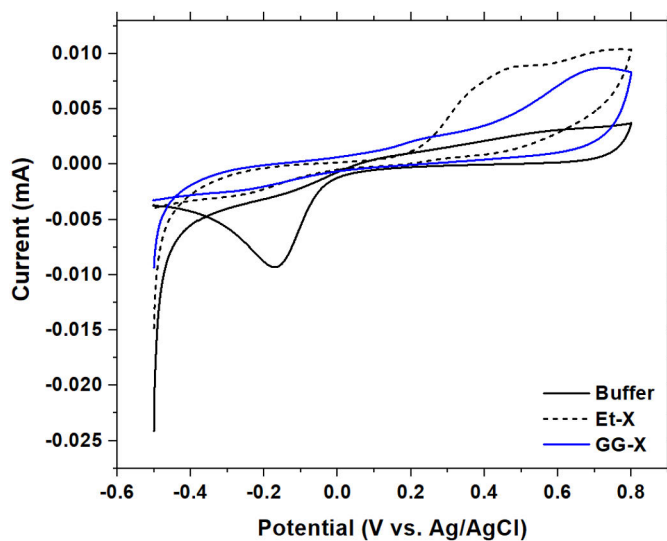
Figure S7. Cyclic voltammograms of carbonate-bicarbonate buffer, Et-X and GG-X solutions. The potential scan rate is 50 mV/s

6. Synthesis of GG-X under aerobic (O$_2$) and anaerobic (N$_2$) atmospheres
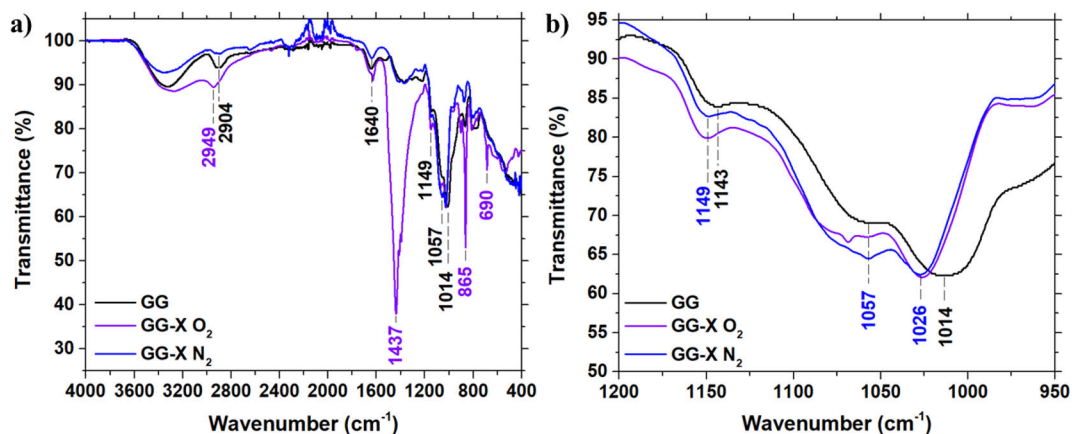
Figure S8. FTIR spectra of GG reference and GG-X synthesized under aerobic and anaerobic atmospheres

7. Synthesis of copper sulfide (CuS) reference

Synthetic route 1 to yield **CuS (OH⁻):** 608 mg CuCl$_2$ (4.386 mmol) was dissolved in 8 mL water and this solution was added into a 32 mL-aqueous solution at pH 10.5 to mimic a GG-X solution. At the same time, 1088 mg of Na$_2$S.9H$_2$O (4.52 mmol) was dissolved in 45.3 mL water. The Na$_2$S solution was then added dropwise to the CuCl$_2$ solution. Subsequent sonication, concentration at high temperature and purification were done similarly to that of GG-X/CuS samples.

Synthetic route 2 to yield **CuS (S²⁻):** 1088 mg of Na$_2$S.9H$_2$O (4.52 mmol) was first dissolved in 45.3 mL water and pH-adjusted to yield a S²⁻ solution at pH 10.5, followed by the dissolution of 608 mg CuCl$_2$ (4.386 mmol) in 40 mL water to give Cu²⁺ solution. The Cu²⁺ solution was then added dropwise to the S²⁻ solution to obtain CuS. Similar sonication, concentration and purification were also carried out.

8. Crystallite size of CuS synthesized in different reaction conditions

Crystallite size is approximated using Scherrer equation: $D = \dfrac{\text{K}\cdot}{FWHM\cdot\cos(\ )}$, in which

D	nm	crystallite size

K	0.9	Scherrer constant
λ	0.15418 nm	X-ray wavelength
FWHM	radian	full width at half maximum
θ	radian	Bragg angle (half of the 2θ position of the (110) diffraction

peak)

Table S2. Crystallite sizes of CuS (S^{2-}), CuS (OH$^-$), GG/CuS, GG-X/CuS

Samples	2θ (º)	FWHM (º)	D (nm)
CuS (S^{2-})	47.97913	0.74581	11.66809
CuS (OH$^-$)	48.05562	0.95662	9.09950
GG/CuS	47.81350	1.69476	5.13146
GG-X/CuS	47.96393	0.55825	15.58739

9. SEM
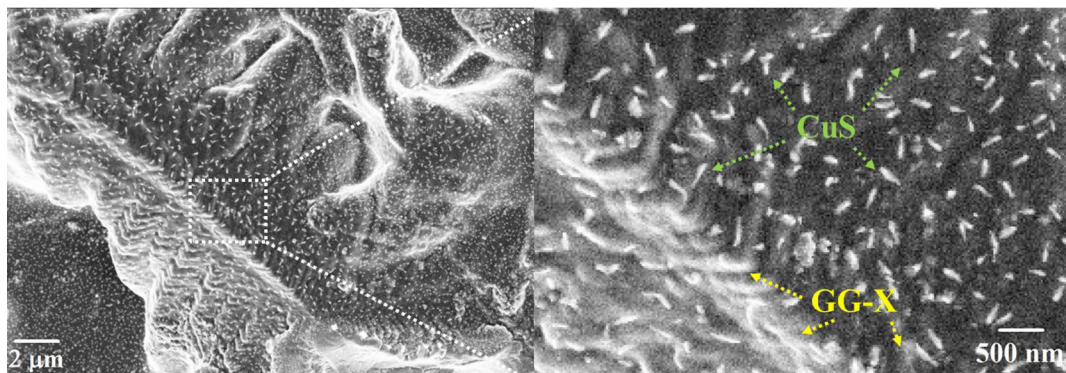
Figure S9. Scanning electron micrographs of GG-X/CuS
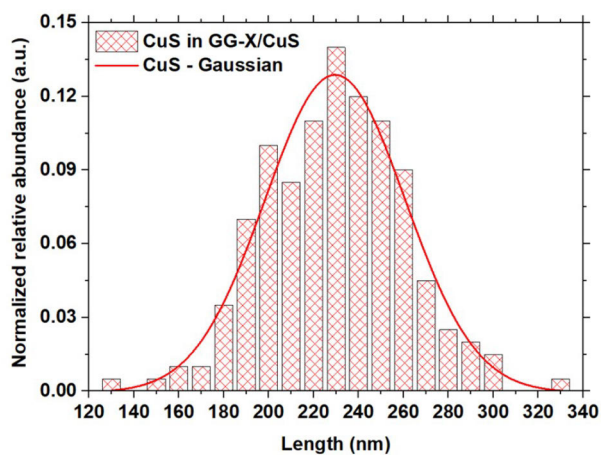
Figure S10. Particle size distribution of CuS in GG-X/CuS

10. XPS

Table S3. Elemental composition of GG

State	B.E. (eV)	FWHM	% Atomic conc.	Library RSF	Possible binding mode
O 1s a	531.09	1.8	2.48	0.733	C-O-C\P-O
O 1s b	532.74	1.8	19.42	0.733	C-OH
O total			**21.90**		
N 1s	399.96	1.64	2.10	0.499	
N total			**2.10**		
C 1s a	284.8	1.28	47.04	0.314	C-C
C 1s b	286.35	1.28	19.44	0.314	C-O
C 1s c	287.7	1.28	6.34	0.314	C=O
C 1s d	288.94	1.28	2.67	0.314	ads $CO\backslash CO_2\backslash CO_3^{2-}$
C total			**75.49**		
P 2p 3	133.36	1.43	0.35	0.604625	PO_4^{3-}
P 2p 1	134.21	1.43	0.17	0.604625	

P total			0.52		
Total			100.01		

Table S4. Elemental composition of Et-X

State	B.E. (eV)	FWHM	% Atomic conc.	Library RSF	Possible binding mode
O 1s a	531	1.83	6.23	0.733	S-O
O 1s b	533.12	1.46	11.31	0.733	C-O
O total			**17.54**		
C 1s a	284.8	1.21	15.56	0.314	C-C
C 1s b	286.1	1.14	10.81	0.314	C-O
C 1s c	287.29	1.26	12.9	0.314	C-S
C total			**39.27**		
K 2p 3	292.8	1.27	12.02	1.73358	
K 2p 1	295.58	1.27	6.01	1.73358	
K total			**18.03**		
S 2p 3 a	161.87	1.22	16.03	0.819531	C-S
S 2p 1 a	163.07	1.13	8.02	0.819531	
S 2p 3 c	167.77	1.54	0.75	0.819531	SO_3^{2-}/RSO_2R/R-S=O
S 2p 1 c	169.04	1.54	0.37	0.819531	
S total			**25.17**		
Total			**100.01**		

Table S5. Elemental composition of CuS

State	B.E. (eV)	FWHM	% Atomic conc.	Library RSF	Possible binding mode
Na 1s	1072.15	1.61	2.33	1.102	
Na total			**2.33**		
Cu 2p 3/2 a	932.6	1.1	20.1	2.88335	$CuS/CuCl/Cu_2S$
					CuO, $CuCl_2$, $CuSO_4$,
Cu 2p 3/2 b	933.82	3.05	13.34	2.88335	$Cu(OH)_2$
Cu total			**33.44**		
O 1s a	532.25	1.48	17.68	0.733	C=O
O 1s b	533.46	1.48	3.34	0.733	C-O
O 1s c	536.33	2.9	1.44	0.733	$H_2O/CO/CO_2$
O total			**22.46**		
C 1s a	284.8	2.3	2.93	0.314	C-C
C 1s b	287.42	2.3	1.42	0.314	C=O
C 1s c	290.22	2.3	0.57	0.314	CO_3^{2-}, ads CO, CO_2
C total			**4.92**		
Cl 2p 3 a	198.65	1.3	4.37	1.08215	NaCl
Cl 2p 1 a	200.25	1.3	2.18	1.08215	
Cl 2p 3 b	200.19	1.3	1.13	1.08215	CuCl
Cl 2p 1 b	201.79	1.3	0.57	1.08215	
Cl total			**8.25**		
S 2p 3 a	161.62	0.71	1.97	0.819531	S^{2-}
S 2p 1 a	162.82	0.71	0.98	0.819531	
S 2p 3 b	162.61	0.98	8.85	0.819531	S^{2-}
S 2p 1 b	164.02	0.98	4.42	0.819531	

State	B.E. (eV)	FWHM	% Atomic conc.	Library RSF	Possible binding mode
S 2p 3 c	163.6	0.98	5.00	0.819531	Thiophene
S 2p 1 c	164.8	0.98	2.50	0.819531	
S 2p 3 d	169.06	1.4	3.25	0.819531	SO_4^{2-}
S 2p 1 d	170.26	1.4	1.62	0.819531	
S total			**28.59**		
Total			**99.99**		

Table S6. Elemental composition of GG-X

State	B.E. (eV)	FWHM	% Atomic conc.	Library RSF	Possible binding mode
Na 1s	1071.45	1.67	3.03	1.102	
Na total			**3.03**		
O 1s a	531.07	1.66	5.37	0.733	C-O-C
O 1s b	532.79	1.66	33.33	0.733	C-OH
O total			**38.70**		
N 1s	399.95	1.67	1.08	0.499	C-N
N total			**1.08**		
C 1s a	284.8	1.37	9.29	0.314	C-C
C 1s b	286.39	1.37	33.01	0.314	C-O
C 1s c	287.8	1.37	11.22	0.314	O-C-O
C 1s d	289.21	1.37	3.09	0.314	COOR
C total			**56.61**		
S 2p 3 a	162.2	2.41	0.13	0.819531	S^{2-}
S 2p 1 a	163.4	2.41	0.06	0.819531	
S 2p 3 b	167.68	2.41	0.26	0.819531	Salt/Sulphone
S 2p 1 b	168.88	2.41	0.13	0.819531	

State				
S total		0.58		
Total		100.00		

Table S7. Elemental composition of GG/CuS

State	B.E. (eV)	FWHM	% Atomic conc.	Library RSF	Possible binding mode
Na 1s	1071.68	1.59	0.77	1.102	
Na total			**0.77**		
Cu 2p3/2	932.67	2.4	0.67	2.88335	Cu-S
Cu total			**0.67**		
O 1s a	531.24	1.97	2.05	0.733	C-O-C, S-O
O 1s b	532.87	1.97	26.32	0.733	C-OH
O 1s c	535.9	1.97	0.62	0.733	water/CO/CO_2
O total			**28.99**		
N 1s	400.07	1.84	1.53	0.499	C-N-C
N total			**1.53**		
C 1s a	284.8	1.47	30	0.314	C-C
C 1s b	286.28	1.47	21.78	0.314	C-O
C 1s c	287.44	1.47	10.06	0.314	C=O, O-C-O
C 1s d	288.74	1.47	4.74	0.314	COOR
C total			**66.58**		
S 2p 3 a	162.17	2.5	0.54	0.819531	S^{2-} (CuS)
S 2p 1 a	163.37	2.5	0.27	0.819531	
S 2p 3 b	168.78	2.04	0.42	0.819531	SO_4^{2-} (Na_2SO_4)
S 2p 1 b	169.98	2.04	0.21	0.819531	
S total			**1.44**		

Total			99.98		

Table S8. Elemental composition of GG-X/CuS

State	B.E. (eV)	FWHM	% Atomic conc.	Library RSF	Possible binding mode
Na 1s	1071.8	1.95	16.49	1.102	
Na total			**16.49**		
Cu 2p 3/2 a	931.69	1.4	3.45	2.88335	CuS
Cu 2p 3/2 b	932.98	2.02	1.58	2.88335	Cu_2S, CuCl
Cu total			**5.03**		
O 1s a	532.34	2.06	37.15	0.733	C=O
O total			**37.15**		
N 1s	399.65	1.77	0.28	0.499	C-N-C
N total			**0.28**		
C 1s a	284.8	1.59	8.44	0.314	C-C
C 1s b	286.23	1.59	12.77	0.314	C-O
C 1s c	287.59	1.59	5.01	0.314	C=O
C 1s d	288.9	1.59	2.13	0.314	COOR
C total			**28.35**		
Cl 2p 3 a	198.46	1.69	1.22	1.08215	NaCl
Cl 2p 1 a	200.06	1.69	0.61	1.08215	
Cl 2p 3 b	199.78	1.44	0.23	1.08215	CuCl
Cl 2p 1 b	201.38	1.44	0.12	1.08215	
Cl total			**2.18**		
S 2p 3 a	161.59	1.81	3.03	0.819531	S^{2-} (CuS)
S 2p 1 a	162.79	1.81	1.51	0.819531	

S 2p 3 b	164.15	1.81	0.45	0.819531	
S 2p 1 b	165.35	1.81	0.22	0.819531	
S 2p 3 c	169	1.78	3.54	0.819531	SO_4^{2-}
S 2p 1 c	170.2	1.78	1.77	0.819531	
S total			**10.52**		
Total			**100.00**		

11. TGA-DSC analysis
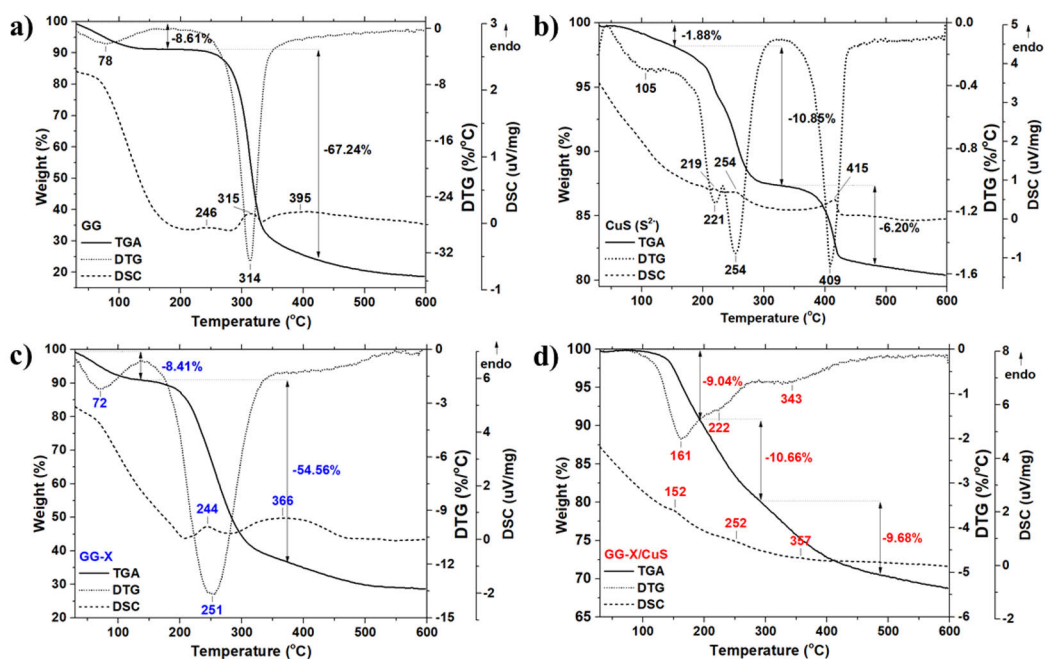
Figure S11. TGA, DTG and DSC thermograms of

GG (a) CuS (S^{2-}) (b), GG-X (c), GG-X/CuS (d)

12. Fabrication of humidity sensors

GG   CuS   GG-X   GG/CuS   GG-X/CuS
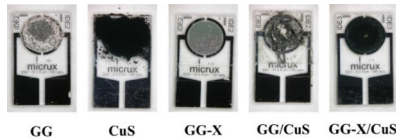
Figure S12. Photographs of GG, CuS (S^{2-}), GG-X, GG/CuS and GG-X/CuS humidity sensors from left to right.
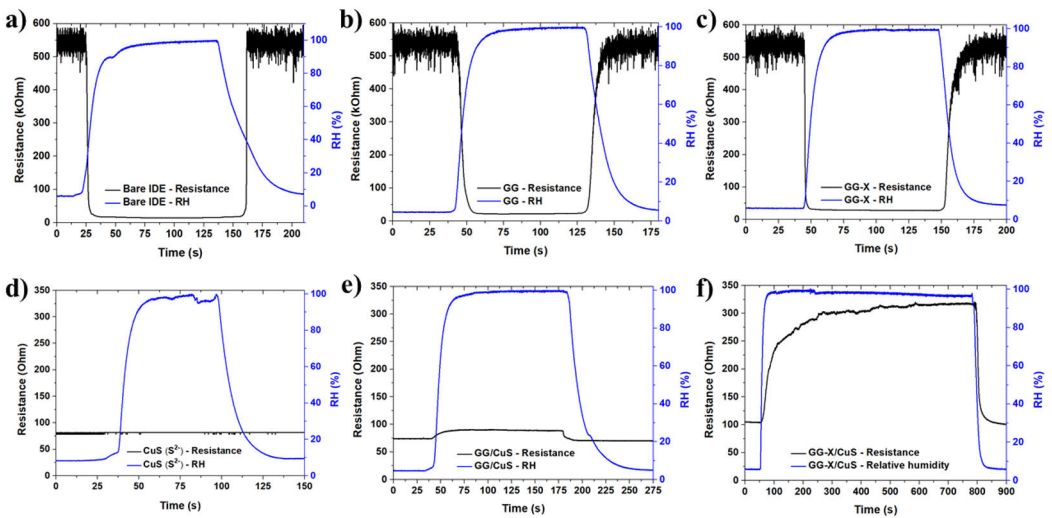
Figure S13. Resistance vs RH curves of bare IDE (a), GG (b), GG-X (c),

CuS (S^{2-}) (d), GG/CuS (e), GG-X/CuS (f)
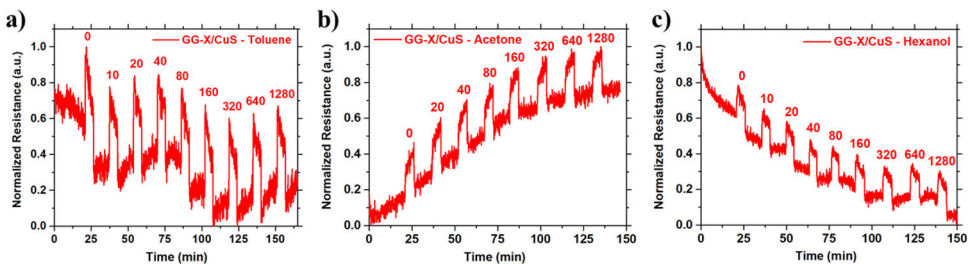
Figure S14. Normalized resistance of GG-X/CuS sensors towards various concentrations (in ppm) of several VOCs (toluene (a), acetone (b), hexanol (c))

Synthesis, characterization and biocompatibility of guar gum-benzoic acid

Trung-Anh Le, Yong Guo, Jun-Nian Zhou, Jiaqi Yan, Hongbo Zhang, and Tan-Phat Huynh*

IV

Synthesis, characterization and biocompatibility of guar gum-benzoic acid

Trung-Anh Le [a], Yong Guo [b,c,d], Jun-Nian Zhou [b,c,e], Jiaqi Yan [b,c], Hongbo Zhang [b,c], Tan-Phat Huynh [a,*]

[a] Laboratory of Molecular Science and Engineering, Faculty of Science and Engineering, Åbo Akademi University, Henrikinkatu 2, 20500 Turku, Finland
[b] Pharmaceutical Sciences Laboratory, Faculty of Science and Engineering, Åbo Akademi University, Porthaninkatu 3–5, 20500 Turku, Finland,
[c] Turku Bioscience Centre, University of Turku and Åbo Akademi University, Turku 20520, Finland
[d] Department of Endocrinology, Key Laboratory of National Health & Family Planning Commission for Male Reproductive Health, National Research Institute for Family Planning, Beijing 100081, China
[e] Experimental Hematology and Biochemistry Lab, Beijing Institute of Radiation Medicine, Beijing 100850, China

ARTICLE INFO

ABSTRACT

A novel chemical functionalization of guar gum (GG) by benzoic acid (BA) via nucleophilic substitution reaction in aqueous solution has been reported. BA moieties are chosen due to coordination chemistry of carboxylic acid moieties, hydrophobicity and intermolecular interaction of aromatic rings. The presence of conjugated BA on guar gum-benzoic acid (GG-BA) with grafting density of 5.5% is confirmed by ^{1}H NMR. Amorphous GG-BA with irregular morphology has been studied by UV–Vis, FTIR, XRD, SEM, TEM, TGA, computational chemistry and contact angle measurement. GG-BA in a concentration range from 0 to 4000 µg mL^{-1} has good biocompatibility to mouse embryonic fibroblasts (MEF), human mammary epithelial cells (MCF-10A) after 48 and 72 h of treatment using WST-1 assay. GG-BA shows great potential for the development of biomaterials such as bio-adhesives, hydrogels, and coacervates.

1. Introduction

Over the years, natural polysaccharides have been of great interest in developing valuable and sustainable materials due to their biocompatibility, nontoxicity, biodegradability, natural availability, and accessibility of chemical synthetic techniques [1,2]. Guar gum (GG), a naturally occurring non-ionic galactomannan polysaccharide obtained from guar seeds, has recently become a popular choice of novel materials research in various fields such as soil treatment [3–6], surface chemistry [7–9], lithium- and zinc-ion batteries [10,11], dye-sensitized solar cells [12],

wound dressing and healing [13–15], drug delivery [16,17]. GG consists of mannose (M) backbones and galactose (G) side chains with an average molecular ratio of 2:1 between M and G. While M monomers are linked together by β-1,4-glycosidc bonds, G monomers are connected to the M backbone via α-1,6-glycosidic bonds. In addition, numerous remaining hydroxyl functional (-OH) groups on galactomannan chains offer GG its hydrophilicity and high water-solubility [18,19].

In order to introduce new properties to GG, remaining -OH groups of GG can be chemically functionalized by different chemical reactions such as etherification, esterification, oxidation, grafting reactions, etc.

Carboxymethylation of GG via ether bonds is one of the most common synthetic routes to synthesize anionic GG [20,21]. Further cross-linking of carboxymethylated GG can be easily carried out using non-covalent interactions by an assistance of multivalent metal ions [22–24]. Complex coacervation between carboxymethylated GG and cationic polymers such as gelatin has also been studied [25]. Moreover, esterification of -OH groups on GG was performed with citric acid to create cross-linked polymer systems for wound healing [14], while those -OH groups of GG could also form covalent bonds directly with several common cross-linkers such as Ti^{4+} and borate [5,26]. In addition, oxidation of -OH groups to aldehydes is also another option to functionalize and cross-link GG [27]. Even though GG possesses various fascinating properties, intrinsic limitations of GG remain due to its hydrophilicity, leading to uncontrollable swelling properties, as well as its susceptibility to bacterial contamination and rapid biodegradation. Chemical modification of GG is, therefore, of great importance to extend its applicability [28].

Benzoic acid (BA) and its derivatives have been well-known for their chelating capacity and various types of intermolecular interaction such as hydrogen bonding and π stacking [29–35]. BA derivatives, therefore, were widely used to synthesize numerous metal-organic frameworks (MOFs) [36–39] and recognize bioanalytes such as adrenaline and carnosine [40,41]. Moreover, BA can be found in various cosmetic products, medications and food as additives and preservatives to certain approved concentrations [42,43]. BA derivatives were also reported with beneficial antimicrobial, antifungal and antihepatotoxic activity [44–46].

This work aims to synergize GG with BA to offer novel properties based on the following hypotheses. Since BA contains a carboxylic acid functional group which might be deprotonated more readily than alcohol groups of GG, the anionic GG-BA could be more easily obtained at milder alkaline conditions once BA is conjugated to GG. With this ionic form, coordination compounds of GG-BA with various metal cations could also be explored effortlessly. In addition, the aromatic benzene ring on BA could decrease not only the hydrophilicity of GG, hence, overcoming the intrinsic hydrophilicity obstacles of GG, but also could assist the preparation of novel complex materials due to numerous intermolecular interaction that the aromatic benzene ring might offer. Moreover, because of the widely recognized biocompatibility, antimicrobial and antifungal activity of BA, the conjugation of GG with BA might enhance the material stability against bacterial contamination and biodegradation. In order to realize GG-BA, a simple synthetic protocol in water was established for the first time and the newly obtained product was characterized by various techniques such as ^{1}H NMR, UV–Vis, FTIR-ATR, XRD, SEM, TEM, contact angle and TGA-DSC. Computational chemistry was employed to provide valuable insights into electronic properties of GG-BA as well as its molecular orbital diagram and electronic transitions between molecular orbitals. The biocompatibility of GG-BA was confirmed in the study on mouse embryonic fibroblasts (MEF) and human mammary epithelial cells (MCF-10A) using WST-1 assay, which shows great potential for the development of biomaterials.

2. Materials and methods

2.1. Chemicals and reagents

2.1.1. Chemicals for synthesis
GG (MW = 220 kDa), 4-(bromomethyl)benzoic acid (BBA) 97%, sodium hydroxide (NaOH) 97%, hydrochloric acid (HCl) 37%, ethanol 98% (EtOH) and deuterated dimethylsulfoxide (DMSO-d_6) were purchased from Sigma-Aldrich. All chemicals were reagent-grade and used as received without further purification.

2.1.2. Chemicals for cell culture
Dulbecco's modified eagle medium (DMEM) and phosphate buffered saline (PBS) were purchased from Lonza. Fetal bovine serum (FBS), Dulbecco's modified eagle medium/Nutrient mixture F-12 (DMEM/F-12), Trypsin, ʟ-glutamine, and Penicillin/Streptomycin were purchased from Gibco. Human insulin, hydrocortisone, cholera toxin and glucose were purchased from Sigma-Aldrich. Epidermal growth factor (EGF) from Peprotech and cell proliferation reagent WST-1 from Roche were also purchased. All reagents were cell-culture grade.

2.2. Synthesis and preparation

2.2.1. Guar gum benzoic acid (GG-BA)
5.00 g of GG (30.875 mmol AGU) and 5.73 g of NaOH (138.94 mmol, 4.5 eq) were dissolved in 500 mL N$_2$-purged H$_2$O and the solution was stirred in 30 min at room temperature. 6.845 g of BBA (30.875 mmol, 1 eq) was then added into the solution and the mixture was kept under magnetic stirring overnight at room temperature. HCl (37%) was added to quench the reaction and acidify the solution to pH 1. Excess EtOH was used to precipitate and purify GG-BA. The final product was dried in vacuum to yield 7.62 g of GG-BA (83.1% reaction yield).

2.3. Characterization

2.3.1. Proton nuclear magnetic resonance (^{1}H NMR) spectroscopy
^{1}H NMR spectra of samples were measured by Bruker AVANCE-III NMR-system 400 MHz (Bruker Inc., Billerica, MA, USA) at 298.15 K. Dry samples of GG and GG-BA were dissolved in DMSO-d_6 at 50 °C.

2.3.2. UV–Visible spectrophotometry
Solutions of all samples were prepared in H$_2$O at pH 1 and room temperature. UV–Vis spectra were measured in the range of 190 to 700 nm with a resolution of 0.5 nm, using Shimadzu UV-2501PC spectrophotometer (Shimadzu Inc., Kyoto, Japan) and quartz cuvettes.

2.3.3. Fourier-transform infrared spectroscopy - Attenuated total reflectance (FTIR-ATR) spectroscopy
Nicolet™ iS50 FTIR spectrometer (Thermo Scientific Inc., Waltham, MA, USA) equipped with a diamond crystal and a pressure gauge was used to record IR spectra. IR spectra were recorded in the wavenumber range of 400 to 4000 cm^{-1} with a resolution of 4.0 cm^{-1} and averaged from 64 scans.

2.3.4. Powder X-ray diffraction (XRD)
XRD spectra of GG and GG-BA were measured on Bruker D8 Discover (Bruker Inc., Billerica, MA, USA) diffractometer in a diffraction angle range between 10 to 80° and a resolution of 0.04° at room temperature. X-ray K780 (Cu Kα anode) generator was used at 40 kV voltage and 40 mA current.

2.3.5. Scanning electron microscopy (SEM)
LEO Gemini 1530 scanning electron microscope with thermo scientific ultradry silicon drift detector (Leo Electron Microscopy Inc., Thornwood, NY, USA) was used to study the morphology of GG and GG-BA samples. Samples were coated on conductive carbon adhesive tapes. Resultant SEM images were analysed and particle diameters were examined using Image J software. Particle size distribution curves were plotted based on 50 particles of GG and 150 particles of GG-BA.

2.3.6. Transmission electron microscopy (TEM)
JEM-1400 plus transmission electron microscope equipped with an OSIS Quemesa 11 Mpix bottom mounted digital camera (Jeol Ltd., Akishima, Tokyo, Japan) was also employed to characterize the morphology of GG and GG-BA samples. The acceleration voltage was kept at 80.00 kV, while the beam current was 55 μA. The samples were dispersed onto standard copper TEM grids and resultant TEM images were also analysed by Image J software.

2.3.7. Thermogravimetric analysis - differential scanning calorimetry (TGA-DSC)

Netzsch STA 449 F1 Jupiter thermogravimetric analyzer (Netzsch Instruments Inc., Featherstone, Wolverhampton, UK) was employed under N_2 inert atmosphere from 30 to 600 °C at a heating rate of 10 °C min^{-1}. N_2 flow rate was kept at 20 mL min^{-1}. Dry samples were kept in vacuum before the measurements and 2–10 mg of the dry samples were transferred to aluminium DSC pans. Resultant TGA, DTG, DSC curves were analysed by Netzsch TGA software.

2.3.8. Contact angle

Hydrophilicity and hydrophobicity of GG and GG-BA were studied by water static dripping contact angle experiments using a KSV CAM 200 Optical tensiometer (KSV Instruments Ltd., Helsinki, Finland) equipped with a LED light source and a CCD camera with telecentric zoom optics. FTIR hydraulic press was used to prepare 3 pellets of GG and 3 pellets of GG-BA under 10 t of pressure in 15 min for each sample (Fig. S8). For each pellet, 3 random locations were chosen to record the contact angles, hence, 9 measurements were carried out in total for GG and also for GG-BA. Small distilled water droplets of 2.0 μL were released on the film surface at the dispensing rate of 100 μL s^{-1}. Digital pictures were recorded automatically within 24 s for each measurement and CAM software using Young-Laplace fitting method was chosen to calculate the contact angles. From the right and left contact angles, average contact angles were calculated for each picture. The final average contact angles and standard deviations (SD) were then determined from those 9 measurements. The final average equilibrium contact angle was finally determined after 15 s when there was no significant change in the average contact angle values recorded (Fig. S11).

2.4. Computational study

All computational calculations were performed by Gaussian 16 program package. The geometry of all involved structures was fully optimized by the Austin-Frisch-Petersson (APFD) hybrid density functional theory (DFT) method with dispersion, combined with the 6–311+G(d,p) basis set [47]. The UV–Vis absorption wavelengths and oscillator strengths were calculated by means of time-dependent density functional theory (TD-DFT), using the same basis sets [48]. Molecular orbitals (MOs) and electrostatic potential maps of optimized geometry structures were calculated at the same level of theory and visualized using Gaussview 6 [49]. Solvent effects of water were evaluated by employing the self-consistent reaction field (SCRF) method with polarized continuum model (PCM) [50].
.

2.5. Biocompatibility study

2.5.1. Cell culture

Mouse embryonic fibroblasts (MEF) were cultured in DMEM (Lonza) containing 10% FBS (Gibco). Human normal breast cells (MCF-10A) were cultured in DMEM/F12 Medium (Gibco) containing 5% FBS (Gibco), 2 mM L-glutamine (Gibco), human insulin, (Sigma, 10 μg mL^{-1}), glucose (Sigma, 4.5 g L^{-1}), hydrocortisone (Sigma, 0.5 μg mL^{-1}), cholera toxin (Sigma, 0.1 μg mL^{-1}) and epidermal growth factor (EGF, Peprotech, 20 ng mL^{-1}), in a humidified incubator with 5% CO_2. MCF-10A cells were provided by Prof. Jukka Westermarck (Turku Bioscience Centre, Turku, Finland).

2.5.2. Biocompatibility study

MEF cells and MCF-10A cells were placed in a 96-well plate (three parallel wells for each concentration, Corning) at suitable starting cell density (3000 cells per well for 48 h-incubation of GG and GG-BA, and 2000 cells per well for 72 h-incubation of GG and GG-BA) in the complete growth medium at 37 °C, 5% CO_2 overnight. Then, the cell culture medium was replaced with a fresh medium containing GG or GG-BA at

indicated concentrations (0–4000 μg mL^{-1}) for 48 h and 72 h. The GG and GG-BA solutions were prepared in PBS. For WST-1 assay, 10 μL of WST-1 reagent (Roche) was dissolved in 100 μL complete growth medium to replace the GG or GG-BA-contained medium for each well. After two-hour-incubation in cell incubator, the absorbance was measured at 440 nm with a Varioskan™ LUX Multimode Reader (Thermo Scientific Inc., Waltham, MA, USA). WST-1 cell viability data are presented as the means ± standard deviations.

3. Results and discussions

3.1. Synthesis of GG-BA

Hydroxyl groups of GG were first activated by NaOH and the reaction was carried out in aqueous condition at room temperature, which offered a convenient and environmental friendly synthetic route. Nucleophilic substitution was performed on BBA to yield ether chemical bonds between GG and BA moieties (Fig. 1). The original high-molecular-weight GG material has good solubility in H_2O and poor solubility in polar aprotic solvents such as dimethylsulfoxide (DMSO). Meanwhile, the purified GG-BA product shows good solubility in both H_2O and DMSO, indicating the presence of BA moieties in GG-BA.

3.2. Characterization and computational study of GG-BA

3.2.1. Proton nuclear magnetic resonance (^{1}H NMR)

^{1}H NMR analysis of purified GG-BA product was carried out to confirm the successful chemical functionalization of GG and to determine the degree of substitution of GG-BA (Fig. 1 and Section 1 in supplementary data). While a satisfactory ^{1}H NMR spectrum of the original GG in DMSO-d_6 could not be obtained due to low solubility of GG in DMSO (Fig. S2), the ^{1}H NMR spectrum of GG-BA in DMSO-d_6 was easily received. This confirms the existence of BA moieties, which are chemically linked to GG. Aliphatic protons of galactomannan backbone in GG-BA exhibit signals with chemical shifts (δ) ranging between 3.4 and 5.0 ppm. Meanwhile, ortho and meta protons from BA moieties in GG-BA are apparent in the aromatic δ range from 7.3 to 8.0 ppm with equal intensity. The recorded aromatic signals of GG-BA are consistent with chemical shifts of aromatic protons from BBA starting material (7.56 and 7.92 ppm, Fig. S1). Based on the intensity of aliphatic and aromatic protons from GG-BA, the degree of substitution of GG-BA is calculated as 0.1639, while the grafting density is 5.5% and the chemical formula for each anhydrous glucose unit (AGU) is approximated as $C_6H_{9.361}O_5(C_8H_7O_2)_{0.1639}$.
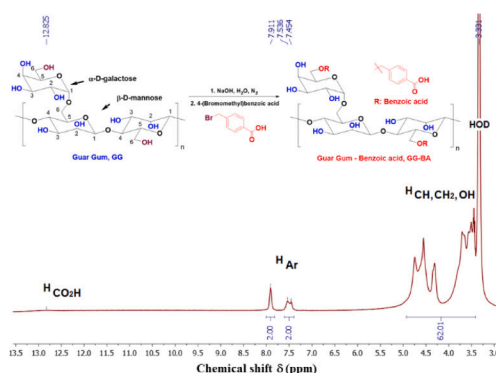

Fig. 1. ^{1}H NMR spectrum of GG-BA in DMSO-d_6.

3.2.2. UV–Vis spectrophotometry

Normalized UV–Vis absorption spectra of GG-BA, GG and BBA references were recorded from 190 to 700 nm in water at pH 1 (Fig. 2a). GG absorbs a wide range of UV–Vis radiation with two absorption maxima at 341.0 and 262.0 nm. Its UV absorption expands drastically towards 190 nm. BBA shows no significant absorption band in the visible range, while a major absorption maximum at 246.5 nm as well as a small absorption band around 290.0 nm are recorded. Similarly to BBA, GG-BA also exhibits no noticeable absorption band in the visible range, but similar absorption bands to BBA in the middle-UV region between 200 and 300 nm. Since the galactomannan backbone and BA moieties of GG-BA have different molar absorption coefficients, as well as almost no absorption band in the visible range is observed, the UV–Vis spectrum of GG-BA can be mainly attributed to the UV–Vis absorption of the newly introduced BA moieties. Comparing to BBA, the absorption maximum of GG-BA spectrum is blue-shifted from 246.5 nm to 236.5 nm. In addition, a small absorption band around 280 nm of GG-BA might be due to either the blue-shifted absorption of BA moieties or the absorption of galactomannan backbone.

3.2.3. Computational study on electronic properties

In an effort of correlating electronic transitions in GG-BA and its experimental UV–Vis absorption data, DFT calculation using APFD/6311+G(d) has been used to model a monomer of GG-BA and study its electronic properties [47]. This is because APFD, including treatments of dispersion effects, represents the best trade-off between accuracy and computational cost for a relatively large system such as GG-BA. Together with 6311+G(d), the model provides good accuracy while being feasible for use on typical computer workstations. The calculation was performed in the presence of water (using SCRF keyword) to mimic the aqueous condition of the UV–Vis measurements. The optimized structure and electrostatic potential (ESP) surface of GG-BA monomer are shown in Fig. 2c and S3. Theoretical UV–Vis absorption spectra of BBA reference and GG-BA monomer (Fig. 2b) were calculated by TD-DFT method to reach a good agreement with the experimental UV–Vis spectra (i.e., calculated absorption maxima at 238.3 and 252.7 nm of GG-BA monomer and BBA, comparing to 236.5 and 246.5 nm for experimental GG-BA and BBA respectively). The calculated UV–Vis absorption band around 238.3 nm of GG-BA monomer is composed of five different electronic transitions from highest occupied molecular orbitals HOMO-4, HOMO-3, HOMO-2, HOMO-1 and HOMO to lowest unoccupied molecular orbitals LUMO. The calculated HOMO-LUMO energy gap of GG-BA monomer is determined as 5.260 eV, which corresponds to 235.7 nm (Fig. 2d). The slight difference between 235.7 and 238.3 nm is
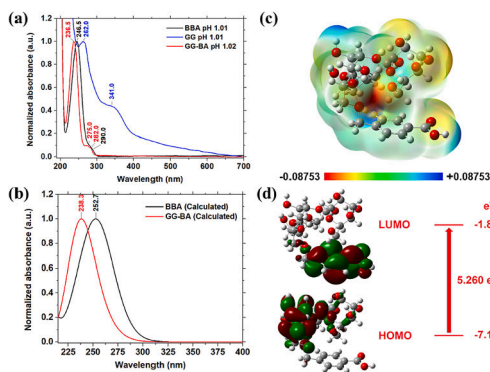
due to electronic effect of water solvent and this also indicates that the HOMO-LUMO electronic transition contributes mainly to the absorption maximum of GG-BA monomer at around 238.3 nm. Moreover, a blue shift in the wavelength of absorption maxima is also observed in the calculated spectra. The MO diagram of GG-BA monomer from HOMO-4 to LUMO+2 can be found in Fig. S4.

3.2.4. Fourier-transform infrared spectroscopy (FTIR)

FTIR spectra of original GG and GG-BA were measured to show that typical IR absorption bands of galactomannan backbone can be observed in both spectra (Fig. 3a). The O—H stretching vibration with intermolecular hydrogen bonding can be found in the wavenumber range between 3000 and 3500 cm^{-1}, followed by C—H stretching of CH_2 group with wavenumber between 2800 and 3000 cm^{-1}. The absorption band of 1645 cm^{-1} is due to ring stretching while strong absorption peaks of 1143, 1065 and 1012 cm^{-1} show C-OH bond, CH_2OH stretching and CH_2 twisting vibrations, respectively. A typical peak of 867 cm^{-1} for galactose and mannose is also observed [51–53]. By comparing IR spectra of GG and GG-BA, the presence of BA moieties in GG-BA can be confirmed. The characteristic C=O stretching absorption band from carboxylic acid groups of GG-BA appears at 1694 cm^{-1}, which is similar to the C=O stretching absorption band of BBA reference at 1678 cm^{-1} (Fig. S5). The C—O stretching vibration from carboxylic acid groups is also observed in GG-BA spectrum at 1255 cm^{-1}, while the IR spectrum of BBA reference shows a strong absorption band for that type of vibration at 1287 cm^{-1} (Fig. S5). The O—H stretching vibration wavenumber of hydroxyl functional groups shifts from 3330 to 3358 cm^{-1}, indicating an increase in the O—H bond strength of GG-BA. This can be explained as the intermolecular hydrogen bonding strength in GG-BA decreases, comparing to that of GG, due to the presence of hydrophobic BA moieties [54].

3.2.5. X-ray diffractometry (XRD)

Fig. 3b shows X-ray diffractograms of GG and GG-BA. Both materials possess broad peaks at similar 2θ values of 17.84, 18.36, 43.12 and 43.72°, showing amorphous phase structure of GG and GG-BA. The slightly broader peak of GG-BA at 18.36° indicates smaller particle size and/or lower crystallinity of GG-BA particles.

3.2.6. Scanning electron microscopy (SEM) and transmission electron microscopy (TEM)

Fig. 4 shows scanning electron micrographs and particle size distribution curves of GG and GG-BA particles. SEM images of GG were not easily obtained since GG has low electrical conductivity, while it was easier to record SEM images for GG-BA. Both GG and GG-BA particles have irregular shapes. To determine the particle size, the shape of particles is approximated as spherical. The particle size distribution is then fitted by Gaussian functions to give average diameters of GG and GG-BA as 637 ± 16 nm and 196 ± 17 nm respectively. In addition, transmission electron micrographs show slightly smaller particle size, of around 400 to 600 nm for GG and around 100 to 200 nm for GG-BA (Figs. S6–7), comparing to SEM images. However, TEM still confirms a smaller particle size of GG-BA comparing to that of GG. The significant changes in
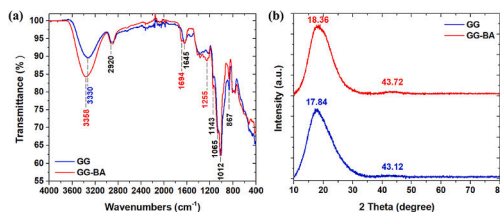

Fig. 2. Experimental (a) and calculated (b) UV–Vis absorption spectra of BBA, GG and GG-BA in water at pH 1. The optimized structure and ESP surface of GG-BA monomer (c) and its HOMO-LUMO gap and MO visualizations (d).

Fig. 3. FTIR spectra of GG and GG-BA (a). XRD spectra of GG and GG-BA (b).
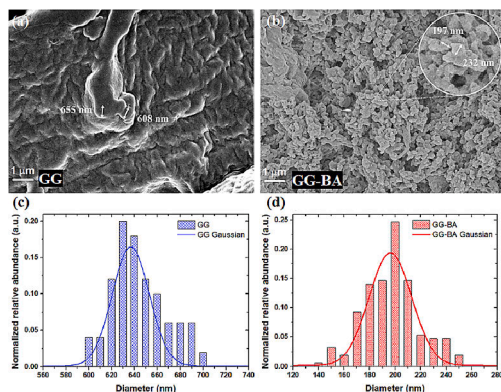
Fig. 4. SEM images (a, b) and particle size distribution curves (c, d) of GG and GG-BA.

particle size between GG and GG-BA can be explained due to the dissolution of GG in water and precipitation of GG-BA product by ethanol during the chemical functionalization.

3.2.7. Contact angle

Static contact angles of distilled water droplets on film surface of GG and GG-BA were measured to study the effect of BA on a decrease in hydrophilicity of GG-BA comparing to GG. In general, contact angles can be correlated to surface energy and roughness, hence, surface wettability and hydrophobicity of materials. The larger the contact angle, the lower the surface energy and higher the surface roughness, resulting in the lower wettability, lower hydrophilicity or higher hydrophobicity of a surface. Hydrophilic, hydrophobic and superhydrophobic surfaces typically have water contact angles of less than 90°, greater than 90° and above 150°, respectively [55–57]. Fig. S9 shows water contact angles on a representative GG reference film. In the first 10 s, contact angles of water on GG are recorded of around 90° on average, which is contradictory to the hydrophilic nature and high water-solubility of GG. In the next 14 s, GG quickly moves from the film surface into the water droplet and starts swelling, hence, contact angles of GG cannot be determined eventually. The same phenomenon is observed in all 9 repetitive measurements on GG. This could be because GG were pressed very strongly into solid films during the sample preparation, therefore, water wetting on the hydrophilic GG surface cannot be established immediately. Then, due to the strong interaction between hydrophilic GG and water droplet, the GG area, which is in direct contact with water, is quickly softened and GG can move from the film to the water droplet. Regarding GG-BA, contact angles of water on GG-BA film surface are well established during 24 s of measurement, in the range between 70 and 60° (Fig. S10). The surface of GG-BA film remains stable during all the measurements and the average equilibrium contact angle of water on GG-BA is determined as 66.0° (Fig. S11), suggesting that GG-BA is still mainly hydrophilic. Based on the observations from these contact angle measurements and the solubility of GG and GG-BA in water and DMSO from NMR measurements (Section 3.2.1), the presence of BA conjugated to GG (GG-BA) can be associated with the decrease in hydrophilicity of GG-BA comparing to GG.

3.2.8. Thermal analysis

In order to study thermal properties of GG and newly prepared GG-BA, TGA-DSC measurements were performed. TGA, DSC and derivative of weight loss (DTG) thermograms of the two materials are shown in Fig. 5a, b. An initial weight loss due to water desorption is observed on
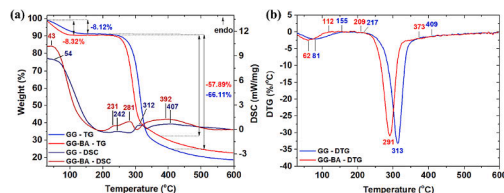

Fig. 5. TGA, DSC thermograms (a) and DTG thermograms (b) of GG and GG-BA in N₂.

DTG at around 62 and 81 °C for GG-BA and GG, respectively. While GG shows a gradual weight loss of 8.12% as the temperature reaches 155 °C, a weight loss of 8.32% of GG-BA is complete at a lower temperature, of around 112 °C. Moreover, DSC curves also show large endothermic peaks for water evaporation processes at temperature less than 200 °C. These DTG, TGA and DSC results are consistent with the previous observations on the decrease in hydrophilicity and the decrease in intermolecular hydrogen bonding of GG-BA due to chemically linked BA groups on GG. Thermal decomposition of galactomannan chains occurs in the temperature range from 209 to 373 and from 217 to 409 °C for GG-BA and GG, with the largest weight loss at 291 and 313 °C based on DTG, respectively. These decomposition temperature ranges are characteristic for galactomannan polysaccharides in N₂ inert atmosphere [51]. In addition, DSC thermograms show three endothermic events at around 231, 281, 392 °C for GG-BA and 242, 312, 407 °C for GG. Temperature and enthalpy values of thermodynamic events of GG and GG-BA are summarized in Table 1. Even though the thermal decomposition of GG-BA happens at a lower temperature range than that of GG, a smaller weight loss of 57.89% is observed in GG-BA while 66.11% is the weight loss of GG from TGA thermograms. This might be due to the smaller grain size of GG-BA comparing to that of GG, resulting in higher surface area of GG-BA particles. The higher surface area allows a much faster and more efficient heat transfer process, hence, lowering the decomposition temperature range of GG-BA.

3.3. Biocompatibility of GG-BA

As mesenchymal and epithelial cells are the two main types of cells that consist of tissues and organs, the most widely used MEF and MCF-10A were chosen to examine the biocompatibility of GG-BA. WST-1-based colorimetric assay is widely used in the detection of cell proliferation, survival and cytotoxicity after drug and biological material treatments on cells [58–60]. The working principle of the assay is based on the conversion of the light-red tetrazolium salt WST-1 (added earlier to the cell culture medium) into the dark-red formazan by the electron coupling reagent and mitrochondrial succinate-tetrazolium-reductase system in the cell mitochondria. Within a certain concentration range, the absorbance of the solution and the cell survival is positively correlated. In this study, a concentration range from 0 to 4000 μg mL⁻¹ for GG-BA together with GG as a control was examined. The obtained values were then standardized by untreated cells (concentration = 0). Fig. 6 shows that after 48 h of treatment up to 4000 μg mL⁻¹, both GG and GG-

Table 1
Temperature and enthalpy values of GG and GG-BA from DSC in N₂.

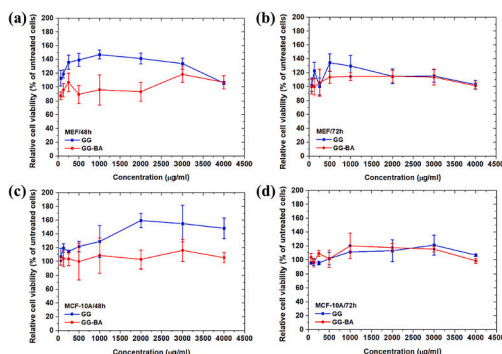| Sample	Peak number	Onset (°C)	T (°C)	Endset (°C)	ΔH (J g⁻¹)
GG	1	30	54	204	+785.5
	2	221	242	277	+7.3
	3	285	312	331	+29.2
	4	335	407	585	+149.5
GG-BA	1	30	43	194	+710.3
	2 + 3	202	231, 281	301	+61.2
	4	305	392	537	+193.4

Fig. 6. Relative cell viability of MEF (a, b) and MCF-10A (c, d) cells treated with GG and GG-BA after 48 and 72 h. The cell viability in each group is normalized to untreated cells by percentage (%).

BA show no cytotoxicity to the two cell types, and GG has a stronger effect on promoting cell proliferation than GG-BA. After 72 h of treatment, the promotion effects of GG and GG-BA on the two kinds of cells appear to be the same, and still no cytotoxicity effect is observed. These results strongly indicate that GG-BA has good biocompatibility to normal mesenchymal cells and epithelial cells. Optical micrographs of cell studies can be found in the supplementary data (Figs. S12–16).

4. Conclusions

In this study, GG has been successfully chemically functionalized with BA moieties to give novel GG-BA materials for the first time. The reported synthetic route in water is simple and environmentally friendly since organic solvents are avoided. Due to the presence of benzene rings, the solubility of GG-BA product in polar aprotic solvents such as DMSO increases noticeably. This allows a straightforward characterization of GG-BA using ^{1}H NMR in DMSO-d_6. Other spectroscopic techniques such as UV–Vis and FTIR spectroscopies also confirm the presence of BA in GG-BA. XRD shows amorphous phase structure of both GG and GG-BA. SEM shows irregular shapes of GG and GG-BA, as well as a significant decrease in particle size of GG-BA. Contact angle measurements and the increase in solubility of GG-BA in DMSO indicate a decrease in hydrophilicity of GG-BA comparing to that of GG. TGA-DSC in N_2 atmosphere shows a lower thermal decomposition temperature and a smaller weight loss of GG-BA comparing to those of GG. Computational study on GG-BA shows good agreements with experimental data and gives a better understanding on the electronic properties of GG-BA. As GG-BA has shown good biocompatibility to living cells together with its rich coordination chemistry of benzoic acid moieties, GG-BA, therefore, is an excellent starting material for the development of new biomaterials such as hydrogels and coacervates for wound dressing, drug delivery, as well as bioadhesives.

CRediT authorship contribution statement

T.-A.L.: Conceptualization, Methodology, Investigation, Writing - Original Draft, Writing - Review & Editing. Y.G.: Methodology, Investigation, Writing - Review & Editing. J.-N.Z.: Methodology, Investigation, Writing - Review & Editing. H.Z.: Methodology, Writing - Review & Editing. T.-P.H.: Conceptualization, Supervision, Writing - Review & Editing, Project administration.

Declaration of competing interest

All authors reviewed and approved the final manuscript. The authors declare that they have no known competing financial interests or personal relationships that could have appeared to influence the work reported in this paper.

Appendix A. Supplementary data

Supplementary data to this article can be found online at https://doi.org/10.1016/j.ijbiomac.2021.11.180.

References

[1] B. Maji, 1 - Introduction to natural polysaccharides, in: S. Maiti, S. Jana (Eds.), Functional Polysaccharides for Biomedical Applications, Woodhead Publishing, 2019, pp. 1–31.

[2] F.G. Torres, O.P. Troncoso, A. Pisani, F. Gatto, G. Bardi, Natural polysaccharide nanomaterials: an overview of their immunological properties, Int. J. Mol. Sci. 20 (20) (2019) 5092.

[3] M.V.G. Paixão, R.D.C. Balaban, Application of guar gum in brine clarification and oily water treatment, Int. J. Biol. Macromol. 108 (2018) 119–126.

[4] E.R. Sujatha, S. Sivaraman, A.K. Subramani, Impact of hydration and gelling properties of guar gum on the mechanism of soil modification, Arab. J. Geosci. 13 (23) (2020) 1278.

[5] N. Thombare, U. Jha, S. Mishra, M.Z. Siddiqui, Borax cross-linked guar gum hydrogels as potential adsorbents for water purification, Carbohydr. Polym. 168 (2017) 274–281.

[6] N. Thombare, S. Mishra, M.Z. Siddiqui, U. Jha, D. Singh, G.R. Mahajan, Design and development of guar gum based novel, superabsorbent and moisture retaining hydrogels for agricultural applications, Carbohydr. Polym. 185 (2018) 169–178.

[7] C. Banerjee, S. Ghosh, G. Sen, S. Mishra, P. Shukla, R. Bandopadhyay, Study of algal biomass harvesting using cationic guar gum from the natural plant source as flocculant, Carbohydr. Polym. 92 (1) (2013) 675–681.

[8] B.S. Gupta, J.E. Ako, Application of guar gum as a flocculant aid in food processing and potable water treatment, Eur. Food Res. Technol. 221 (6) (2005) 746–751.

[9] A. Nakamura, M. Ozaki, K. Murakami, Elucidation of the aggregation mechanism of bentonite with cationic guar gum as flocculant and application to filtration, Colloids Surf. A Physicochem. Eng. Asp. 596 (2020), 124660.

[10] D.V. Carvalho, N. Loeffler, M. Hekmatfar, A. Moretti, G.-T. Kim, S. Passerini, Evaluation of guar gum-based biopolymers as binders for lithium-ion batteries electrodes, Electrochim. Acta 265 (2018) 89–97.

[11] Y. Huang, J. Zhang, J. Liu, Z. Li, S. Jin, Z. Li, H. Zhou, Flexible and stable quasi-solid-state zinc ion battery with conductive guar gum electrolyte, Mater. Today Energy 14 (2019), 100349.

[12] A. Gunasekaran, A. Sorrentino, A.M. Asiri, S. Anandan, Guar gum-based polymer gel electrolyte for dye-sensitized solar cell applications, Sol. Energy 208 (2020) 160–165.

[13] M.U.A. Khan, M.A. Raza, S.I.A. Razak, M.R. Abdul Kadir, A. Haider, S.A. Shah, S. Aftab, Novel functional antimicrobial and biocompatible arabinoxylan/guar gum hydrogel for skin wound dressing applications, J. Tissue Eng. Regen. Med. 14 (10) (2020) 1488–1501.

[14] P. Orsu, S. Matta, Fabrication and characterization of carboxymethyl guar gum nanocomposite for application of wound healing, Int. J. Biol. Macromol. 164 (2020) 2267–2276.

[15] R.R. Palem, K. Madhusudana Rao, T.J. Kang, Self-healable and dual-functional guar gum-grafted-polyacrylamidoglycolic acid-based hydrogels with nano-silver for wound dressings, Carbohydr. Polym. 223 (2019), 115074.

[16] S. Das, D. Bera, K. Pal, D. Mondal, P. Karmakar, S. Das, A. Dey, Guar gum micro-vehicle mediated delivery strategy and synergistic activity of thymoquinone and piperine: an in vitro study on bacterial and hepatocellular carcinoma cells, J. Drug Delivery Sci. Technol. 60 (2020), 101994.

[17] S. Sharma, S. Afgan, Deepak, A. Kumar, R. Kumar, l-Alanine induced thermally stable self-healing guar gum hydrogel as potential drug vehicle for sustained release of hydrophilic drug, Mater. Sci. Eng. C 99 (2019) 1384–1391.

[18] A. George, P.A. Shah, P.S. Shrivastav, Guar gum: versatile natural polymer for drug delivery applications, Eur. Polym. J. 112 (2019) 722–735.

[19] G. Sharma, S. Sharma, A. Kumar, A.A.H. Al-Muhtaseb, M. Naushad, A.A. Ghfar, F. J. Stadler, Guar gum and its composites as potential materials for diverse applications: a review, Carbohydr. Polym. 199 (2018) 534–545.

[20] G. Dodi, D. Hritcu, M.I. Popa, Carboxymethylation of guar gum: synthesis and characterization, Cellul. Chem. Technol. 45 (2011) 171–176.

[21] H. Gong, M. Liu, J. Chen, F. Han, C. Gao, B. Zhang, Synthesis and characterization of carboxymethyl guar gum and rheological properties of its solutions, Carbohydr. Polym. 88 (3) (2012) 1015–1022.

[22] W. Chen, Y. Bu, D. Li, Y. Liu, G. Chen, X. Wan, N. Li, Development of high-strength, tough, and self-healing carboxymethyl guar gum-based hydrogels for human motion detection, J. Mater. Chem. C 8 (3) (2020) 900–908.

[23] T. Reddy, S. Tammishetti, Gastric resistant microbeads of metal ion cross-linked carboxymethyl guar gum for oral drug delivery, J. Microencapsul. 19 (3) (2002) 311–318.

[24] R. Singh, S. Maity, B. Sa, Effect of ionic crosslink on the release of metronidazole from partially carboxymethylated guar gum tablet, Carbohydr. Polym. 106 (2014) 414–421.

[25] R.T. Thimma, S. Tammishetti, Study of complex coacervation of gelatin with sodium carboxymethyl guar gum: microencapsulation of clove oil and sulphamethoxazole, J. Microencapsul. 20 (2) (2003) 203–210.

[26] W. Xie, Z. Song, Z. Liu, X. Qian, Surface modification of PCC with guar gum using organic titanium ionic crosslinking agent and its application as papermaking filler, Carbohydr. Polym. 150 (2016) 114–120.

[27] L. Dai, L. Zhang, B. Wang, B. Yang, I. Khan, A. Khan, Y. Ni, Multifunctional self-assembling hydrogel from guar gum, Chem. Eng. J. 330 (2017) 1044–1051.

[28] R.R. Palem, G. Shimoga, K.S.V.K. Rao, S.-H. Lee, T.J. Kang, Guar gum graft polymer-based silver nanocomposite hydrogels: synthesis, characterization and its biomedical applications, J. Polym. Res. 27 (3) (2020) 68.

[29] K.V. Korpany, D.D. Majewski, C.T. Chiu, S.N. Cross, A.S. Blum, Iron oxide surface chemistry: effect of chemical structure on binding in benzoic acid and catechol derivatives, Langmuir 33 (12) (2017) 3000–3013.

[30] P. McArdle, Y. Hu, A. Lyons, R. Dark, Predicting and understanding crystal morphology: the morphology of benzoic acid and the polymorphs of sulfathiazole, CrystEngComm 12 (10) (2010) 3119–3125.

[31] L. Moreno-Gómez, F. Sánchez-Férez, T. Calvet, M. Font-Bardia, J. Pons, Zn(II) and Cd(II) monomer, dimer and polymer compounds coordinated by benzoic acid and 4-acetylpyridine: synthesis and crystal structures, Inorg. Chim. Acta 506 (2020), 119561.

[32] F. Qin, Y. Ma, L. Miao, Z. Wang, L. Gan, Influence of metal-ligand coordination on the elemental growth and alloying composition of Pt–Ni octahedral nanoparticles for oxygen reduction electrocatalysis, ACS Omega 4 (5) (2019) 8305–8311.

[33] C.V.K. Sharma, K. Panneerselvam, T. Pilati, G.R. Desiraju, Molecular recognition involving an interplay of O-H⋯O, C-H⋯O and π⋯π interactions. The anomalous crystal structure of the 1: 1 complex 3,5-dinitrobenzoic acid–4-(N, N-dimethylamino)benzoic acid, J. Chem. Soc. Perkin Trans. 2 (11) (1993) 2209–2216.

[34] W. Tang, M. Zhang, H. Mo, J. Gong, J. Wang, T. Li, Higher-order self-assembly of benzoic acid in solution, Cryst. Growth Des. 17 (10) (2017) 5049–5053.

[35] C.R. Vestal, Z.J. Zhang, Effects of surface coordination chemistry on the magnetic properties of MnFe2O4 spinel ferrite nanoparticles, J. Am. Chem. Soc. 125 (32) (2003) 9828–9833.

[36] R.A. Agarwal, N.K. Gupta, CO2 sorption behavior of imidazole, benzimidazole and benzoic acid based coordination polymers, Coord. Chem. Rev. 332 (2017) 100–121.

[37] K.P. Carter, J.A. Ridenour, M. Kalaj, C.L. Cahill, A thorium metal-organic framework with outstanding thermal and chemical stability, Chem. Eur. J. 25 (29) (2019) 7114–7118.

[38] M. Jahan, Q. Bao, J.-X. Yang, K.P. Loh, Structure-directing role of graphene in the synthesis of Metal−Organic framework nanowire, J. Am. Chem. Soc. 132 (41) (2010) 14487–14495.

[39] S. Yuan, T.-F. Liu, D. Feng, J. Tian, K. Wang, J. Qin, H.-C. Zhou, A single crystalline porphyrinic titanium metal–organic framework, Chem. Sci. 6 (7) (2015) 3926–3930.

[40] T.-P. Huynh, K.C.C. Bikram, W. Lisowski, F. D'Souza, W. Kutner, Molecularly imprinted polymer of bis(2,2′-bithienyl)methanes for selective determination of adrenaline, Bioelectrochemistry 93 (2013) 37–45.

[41] A. Wojnarowicz, P.S. Sharma, M. Sosnowska, W. Lisowski, T.-P. Huynh, M. Pszona, W. Kutner, An electropolymerized molecularly imprinted polymer for selective carnosine sensing with impedimetric capacity, J. Mater. Chem. B 4 (6) (2016) 1156–1165.

[42] J.R. Chipley, Sodium benzoate and benzoic acid, in: P.M. Davidson, A.L. Branen (Eds.), Antimicrobialsin Foods, Marcel Dekker, New York, 1993, pp. 11–48.

[43] W. Johnson, W.F. Bergfeld, D.V. Belsito, R.A. Hill, C.D. Klaassen, D.C. Liebler, F. A. Andersen, Safety assessment of benzyl alcohol, benzoic acid and its salts, and benzyl benzoate, Int. J. Toxicol. 36 (3_suppl) (2017) 5S–30S.

[44] B.-E. Amborabé, P. Fleurat-Lessard, J.-F. Chollet, G. Roblin, Antifungal effects of salicylic acid and other benzoic acid derivatives towards eutypa lata: structure–activity relationship, Plant Physiol. Biochem. 40 (12) (2002) 1051–1060.

[45] C. Gadgoli, S.H. Mishra, Antihepatotoxic activity of p-methoxy benzoic acid from Capparis spinosa, J. Ethnopharmacol. 66 (2) (1999) 187–192.

[46] E.-S. Park, W.-S. Moon, M.-J. Song, M.-N. Kim, K.-H. Chung, J.-S. Yoon, Antimicrobial activity of phenol and benzoic acid derivatives, Int. Biodeterior. Biodegrad. 47 (4) (2001) 209–214.

[47] A. Austin, G.A. Petersson, M.J. Frisch, F.J. Dobek, G. Scalmani, K. Throssell, A density functional with spherical atom dispersion terms, J. Chem. Theory Comput. 8 (12) (2012) 4989–5007.

[48] C. Adamo, D. Jacquemin, The calculations of excited-state properties with time-dependent density functional theory, Chem. Soc. Rev. 42 (3) (2013) 845–856.

[49] R. Dennington, T.A. Keith, J.M. Millam, GaussView, Version 6.1, Semichem Inc, Shawnee Mission, KS, 2016.

[50] G. Scalmani, M.J. Frisch, Continuous surface charge polarizable continuum models of solvation. I. General formalism, J. Chem. Phys. 132 (11) (2010), 114110.

[51] M.A. Cerqueira, B.W.S. Souza, J. Simões, J.A. Teixeira, M.R.M. Domingues, M. A. Coimbra, A.A. Vicente, Structural and thermal characterization of galactomannans from non-conventional sources, Carbohydr. Polym. 83 (1) (2011) 179–185.

[52] Z. Movasaghi, S. Rehman, D.I. ur Rehman, Fourier Transform Infrared (FTIR) spectroscopy of biological tissues, Appl. Spectrosc. Rev. 43 (2) (2008) 134–179.

[53] D. Mudgil, S. Barak, B.S. Khatkar, X-ray diffraction, IR spectroscopy and thermal characterization of partially hydrolyzed guar gum, Int. J. Biol. Macromol. 50 (4) (2012) 1035–1039.

[54] R.M. Silverstein, F.X. Webster, D.J. Kiemle, D.L. Bryce, Spectrometric Identification of Organic Compounds, 8th ed., Wiley, NJ, USA, 2014.

[55] K. Jayaramulu, F. Geyer, A. Schneemann, Š. Kment, M. Otyepka, R. Zboril, R. A. Fischer, Hydrophobic metal-organic frameworks, Adv. Mater. 31 (32) (2019) 1900820.

[56] K.-Y. Law, Definitions for hydrophilicity, hydrophobicity, and superhydrophobicity: getting the basics right, J. Phys. Chem. Lett. 5 (4) (2014) 686–688.

[57] K.L. Menzies, L. Jones, The impact of contact angle on the biocompatibility of biomaterials, Optom. Vis. Sci. 87 (6) (2010) 387–399.

[58] R. Kanchanapally, S. Deshmukh, S. Chavva, N. Tyagi, S. Srivastava, G. Patel, S. Singh, Drug-loaded exosomal preparations from different cell types exhibit distinctive loading capability, yield, and antitumor efficacies: a comparative analysis, Int. J. Nanomedicine 14 (2019) 531–541.

[59] I. Salcedo, C. Aguzzi, G. Sandri, M.C. Bonferoni, M. Mori, P. Cerezo, C. Caramella, In vitro biocompatibility and mucoadhesion of montmorillonite chitosan nanocomposite: a new drug delivery, Appl. Clay Sci. 55 (2012) 131–137.

[60] H. Tominaga, M. Ishiyama, F. Ohseto, K. Sasamoto, T. Hamamoto, K. Suzuki, M. Watanabe, A water-soluble tetrazolium salt useful for colorimetric cell viability assay, Anal. Commun. 36 (2) (1999) 47–50.

Supplementary Data:

Synthesis, characterization and biocompatibility of guar gum-benzoic acid

Trung-Anh Le[1], Yong Guo[2,3,4], Jun-Nian Zhou[2,3,5], Jiaqi Yan[23], Hongbo Zhang[2,3], Tan-Phat Huynh*,[1]

[1] Laboratory of Molecular Science and Engineering, [2] Pharmaceutical Sciences Laboratory, Faculty of Science and Engineering, Åbo Akademi University, Porthaninkatu 3–5, 20500 Turku, Finland;

[3] Turku Bioscience Centre, University of Turku and Åbo Akademi University, Turku, 20520, Finland;

[4] Department of Endocrinology, Key Laboratory of National Health & Family Planning Commission for Male Reproductive Health, National Research Institute for Family Planning, Beijing 100081, China;

[5] Experimental Hematology and Biochemistry Lab, Beijing Institute of Radiation Medicine, Beijing 100850, China

E-mail: tan.huynh@abo.fi

1. ¹H-NMR and DS calculation
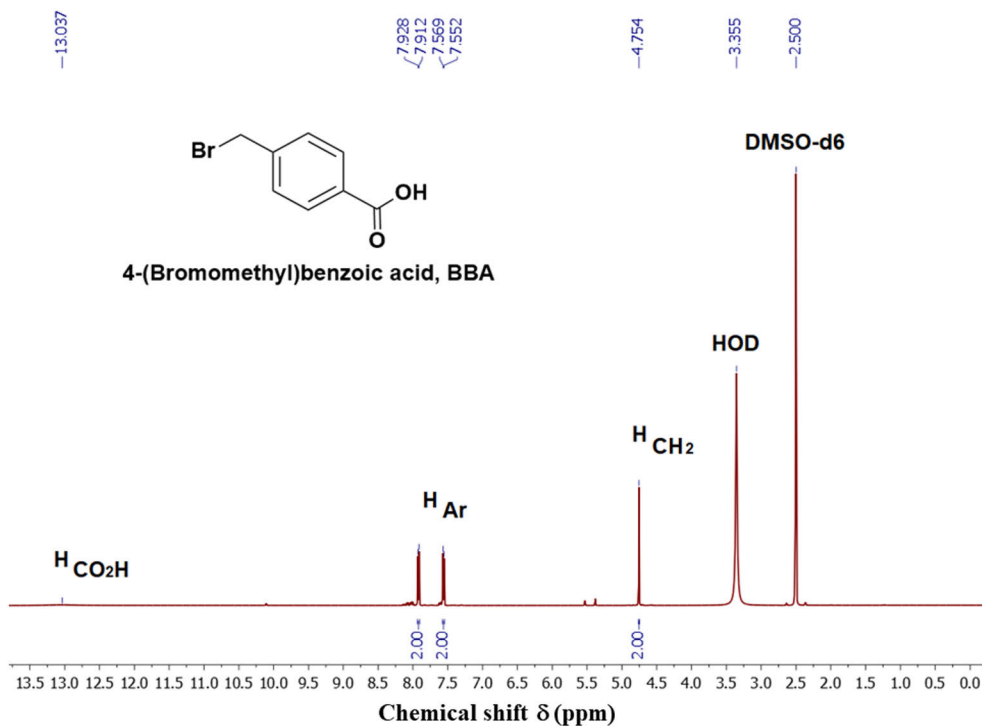
Figure S1. ¹H-NMR spectrum of 4-(bromomethyl)benzoic acid (BBA) in DMSO-d6
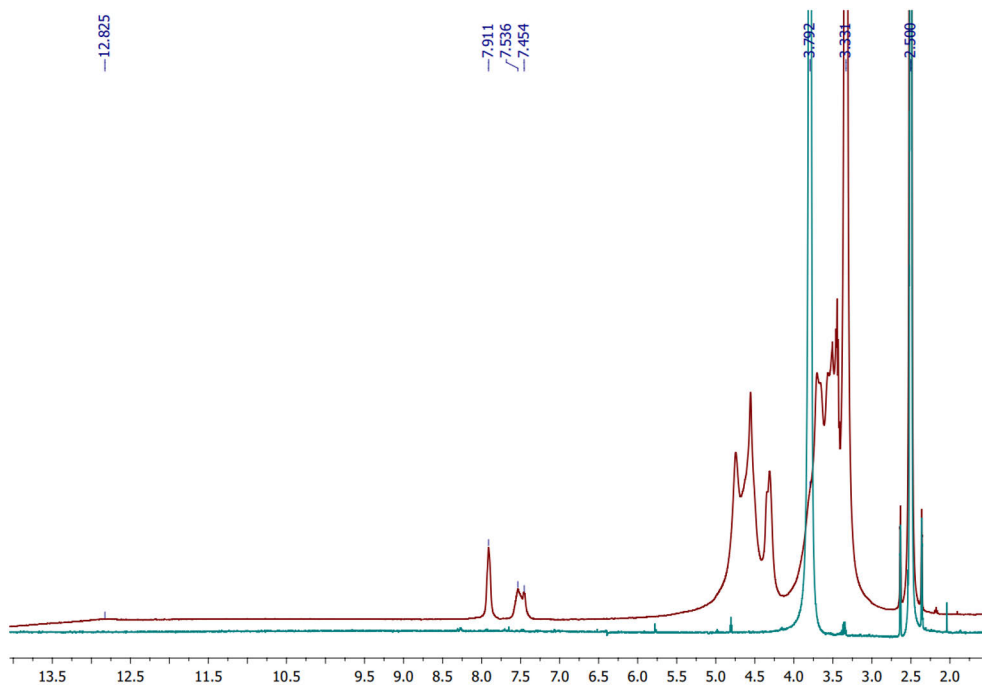
Figure S2. The superimposed ¹H-NMR spectra of GG (green) and GG-BA (red) in DMSO-d6

Calculations for the degree of substitution DS and grafting density GD of GG-BA in DMSO-d6 from ^{1}H-NMR spectrum:

For every x mol of BBA, there are 4x mol of H_{Ar} and 2x mol of H_{CH2}.

For every y mol of anhydrous glucose unit (AGU) of GG ($C_6H_{10}O_5$), there are 0 mol of H_{Ar} and 10y mol of $H_{CH, CH2, OH}$.

For every x mol of BA moieties replacing x mol of H from y mol of AGU from GG to form

GG-BA, $\dfrac{H_{Ar}}{H_{CH,CH_2,OH}} = \dfrac{4x}{10y-x+2x} = \dfrac{4.00}{62.01}$. Hence, $\dfrac{x}{y} = \dfrac{10}{61.01} \approx 0.1639$

The DS for each AGU of GG is 0.132 and the molecular formula of AGU can be approximated as $C_6H_{9.361}O_5(C_8H_7O_2)_{0.1639}$.

Each AGU of GG has 3 -OH groups and 0.1639 3 -OH group has been replaced by BA moieties hence, $GD = \dfrac{0.1639}{3}\ 100\% = 5.5\ \%$

2. Electronic properties of GG-BA
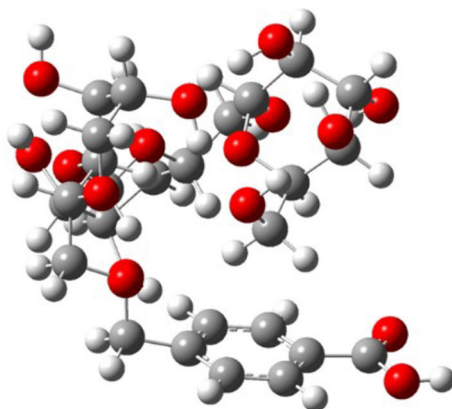
Figure S3. Optimized chemical structure of GG-BA monomer

MOs		eV
LUMO+2	——	-0.0909
LUMO+1	——	-0.7557
LUMO	——	-1.867
	5.260 eV	
HOMO	——	-7.127
HOMO-1	——	-7.3381
HOMO-2	——	-7.4045
HOMO-3	——	-7.538
HOMO-4	——	-7.628
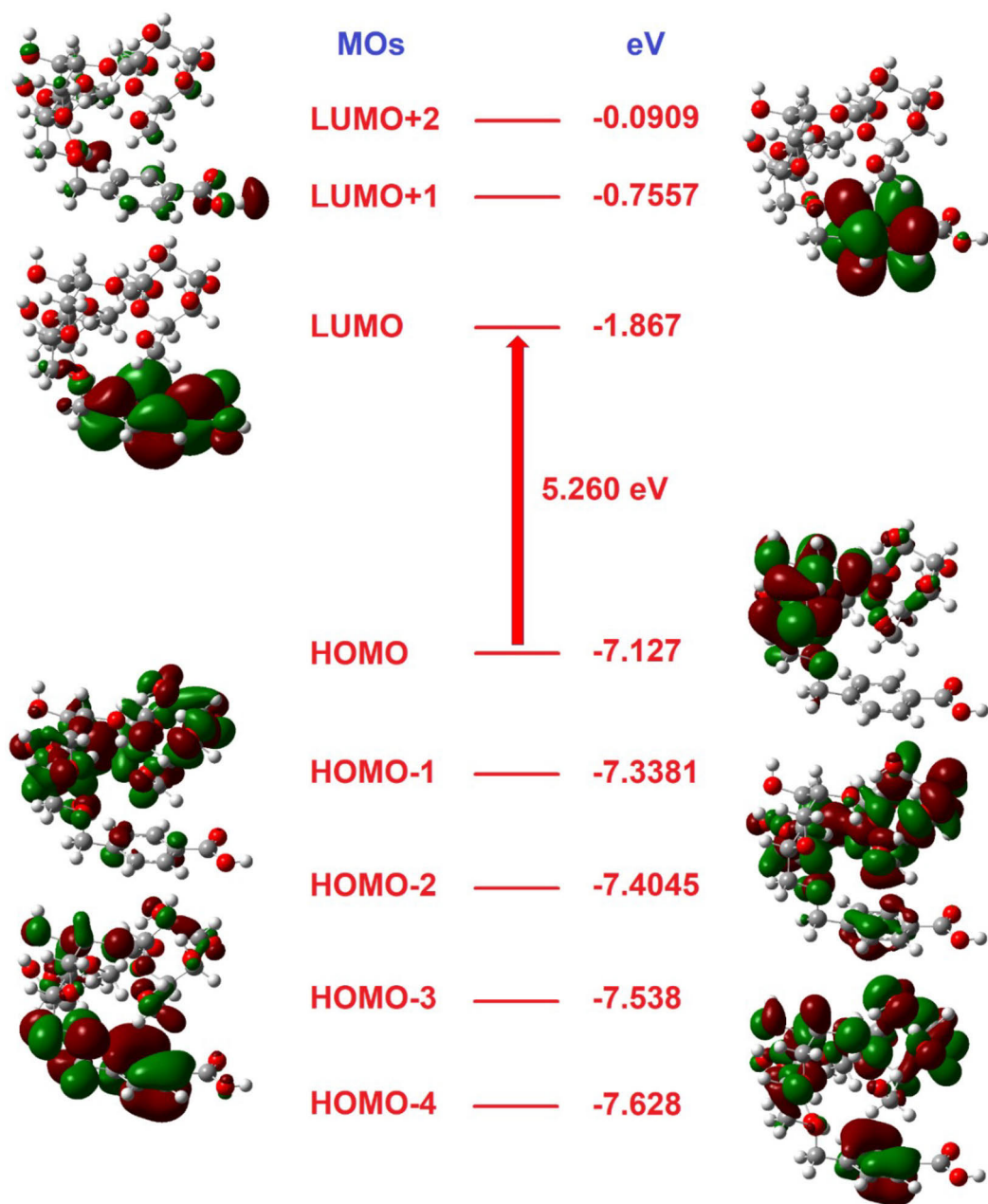
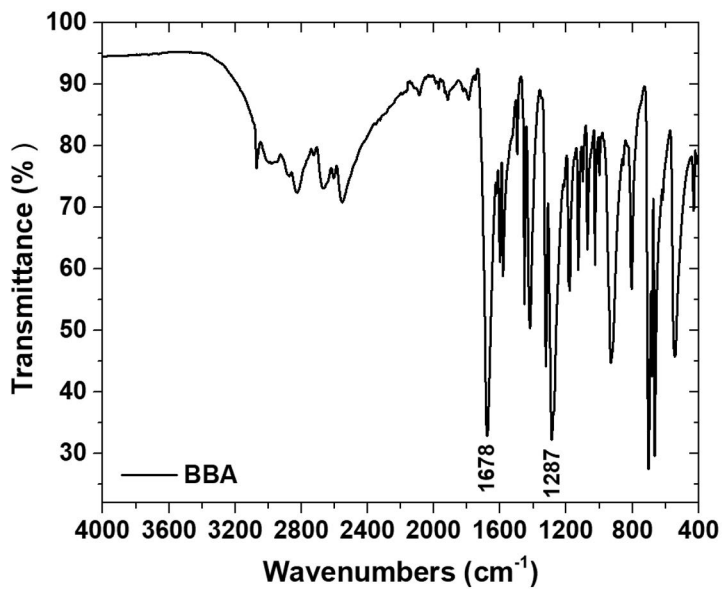Figure S4. MO diagram from HOMO-4 to LUMO+2 of GG-BA monomer

3. FTIR

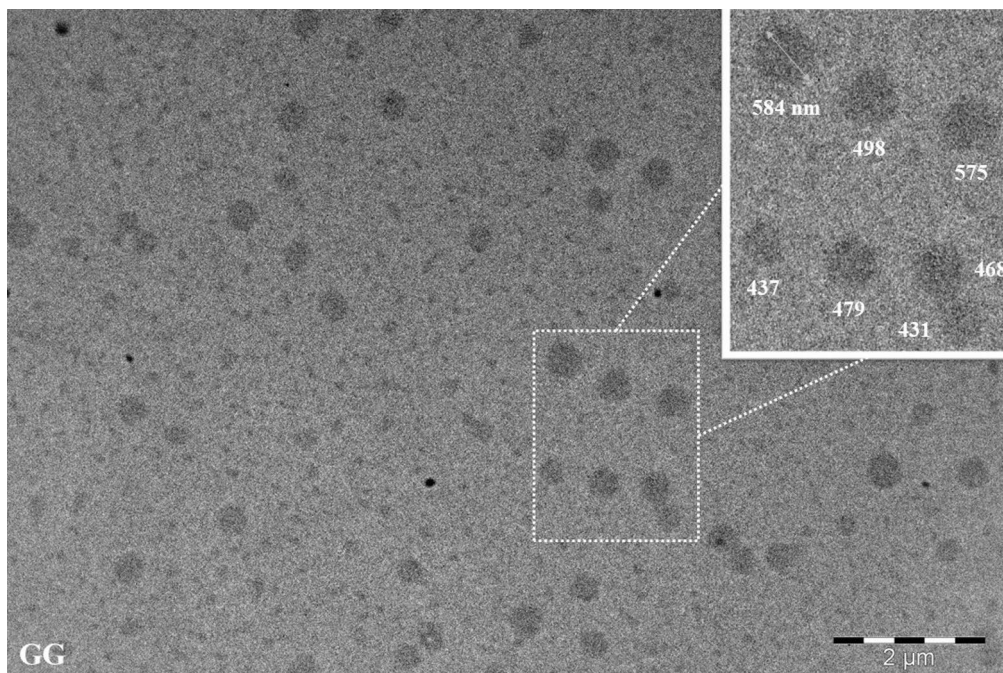

Figure S5. FTIR spectra of solid BBA reference

4. TEM
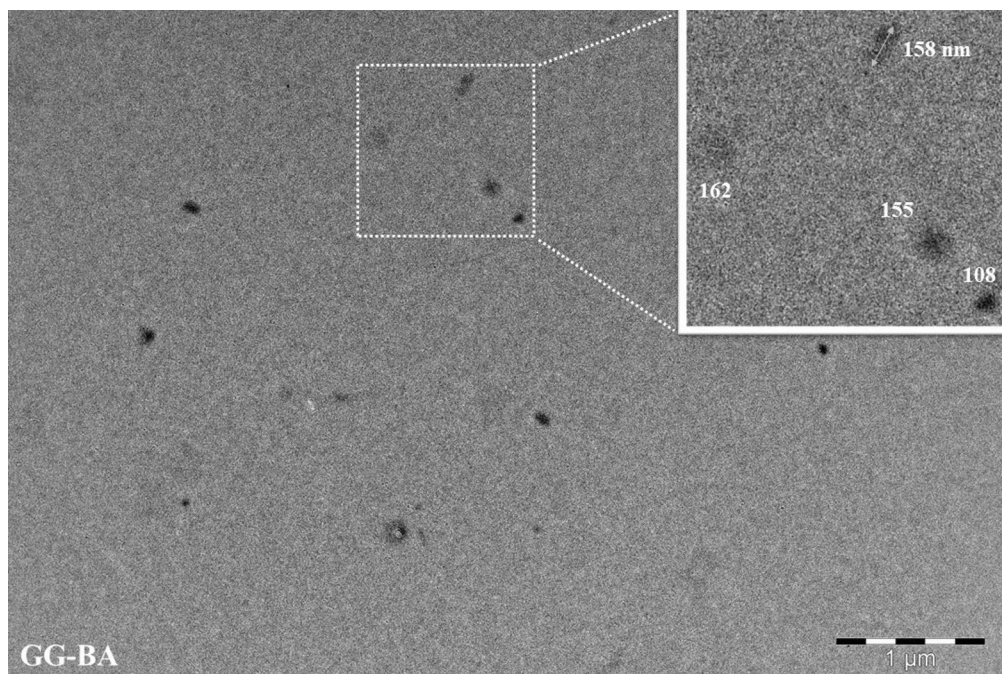

Figure S6. TEM image of GG particles
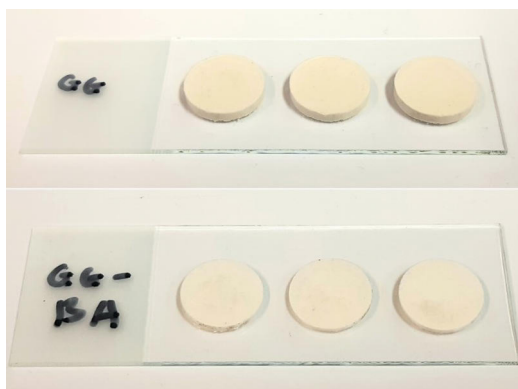
Figure S7. TEM image of GG-BA particles

5. Contact angle

Figure S8. GG and GG-BA pellets

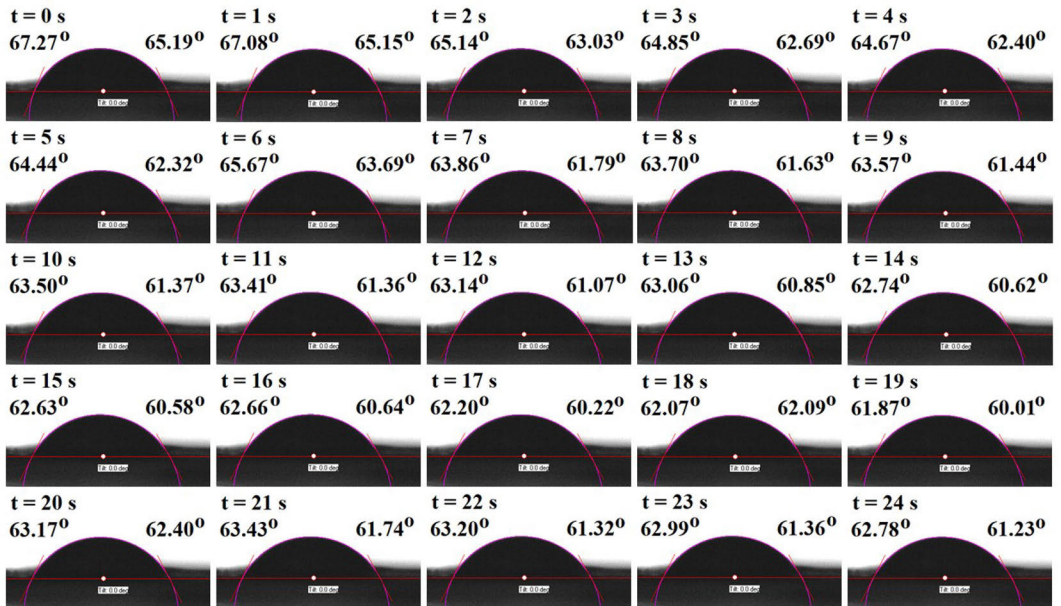Figure S9. Temporal changes of the contact angle of GG in 24 seconds

Figure S10. Temporal changes of the contact angle of GG-BA in 24 seconds
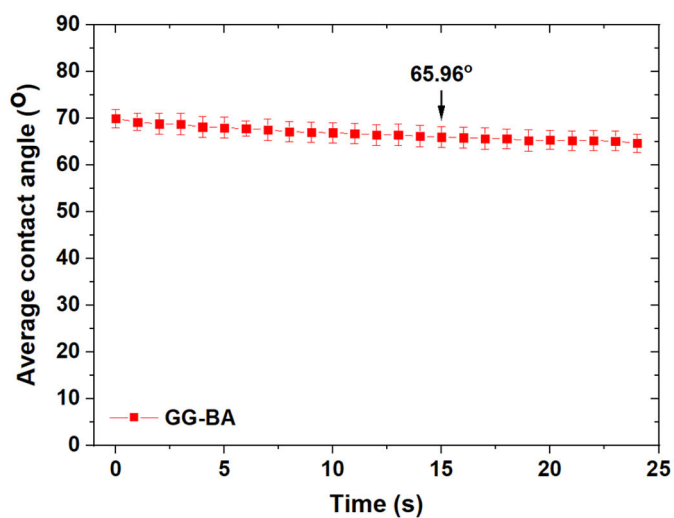
Figure S11. Average contact angle of GG-BA from 9 measurements of 3 GG-BA samples

6. Thermal analysis

Table S1. Enthalpy calculation of GG and GG-BA based on DSC curves

Sample	Peak number	Δt (s)	DSC (mW/mg)	ΔH = Area of DSC vs Δt (J/g)
GG	1	522	1.50479	+ 785.5
	2	168	0.04345	+ 7.3
	3	138	0.21159	+ 29.2
	4	750	0.199333	+ 149.5
GG-BA	1	492	1.443701	+ 710.3
	2 + 3	202	0.302971	+ 61.2
	4	305	0.634098	+ 193.4

7. Cell study
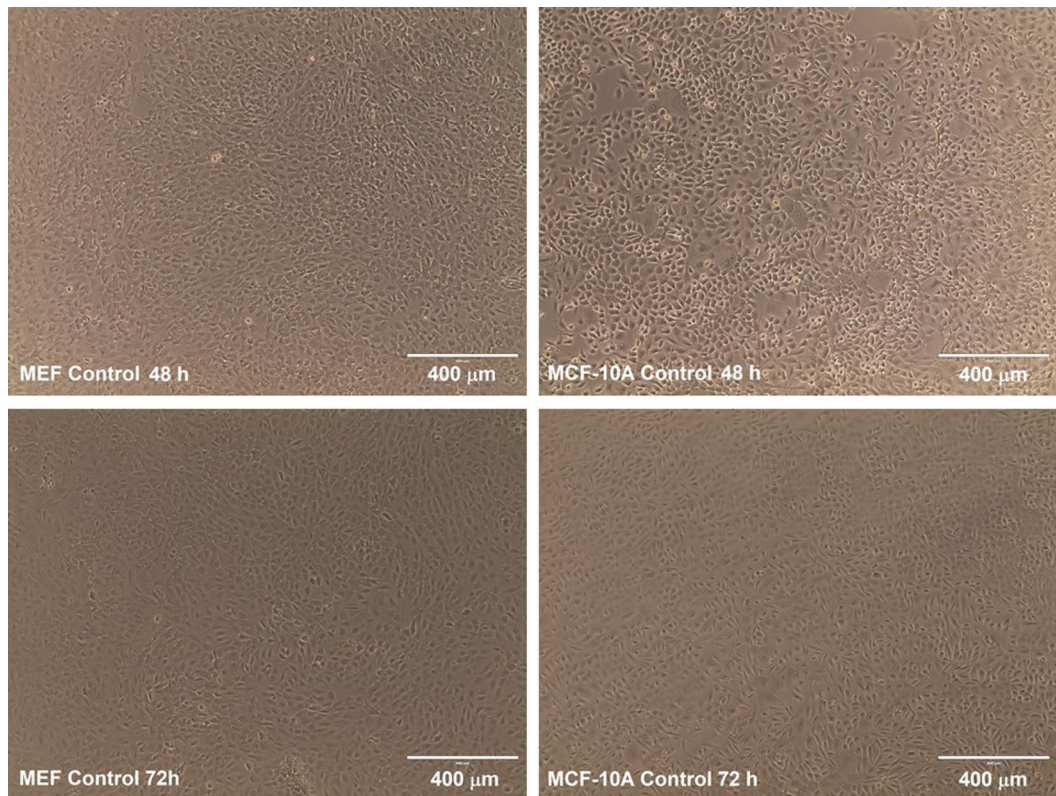

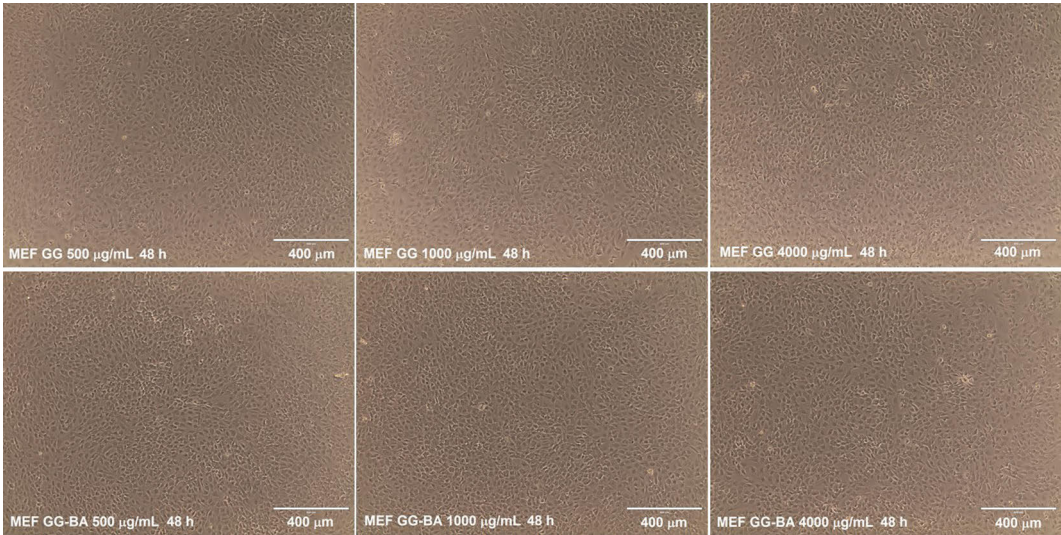Figure S12. Brightfield photo of MEF and MCF-10A control after 48 and 72 h

Figure S13. Brightfield photo of MEF GG and GG-BA 500 - 4000 µg/mL after 48 h
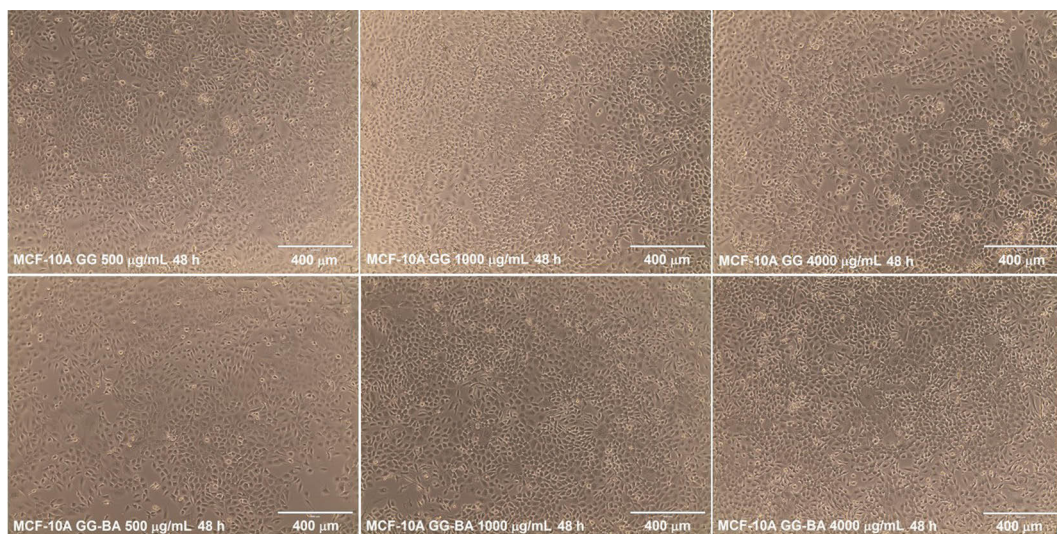
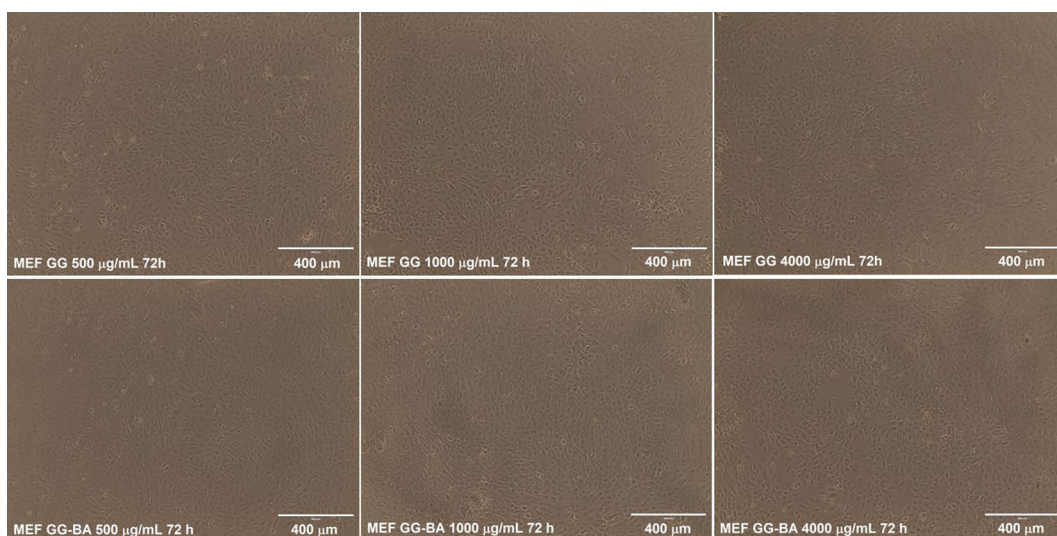Figure S14. Brightfield photo of MCF-10A GG and GG-BA 500 - 4000 µg/mL after 48 h

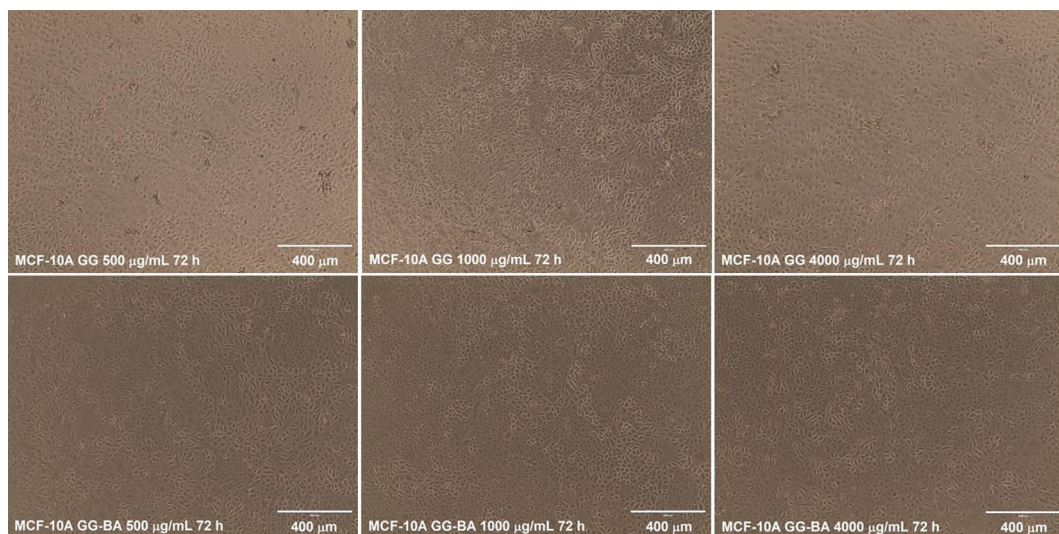Figure S15. Brightfield photo of MEF GG and GG-BA 500 - 4000 µg/mL after 72 h

Figure S16. Brightfield photo of MCF-10A GG and GG-BA 500 - 4000 µg/mL after 72 h